UNIVERSITÀ DEGLI STUDI DI TRIESTE

UNIVERSITÀ DEGLI STUDI DI TRIESTE

XXXVIII CICLO DEL DOTTORATO DI RICERCA IN

INGEGNERIA INDUSTRIALE E DELL'INFORMAZIONE

Finanziato dall'Unione europea - NextGenerationEU

Design Framework for Multiphysics Integration of DTT Divertor

Settore scientifico-disciplinare: IIND-03/B

DOTTORANDO
NICOLA MASSANOVA

COORDINATORE
PROF. FULVIO BABICH

SUPERVISORE DI TESI
PROF. DOMENICO MARZULLO

ANNO ACCADEMICO 2024/2025

Abstract

The design and verification of in-vessel components for fusion devices require the coordinated handling of complex geometric constraints, multiphysics loads, structural integrity criteria, and assembly requirements. Among these components, the divertor plays a critical role, being subjected to severe thermal, electromagnetic, and mechanical loads while operating under stringent spatial and remote handling constraints. Ensuring the structural reliability of such systems demands a consistent and traceable integration of design and analysis activities across multiple disciplines. This PhD thesis investigates the application of an integrated design and structural verification workflow to the Divertor Tokamak Test (DTT) divertor. The work follows the complete design path, from parametric geometry definition to multiphysics load assessment and detailed finite element structural analyses, within an iterative and coherent process. Particular attention is devoted to the role of interfaces, load paths, constraints, and assembly-related effects in determining the mechanical response of the divertor system. Starting from a parametric geometric description, the workflow enables the management of strong couplings between geometric constraints, cooling system requirements, remote handling interfaces, and structural performance. This approach supports controlled design iterations and ensures consistency between evolving design solutions and the associated multiphysics loading conditions.A significant part of the work is dedicated to the assessment of electromagnetic loads induced by plasma disruption events. A broad set of disruption scenarios was analyzed with specific reference to their structural impact on the divertor cassette, leading to the identification of the most critical loading condition. The resulting electromagnetic force distributions were benchmarked against JOREK simulations, providing confidence in their use for structural verification purposes. The structural behavior of the divertor cassette was investigated using advanced finite element models, including detailed representations of contact interactions, preload application procedures, and load sequencing. Within this context, two alternative outboard fixation concepts—the knuckle and wedges systems—were developed and assessed. Numerical analyses were complemented by a dedicated experimental campaign, involving the design and realization of a representative test rig to characterize the mechanical response of the fixation systems.

Contents

Abstract ..... **ii**

1 Introduction **1**

1.1 Global energy demand 1

1.2 Nuclear fusion 2

1.3 Magnetically confined fusion 3

1.4 The tokamak device 6

1.5 Eurofusion Roadmap: Toward the Realization of Commercial Fusion Power Plants 11

2 Divertor Tokamak Test (DTT) as a test facility for DEMOnstration Power Plant (DEMO) oriented solutions **13**

2.1 Role and objectives 13

2.2 Radial Build 18

2.3 Tokamak Main Components Layout 19

2.4 Magnetic Configurations 21

2.5 Divertor role in the reactor 24

3 DTT Divertor Design workflow: from CAD to multiphysics integration **28**

3.1 Design Workflow 31

3.2 Divertor Requirements 33

3.3 Divertor Poloidal Profile Definition 37

3.4 Divertor Design Rationale 39

3.4.1 Plasma Facing Components (PFC) 39

3.4.2 Cassette Body 45

3.4.2.1 Manufacturing issue 49

3.4.2.2 Uncompressed configuration 55
3.4.3 Fixation Systems 60
3.4.3.1 DTT Divertor fixation system test rig prototyping 77
3.4.3.1.1 Knuckle fixation system 78
3.4.3.1.2 Wedges fixation system 80
3.4.3.1.3 Prototype hardware delivery 83
3.4.3.1.4 Acceptance tests 85
3.4.3.1.5 Deformation evaluation after assembly 89
3.4.4 Pipes stumps 91
3.4.5 CMM grasping interface 92
3.4.6 Diagnostic interfaces 94
4 JOREK crosscheck verification: benchmarking maxFEA results for DTT disruption simulation 96
4.1 Integrated Workflow for Electromagnetic Load Evaluation 96
4.2 Disruption simulation and Electromagnetic Loads Evaluation 98
4.2.1 Background overview on disruption phenomena 98
4.3 DTT data integration in Integrated Modeling and Analysis Suite (IMAS) 102
4.3.1 IMAS 102
4.3.2 Required IMAS ids for DTT JOREK disruption initialization 105
4.3.3 Machine description (pf_active ids, pf_passive ids, wall ids) 106
4.3.4 Equilibrium ids 117
4.3.5 Core_profile ids 123
4.3.6 Pf_active ids including current 126
4.3.7 DTT populated IMAS shots 127
4.4 JOREK background 128
4.5 DTT STARWALL-JOREK model building 133

4.6 DTT JOREK unmitigated disruption 134
4.7 DTT JOREK mitigated disruptions 137
4.7.1 Mitigated UVDE 137
4.7.2 Mitigated DVDE 141
4.8 JOREK – maxFEA Unmitigated Downward Vertical Displacement Event results comparison 146
5 DTT Divertor Cassette Body structural verification 150
5.1 Preload assessment 150
5.2 Structural assessment against operating and off normal conditions 153
5.2.1 Scope of the assessment 153
5.2.2 Geometry included in simulation 154
5.3 Engineering Model building 160
5.3.1 Mesh 160
5.3.2 Materials 162
5.3.3 Connections and boundary conditions 163
5.3.4 Loads step definition 171
5.3.5 Slow DVDE scenario EM load distribution interpolation 184
5.3.6 Solutions options and procedure 188
5.3.7 Displacement results 196
5.3.8 Stress results 200
5.4 Stress classification lines (SCL) linearized stress assessment 206
5.4.1 XM-19 components 209
5.4.2 AISI 316 LN components 212
5.5 Bolted connections assessment 214

5.5.1 Thermal quench PFU center lines force distribution (10.1850 s EM simulation time) 215

5.5.2 End of current quench PFU center lines force distribution (10.203 s simulation time) 217

5.5.3 Thermal quench assessment 218

5.5.4 End of current quench assessment 226

Conclusion and future work 232

Annex A – DTT Divertor System Requirements 234

Annex B - DTT required data and IDS for JOREK initialization 261

Annex C - Python routines for DTT IMAS shot integration 269

Routine for vessel loop discretization 269

Full routine for DTT IMAS Machine Description integration 270

Full routine for DTT IMAS integrated equilibrium scenario integration 281

Annex D – Set of contacts for structural assessment 297

Frictional contacts 297

Bonded contacts 300

Annex E – DTT Divertor Fixation System Test Rig Technical Drawings 305

Knuckle test rig 305

Wedges fixation system 305

Geared Knuckle 305

References 306

List of figures

Figure 1 Different energy sources global consumption overtime 1
Figure 2 Energy consumption per capita in each nation vs human development index 1
Figure 3 Schematic representation of deuterium tritium reaction 2
Figure 4 Tokamak main functional components 4
Figure 5 Stellarator main functional components 4
Figure 6 Tokamak magnetic confinement system, toroidal and poloidal magnetic field 7
Figure 7 Tokamak schematic diagram [12] 8
Figure 8 Typical diagnostic systems in a tokamak device 9
Figure 9 Tokamak fusion power plant schematic 10
Figure 10 Eurofusion road map showing the milestone and main devices needed to address all the main knowledge domains to be explored to reach a fusion power plant [13] 11
Figure 11 Poloidal cross-section of a tokamak plasma for DEMO with a single magnetic null divertor configuration, illustrating the regions of the plasma and the boundary walls where important PMIs and atomic physics processes take place. The characteristic regions are: (i) the plasma core, (ii) the edge region just inside the separatrix, (iii) the scrape-off-layer (SOL) plasma outside the separatrix, and (iv) the divertor plasma region, which is an extension of the SOL plasma along field lines into the divertor chamber. The baffle structure is designed to prevent neutrals from leaving the divertor. In the private flux region below the 'X' point, the magnetic field surfaces are isolated from the rest of the plasma.[20] 14
Figure 12 Attached vs detached plasma [22] 15
Figure 13 DTT machine schematic 17
Figure 14 Poloidal section of DTT main functional components 18
Figure 15 DTT magnetic system 20
Figure 16 DTT vacuum vessel and ports 20
Figure 17 DTT NNBI, ECRH, ICRH 21
Figure 18 Baseline magnetic configurations (for which DTT control systrem and geometry are already optimized) and future scenarios not optimized 23
Figure 19 ITER Divertor (blu) mounted in the tokamak 24
Figure 20 ITER Tungsten Divertor Outer Target (left)-ITER Divertor Cassette Body (right) 25
Figure 21 DTT Divertor cassette system 28
Figure 22 DTT divertor single module layout 28
Figure 23 Divertor Design Workflow 32
Figure 24 V-model schematic [40] 34
Figure 25 The DTT four target divertor scheme (targets in red) 37
Figure 26 The divertor options - (a) solution with "short" outer target – (b) solution with "long" outer target 38
Figure 27 Compatibility studies of DTT plasma magnetic configurations for "short" (blue line) and "long" (red line) outer target for – (a) SN – (b) XD – (c) SN-NT 38
Figure 28 Outer vertical target length optionsd 39
Figure 29 Lateral view of the three PFC: IVT, dome and OVT 40
Figure 30 Schematic representation of targets toroidal shaping 41
Figure 31 DTT PFU divertor assembly tolerance 41
Figure 32 Inter-cassette leading edge (being α the (exaggerated) grazing angle). 42
Figure 33 Orientation of the tilting (view from top) 42
Figure 34 PFC toroidal shaping (note different axes' orientation) 44
Figure 35 PFU support design 44
Figure 36 PFU supports layout 45
Figure 37 Divertor loop cooling circuit 46
Figure 38 Cassette body main features 47
Figure 39 Pumping region for neutral injection 48
Figure 40 Divertor sector (20°) 48

Figure 194 – Exploded view of cassette body 50
Figure 41 Faceted design for flange-back plates interfacing (figure shows the solution implemented on the OVT flange-back plate) 54
Figure 42 Seating surfaces for connection screws heads 55
Figure 43 Faceted interfaces modeled on back plates side 55
Figure 195 – Application of preload and locking of the knuckle system 56
Figure 196 – Deformation of the cassette under inverse load 57
Figure 197 – Strain on the cassette after preload 57
Figure 198 – Set of points used for reconstruction of the CAD model 58
Figure 199 – Positioning error on OVT and DOME backplates 58
Figure 200 – Positioning error on IVT backplate 59
Figure 44 Remote Handling dedicated sectors and ports 61
Figure 45 Four main frames of the simulation of right lateral cassette (second cassette right (SC-r)) removal by CMM in Case A (CMM – SC Grabbing Pose provided by CMM design team): 1) CMM grabs the SC-r; 2) CMM toroidally moves the SC-r towards the sector's centre; 3) CMM lifts up the SC-r to make it pass over the Outboard Divertor Coil; 4) CMM extracts the SC-r through the duct. 61
Figure 46 VNS and DTT Divertor- the bulky shape of VNS divertor would be too difficult to deform (with a reasonable amount of force) 63
Figure 47 DTT Divertor Fixation System 64
Figure 48 Fixation system components located in vessel 64
Figure 49 Knuckle first design iteration 65
Figure 50 Knuckle anchoring points 66
Figure 51 Knuckle case (knuckle cassette body interface) features 67
Figure 52 Nose features 68
Figure 53 Lower stop 69
Figure 54 Divertor parking position 69
Figure 55 Knuckle extraction 70
Figure 56 Divertor rigid displacement-nose engagement 71
Figure 57 Pin extraction 71
Figure 58 Central cassette coupled with dummy rail 72
Figure 59 Geared Knuckle alternatives 73
Figure 60 Geared Knuckle assy exploded view and BOM 74
Figure 61 CMM end effector anchored for preloading 75
Figure 62 Necessary torque at knuckle shaft axis, equivalent to 20kN preload 75
Figure 63 Paired wormgear-rack system 76
Figure 201 – Test rig CAD model coupled with Knuckle 79
Figure 202 – Test rig-Knuckle exploded view 79
Figure 203 – Test rig CAD model coupled with wedges fixation system 80
Figure 204 – Wedges fixation system section view 81
Figure 205 Wedges fixation system retracted and extended configuration 81
Figure 206 – Wedges mechanism exploded view 82
Figure 207 – DTT Divertor Test rig coupled with knuckle fixation system 83
Figure 208 – DTT Divertor Test rig coupled with wedges fixation system 83
Figure 209 – Knuckle fixation system 84
Figure 210 – Wedges fixation system 84
Figure 211 Extracted and retracted geared knuckle 85
Figure 212 Conical gears-worm gear train 85
Figure 64 Lateral cassette pipe stumps 91
Figure 65 In duct divertor feeding pipes routing 91
Figure 66 Welding tool 92
Figure 67 CMM grasping interface 93

Figure 68 Identified location for divertor diagnostic 94
Figure 69 EM loads evaluation-structural verification integrated workflow 97
Figure 70 List of IDS in the versione 4.0.0 of the IMAS Data Dictionary 102
Figure 71 Required ids for JOREK initialization 106
Figure 72 107
Figure 73 DTT magnetic coils poloidal profile integrated in IMAS 110
Figure 74 Vacuum Vessel and Ports CAD model 111
Figure 75 Stabilizing Plates CAD model 111
Figure 76 Example of pf_passive oblique loop 112
Figure 77 Example of a triplet of points defined to discretize the VV shells 113
Figure 78 DTT VV and SP discretization integrated in IMAS 114
Figure 79 Wall outline including First Wall and Divertor shape 115
Figure 80 DTT poloidal profile integrated in IMAS 116
Figure 81 left) 2D Contour of poloidal flux on the set grid); right) $q95$ vs poloidal flux 123
Figure 82 Main 1D quantities related to the end of the flat top of the reference SN scenario at full power (5.5 MA and 6T) 123
Figure 83 JINTRAC original profiles (pressure profile features the pedestal evidence of H-mode confinement) 125
Figure 84 JINTRAC psi, electron temperature, ion temperature, electron density vs $\rho norm$ 125
Figure 85 Main integrated core_profiles, consistent with equilibrium ids 126
Figure 86 DTT STARWALL model (left)-FE grid and Separatrix computed through free boundary equilibrium with JOREK and LCFS integrated in IMAS (right) 133
Figure 87 Unmitigated DVDE total thermal energy and $q95$ 134
Figure 88 Unmitigated DVDE 2D contour of temperature evolution 135
Figure 89 Unmitigated DVDE 2D contour of toroidal current density evolution 135
Figure 90 Unmitigated DVDE Radial and vertical position of the magnetic axis and the current center 136
Figure 91 Unmitigated DVDE Total plasma current and HALO current profiles 136
Figure 92Mitigated UVDE 2D contour of the electron temperature 139
Figure 93 Mitigated UVDE 2D contour of the toroidal current density (Jt) (it's clear that the time scale of the event is much smaller if compared to the unmitigated case) 139
Figure 94 Mitigated UVDE main plasma global quantities 140
Figure 95 Unmitigated DVDE-mitigated UVDE total plasma current comparison 140
Figure 96 Unmitigated DVDE-mitigated UVDE halo current comparison 141
Figure 97 Mitigated DVDE radial and vertical position of the plasma magnetic axis and current center 142
Figure 98 Mitigated DVDE 2D contour of the electron temperature 142
Figure 99 Mitigated DVDE 2D contour of the toroidal current density (Jt) 143
Figure 100 Mitigated DVDE plasma total thermal energy and internal inductance 144
Figure 101 Mitigated DVDE poloidal beta and edge safety factor 144
Figure 102 Unmitigated DVDE-Mitigated DVDE total plasma current comparison 144
Figure 103 Unmitigated DVDE-Mitigated DVDE halo current comparison 145
Figure 104 (left)Reference JOREK equilibrium LCFS – (right) Reference LCFS maxFEA equilibrium 146
Figure 105 Total toroidal plasma current comparison between maxFEA and JOREK unmitigated DVDE 147
Figure 106 Halo current comparison between maxFEA and JOREK unmitigated DVDE 148
Figure 107 JOREK-maxFEA unmitigated DVDE $Raxis$ and $Zaxis$ comparison 149
Figure 108 JOREK-maxFEA unmitigated DVDE $q95$ and $li3$ comparison 149
Figure 109 EM forces resultants on Divertor Cassette body(left) and PFCs (right) induced by 40 ms major DVDE 150
Figure 110 Knuckle pins not aligned (left picture); Knuckle pins aligned (right picture 151
Figure 111 $F(x)$(radial) nose constraint reaction 152
Figure 112 Knuckle outer pin total constraint force (joint reaction) 152
Figure 113 DTT divertor module and its interfaces 155
Figure 114 Minimum gap between two adjacent divertor modules 155

Figure 115 Bolted connections between knuckle case and cassette body;bolted connections between nose and cassette body -bolted connections between flanges and targets back plates (right) 157
Figure 116 DTT divertor CAD model, input for FEA vs Defeatured geometry included into the simulation 158
Figure 117 DTT divertor cassette body subject to verification process- Section of the DTT divertor cassette body....159
Figure 118 – Structural mesh 160
Figure 119 Region of major interest (high stress foreseen, contact definition etc.) 160
Figure 120 Detailed PFU support model....161
Figure 121 Ansys Mechanical APDL element shape testing summary 161
Figure 122 - Mesh element quality metrics....162
Figure 123 - Element jacobian ratio 162
Figure 124 Defeatured geometry included in simulation and related materials....162
Figure 125 Frictional contacts between nose and inboard rail....163
Figure 126 Frictional contacts between nose and cassette body nose pad 164
Figure 127 Frictional contact between knuckle lateral surfaces – knuckle case lateral surfaces 164
Figure 128 Frictional contact between knuckle dummy pins and knuckle case....165
Figure 129 Knuckle pins not aligned (left picture); Knuckle pins aligned (right picture)....165
Figure 130 Frictional contact between screw head and seting surface (left)- Bonded contact between bolt thread and back plate threaded hole 166
Figure 131 Cassette body components sharing topology....167
Figure 132 Graphic visualization of constraint equations generated for imposed bonded contacts and joints....170
Figure 133 Revolute joints set between knuckle outer pin holes-outboard rail holes, knuckle winding shaft holes-knuckle case winding shaft holes 170
Figure 134 - Fixed supports set on inboard rail and nose- Compression only support to simulate the lower stop....171
Figure 135 Bolt pretension application 173
Figure 136 Preload applied on knuckle case-knuckle surfaces....174
Figure 137 Surfaces subjected to normal operating pressure....176
Figure 138 - Disruptive event classification....176
Figure 139 Divertor EM loads resultant comparison (fast-slow disruptive event)....177
Figure 140 IVT EM loads resultant comparison (fast-slow disruptive event) 178
Figure 141 DOME EM loads resultants comparison (fast-slow disruptive event)....178
Figure 142 OVT EM loads resultants comparison (fast-slow disruptive event) 179
Figure 143 EM force distribution map imported on divertor structural model 180
Figure 144 – Force and moment resultants overtime (slow DVDE with 40 ms current quench duration)....181
Figure 145 Heat flux map on PFC and pipes centerlines....181
Figure 146 Elbow's surfaces affected by direct heat flux....182
Figure 147 Thermal map result of the thermal steady state simulation 183
Figure 148 Divertor mesh 184
Figure 149 Divertor FEM subsystems....184
Figure 150 CAD model PFC finger – Engineering model PFC finger (i.e. OVT in figure)....190
Figure 151 CAD model PFU pipes – Engineering model PFU pipes....190
Figure 152 (Right)CAD model Center of Mass position-(Left) Engineering model center of mass position 191
Figure 153 Section view of engineering model highlighting the feeding pipes holes only on one side....192
Figure 154 Knuckle rigid rotation about outboard rail pin axis during preload....196
Figure 155 ux, uy, uz displacement at step 4 (Preload + Pin contacts activation)....196
Figure 156 Total displacement at step 4 (Preload + Pin contacts activation)....197
Figure 157 ux, uy, uz displacement at step 5 (Preload + Pin contacts activation + Dead Weight)....197
Figure 158 Total displacement at step 5 (Preload + Pin contacts activation + Dead Weight)....198
Figure 159 X displacement at step 7 (Preload + Pin contacts activation +Dead Weight + Pressure + EM loads) 198
Figure 160 Y displacement at step 7 (Preload + Pin contacts activation + Dead Weight + Pressure + EM loads) 199
Figure 161 Z displacement at step 7 (Preload + Pin contacts activation + Dead Weight + Pressure + EM loads)....199

Figure 162 Total displacement at step 7 (Preload + Pin contacts activation + Dead Weight + Pressure + EM loads) 199
Figure 163 Equivalent von Mises stress contour on Divertor (Preload) 200
Figure 164 Equivalent von Mises stress contour on cassette body section (Preload) 201
Figure 165 Contact status - Equivalent von Mises stress -Contact pressure on nose (Preload) 202
Figure 166 Contact status - Equivalent von Mises stress -Contact pressure on knuckle – knuckle case (Preload) 202
Figure 167 Equivalent von Mises stress contour on Divertor (Preload + Dead Weight + Pressure) 203
Figure 168 Equivalent von Mises stress contour on cassette body section (Preload + Dead Weight + Pressure) 203
Figure 169 Outlet and inlet manifold 203
Figure 170 Outlet manifold Equivalent von Mises stress- Inlet manifold Equivalent von Mises stress 204
Figure 171 Equivalent von Mises stress contour on Divertor (Preload + Dead Weight + Pressure + EM loads) 204
Figure 172 Contact status - Equivalent von Mises stress -Contact pressure on knuckle – knuckle case (Preload + Dead weight + Pressure + EM loads) 205
Figure 173 Contact status - Equivalent von Mises stress -Contact pressure on knuckle – knuckle case (Preload + Dead Weight + Pressure + EM loads) 205
Figure 174 Equivalent von Mises stress contour on Divertor (Preload + Dead Weight + Pressure + EM loads + Thermal) 205
Figure 175 SDC/IC criterial levels vs loading categories and damage limits 206
Figure 176 Outboard elbow region for SCL A, SCL B, SCL C, SCL J definition 209
Figure 177 Inboard elbow region for SCL E, SCL F, SCL G definition 209
Figure 178 Outboard elbow region for SCL D, SCL H, SCL I definition 210
Figure 179 Region for SCL K, SCL L definition 212
Figure 180 Region for SCL N definition 212
Figure 181 Region for SCL N, SCL O, SCL P, SCL Q definition 212
Figure 182 PFC center lines keypoints on linear abscissa 215
Figure 183 PFC center lines keypoints on linear abscissa and Local CSs on PFU support 215
Figure 184 Local forces on linear abscissa-PFU 2 center line at thermal quench (10.1850 s)- Local forces on linear abscissa-PFU 3 center line at thermal quench (10.1850 s) 216
Figure 185 Local forces on linear abscissa-PFU 4 center line at thermal quench (10.1850 s) - Local forces on linear abscissa-PFU 5 center line at thermal quench (10.1850 s) 216
Figure 186 Local forces on linear abscissa-PFU 6 center line at thermal quench (10.1850 s) - Local forces on linear abscissa-PFU 7 center line at thermal quench (10.1850 s) 216
Figure 187 Local forces on linear abscissa-PFU 8 center line at thermal quench (10.1850 s) 216
Figure 188 Local forces on linear abscissa-PFU 2 center line at the end of the current quench (10.203 s) - Local forces on linear abscissa-PFU 3 center line at the end of the current quench (10.203 s) 217
Figure 189 Local forces on linear abscissa-PFU 4 center line at the end of the current quench (10.203 s) - Local forces on linear abscissa-PFU 5 center line at the end of the current quench (10.203 s) 217
Figure 190 Local forces on linear abscissa-PFU 6 center line at the end of the current quench (10.203 s) - Local forces on linear abscissa-PFU 7 center line at the end of the current quench (10.203 s) 218
Figure 191 Local forces on linear abscissa-PFU 8 center line at the end of the current quench (10.203 s) 218
Figure 192 Back plates targets-flange bolted connections IDs 219
Figure 193 Local coordinate systems defined to evaluate the solicitations on the screws 219
Figure 213 Frictional contacts between knuckle case surfaces and cassette body interface 297
Figure 214 Frictional contacts between IVT connection screws heads and IVT back plate flanges 297
Figure 215 Frictional contacts between Dome connection screws heads and Dome flanges 297
Figure 216 Frictional contacts between OVT connection screws heads and OVT flanges 298
Figure 217 Frictional contacts between knuckle case connection screw heads and knuckle case 298
Figure 218 Frictional contacts between nose connection screws heads and nose 298
Figure 219 Frictional contacts between IVT back plate and IVT flanges (as shown in figure the connection is faceted type) 299
Figure 220 Frictional contacts between OVT back plate and OVT flanges (as shown in figure the connection is faceted type) 299
Figure 221 Frictional contacts between Dome back plate and Dome flange (as shown in figure the connection is faceted type) 299
Figure 222 Bonded contacts between IVT back plate and PFU 300

Figure 223 Bonded contacts between DOME back plate and PFU 300
Figure 224 Bonded contacts between OVT back plate and PFU 300
Figure 225 Bonded contacts between IVT PFU and PFU supports 301
Figure 226 Bonded contacts between DOME PFU and PFU supports 301
Figure 227 Bonded contacts between OVT PFU and PFU supports 301
Figure 228 Bonded contacts between upper IVT pipes and PFU 302
Figure 229 Bonded contacts between inner manifold and IVT upper pipes 302
Figure 230 Bonded contacts between OVT upper pipes and PFU 302
Figure 231 Bonded contacts between outer manifold and OVT upper pipes 303
Figure 232 Bonded contacts between DOME-IVT pipes and IVT PFU 303
Figure 233 Bonded contacts between DOME-IVT pipes and DOME PFU 303
Figure 234 Bonded contacts between DOME-OVT pipes and OVT PFU 304
Figure 235 Bonded contacts between DOME-OVT pipes and DOME PFU 304
Figure 236 Bonded connections between bolts thread and back plates threaded holes 304

List of tables

Table 1 Pros and cons of tokamak and stellarator device 5
Table 2 Main DTT parameters 17
Table 3 Toroidal shaping of divertor PFC (global tilting). * These bevels are doubled to consider the effect of dome and OHT profile symmetrical shape) 42
Table 4 Monoblock toroidal shapin -The height of total bevel is the sum of inter-cassette and inter-MB bevels for dome and OHT. This applies only to side PFUs because the other PFUs are flat. 43
Table 5 Monoblock's support components chosen materials 45
Table 52 – Raw materials per component 49
Table 6 Geared knuckle main parameters 76
Table 7 Embedded divertor diagnostics 95
Table 8 Disruption scenario categorization 99
Table 9 DTT magnetic coil system coordinates, dimensions and number of turns 108
Table 10 DTT Machine Description shots 116
Table 11 a) Coordinate conventions for each COCOS index. COCOS ≤ 8 refers to ψ divided by (2π) and thus with $eBp = 0$ while COCOS ≥ 11 refers to full poloidal flux with $eBp = 1$. Otherwise COCOS = i and COCOS = 10 + i have the same coordinate conventions. The cylindrical (with the related $\sigma R\phi Z$ value) and poloidal (with $\sigma\rho\theta\phi$) right-handed coordinate systems are given as well. b) The indications in this subtable (last three columns) are assumingIp and $B0$ positive in the related coordinate system, that is in the direction of the related ϕ. 119
Table 12 Main variables contained in an EQDSK file, including grid geometry, magnetic flux data, flux-surface quantities, and plasma boundary definitions. 120
Table 13 0D Parameters related to the full power SN reference scenario(note that the included parameters are related to the end of the flat top at 43s) 121
Table 14 SN Full power scenario, coil currents and turns 126
Table 15 DTT IMAS official databases 127
Table 16 Sub systems integrated in the engineering model 158
Table 17 Summary of frictional contacts set 167
Table 18 Summary of bonded contacts set 168
Table 19 Contacts initial conditions 169
Table 20 – Load steps 172
Table 21 Bolts dimension and applied preload 173
Table 22 Comparison EM force and moment resultants of fast and slow disruptive event 179
Table 23 - Force and moment resultants comparison between force distribution on structural mesh and source EM on whole divertor .185
Table 24 Force and moment resultants comparison between force distribution on structural mesh and source EM on Inner vertical target (PFU + PFU supports+IVT back plate) 185
Table 25 Force and moment resultants comparison between force distribution on structural mesh and source EM on Outer vertical target (PFU + PFU supports+OVT back plate) 186
Table 26 Force and moment resultants comparison between force distribution on structural mesh and source EM on central target (PFU + PFU supports+IVT back plate). 186
Table 27 Force and moment resultants comparison between force distribution on structural mesh and source EM on Cassette body main shell. 187
Table 28 Comparison between mass and center of mass coordinate of CAD model and engineering model 191
Table 29 Force reactions on fixed supports 193
Table 30 Force reactions on compression only support (lower stop) 193
Table 31 Force reaction on fixed supports due to isolated load contribution 194
Table 32 Force reaction on compression only supports due to isolated load contribution 194
Table 33 Total force reactions (fixed supports + compression only) 195
Table 34 Force and moment resultants acting on divertor (Reference pole (0,0,0) of GCS) 195
Table 35 AISI 316 LN variation of $Keff, rect$ with irradiation displacement dose at 20-350 °C 207

Table 36 AISI 316 LN Sm values for unirradiated conditions 209
Table 37 XM-19 Sm values for unirradiated conditions 209
Table 38 XM-19 components verification results 210
Table 39 AISI 316 LN verification results 213
Table 40 OVT connections screws solicitations at the thermal quench 220
Table 41 IVT connections screws solicitations at the thermal quench 221
Table 42 Dome connections screws solicitations at the thermal quench 222
Table 43 OVT bolted connections assessment results at the thermal quench 223
Table 44 IVT bolted connections assessment results at the thermal quench 224
Table 45 Dome bolted connections assessment results at the thermal quench 225
Table 46 OVT connections screws solicitations at the end of current quench 226
Table 47 IVT connections screws solicitations at the end of current quench 227
Table 48 Dome connections screws solicitations at the end of current quench 228
Table 49 OVT bolted connections assessment results at the end of current quench 229
Table 50 IVT bolted connections assessment results at the end of current quench 230
Table 51 Dome bolted connections assessment results at the end of current quench 231
Table 53 pf_active ids required data for disruption simulation 261
Table 54 equilibrium ids required data for disruption simulation 265
Table 55 core_profiles ids required data for disruption simulation 266
Table 56 pf_passive required data for disruption simulation 267
Table 57 wall required data for disruption simulation 268

List of abbreviations

Abbreviation	**Meaning**
ADX	Advanced Divertor Experiment
CAD	Computer Aided Design
CB	Cassette Body
CMM	Cassette Multifuncional Mover
COCOS	COordinate COnventionS
CQ	Current Quench
CS	Central Solenoid
CT-DOME	Central Target
CTM	Cassette Toroidal Mover
DEMO	Demostrative Reactor
DIV	Divertor
DMS	Disruption Mitigation System
DN	Double Null
DOF	Degree Of Freedom
DPA	Displacements Per Atom
DVDE	Downward Vertical Displacement Event
EAST	Experimental Advanced Superconducting Tokamak
ECRH	Electron Cyclotron Resonance Heating

ELMs	Edge Localized Modes
EM	Electromagnetic
FAST	Fusion by Advanced Superconducting Tokamak
FEA	Finite Element Analysis
FEM	Finite Element Method
FTU	Frascati Tokamak Upgrade
HC	Halo Currents
HTS	High Temperature Superconductor
ICRH	Ion Cyclotron Resonance Heating
ID	Identificative
IDS	Interface Data Structure
IMAS	Integrated Modeling & Analysis Suite
ITER	International Thermonuclear Experimental Reactor
IT-IVT	Inner Target
JET	Joint European Torus
LCFS	Last Closed Flux Surface
MAST	Mega Ampere Spherical Tokamak
MAST-U	Mega Ampere Spherical Tokamak - Upgrade
MGI	Massive Gas Injection
MHD	Magneto Hydro Dynamic
MD	Machine Description
NBI	Neutral Beam Injection
NT	Negative Triangularity
OHT	Outer Horizontal Target
OT-OVT	Outer Target
OVT	Outer Vertical Target
PF	Poloidal Field
PFU	Plasma Facing Unit
PFV	Poloidal Field Variation
PFC	Plasma Facing Units -Poloidal Field Coil
RCC-MRX	Design and Construction Rules for Mechanical Components in High-Temperature Structures, Experimental Reactors, and Fusion Reactors
RE	Runaway electrons
RH	Remote Handling
SCL	Stress Classification Line
SDC IC	System Design Criteria – Invessel Components
SE	System Engineering
SFD	Snow Flakes Divertor

SN	Single Nulla
SOL	Scape off layer
SOLPS	Scrape off layer solver
SPI	Shattered Pellet Injection
SP	Stabilizing Plate
SS	Stainless Steel
SXD	Super X Divertor
TCV	Tokamak à Configuration Variable
TF	Toroidal Field
TFV	Toroidal Field Variation
TQ	Thermal Quench
UKAEA	United Kingdom Atomic Energy Authority
UVDE	Upward Vertical Displacement Event
VDE	Vertical Displacement Event
VNS	Volumetric Newtron Source
VS	Vertical Stabilization
VV	Vacuum Vessel
XD	X Divertor

1 Introduction

1.1 Global energy demand

Within the scientific community, particularly among physicists, problems are often examined through the lens of energy—its production, consumption, and transformation. Applying this perspective to human society reveals interesting insights into our energy demands and patterns. Throughout history, global energy consumption has steadily risen, experiencing significant acceleration in recent decades (Figure 1).

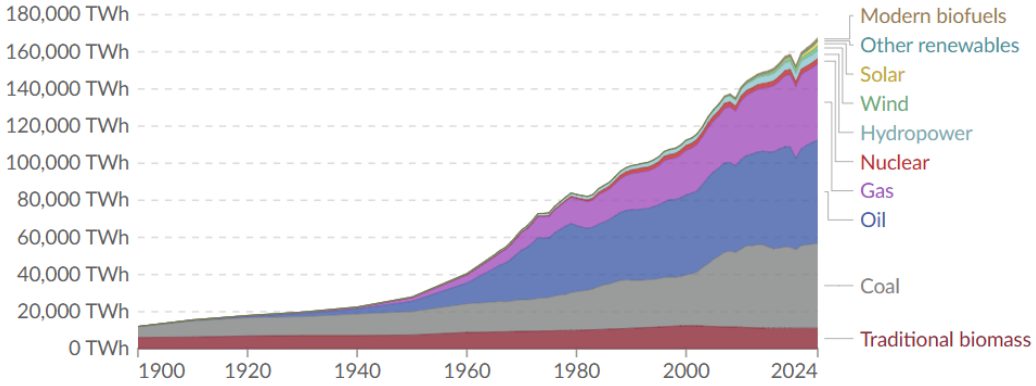

Figure 1 Different energy sources global consumption overtime

This increasing demand has necessitated the integration of new energy sources into the global energy mix. A strong correlation exists between a nation's Human Development Index and its per capita energy consumption, indicating that a certain level of energy consumption is required to achieve a high standard of living in developed countries (Figure 2).

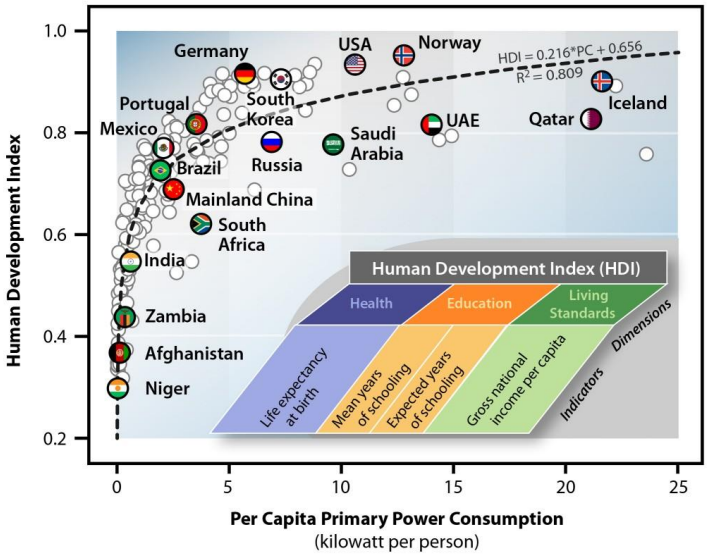

Figure 2 Energy consumption per capita in each nation vs human development index

While this correlation provides an instantaneous view, historical analyses of nations' catch-up paths to their current HDI levels further support the hypothesis that this trend will continue. These observations lead to the conclusion that future energy consumption will not decrease. The combination of a constantly growing global population and the drive for improved human conditions, particularly through increased access to electric energy, will inevitably cause energy demand to continue its upward trajectory.

1.2 Nuclear fusion

Nuclear fusion, the process powering stars like our Sun, offers a compelling solution for global energy demands, positioning itself as a key technology for human advancement in the shift towards sustainable energy. It promises an abundant, clean, and dependable power source with minimal environmental impact, thereby addressing the pressing need for carbon emission reduction and mitigating climate change. The principle of nuclear fusion involves combining light atomic isotopes, primarily deuterium (D) and tritium (T) at extremely high temperatures and pressures to form heavier nuclei, typically helium, while releasing substantial energy (Figure 3). This process, which mimics energy production in stellar cores, requires the creation and confinement of a plasma, defined as a quasi-neutral ionized gas composed of charged particles, at temperatures often exceeding $1.5 \cdot 10^8\ K$ (approximately 13 keV). At these conditions, the D-T reaction exhibits significant thermodynamic spontaneity and reactivity, making it the most promising candidate for terrestrial fusion reactors [1].

$$D\ +\ T\ \rightarrow\ n\ (14.07\ MeV)\ +\ 4\ He\ (3.52\ MeV)$$

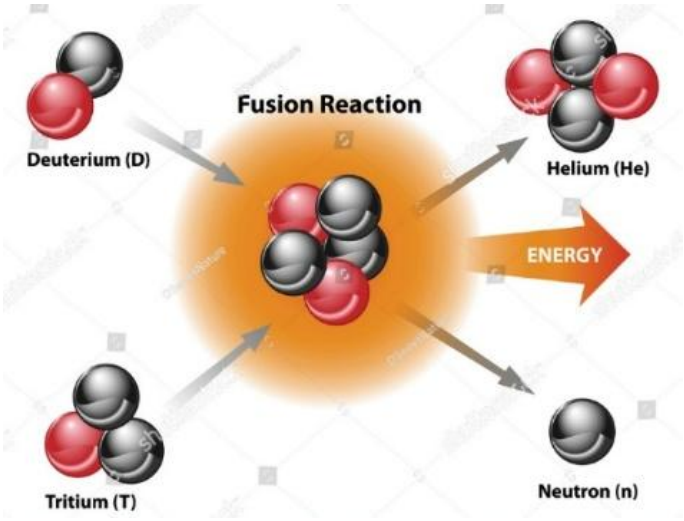

Figure 3 Schematic representation of deuterium tritium reaction

Pros of Fusion Energy:

- **Abundant Fuel Sources:** Deuterium is readily available from water, and tritium can be generated within the fusion reactor itself through reactions with lithium in a component called the breeding blanket.
- **Minimal Radioactive Waste:** Fusion reactions produce low-level radioactive waste that decays much faster than waste from nuclear fission, reducing long-term storage challenges.
- **Clean Energy Production:** Fusion does not rely on fossil fuels, leading to significantly lower greenhouse gas emissions over its lifecycle.
- **Inherent Safety:** Fusion reactors are designed to be inherently safe. The fusion process cannot undergo a runaway chain reaction, and any disruption to the plasma confinement or operating conditions would lead to an immediate cessation of the reaction, preventing a meltdown.

Cons and Challenges of Fusion Energy:

- **Technical Complexity:** Achieving and maintaining the extreme conditions required for sustained fusion is an immense technological and scientific challenge.
- **Material Limitations:** Developing materials that can withstand the intense heat fluxes, high neutron bombardment, and other harsh conditions within the reactor is critical.
- **Cost and Development Time:** Fusion research and development are capital-intensive, with significant construction costs and long timelines, indicating that widespread commercialization is still decades away

1.3 Magnetically confined fusion

To control the superheated plasma and prevent it from damaging reactor components, magnetic confinement fusion devices employ powerful magnetic fields. Various designs exist, including stellarators, reversed field pinches, and tokamaks.

A tokamak [2] [3] is a magnetic confinement device characterized by its toroidal (doughnut-shaped) vacuum chamber, which uses a combination of powerful magnetic fields to confine superheated plasma. The primary confinement in a tokamak is achieved through strong toroidal magnetic field coils, producing a magnetic field around the torus. An additional

poloidal magnetic field, crucial for shaping and stabilizing the plasma, is generated by external poloidal field coils and a large electrical current induced within the plasma itself by a central solenoid. This plasma current also contributes significantly to plasma confinement and heating (Figure 4).

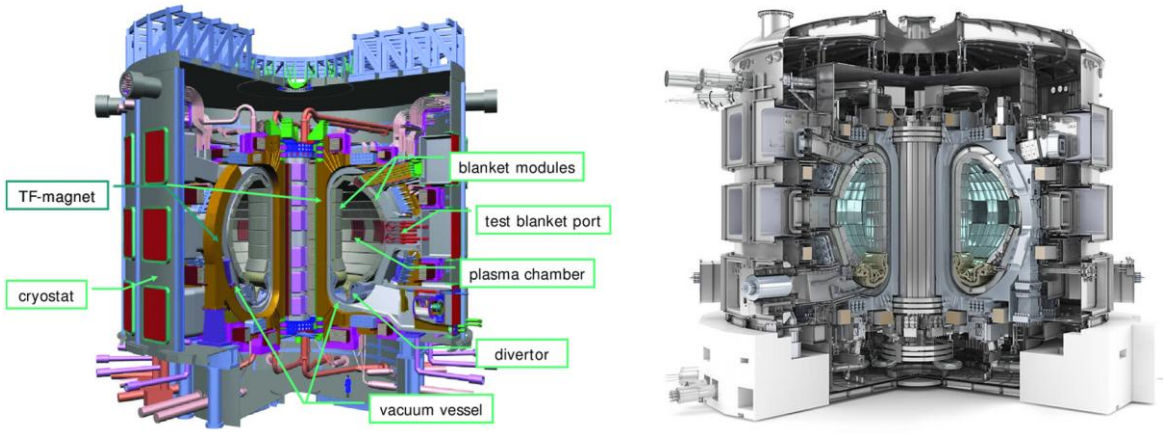

Figure 4 Tokamak main functional components

A stellarator [4], conversely, is also a magnetic confinement device for plasma, but it relies exclusively on complex, three-dimensional external magnetic coils to create the necessary helical magnetic field for plasma confinement. Unlike tokamaks, stellarators do not induce a large net current in the plasma to provide rotational transform, which means they do not suffer from current-driven instabilities that can plague tokamaks (Figure 5).

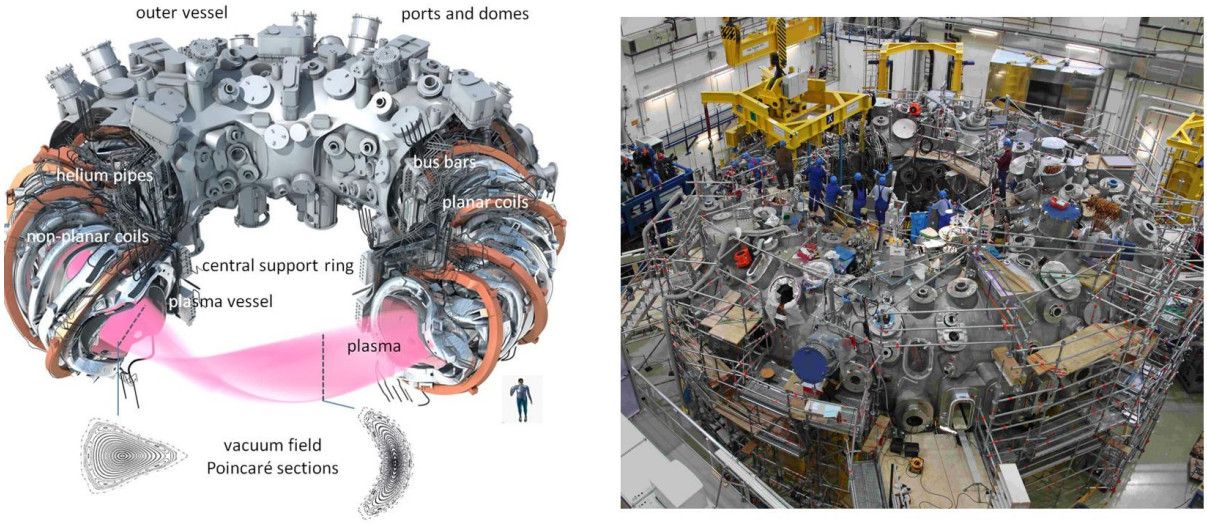

Figure 5 Stellarator main functional components

Table 1 includes a comparison of their confinement strategies, pros, and cons:

Table 1 Pros and cons of tokamak and stellarator device

Feature	Tokamak	Stellarator
Confinement Strategy	Utilizes a combination of toroidal field coils, poloidal field coils, and a significant plasma current (induced by a central solenoid) to create nested magnetic surfaces that confine the plasma.	Relies entirely on external, complex, non-axisymmetric magnetic coils to create a helical magnetic field for plasma confinement, without the need for a large net plasma current
Pros	Considered the most well-assessed and widely researched approach in magnetic confinement fusion, representing the highest-performance strategy toward achieving steady-state fusion. Less mathematically complex in its magnetic field configuration compared to stellarators	Inherently steady-state operation due to no reliance on plasma current for confinement, avoiding current-driven instabilities. Potentially less prone to plasma disruptions.
Cons	Requires a significant plasma current, which can lead to current-driven instabilities and limits continuous (steady-state) operation without advanced current drive techniques. More susceptible to plasma disruptions, which can cause significant damage.	Complex and challenging to design and construct due to the intricate 3D magnetic coil systems. Magnetic field optimization is computationally intensive.

1.4 The tokamak device

The tokamak design has emerged as the most well-assessed and widely researched approach in magnetic confinement fusion, representing the highest-performance strategy toward achieving steady-state. Its success has led to its adoption for major international projects like ITER, which aims to demonstrate the scientific and technological feasibility of fusion power [5]. While other concepts like stellarators are also pursued, tokamaks are considered less mathematically complex in their magnetic field configuration, which has historically made them more straightforward to design, build, and operate for experimental purposes, accelerating their development and assessment over stellarators.

A tokamak is an intricate machine with several key components working synergistically to achieve and sustain fusion reactions:

- **Vacuum Vessel:** This toroidal, or doughnut-shaped, chamber forms the primary containment for the plasma and is maintained under an ultra-high vacuum. Made typically of austenitic stainless steel, the VV is constructed in sections and must accommodate interfaces for in-vessel components and diagnostics [6]. During operation, the double-walled cavity of the VV may be filled with water to enhance neutron shielding [7].
- **Magnetic Confinement System** [8]**:** This system generates the powerful magnetic fields necessary to confine the plasma (Figure 6):
    - **Toroidal Field Coils:** These large, superconducting coils encircle the vacuum vessel, producing a strong magnetic field running around the torus. This field is crucial for the primary confinement of the plasma [9].
    - **Poloidal Field Coils:** Located outside the TF coils, these superconducting coils create magnetic fields that are perpendicular to the toroidal field. These poloidal fields are essential for shaping the plasma, stabilizing its position, and controlling its current [1].
    - **Central Solenoid:** Situated in the center of the torus, the central solenoid is a stack of independently fed superconducting coil modules. It plays a critical role in inducing a strong electrical current within the plasma itself, which generates an additional poloidal magnetic contributing to the overall magnetic flux swing for pulse operation [1].

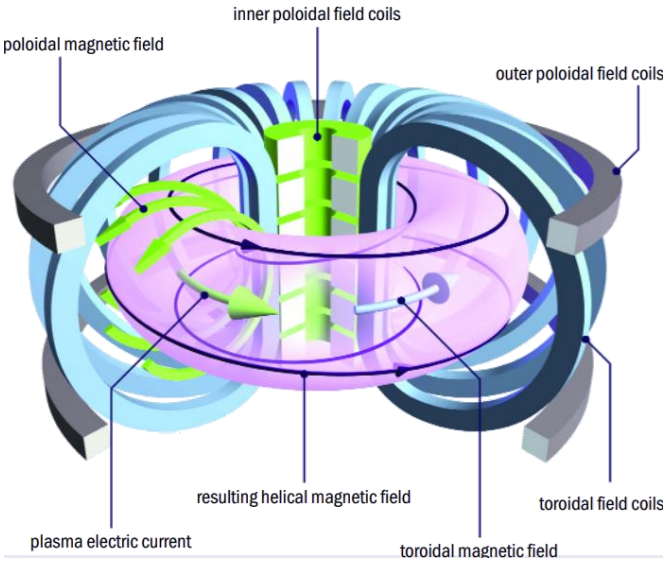

Figure 6 Tokamak magnetic confinement system, toroidal and poloidal magnetic field

- **Heating Systems:** To bring the plasma to fusion-relevant temperatures, various auxiliary heating systems are employed [10].:
    - **Electron Cyclotron Resonance Heating:** Utilizes high-frequency microwaves to heat electrons.
    - **Neutral Beam Injection:** Injects high-energy neutral particles that penetrate plasma, become ionized, and transfer their energy to the plasma particles.
    - **Ion Cyclotron Resonance Heating:** Employs radiofrequency waves to heat the plasma ions.
- **Divertor:** Positioned at the bottom of the vacuum vessel, the divertor is a component designed to manage the extreme heat and particle [11] exhaust from the plasma. It funnels impurities away from the core plasma and protects the main chamber walls from erosion, often utilizing advanced plasma-facing components.
- **Pumping System:** A system of pumps, frequently cryogenic, is integrated beneath the divertor to remove spent fuel and impurities from the vacuum vessel.
- **In-Vessel Coils:** These non-axis-symmetric coils are located inside the vacuum vessel and are used for active control of plasma instabilities, such as Edge Localized Modes, and for compensating error fields that could otherwise degrade plasma performance.

- **Blanket:** Surrounding the vacuum vessel, the blanket absorbs the high-energy neutrons produced by the fusion reactions, converting their kinetic energy into heat for electricity generation. Furthermore, the blanket contains lithium, which reacts with neutrons to breed new tritium fuel, ensuring a self-sufficient fuel cycle for the reactor.

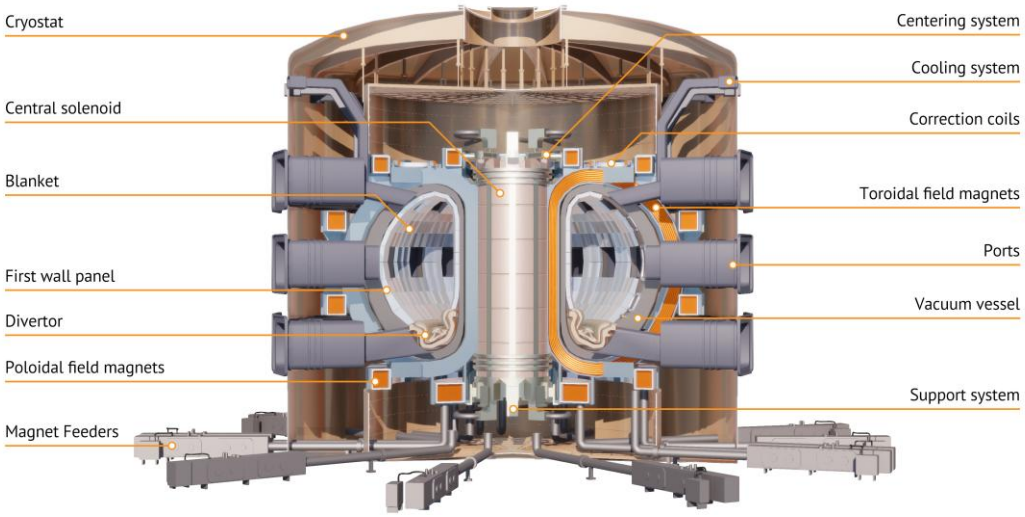

Figure 7 Tokamak schematic diagram [12]

Depending on the specific role or activity of a tokamak, certain components may or may not be integrated into its layout. For instance, ITER does not include any blanket modules for tritium breeding; however, a dedicated testing module will be installed to evaluate tritium breeding under relevant fusion conditions [5]. Beyond the core components dedicated to plasma confinement and heating, a comprehensive array of auxiliary systems is intrinsically vital for the operational viability, inherent safety, and sustained performance of a fusion reactor. These systems are fundamental across all phases of operation, from the initial establishment and sustainment of the plasma to the meticulous management of thermal loads and radiation, and the long-term maintenance of the device itself. The electrical power supply infrastructure, for instance, must deliver immense quantities of electricity to energize the intricate magnetic confinement apparatus, various auxiliary heating mechanisms, and a multitude of other operational subsystems. The superconducting magnets, encompassing the toroidal, poloidal, and central solenoid coils, necessitate exceptionally high currents. These are typically furnished by sophisticated AC/DC converters, which might employ thyristor-based designs for managing pulsed loads or utilize Insulated Gate Bipolar Transistors to achieve more rapid control and independent module feeding. Large-scale projsects like ITER

exemplify this requirement, with projections indicating significant power draw for both pulsed operations and continuous auxiliary functions [13]. Dedicated high-power supplies are also essential for auxiliary heating systems, such as neutral beam injectors and radiofrequency heaters. The thermal management of a fusion reactor extends significantly beyond the blanket's role in converting neutron energy into useful heat. Extensive cooling systems are critically important throughout the entire tokamak structure. Plasma-facing components, particularly the divertor, are exposed to extreme heat fluxes, often exceeding specific thresholds, and thus require active cooling to manage these intense thermal loads. Superconducting magnets necessitate advanced cryogenic cooling systems, frequently relying on the forced flow of supercritical helium, given their operational requirements at exceptionally low temperatures. Moreover, many diagnostic instruments, especially those positioned in regions of high heat or neutron flux, demand dedicated cooling circuits to preserve their functional integrity and accuracy. Maintaining an ultra-high vacuum within the toroidal chamber is a prerequisite for plasma purity and efficient reactor operation. This involves not only pumping systems integrated beneath the divertor for particle exhaust but also a comprehensive vacuum infrastructure tasked with establishing and sustaining the initial vacuum before plasma ignition. A wide array of diagnostic systems (Figure 8) is indispensable for the continuous monitoring, comprehensive understanding, and precise control of plasma behavior. These tools measure critical plasma parameters, including temperature, density, and the configurations of magnetic fields. Advanced diagnostics also provide data on neutron flux, the distribution functions of fast ions, and the thermal performance of plasma-facing components, often employing techniques such as infrared thermography. The real-time data generated by these diagnostics is fundamental for optimizing reactor performance, validating theoretical models, and ensuring safe operational envelopes.

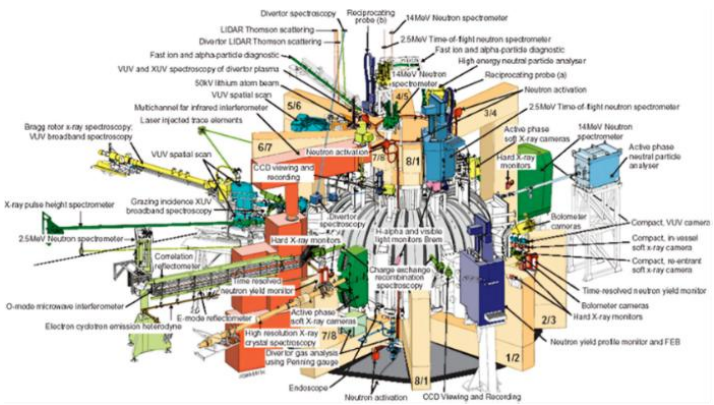

Figure 8 Typical diagnostic systems in a tokamak device

The precise introduction of deuterium and tritium into the vacuum vessel is another critical aspect, necessary for regulating plasma density and optimizing fuel composition. Various fueling methodologies are employed, including gas puffing, pellet injection, and neutral beam injection, each tailored to meet specific operational requirements. Regarding tritium, its radioactive nature and scarcity necessitate specialized systems for its extraction from the breeding blanket, subsequent purification, recycling, and secure storage. These integrated systems are fundamental for establishing a closed fuel cycle, which is a key element of fusion energy's long-term sustainability and minimizes reliance on external tritium sources. Due to the neutron activation of in-vessel components, direct human intervention for maintenance is precluded. Consequently, sophisticated remote handling and maintenance systems are imperative for tasks such as repair, replacement, and refurbishment. These systems involve specialized robotic equipment and shielded facilities designed for the safe manipulation of radioactive materials. The development of highly efficient remote maintenance strategies is crucial for minimizing reactor downtime, maximizing operational availability, and underpinning the long-term economic viability of future fusion power plants.

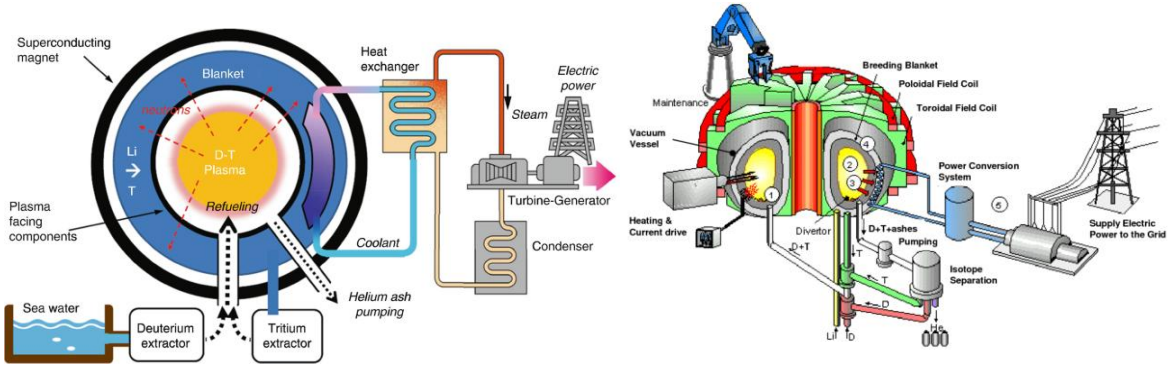

Figure 9 Tokamak fusion power plant schematic

Finally, the entire complex enterprise is governed by an integrated and highly sophisticated control and instrumentation system. This system acts as the central intelligence of the fusion reactor, coordinating the operation of all constituent components, managing plasma dynamics in real-time, responding adeptly to off-normal events, and ultimately guaranteeing the overall stability and safety of the reactor. It synthesizes data from numerous diagnostics and executes intricate control algorithms to maintain optimal operating conditions.

Thus, it is this vast, interconnected network of primary and auxiliary systems that collectively forms the intricate operational chain essential for a functional, and eventually, commercially viable fusion reactor.

The European Union has a well-defined and comprehensive strategy to achieve the goal of generating fusion electricity by 2050, as outlined in its "Roadmap to the realization of fusion energy," which was first published in 2012. This ambitious endeavor is primarily implemented through the European Fusion Consortium, which is responsible for coordinating research efforts across its member states and implementing this roadmap. The roadmap adopts a goal-oriented approach, structured around eight distinct missions, each addressing specific challenges on the path to fusion power.

1.5 Eurofusion Roadmap: Toward the Realization of Commercial Fusion Power Plants

The European roadmap's ultimate goal is to bring fusion electricity to the grid as quickly as possible (Figure 10). This involves a broad range of scientific and technological advancements across various fields, including plasma physics, materials science, engineering, and neutronics [14] [15]

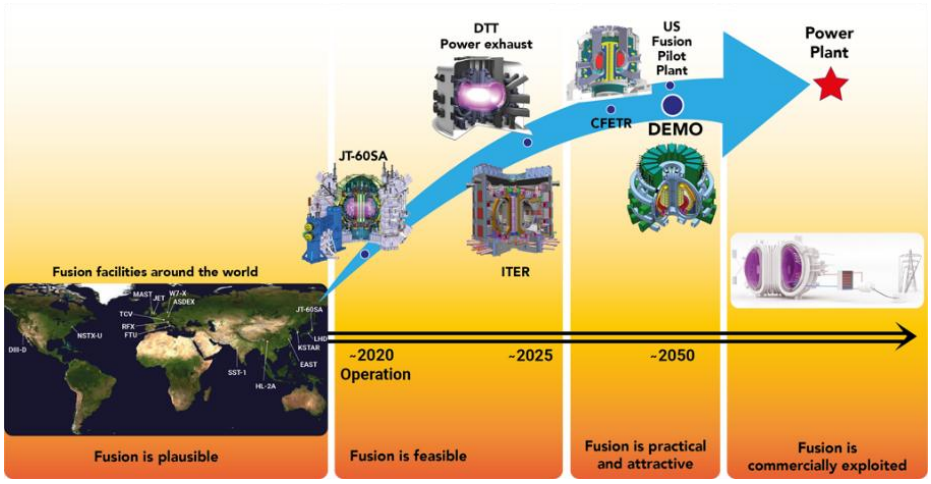

Figure 10 Eurofusion road map showing the milestone and main devices needed to address all the main knowledge domains to be explored to reach a fusion power plant [14]

The Joint European Torus has played a pivotal role as a predecessor to ITER, providing significant information and insights into nuclear fusion understanding and technology. JET, which began operation in 1983, has been the world's largest operating tokamak and the only machine capable of operating with the deuterium-tritium fuel mixture foreseen for a fusion reactor. For over 20 years, it was operated as a joint undertaking before transitioning to UKAEA under contract to the European Commission from January 2000. Its experimental campaigns have directly supported ITER, which is now expected to achieve most of the critical milestones for demonstrating fusion power.A significant focus of the roadmap, as highlighted by Mission 2, is dedicated to developing effective heat-exhaust systems. This is

considered a crucial challenge, as the heat and particle fluxes anticipated in a future Fusion Power Plant are significantly higher and more demanding than those in current experimental devices [16]. The power crossing the magnetic separatrix in a tokamak is channeled into a narrow radial layer towards the divertor, where it must be exhausted on actively cooled targets. To address the inherent risks and uncertainties associated with the baseline strategies, particularly concerning heat exhaust, the European program actively investigates alternative solutions. This strategic foresight is crucial to prevent significant delays in the realization of fusion should conventional approaches prove insufficient. A vast majority of resources in European fusion research are currently dedicated to supporting ITER and its accompanying experiments. The European roadmap is closely tied to the ITER schedule, with preparations for the construction of the demonstration power plant proceeding in parallel with ITER's exploitation phase in the 2030s. One important example of this commitment is the Divertor Tokamak Test Facility (DTT) in Italy. DTT reflects Europe's determination to explore innovative techniques for plasma exhaust and to investigate various divertor concepts under conditions relevant both to ITER and DEMO. Its primary objective is to test alternative divertor configurations, including those based on liquid plasma-facing components. Alongside DTT, proof-of-principle experiments such as MAST-U and TCV play a crucial role. MAST-U focuses on the super-X divertor, while TCV investigates snowflake divertor configurations. Both facilities are either operational or under development and are designed to assess the performance of alternative geometries and liquid metals. These efforts provide essential data for model validation and directly inform the design of DEMO. To coordinate this large-scale effort, EUROfusion employs a Work Breakdown Structure that ensures efficient collaboration across its members.

2 Divertor Tokamak Test (DTT) as a test facility for DEMOnstration Power Plant (DEMO) oriented solutions

2.1 Role and objectives

One of the primary challenges for future fusion power plants, as outlined in the European Fusion Roadmap, is creating an effective system for managing the high heat and particle loads anticipated in the divertor of a DEMO reactor. ITER, currently under construction, plans to test a standard divertor operating under detached conditions. However, this approach is highly complex and may pose a significant obstacle to achieving a functional fusion power plant.

Consequently, the Roadmap launched the Divertor Tokamak Test facility project to explore alternative solutions for DEMO's power and particle exhaust. DTT aims to conduct experiments that replicate the key aspects of DEMO's power and particle exhaust challenges, requiring adaptability to test various magnetic configurations and liquid-metal targets, among other potential innovations [17].

The proposed DTT design is optimized to mimic DEMO's edge plasma conditions, particularly concerning the dimensionless parameters governing the scrape-off layer and divertor, while aligning with DEMO's core plasma performance requirements. This design balances maximum versatility with a project cost of €500 million.

While the European Program has contributed approximately €60 million through Horizon 2020, the Italian Government has offered additional funding to establish a dedicated facility in Italy for the European fusion community.

Other international efforts are also addressing the exhaust issue: the U.S. is exploring the ADX device [18], a compact, high-field machine, and China's superconducting EAST tokamak has been upgraded to test alternative divertor magnetic configurations, though its plasma conditions are still far from reactor-relevant levels [19].

In contrast, DTT will directly tackle the integrated bulk-edge power exhaust problem, operating under plasma conditions and power loads closely mirroring DEMO in a scaled experimental setup.

The ultimate goal for DTT, among others, is to provide DEMO with a dependable and resilient exhaust solution, defined as one that is technologically feasible and does not compromise plasma performance. Plasma confinement in a tokamak relies on a magnetic

field structure creating nested magnetic surfaces. At the plasma's edge, the Scrape-Off Layer, a region of open field lines, directs escaping particles and heat towards the divertor, where they interact with target plates (Figure 11).

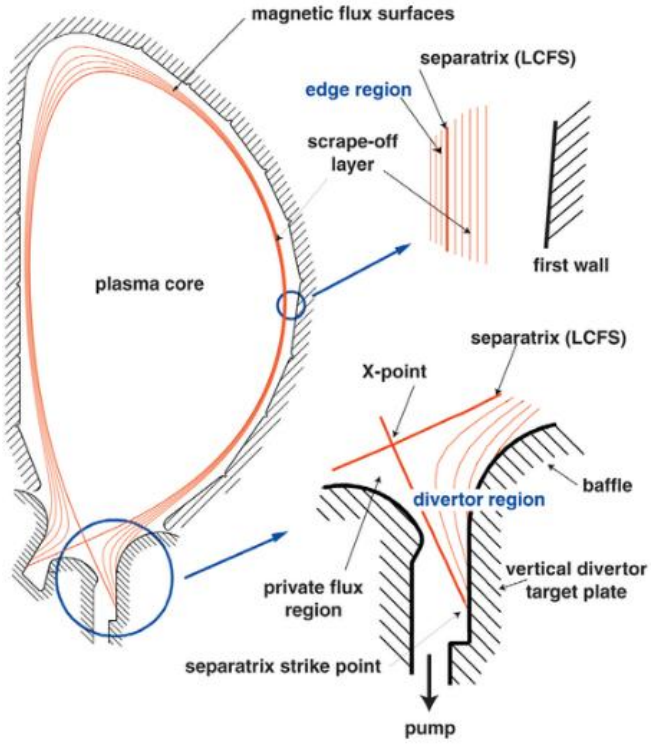

Figure 11 Poloidal cross-section of a tokamak plasma for DEMO with a single magnetic null divertor configuration, illustrating the regions of the plasma and the boundary walls where important PMIs and atomic physics processes take place. The characteristic regions are: (i) the plasma core, (ii) the edge region just inside the separatrix, (iii) the scrape-off-layer (SOL) plasma outside the separatrix, and (iv) the divertor plasma region, which is an extension of the SOL plasma along field lines into the divertor chamber. The baffle structure is designed to prevent neutrals from leaving the divertor. In the private flux region below the 'X' point, the magnetic field surfaces are isolated from the rest of the plasma.[20]

The current strategy, to be tested at ITER, involves optimizing plasma operations with a standard divertor in detached plasma conditions.

This method involves cooling the plasma by losing energy as radiation (a process called radiative cooling) before the plasma reaches the divertor along the magnetic field lines, turning it into gas. By doing this, the high-temperature plasma no longer comes into contact with the structure (detachment, Figure 12), significantly reducing the influx of heat [21].

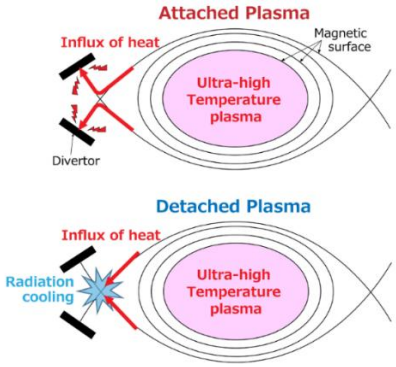

Figure 12 Attached vs detached plasma [22]

However, since the outer edge region of the plasma is cooled down, if not carefully managed, this low-temperature state can propagate upstream along the magnetic field lines and degrade the ultra-high temperature plasma in the core.

This strategy includes developing plasma-facing components resilient to extreme heat fluxes, optimizing divertor geometry and magnetic flux expansion to distribute heat over a larger area, reducing heat load on the target, and mitigating plasma energy before it reaches the divertor by inducing impurity radiation, increasing edge plasma density, and injecting impurities into the SOL to lower the power fraction reaching the divertor to manageable levels. It also involves increasing plasma density near the target and reducing temperatures to achieve detachment, thereby reducing plasma flux to the divertor.

However, significant uncertainties remain in applying this strategy to ITER, DEMO, and future fusion power plants. Current experiments operate under SOL conditions that differ significantly from those anticipated for ITER and DEMO. Existing SOL models and simulations may not accurately predict behavior under reactor conditions. Furthermore, ITER's baseline strategy might not scale effectively to a fusion power plant due to challenges such as the stability of the detachment front under reactor conditions, integration with the plasma core and other tokamak systems, compatibility with high radiated power fractions, pumping efficiency, monitoring of erosion and temperature, and material limitations including component lifespan and maintaining low divertor temperatures to minimize erosion.

To address these issues, a dedicated project has been initiated to investigate alternative power exhaust solutions for DEMO, leading to the design of the Divertor Tokamak Test facility. DTT will conduct scaled experiments that integrate crucial aspects of DEMO's power and particle exhaust. Role and Objectives of DTT:

Developing a reliable power and particle exhaust system is identified as a major hurdle in achieving a fusion power plant [23]. There is a risk that ITER's conventional divertor approach may prove unsuitable for DEMO, necessitating the exploration of alternative solutions. While concepts like the lithium-cooled limiter in FTU or the Super-X divertor in MAST-U are being investigated, extrapolating results from current devices to DEMO is considered unreliable.

DTT is an integral part of the European fusion research program, designed to bridge the gap between initial proof-of-principle experiments and the DEMO reactor.

While ITER will test a conventional divertor, DTT aims to proactively investigate and qualify alternative solutions, given the concerns about ITER's approach scalability to a power-producing reactor.

Its primary objectives include:

- **Integrated Exhaust Solution:** DTT is proposed to tackle the integrated bulk-edge power exhaust problem and identify a reliable and robust solution for DEMO.
- **Testing Advanced Concepts:** It will explore a variety of advanced concepts, including different magnetic configurations, advanced plasma-facing components, impurity seeding strategies, and liquid metals as plasma-facing components.
- **ITER Relevance:** With ITER's decision to switch to a full-tungsten first wall, DTT, being the only breakeven-class device globally with full tungsten actively cooled components before ITER, serves as an ideal tool for testing relevant plasma scenarios and engineering solutions in advance.
- **Scientific Program:** The DTT scientific program focuses on identifying and qualifying integrated core-edge solutions that achieve simultaneously high-radiated fractions and good confinement. Key research areas include the development and assessment of baseline and advanced scenarios for various divertor configurations, optimization and control of detached regimes through impurity seeding, and disruption studies in support of ITER.

DTT is designed as a high-field, compact tokamak capable of producing plasma conditions similar to those in ITER and DEMO in steady-state operation. It will reproduce the level of divertor heat loads foreseen in these future devices, thanks to a substantial amount of external heating power.

The main parameters for the DTT device are summarized in Table 2 [17]:

Table 2 Main DTT parameters

Parameter	*Value*
Plasma radius at magnetic axis (R_{ax})	2.19 m
a	0.70 m
Toroidal field at the magnetic axis (B_t)	5.85 T
Maximum Single Null conf. plasma current (I_p)	5.5 MA
Maximum foreseen heating power (P)	45 MW (28.8 $ECRH$ / 9.5 NBI / 6.7 $ICRH$)
t_{pulse}	100 s

The DTT is designed to explore a wide range of plasma shaping and to exhaust heat fluxes in excess of 20 MW/m^2. The central solenoid flux swing is designed to meet requirements for 5.5 MA/100 s pulses. The machine will guarantee high reliability and availability with 100 operation days per year, expected to explore a variety of different magnetic configurations under extreme conditions (high heat-flux, large electromagnetic loads). A general overview of DTT layout is shown in Figure 13.

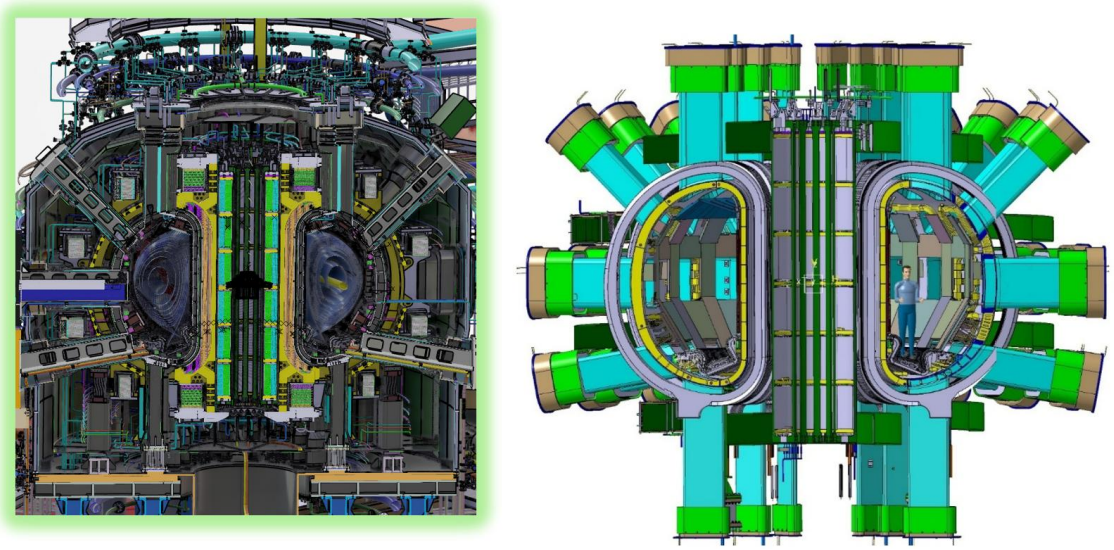

Figure 13 DTT machine schematic

2.2 Radial Build

The inboard radial build takes into account the inboard radius of the plasma (1.47 m), a minimum clearance of 30 mm between plasma and first wall, with 55 mm for the first wall structure and the in-vessel magnetic diagnostics. In the inboard side, the vacuum vessel is a structure with two shells of SS AISI 316 LN, each of them 15 mm thick, separated by a neutron shield of 90 mm with 65 mm of borated water and 25 mm of SS/B4C/W/B4C/SS sandwich. A 20 mm thick thermal shield operating at 80 K is located behind the vacuum vessel with a gap of 20 mm. The structure of the inner legs of the TF (toroidal field) coils spans from 820 to 1180 mm (whereas the winding pack spans from 908 to 1149 mm). Finally, the Central Solenoid (CS) consists of six identical modules wound in two layers, spanning from 437 to 759 mm. This radial build allows also for the insertion of an independent High Temperature Superconducting (HTS) coil. This additional solenoid might test this enabling technology for next generation fusion reactors and increase the flat top duration, raising the stored magnetic flux by about $1\ Vs$.

The radial build in the outboard is driven by the requirement on the ripple $(B_{max} - B_{min})/2B_0 < 0.5\%$. To achieve this, the winding pack of the outboard TF coil leg in the equatorial plane spans from 3721 to 3962 mm. This leaves a large amount of space in the outboard, where the first wall is located at a radius of 2.86 m, i.e. with a gap of 110 mm from the nominal single null plasma. This guarantees suitable flexibility for alternative plasma shapes. The vacuum vessel in the outboard has two 15 mm thick shells, with an inner radius of 3.17 m, leaving space to the in-vessel coils and the magnetic diagnostics. The cavity between the shells in which the borated water flows is larger than the inboard (200 mm) [24]. The 2D poloidal profile is outlined in Figure 14.

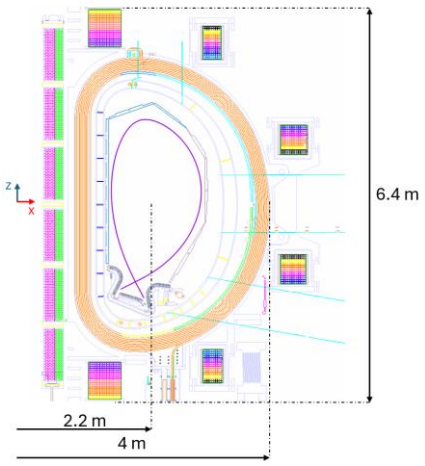

Figure 14 Poloidal section of DTT main functional components

2.3 Tokamak Main Components Layout

To allow the DTT machine to investigate the wide range of anticipated scenarios, the present **Magnet System** (Figure 15) consists of:

- **18 Toroidal Field (TF) Nb_3Sn coils**, operating at a peak magnetic field of 11.8 T and a conductor operational current of 44.0 kA [25]
- **6 independently fed Central Solenoid (CS) modules**, operating at 13.2 T and 29.9 kA [26]
- **6 Poloidal Field (PF) coils**, of which 2 reach about 8.5 T and 35.0 kA (made of Nb_3Sn CICCs), while the other 4 operate at lower fields and currents using NbTi conductor technology [27]

The magnet system is fully symmetric with respect to the equatorial plane, with PF coils designed in identical pairs [17]. The TF coils are wound in **double pancakes** and operate in a **wedged configuration**. A complete set of **Inner Inter-coil Structures** (superbolts and pins) is provided to resist shear forces between adjacent TF coils, while **Outer Inter-coil Structures (OIS)** are specifically designed to support out-of-plane loads.

The **graded design** of the CS allows a saving of approximately 8 tons of costly Nb_3Sn strand and enables achievement of the required high performance in terms of engineering current density, thereby providing the necessary magnetic flux (approximately ±16.2 Vs). The system is also compatible with a potential future upgrade, involving the insertion of an additional **High Temperature Superconductor (HTS) coil** inside the original CS bore. Although this insert would produce only a modest increase in flux (about ±1 Vs), it would serve the technological goal of demonstrating the feasibility of fusion magnetic confinement using HTS [28].

The PF system additionally includes **six in-vessel copper coils**:

- **Two coils** for radial and vertical stabilization and control;
- **Three divertor coils** for magnetic control of the Scrape-Off Layer (SOL) and strike point sweeping.

Special attention has been given to **diagnostics and control systems**, particularly for plasma control in the divertor region, with the aim of ensuring strong compatibility with DEMO operating conditions.

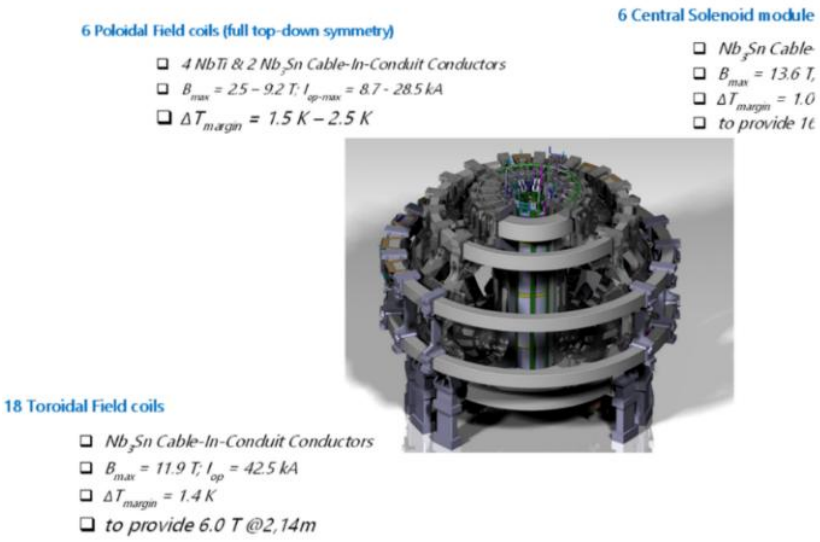

Figure 15 DTT magnetic system

The **vacuum vessel**, which was originally a single INCONEL shell, has been redesigned as a **double-wall structure with ribs**, consisting of two shells of **SS AISI 316LN**, each 15 mm thick, separated by a **neutron shield** through which borated water flows at 50–80 °C. The neutron shield thickness is 90 mm inboard (including 25 mm of solid components) and 200 mm outboard [29].

This shield is designed to handle a **DD neutron yield rate of 1.5 × 10^{17} n/s**, plus 1.5 × 10^{15} n/s of 14 MeV neutrons from triton burn-up during the high-performance phase, keeping nuclear heating of the first TF coil layer below 1 mW/cm³.

The vacuum vessel is divided into **18 sectors**, joined by welding. Each shell is 15 mm thick, while the **five ports per sector** have a 25 mm thick single shell (Figure 16). The **elongation of the vessel cross-section** has been increased to provide sufficient space for the divertor region.

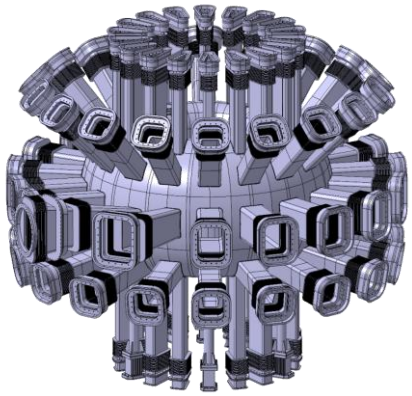

Figure 16 DTT vacuum vessel and ports

The **DTT device requires a significant amount of heating power** for its size. During the initial phase, **25 MW** will be available, distributed as follows [10]:

- **15 MW** of Electron-Cyclotron Radiofrequency Heating (ECRH) at 170 GHz, delivered by 16 gyrotrons;
- **3 MW** of Ion-Cyclotron Radiofrequency Heating (ICRH) at 60–90 MHz;
- **7.5 MW** of Negative Neutral Beam Injection (NNBI), provided by a single tangential injector.

The heating mix for full DTT performance will be determined at a later stage, within the following ranges:

- **20–30 MW** of ECRH;
- **3–9 MW** of ICRH;
- **7–15 MW** of NNBI.

Figure 17 shows an overall view of the NNBI system (based on 400 keV beam energy), the ECRH transmission lines (to be implemented in vacuum), and the different ICRH antenna concepts currently under consideration.

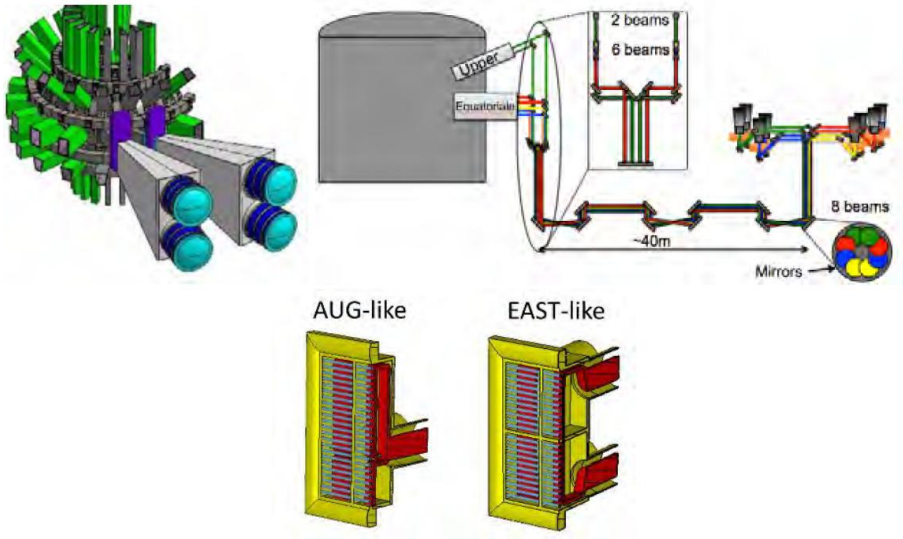

Figure 17 DTT NNBI, ECRH, ICRH

2.4 Magnetic Configurations

As mentioned, flexibility is a primary requirement for DTT, allowing it to test different divertor magnetic configurations[17]. The initial DTT divertor design was based on the W-

shaped solid FAST-like divertor modules, which are an ITER-like segmented divertor in 72 toroidal sectors. The design of the first DTT divertor has been agreed upon with EUROfusion to test various plasma and exhaust scenarios [30]. In its first phase of exploitation, DTT will be capable of demonstrating (Figure 18):

- **Single Null (SN):** This is a foundational magnetic geometry in tokamaks, characterized by a single "X-point" at either the top or bottom of the plasma cross-section. DTT is designed to operate with a maximum plasma current of up to 5.5 MA in this standard configuration, allowing for the study of its effectiveness under DEMO-relevant conditions.
- **X-Divertor (XD):** The X-Divertor is an advanced divertor configuration aimed at improving heat and particle handling in DTT. It works by modifying the magnetic field lines near the X-point to expand the region where the plasma interacts with the divertor plates. DTT will explore the X-Divertor configuration with a maximum plasma current of up to 4.5 MA, contributing to the development of robust exhaust solutions for future reactors.
- **Negative Triangularity (NT):** Negative Triangularity refers to a plasma shape where the outer midplane is indented, a configuration DTT will explore with a maximum plasma current of up to 4 MA. Research indicates that negative triangularity plasmas can achieve longer energy confinement times and may help in mitigating or suppressing plasma instabilities like Edge Localized Modes

In further stages, DTT control system will be also optimized for:

- **Double Null (DN):** The Double Null configuration in DTT will feature two X-points, situated at both the top and bottom of the plasma cross-section, enabling symmetric exhaust of heat and particles. By channeling exhaust to divertors at both ends, the double null configuration can reduce peak heat loads on individual divertor plates. DTT will operate in this configuration with a maximum plasma current of up to 4 MA, providing valuable data on its performance for reactor designs.
- **Snowflake Divertor (SFD):** The Snowflake Divertor is an advanced magnetic configuration characterized by the presence of two near poloidal field nulls and four strike points. The SFD achieves this by substantially increasing both the magnetic field line length and the magnetic flux expansion within the divertor region. These

features facilitate a more distributed deposition of heat and particles, thereby reducing the peak heat flux density on the divertor targets and promoting efficient plasma detachment.

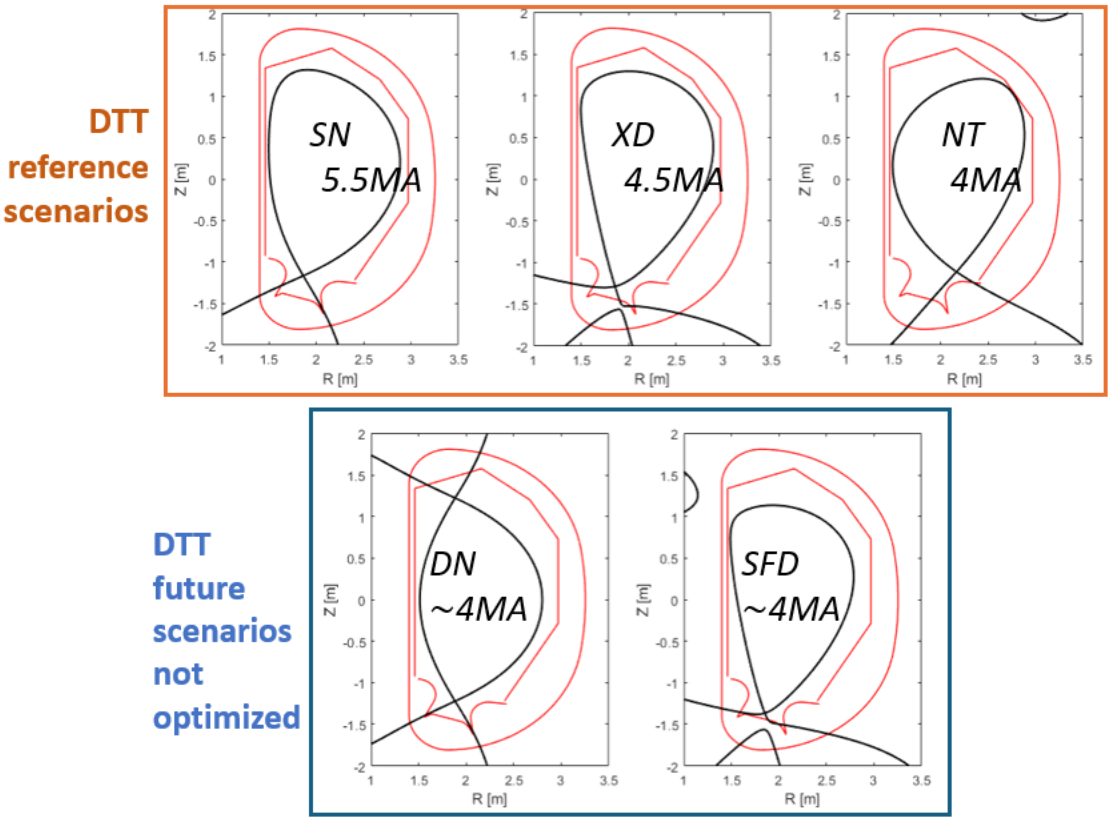

Figure 18 Baseline magnetic configurations (for which DTT control systrem and geometry are already optimized) and future scenarios not optimized

2.5 Divertor role in the reactor

The **divertor** is a critical component of a tokamak designed to manage the plasma edge. It is typically located at the bottom (Figure 19) (or sometimes the top) of the vacuum vessel and serves several key functions: it **removes excess heat and fusion byproducts** from the plasma; **minimizes contamination** of the core plasma by impurities; and **protects the tokamak's structural components** from extreme thermal and particle loads.

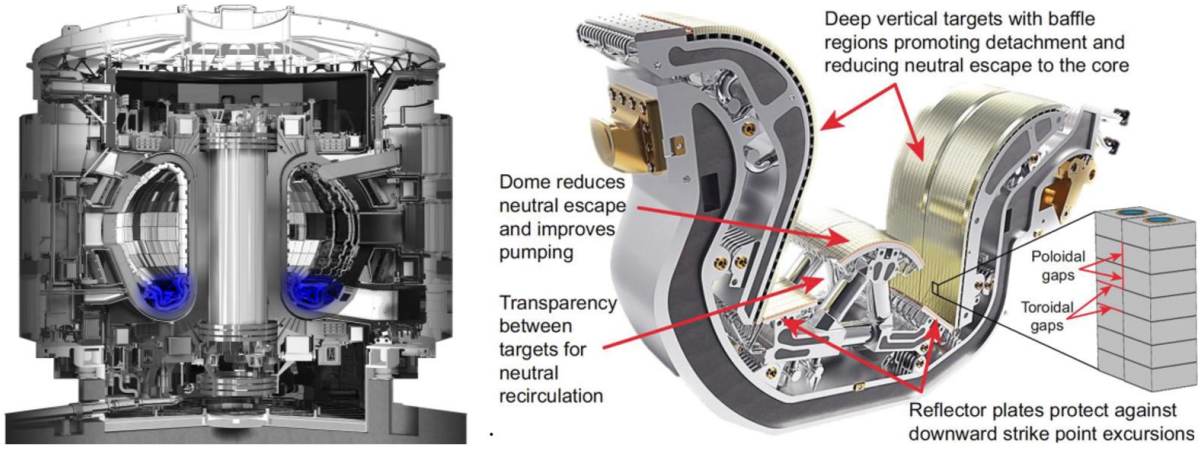

Figure 19 ITER Divertor (blu) mounted in the tokamak [31]

The divertor intercepts plasma particles along magnetic field lines in designated strike zones, where the energy of these particles is converted into heat. This heat is then removed via **active cooling systems**, often using water-cooled structures. To withstand the intense heat and particle flux, divertor surfaces are typically made from **high-performance, refractory materials** such as tungsten. In modern tokamaks, the divertor often includes modular components that can be **monitored and replaced remotely** due to the harsh operating conditions. In addition to handling heat and particles, the divertor may host **diagnostic tools** to aid in plasma control and optimization. The divertor is often composed by two main sub systems (Figure 20):

- the Divertor Cassette Body (often referred as CB) representing the main structural support
- the Plasma Facing Components (PFCs) that, as mentioned, are directly interfaced with plasma in targeted regions.

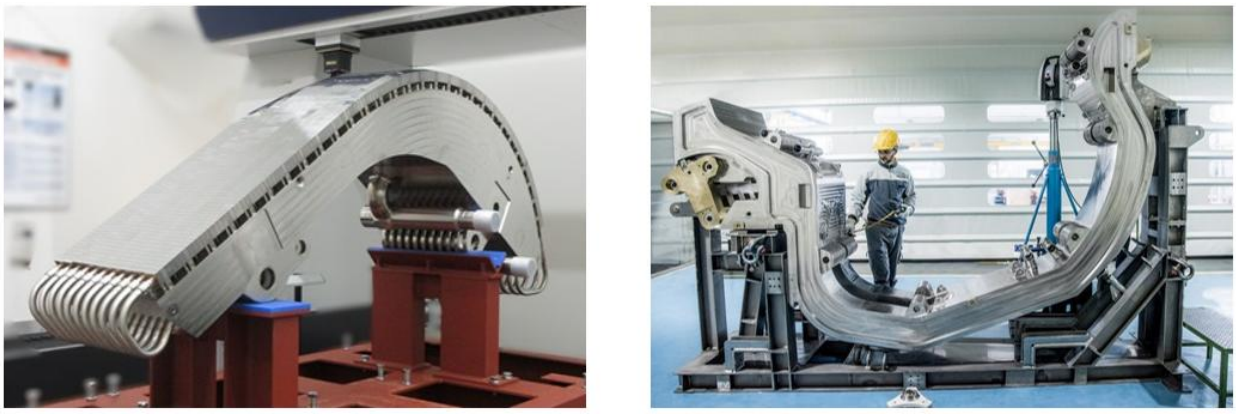

Figure 20 ITER Tungsten Divertor Outer Target (left)-ITER Divertor Cassette Body (right) [31]

The divertor's primary role is multifaceted:

- **Heat Exhaust:** It funnels extreme heat away from the core plasma. Without mitigation, the heat flux in the SOL, i.e in devices like ITER [31] and DEMO [32], could surpass that of the Sun's surface. The divertor is designed to distribute this intense heat over a larger area, often by optimizing its geometry and magnetic flux expansion, and to reduce the plasma energy before it reaches the divertor plates.
- **Particle Exhaust and Impurity Removal:** The divertor collects unreacted fuel (deuterium and tritium) and impurities, such as helium and eroded material from the reactor walls. These particles are then removed by pumping systems, maintaining the purity of the main plasma.
- **Protection of Reactor Walls:** By redirecting energetic particles and heat away from the main vacuum vessel walls, the divertor prevents damage, erosion, and excessive heating of these critical components, thereby extending the operational lifetime of the reactor.

The design of divertors for fusion reactors presents significant multiphysics challenges, driven by the extreme operating conditions and the complex interplay of various physical phenomena.

The primary multiphysics challenges in divertor design include:

- **Extreme Heat Fluxes and Thermal Management:** Divertor components are subjected to some of the highest heat loads within a fusion device, with heat fluxes potentially exceeding $20\ MW/m^2$ during normal operation and even higher during transient events like Edge Localized Modes. Components must be designed to

withstand thermal stresses and prevent melting or excessive erosion. Strategies to reduce heat loads include optimizing divertor geometry and magnetic flux expansion, and inducing impurity radiation to lower plasma energy before it reaches the divertor.

- **Neutronic Effects and Material Degradation:** The divertor operates in an environment of high-energy neutron bombardment, which significantly degrades the physical and mechanical properties of structural materials over time. Neutron fluences in future devices like DEMO will be vastly greater than in current tokamaks, leading to accumulation of radiation damage. This necessitates the development of materials capable of long-term operation under such conditions, enduring radiation damage and maintaining structural integrity and thermal performance.
- **Electromagnetic Loads:** Divertor structures experience substantial electromagnetic forces during both normal operation and, critically, during off-normal events like plasma disruptions. These EM loads, arising from toroidal flux variations, halo currents, and poloidal flux variations, can induce significant eddy currents, stresses, and deformations in components. Detailed EM analyses are mandatory for correctly dimensioning divertor components and ensuring their structural assessment and integrity.

The materials used in divertors, particularly for the plasma-facing components that directly interact with the plasma, must withstand exceptionally harsh conditions.

Given these challenges, advanced materials are crucial. Tungsten (W) has emerged as a leading candidate for divertor PFCs, especially for high-heat flux areas, due to its high melting point, good thermal conductivity, and low sputtering yield [33]. Recently, ITER has decided to switch to a full-tungsten first wall, making DTT, with its full tungsten actively cooled components, an ideal testbed. The design of the first DTT divertor was based on W-shaped solid FAST-like divertor [34].

Impurities, especially high atomic number (high-Z) elements, can significantly cool the plasma through radiation, thereby hindering the fusion reaction. Research into plasma-facing components specifically addresses erosion challenges to maximize device availability while mitigating harmful effects such as plasma contamination, hydrogen co-deposition, and dust production, as highlighted in the European fusion research roadmap.

Historically, carbon fiber composites were used in some divertor designs, offering good thermal shock resistance. However, carbon is being phased out in next-generation reactors because it has a high rate of fuel retention through co-deposition. This process traps hydrogen isotopes (deuterium and tritium) within layers of carbon eroded from the wall and redeposited, leading to a significant accumulation of valuable fuel and radioactive tritium.

Carbon dust produced by erosion also retains tritium, posing a safety concern. Furthermore, liquid metals, such as lithium, gallium, or tin, are also under investigation as potential PFCs. These materials can inherently avoid solid material erosion and some, like lithium, can even absorb hydrogen isotopes, potentially reducing fuel retention issues observed with solid surfaces. DTT, for instance, aims to explore various divertor concepts, including those based on liquid plasma-facing components.

3 DTT Divertor Design workflow: from CAD to multiphysics integration

The DTT Divertor is composed of 54 Cassette Assemblies (CA) or modules installed at the bottom part of the vacuum vessel (Figure 21).

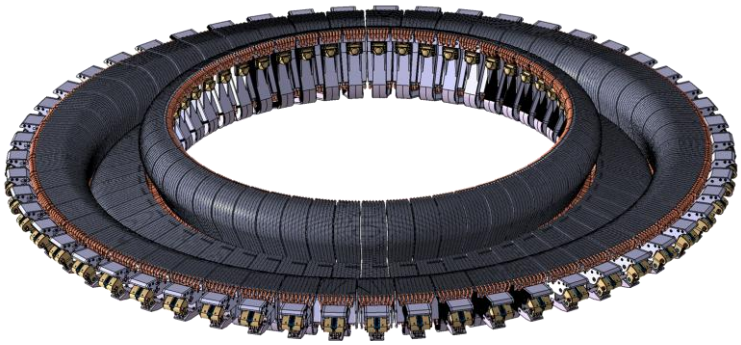

Figure 21 DTT Divertor cassette system

Each module includes the Cassette Body (CB) (comprehensive of all the auxiliary systems) or cassette and three plasma-facing components (PFCs), namely the Inner Target (IT), the Outer Target (OT), and the Central Target (or Dome) (Figure 22) [34]. The full divertor procurement package includes fifty-six divertor modules, three for each 20° sector plus two spares. Fifty-two are standard modules and four are the so-called test modules, where advanced divertor configurations can be tested at a later stage.

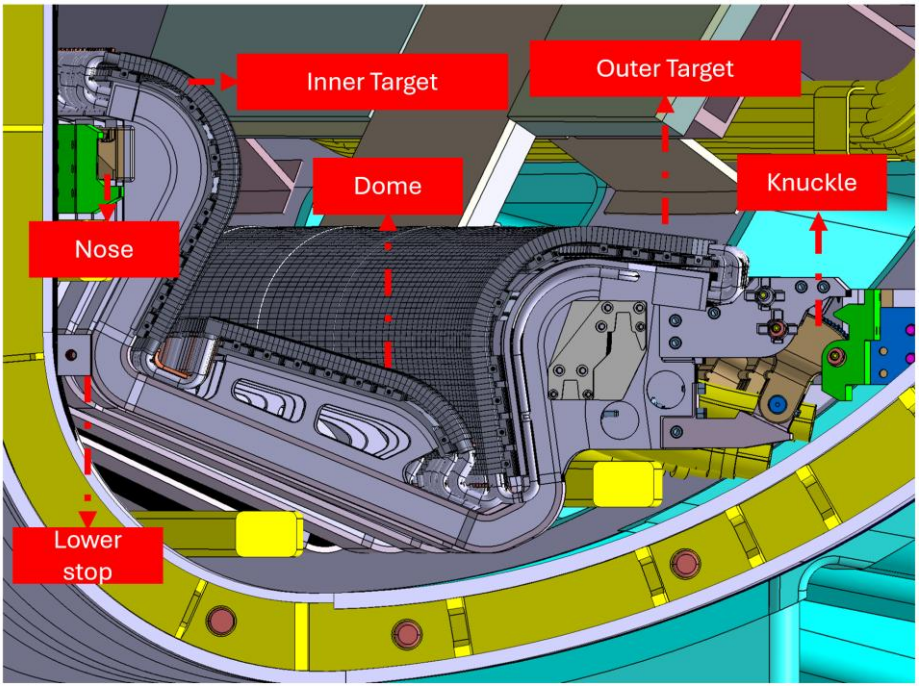

Figure 22 DTT divertor single module layout

The CB provides neutron shielding for the Vacuum Vessel and magnet coils and routes the coolant to the PFCs. The IVTs and OVTs and Dome intercept the magnetic field lines and therefore must remove the heat load coming from plasma via conduction and convection during normal and transient operations as well as during the off-normal events. The vertical targets are inclined to intercept the magnetic field lines of the separatrix at an acute angle, giving deep inboard and outboard channels in which to establish a detached or partially detached plasma regime. In these regimes, while the plasma remains attached in the outer region of the SOL, the plasma is detached from the PFCs in the region near the separatrix causing the power profile to broaden and power to be radiated to other surfaces.

The curved upper part of the IVTs and OVTs provides a baffle for neutral particles. The dome, depending on plasma scenario, can work only as a baffle for neutrals or as a target for charged particles and baffle for neutrals. The PFCs also protect the CB and diagnostics from direct interaction with the plasma. In a standard module the PFC configuration is based on the W monoblock concept, i.e. CuCrZr actively cooled tubes protected by W massive tiles. This choice relies on proven technologies already qualified for ITER (5000 cycles at $10\ MW/m^2$, followed by 300 cycles at $20\ MW/m^2$). The PFCs are cooled in series, and the water coolant is routed via the CB. Each Divertor cassette is connected to the primary cooling loop through a pair of radial pipes entering the vessel from port 4 [35]. The water-cooling system parameters chosen for the standard divertor modules are given in Sect.4. The divertor system has an allocated maximum volume to accommodate water-cooling, different plasma configurations and to be compliant with the available space for its extraction through port 4 of the four RH sectors (see 3.4.3). The RH window is limited vertically to 650mm and toroidally to 350mm. A rough estimation of the weight of a single divertor module is 300 kg.

According to the DTT Balance of Plant Auxiliary System Process Basis of Design the maximum power to be absorbed by the divertor is 32 MW. The 54 modules composing the DTT divertor are cooled in parallel by pressurized water with a total mass flow rate of about 570 kg/s [35].

The inlet water conditions foresee a pressure of 50 bars and a temperature that can be selected for each tokamak campaign between 30 °C and 130 °C with a maximum variation of ± 5 °C. The estimated total pressure drops (cassette in-out) shall not exceed 2 MPa [36].

Each divertor module is provided with a shut-off valve for leak detection. Moreover, in the four RH sectors all the 3 modules are instrumented with pressure monitor and inlet-outlet flow meter and thermocouples.

During baking, the coolant supplied to the divertor has a pressure of 5 MPa and a temperature of:

- 200°C during the so-called Strong Baking (SBAK).
- 130°C during the Light Baking (LBAK).

As already said, DTT can also host divertor test modules together with standard module. It is foreseen that the central cassettes of the four RH sectors can be replaced by four test modules, eventually fed by a dedicated cooling loop. Since the design of the test modules is not yet available, the dedicated cooling loop shall supply water with a temperature ranging from 30 °C to 250 °C (± 5 °C) and a pressure ranging from 50 to 150 bar. The maximum mass flow rate per test module is 16 Kg/s with a total of 64 Kg/s for the four test modules. The inlet-outlet delta T and pressure drop are 20 °C and 2 MPa respectively.

3.1 Design Workflow

The design workflow of the DTT divertor is grounded in a Systems Engineering approach and is characterized by a strongly iterative and multidisciplinary process. The first and fundamental step of the process consists in the identification, definition and classification of the system requirements.

These requirements are derived from primary customer and stakeholder needs, including operational objectives, safety regulations, availability and cost constraints, and maintenance considerations, and are structured following established Systems Engineering practices. The outcome of this phase is the definition of the divertor system mission and a preliminary, traceable set of system requirements that constitutes the reference baseline for all subsequent design activities.

Starting from the requirements baseline, the detailed design workflow proceeds with the definition of the divertor geometry. As for all in-vessel components, this phase begins with the definition of the poloidal profile, which is derived from the reference magnetic configuration of the DTT plasma scenario and must ensure compatibility with the magnetic equilibrium and strike-point locations.

Once the poloidal profile is established, the toroidal profile of the plasma-facing units is defined, accounting for the interaction between magnetic field lines and material surfaces, power spreading effects and alignment constraints aimed at minimizing localized heat loads. The combined definition of poloidal and toroidal geometries establishes the plasma-facing envelope of the divertor and provides the geometric basis for subsequent analyses.

The geometry definition enables the evaluation of the main design-driving conditions, which impose the most severe constraints on the divertor design. In particular, thermo-fluid dynamic analyses are carried out to ensure safety and operability of the system under both normal operating conditions and off-normal scenarios, as well as to guarantee adequate cooling of plasma-facing and structural components.

The design of the cooling circuits therefore plays a central role in the workflow and is tightly coupled with thermal and structural assessments. Thermal loads are mainly associated with plasma–PFU interaction, which represents the dominant heat source and dictates the required heat removal capability of the cooling system. A secondary contribution arises from neutron interaction; however, in the DTT device this effect is not a primary design driver in terms of material heating or irradiation-induced degradation, although it is considered in the

definition of boundary conditions for completeness. The outputs of the thermal and fluid dynamic analyses are subsequently integrated into structural assessments aimed at verifying the mechanical integrity and lifetime of the divertor components.

The most demanding structural loads include those induced by the internal pressure of the cooling system, loads associated with off-normal plasma events such as disruptions, and seismic loads derived from site-specific seismic hazard assessments for the reactor location. All these analyses are embedded within iterative design cycles whose objective is to converge towards one or more baseline design candidates. The feasible design domain is constrained by technological limits, results from research and feasibility studies, and by risk minimization and mitigation strategies.

Throughout the entire workflow, requests for change may arise due to evolving requirements or interactions with other systems. For this reason, particular attention is devoted to the assessment of mutual coupling between systems and to the evaluation of the impact of requirement changes on the overall design, with the objective of minimizing rework and supporting an efficient and robust convergence of the design process.

The main nodes and information characterizing this workflow are summarized in the flowchart in Figure 23.

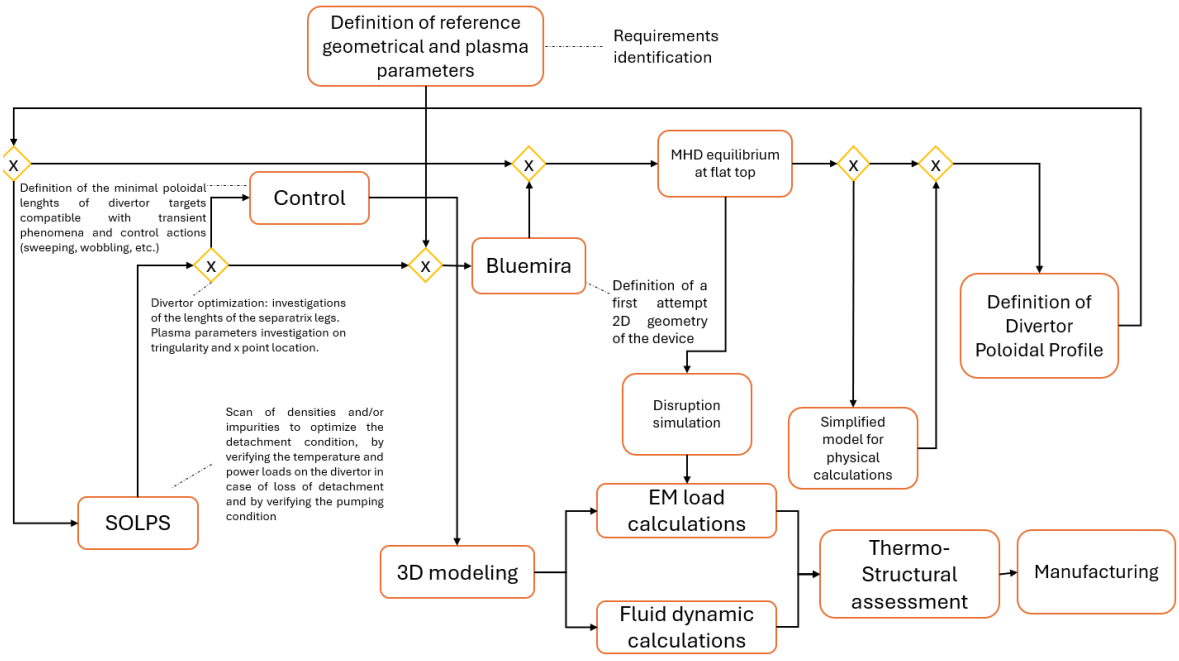

Figure 23 Divertor Design Workflow

3.2 Divertor Requirements

When requirements are formulated, they must be systematically assessed through two key processes: **requirements validation** and **requirements verification**. Within a Systems Engineering (SE) framework, these activities are essential to ensure both the correctness of the requirements and the compliance of the system with those requirements throughout the entire development lifecycle [37]. **Requirements validation** is the process of ensuring that the requirements set is complete, correct, compatible, and aligned with stakeholder needs. Validation confirms that the system, as built or planned, provides the appropriate solution to the stakeholders' problem, essentially ensuring that the project is *"building the right thing."* It assesses whether the system performs all the functions it should perform and avoids those it should not. While validation assesses whether the system is the *correct* response to stakeholder needs, **system verification** determines whether the system and its elements *meet their specified requirements*, that is, whether the system is *"building the thing right."* Verification involves tasks and activities aimed at evaluating the progress and performance of the evolving system and measuring its compliance with the defined requirements. It ensures that system specifications, designs, processes and products are fully consistent with the baseline requirements. Continuous feedback from verification activities reduces risks and allows early identification of discrepancies. A complete verification strategy is typically established once a preliminary design concept is available. In a Systems Engineering context, each requirement is associated with a dedicated verification activity and can be traced through a **requirements traceability matrix (RTM)** [38]. Each requirement is assigned a unique identifier that links it to test plans, test procedures and verification reports, thus establishing a closed-loop verification process from requirement to demonstrated capability.

Verification activities fall into the following fundamental categories:

- **Inspection**: visual or dimensional examination of an item to confirm compliance with the applicable documentation.
- **Analysis**: use of analytical data or simulations to demonstrate theoretical compliance when physical testing is unfeasible or impractical.
- **Demonstration**: qualitative exhibition of functional performance with minimal instrumentation, appropriate for requirements defined in statistical or behavioral terms.

- **Test**: quantitative assessment of operability, endurance, or performance under controlled real or simulated conditions, often requiring specialized test equipment.
- **Similarity/Analogy**: verification by comparison with previously validated, similar items, provided that design, fabrication, use conditions, and verification rigor are equivalent or more stringent.

An important SE tool in this context is the **requirements traceability matrix**, which documents the relationships between user requirements and the system being developed. It ensures that each requirement is properly addressed by one or more verification methods and that the system receives an adequate level of testing. Another cornerstone of Systems Engineering relevant to the development and assessment of requirements is the **V-Model development framework**. The V-Model describes the lifecycle from requirements definition down to detailed design, followed by integration, verification and validation, represented in the upward branch of the V [39]. Each stage on the left side of the V has a corresponding verification or validation activity on the right side, underscoring the continuous role of requirements engineering throughout system development. The V-model is widely adopted in industrial environments for its ability to reduce risks, improve communication between stakeholders, enhance planning accuracy, and ensure high product quality. By coupling each development phase with a specific test activity, it supports early identification of design inconsistencies and avoids redundant work, ensuring that all tasks are executed in the correct order and at the proper time.

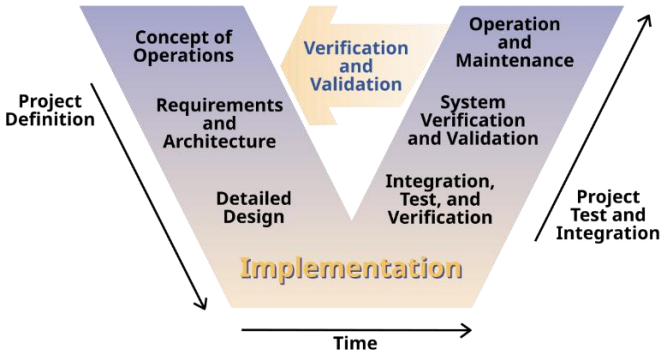

Figure 24 V-model schematic [40]

For the DTT Divertor System, the requirements definition followed a structured Systems Engineering approach [41]. The ITER System Requirement Document (SRD), which lists the main ITER requirements approved on 19 November 2018, served as a

key reference. Following the structure of the ITER SRD, the DTT divertor requirements were organized into the following categories:

- General requirements
- System-specific requirements
- Structural requirements
- Mechanical requirements (including load conditions)
- Seismic requirements
- Fire protection requirements
- Electrical requirements
- Grounding and insulation requirements
- Instrumentation and control requirements
- Computer hardware and software requirements
- HVAC requirements
- Vacuum requirements and vacuum classification
- Thermal management requirements
- Electromagnetic requirements
- Nuclear shielding requirements
- Chemical requirements
- Material requirements
- Manufacturing requirements
- Construction requirements
- Installation requirements
- Testing and inspection requirements
- Decommissioning requirements
- Design and safety requirements

- Assembly requirements
- Qualification requirements
- Environmental impact requirements
- Reliability requirements
- Other specific requirements

Each requirement was represented through multiple attributes, including a unique identifier (HEL code), requirement statement, object type (heading, requirement, information), requirement type (functional, operational, non-functional, implementation, or interface), comments and development status (e.g., In Work, Proposed, Accepted, Reviewed, Approved).The whole set of identified requirements has been included in ***Annex A – DTT Divertor System Requirements.***

3.3 Divertor Poloidal Profile Definition

As already stated, the main objective of the DTT project is to test different divertor configurations. Therefore, the machine is designed so as to be compatible with the Single Null (SN) configuration and also other alternative ones such as X Divertor (XD), negative triangularity (NT) single null and eventually Double Null (DN), Super-X divertor (SXD) and Snow Flake Divertor (SFD). In order to deal with the three basic configurations of SN, XD and NT, the selected divertor architecture includes four targets, namely inner target, dome target, outer vertical target and outer horizontal target (OHT) Figure 25.

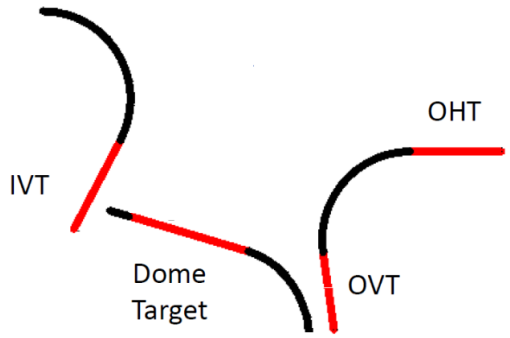

Figure 25 The DTT four target divertor scheme (targets in red)

The current divertor poloidal profile is a result of an optimization performed in years 2020-2023. The DTT basic SN divertor design started from the definition of a draft poloidal profile driven by early design inputs of the vertical targets, in particular the distances and grazing angles [42]. In 2021 a decision on the DTT divertor shape was taken: this consisted in a wide divertor with an almost flat dome. The selected configuration allows, in principle, better performances and a higher configuration flexibility with respect to a narrow divertor with curved dome. Then, some further modifications were implemented to increase the space between the vessel and the divertor bottom part, slightly moving up the divertor poloidal profile.

Afterwards, the possibility to increase the length of the external vertical target was considered in order to allow a wider sweeping and a possible improvement in terms of divertor closure, but with the disadvantage of a possible worsening of the negative triangularity configuration.

Therefore, two possible solutions of DTT divertor have been analysed, i.e. the wide divertor with a short and a long outer target. In these configurations the inner target is unchanged.

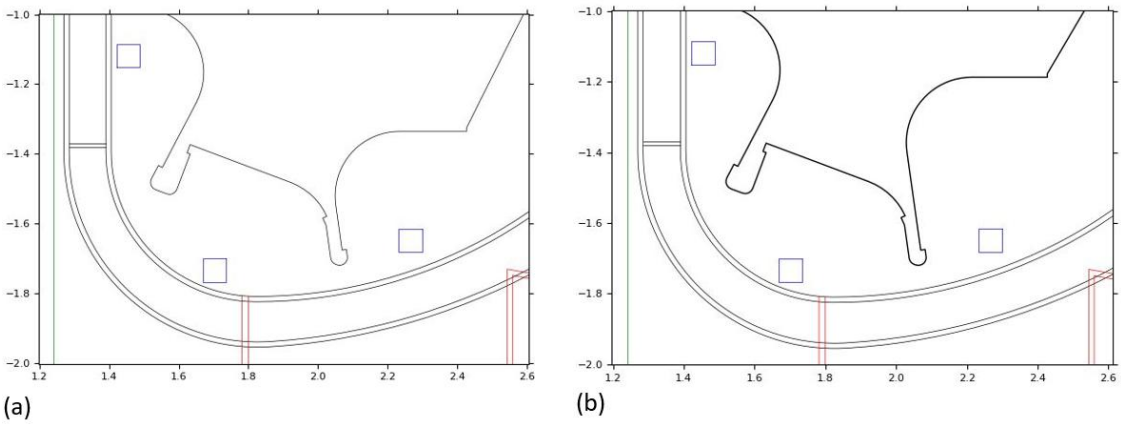

Figure 26 The divertor options - (a) solution with "short" outer target – (b) solution with "long" outer target

The investigation has shown that the SN and XD configurations are compatible with both the divertor options (Figure 26- a), b)) but for NT the X point position had to be modified even if without loss of performances in term of allowed maximum plasma current.

The conclusion of the entire exercise was that the two divertor options appear somehow equivalent for the development of the plasma magnetic configurations and decisions were taken based on the following considerations:

- the divertor with short outer target is abandoned because of limited flexibility, i.e. is compatible only with a precise position of the outer strike point;
- the divertor with longer target is retained even if it is more demanding in terms of costs and divertor remote handling (Figure 27).

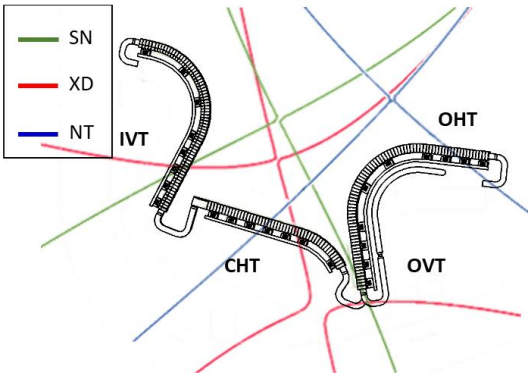

Figure 27 Compatibility studies of DTT plasma magnetic configurations for "short" (blue line) and "long" (red line) outer target for – (a) SN – (b) XD – (c) SN-NT

Then further analysis was performed in terms of power exhaust by investigating the advantage of increasing the length of the outer target. In particular three different divertors have been considered, they differ only on the length of the external target (130, 180 and 280 mm), all the other divertor parameters as well as the magnetic configuration remaining equal

(see Figure 28). In all cases the results confirmed the improvement of the neutral compression by increasing the outer target length and consequently a higher pumping throughput although, for the SN and SXD configurations, no advantage was observed in terms of an easier detachment or a lower plasma contamination. Therefore, at beginning of year 2023 it has been decided to increase the length of the outer target to 180 mm in order to allow a wider sweeping and more flexibility in the position of the strike point on the outer target. As a result of all the above findings the selected inner and outer target poloidal profile corresponds to the geometry of Figure 28 (b). For the dome the wide and flat configuration is selected. Further investigation is ongoing with the aim to optimize the divertor outer channel in terms of pumping efficiency and thermal/particle shielding.

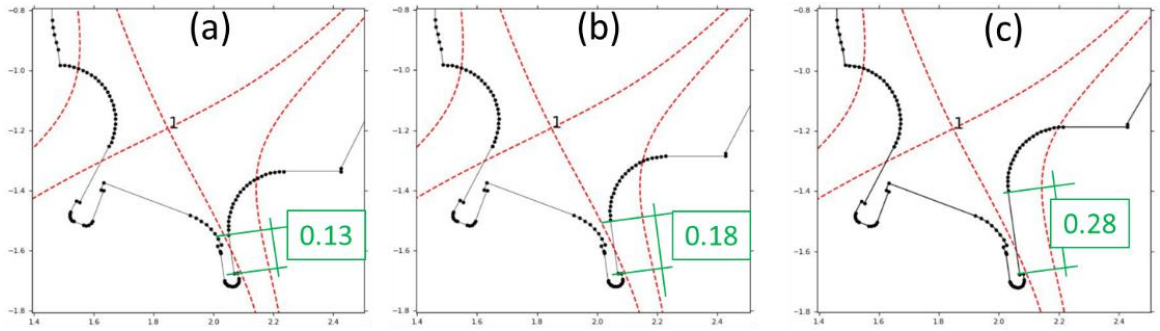

Figure 28 Outer vertical target length optionsd

3.4 Divertor Design Rationale

3.4.1 Plasma Facing Components (PFC)

The DTT divertor PFCs (inner and outer target and dome) are based on ITER full W divertor target concept which consists in W monoblock tiles joined to 12-15 mm ID-OD pipes. Such a component is also referred as PFU. A pure copper swirl tape turbulence promoter (0.8 mm thick, twist ratio 2) is inserted in the straight part of the inner and outer target strike region. Due to its manufacturing peculiarity, the dome cannot be provided with a swirl tape. The PFU pipes are made of precipitation hardened Copper Chromium Zirconium alloy. The assembly of PFUs in each divertor module includes the following steps:

- the single PFUs of the OVT, dome and IVT are welded together one-by-one,
- all the module PFUs are first mechanically attached to interface plates,
- the interface plates (with PFUs) are mechanically connected to the cassette,
- the PFU pipes are hydraulically linked to the cassette inlet-outlet manifolds.

As detailed before, three components can be identified: the inner target consisting of inner vertical target (IVT) and inner baffle; the dome, consisting of central horizontal target (CHT) and baffle; and the outer target, consisting of outer vertical target (OVT), a baffle and an outer horizontal target (OHT). The targets are the straight part devoted to sustaining the strike point, whilst the baffle is the curved part mainly needed to absorb the radiation thermal flux. All the baffle pipes have a curvature radius of about 170 mm: the inner and outer with an angular span of 105° and the dome with 48° (see Figure 29).

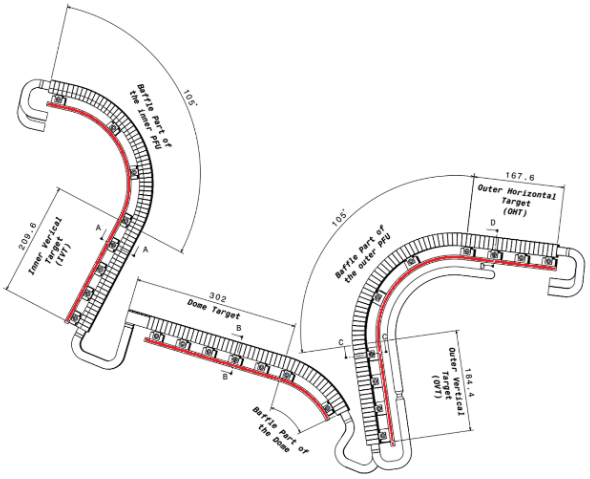

Figure 29 Lateral view of the three PFC: IVT, dome and OVT

One PFU of each component (outer target, dome and inner target) has to be welded in series and then fixed to three back-plates. The back-plates have the role of interface with the cassette body; when all PFUs are fixed on the back-plates, they can slide on the cassette surface and be fixed to it from the bottom side. In order to protect the leading edges of the PFCs and reduce the overheating of concerned PFUs, an asymmetric toroidal shaping has been adopted for all the targets. Figure 30 shows a schematic representation of the toroidal shaping of the four targets.

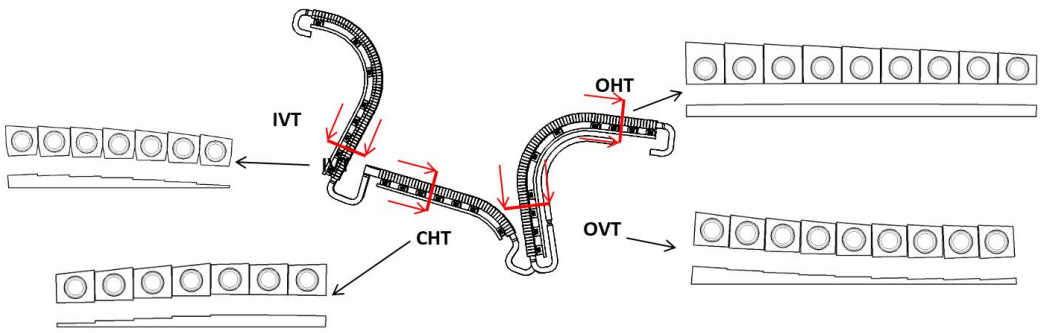

Figure 30 Schematic representation of targets toroidal shaping

The IVT and OVT have the main role to accommodate the strike points in the SN configuration. Their toroidal shaping is optimized for this configuration where a grazing angle of about 2° is foreseen. The IVT will have also to receive the inner leg of the XD configuration. The external leg of the XD shares the CHT with the internal leg of the NT whose external leg impinges the OHT. The PFCs shall be angled to avoid exposing the leading edges of the armour to the plasma SOL, otherwise the near normal incidence of the SOL on these edges would cause large amounts tungsten melted with the risk of poisoning of the plasma and/or inducing a critical heat flux event in the water coolant. The PFC leading edges are magnetically shadowed by providing a global tilting of the PFCs mounted on the cassette, whose orientation in the VV is perfectly radial. As a general rule, the manufacturing and assembly tolerances shall be minimised, since the larger the tolerance, the mgore the targets need to be angled in order to protect leading edges, and the greater the angle, the higher the heat flux on the target. For DTT an inter-cassette radial misalignment of ±2.0 mm is considered on the base of tolerance build up (Figure 31) [43].In addition to the cassette radial displacement, PFC tilting has to compensate also the additional exposure of the leading edge resulting from the inter-cassette toroidal gap. This results in an additional PFC tilting. For DTT the design inter-cassette gap ranges from 7.5 to 12 mm depending on the faced PFC. The amount of the tilting of the PFC has to compensate:

- a potential maximum radial step of ±2 mm coming from the fabrication tolerances;
- the radial component of the field line passing through the inter cassette toroidal gap (Figure 32).

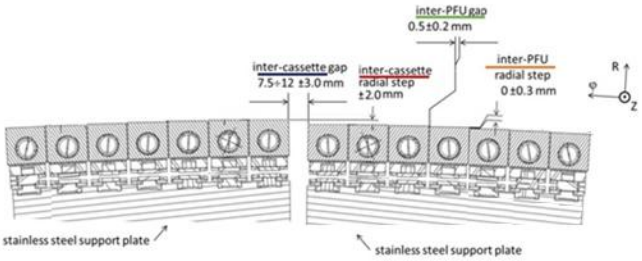

Figure 31 DTT PFU divertor assembly tolerance

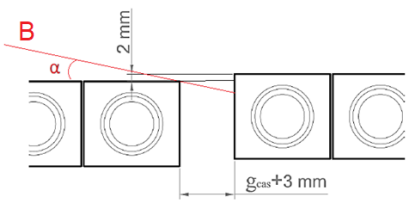

Figure 32 Inter-cassette leading edge (being α the (exaggerated) grazing angle).

The orientation of the tilting is determined according to the reference directionality of the toroidal current and field. In DTT plasma current is anticlockwise looking from above, toroidal field has clockwise direction, giving a downward (towards divertor X-point) ion grad-B drift direction. The directionality of the toroidal current and field determines the orientation of the tilting (see Figure 33)

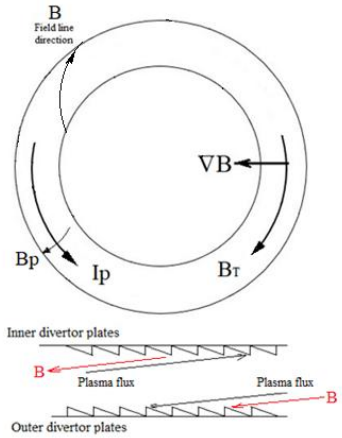

Figure 33 Orientation of the tilting (view from top)

Table 3 summarizes the findings of the toroidal shaping for the divertor PFCs to compensate inter-cassette radial misalignment. The tilting is applied only to the IVT and OVT strike point region. No tilting is applied to the dome and OHT part of OVT [43]: in this case the radial misalignment is compensated by steep bevels given to the monoblocks of the 2 extreme plasma facing units, left and right side (so called roof shaping). XD configuration does not constrain significantly the toroidal shaping due to higher flux expansion and shallow grazing angle. To be noted that the IVT and OVT tilting is generated by radial adjustment of the position of each plasma facing units, in such a way to generate a tilting of the plasma mating surface.

*Table 3 Toroidal shaping of divertor PFC (global tilting). * These bevels are doubled to consider the effect of dome and OHT profile symmetrical shape)*

PFC	Grazing angle α (°)	Inter-cassette gap- g_{CAS-} (mm)	Inter-cassette total gap (mm)	Field line radial component (mm)	Inter cassette radial step (mm)	MB width (mm)	PFC toroidal width	Tilt angle (°)	h bevel* (mm)

IVT	2(SN)	7.5	10.5	0.37	2	24	171.0	0.797	-
OVT	2(SN)	10	13	0.45	2	24.5	224.5	0.625	-
Dome	5.2(NT)	9.5	12.5	1.14	2	25.5	181.5	0	3.14
OHT	1.3(NT)	12	15	0.34	2	27.5	251,5	0	2.34

Previous R&D and ITER prototyping results have shown that the achievable monoblock tolerance in radial direction is ±0.3 mm. Therefore, this potential small misalignment has to be compensated by monoblock toroidal shaping.

A simple solution for monoblock plasma facing surface shaping is a planar toroidal bevel of height sufficient to protect the worst case radial misalignment (as said 0.3 mm). Unfortunately, the increased angle (typically less than 1.0 °) afforded by the inclusion of this bevel, added to that resulting from the global PFC tilting (see Table 3), increases the impact angle for plasma thermal fluxes on the MB surface and hence the power flux density compared with a nearly axisymmetric divertor system. The decision for toroidal shaping and its amount is, in principle, a matter of the trade-off between the increased power flux density, which has implications for both steady state and transient power handling, and the protection against melting of protruding edges. For DTT the chosen bevel height for the different PFC is summarized in table Table 4

Table 4 Monoblock toroidal shapin -The height of total bevel is the sum of inter-cassette and inter-MB bevels for dome and OHT. This applies only to side PFUs because the other PFUs are flat.

PFC	Grazing angle α (°)	Inter-MB gap (mm)	Field line radial component (mm)	Inter MB radial misalignment (mm)	h bevel (mm)	Bevel angle (°)	h total bevel* (mm)	Monoblock width (mm)
IVT	2(SN)	0.5+0.2	0.024	0.3	**0.32**	0.764	-	24
OVT	2(SN)	0.5+0.2	0.024	0.3	**0.32**	0.748	-	24.5
Dome	5.2(NT)	0.5+0.2	0.063	0.3	0.36	-	**3.50**	25.5
OHT	1.3(NT)	0.5+0.2	0.016	0.3	0.32	-	**2.66**	27.5

It was decided to provide IVT and OVT with both the global tilting and the monoblock bevel.

For the dome and OHT no global tilting is applied (flat profile); as already mentioned, the inter cassette radial misalignment is compensated by steep bevels given to the monoblocks

of the 2 extreme plasma facing units. The intermediate PFUs are left flat, i.e. with no bevel: this solution is justified by the lower amount of particle flux that can, in principle, came from both toroidal directions.

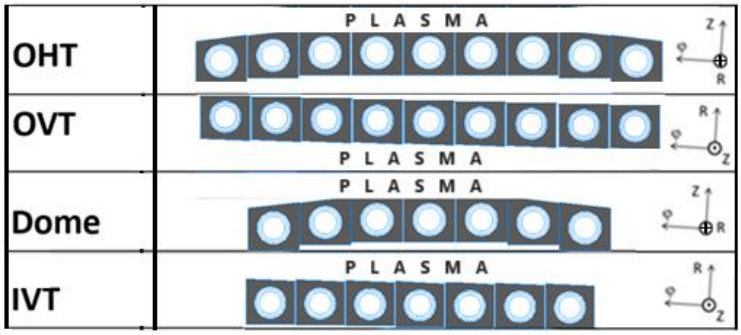

Figure 34 PFC toroidal shaping (note different axes' orientation)

The chosen design of ***the monoblocks with support*** is shown in Figure 1. As it can be seen the U shaped monoblock support (12mm wide) is 4mm wider than the monoblock (8mm wide) in order to accommodate a customized bolt with a diameter that has the capability to withstand the EM and thermal loads. The number of supports was decided based on the FEM mechanical analysis with the preliminary thermal and EM loads. In particular, for the OTs it was decided to introduce a support every 6 monoblocks for the straight targets (Outer Vertical Target and Outer Horizontal Target) whilst in the curved baffle only two equally spaced support have been considered (see Figure 36). The choice of two support in the baffle region allows a free expansion of the PFU under thermal loads.

- $u_y = free$
- $rot_Z = free$

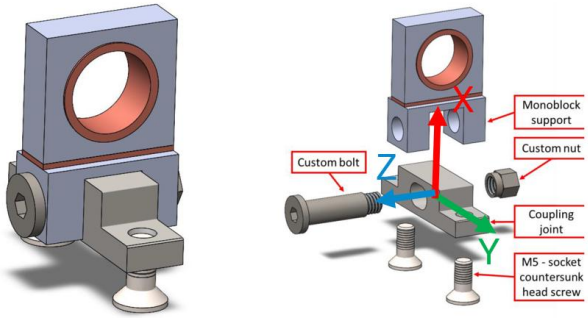

Figure 35 PFU support design

The monoblocks with support are connected to the slotted hole (allowing thermal expansion and fixing movement toward the plasma) of the coupling joint through a customized bolt (Ø 7mm – M6 head thread) and nut (M6 thread with hexagonal head). Only one connection

joint has a hole instead of elongated hole to avoid any liability of the PFUs. The coupling joint is then connected to the cassette backplate by means of two M5 socket countersunk head screw (Figure 35).

The necessity of a customized bolt derives from the very small room between PFU. These two screwed connections have been designed considering that the PFUs must be assembled (and disassembled) several times for qualification controls on the HHF test frame and cassette. Further improvements could be made in a second phase in the view of the series manufacturing.

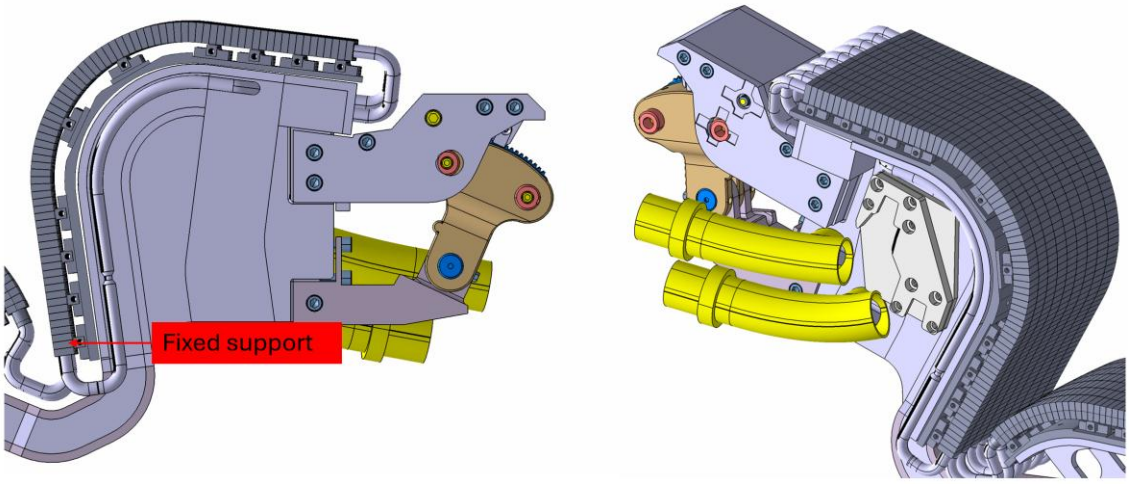

Figure 36 PFU supports layout

The materials adopted for the monoblock supports and the connection system are resumed in the next table (Table 5).

Table 5 Monoblock's support components chosen materials

Component	Material
Monoblock Support	XM-19 stainless steel
Bolt	Inconel 718
Nut	Inconel 718
Coupling joint	XM-19 stainless steel

3.4.2 Cassette Body

The DTT divertor cassette body is a robust structure consisting in a combination of AISI 316L and XM-19 stainless steel [44] This body integrates several functional apparatuses designed to meet specific functional and geometrical requirements. The cassette and the PFC

represent a single loop cooling circuit (Figure 37) since the operating temperature and pressure (see 3.4.1) of both systems are the same. This is not an obvious solution since the PFC and cassette body of other divertor in several machines need to operate at different temperatures and pressure due to several technological and physics driven reasons [45].

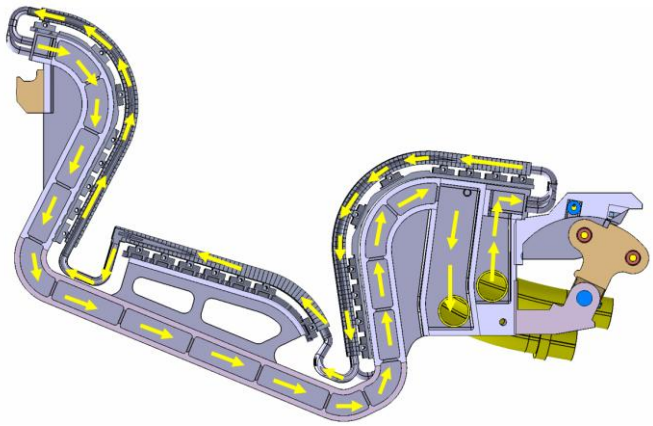

Figure 37 Divertor loop cooling circuit

The following key sub-components are integrated:

- **Main Central Shell**: This omega-shaped component forms the core of the cassette body and houses the larger cooling channels of the divertor. It is divided by a poloidal rib for structural stiffening, which also serves to partition the water flow into two main sections. The Main Central Shell serves as a dedicated shell primarily for the passage of water within the DTT divertor cassette. Its principal body is distinctly divided by an omega-shaped poloidal rib, which is crucial not only for the structural stiffening of the cassette but also for partitioning the water flow into two significant macro-sections. This shell maintains is further reinforced by toroidal ribs that connect centrally to the poloidal rib. These toroidal ribs are specifically slotted to ensure the passage of water. Their inclusion is designed to ensure structural integrity against an internal pressure load of 5 MPa. Moreover, as will be detailed in the manufacturing section, these ribs play a role in the manufacturing process of the central body of the cassette, contributing to the mitigation of deformations induced by machining.
- **Inboard Manifold**: It collects the main central shell water and drives it into the Inner target cooling pipes
- **Inlet Manifold**: Responsible for collecting water from the inlet pipes, this manifold then directs the coolant towards the outboard manifold. Its outer section also acts as an interface for the outboard fixation system.

- **Outlet Manifold**: After circulating through the cooling system, this manifold collects the water from the main body shell and channels it out through the outlet feeding pipe. The outer part of the manifold serves as interface for the Outboard Fixation System.
- **Interface to the Inboard Fixation System**: This provides the necessary connection point for securing the cassette body to the machine's inboard fixation system.
- **Flanges for Back Plate Interfacing**: They serve as the connection points for the back plates that support the Plasma-Facing Components of the divertor targets, effectively integrating them with the cassette body.

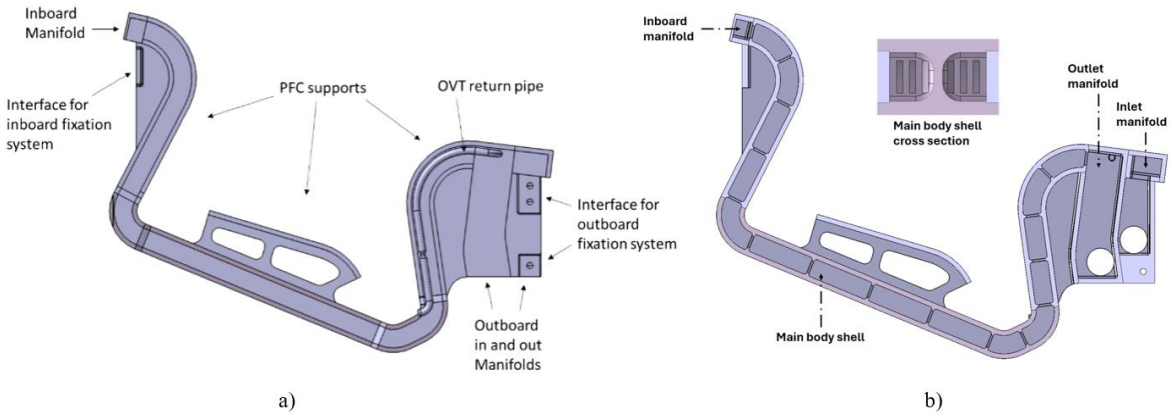

Figure 38 Cassette body main features

The main body shell of the divertor cassette has been designed with a smaller toroidal width than the Plasma Facing Components (PFCs). Consequently, the toroidal span of the cassette body (96 mm) is smaller than the overall toroidal envelope defined by the PFCs. This configuration results from several considerations, involving both physics requirements and geometrical as well as handling constraints. Unlike the ITER divertor cassette, in the DTT design the pumping of neutral species (such as Ne, He, and other impurities injected to achieve plasma detachment and divertor protection) is carried out through the evacuation of these species within the space between the dome and the outer target (OT), and between the central and inner targets (CT/IT). For this reason, a finite and relatively wide toroidal gap is intentionally maintained between the main body shells of two adjacent cassettes. This gap allows effective toroidal communication between the divertor volumes of neighboring cassettes, thereby facilitating the transport and removal of neutral particles. The configuration improves the overall pumping efficiency of the divertor region, ensuring an adequate exhaust of neutrals and maintaining suitable plasma conditions during detached

operation. The regions dedicated to neutral particle pumping, as well as the corresponding flow paths, are shown in Figure 39.

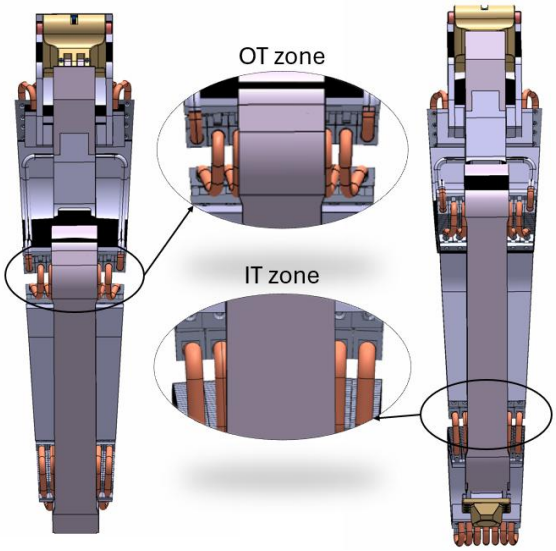

Figure 39 Pumping region for neutral injection

Moreover, the reduced toroidal width of the cassette body was also required to ensure compatibility with the feeding pipe layout. In fact, it was not possible to connect the pipes from the front side of the cassette, as this would have occupied a critical region within the port, interfering with the diagnostic systems and obstructing their lines of sight. By designing the cassette body narrower than the PFC envelope, the feeding pipes could instead protrude laterally, thus avoiding interference between adjacent cassettes and ensuring sufficient clearance for installation and maintenance operations.

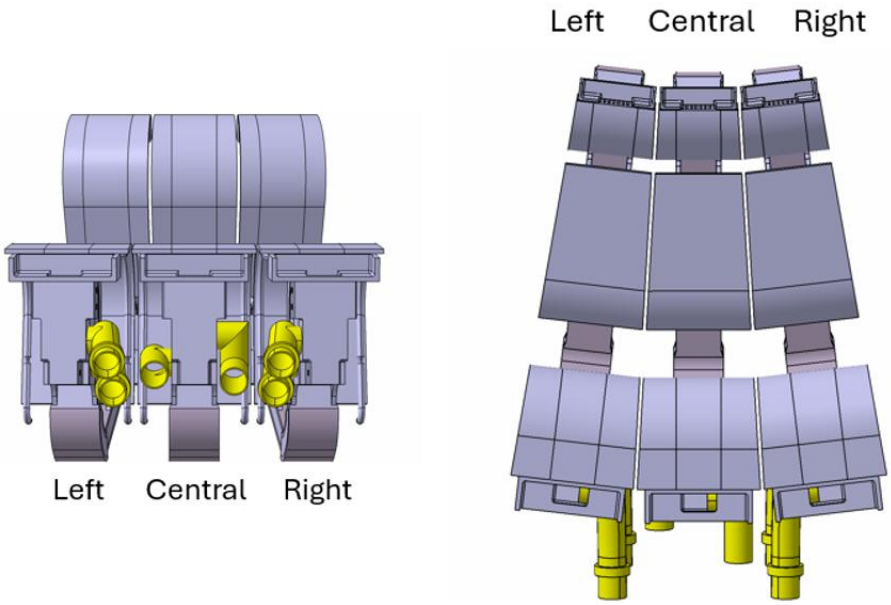

Figure 40 Divertor sector (20°)

3.4.2.1 Manufacturing issue

The divertor CB will be manufactured in sections, which are to be machined individually and then welded. Careful attention to tolerances should be paid at every point in the assembly sequence, in particular in relation to thermal deformations introduced by the welding process. Intermediate machining steps should be performed when necessary.

The rationale in the definition of the manufacturing process is to minimize the number of welds, which create weak points for mechanical loads, introduces thermal distortions, and necessitate volumetric inspections.

Nonetheless, in order to realize the internal structure and comply to the vacuum requirements, a fair number of welded joints will be necessary. Because of the vacuum requirements, all welds are supposed to be full penetration and volumetric inspection of all welds is required.

The CB has been separated for manufacturing in 22 parts (Figure 41).

For each part, the weight and type of raw material has been defined, as seen in Table 6.

Table 6 – Raw materials per component

MATERIAL		**COMPONENT**	**APPROX. WEIGHT (raw materials)**
AISI 316l	Forged	Cassette body (inboard)	20 kg
		Cassette body (outboard)	20 kg
		Inboard manifold	3 kg
		Outboard manifolds	50 kg
		Inboard ribs	11 kg
		Outboard ribs	13 kg
	Plate	Side plates	6 kg
		IVT flanges	8 kg
		OVT flanges	8 kg

		Dome ribs	5 kg
		144 kg	
XM-19	Forged	Cassette body (bottom)	40 kg
	Plate	Side plates	4 kg
			44 kg
TOTAL		**Single divertor cassette**	**188 kg**

ID	Part name
1	Cassette body
2	Target flanges
3	Dome flange
4	Side plates
5	Outboard manifolds
6	Outboard ribs
7	Dome ribs
8	Inboard ribs
9	Inboard manifold

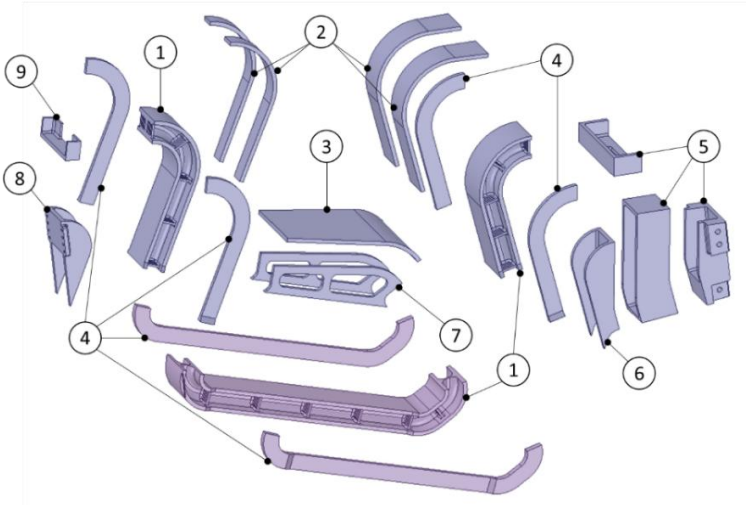

Figure 41 – Exploded view of cassette body

The proposed manufacturing sequence is described in detail in this section of the document.

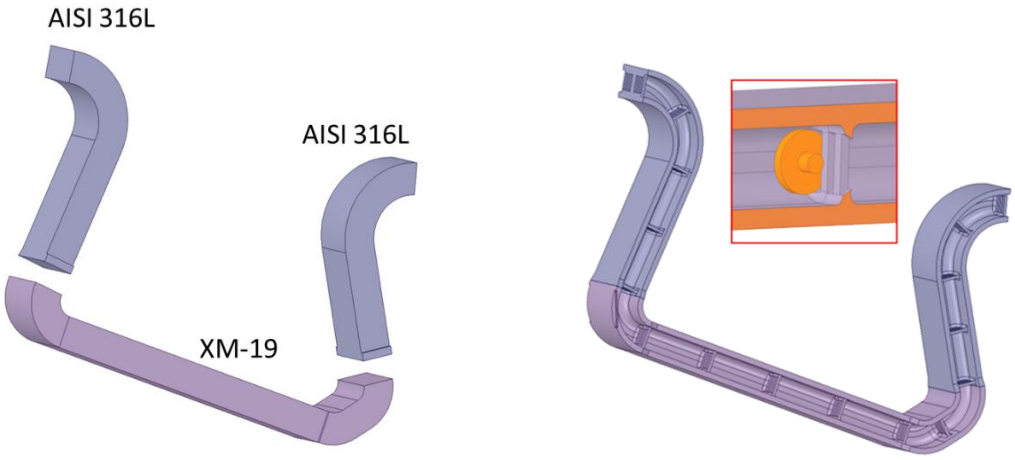

1. Cassette body blanks are assembled from the different materials. The joining process involves multiple weld passes with intermediate examinations, to realize full penetration welds across the whole thickness (> 96mm)

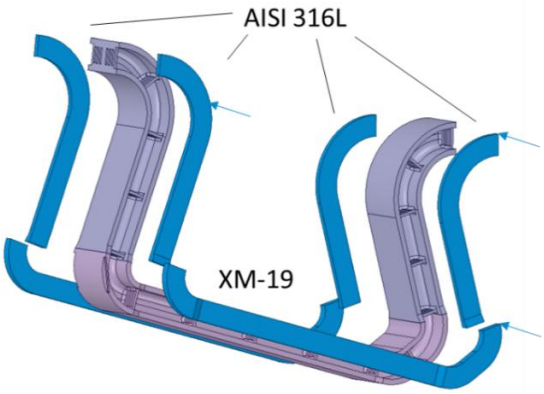

2. Cassette body is machined in one piece to obtain the internal geometry. Machining of the rib cuts can be performed from the sides using a disc cutter.

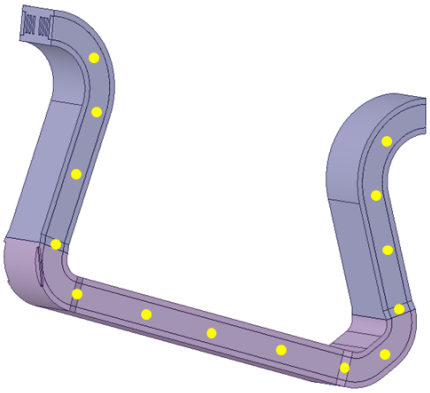

3. Side panels are welded to the sides to close the channels. The panels too are manufactured in different materials, following the same subdivisions as the main body.

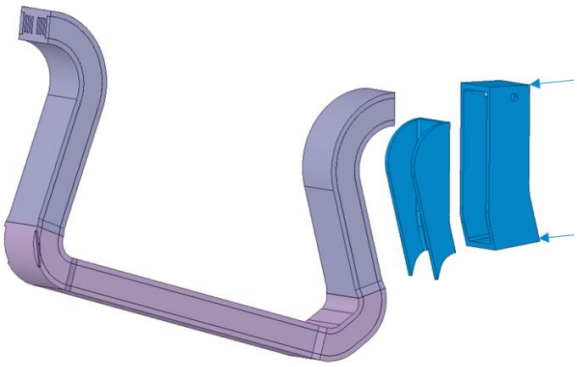

4. Spot welds are performed in correspondence of the ribs, to provide support against internal pressure.

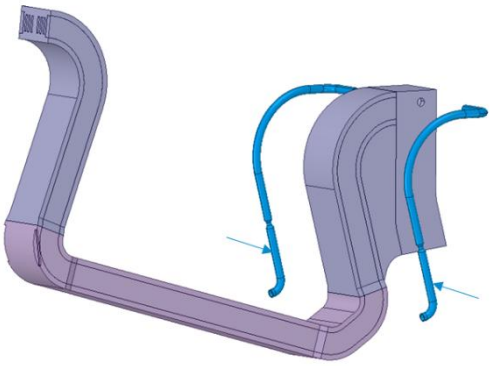

5. Outlet manifold and outboard ribs are welded to the Main Body.

6. OVT Returning pipes are welded to the manifold. This step should be executed before step 9 to have access to the weld.

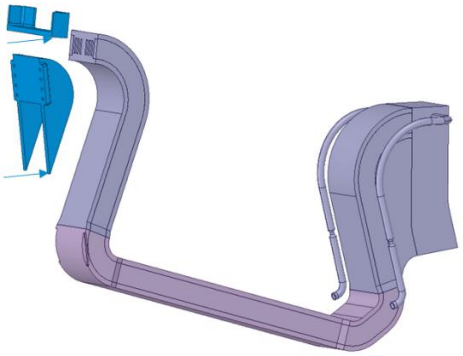

7. Inboard manifold and inboard ribs are welded to the main body.

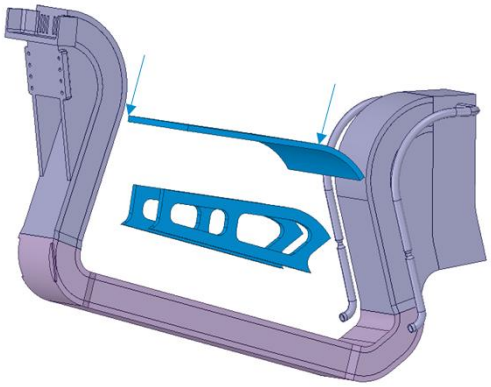

8. Dome supports and Dome flange are welded to the main body.

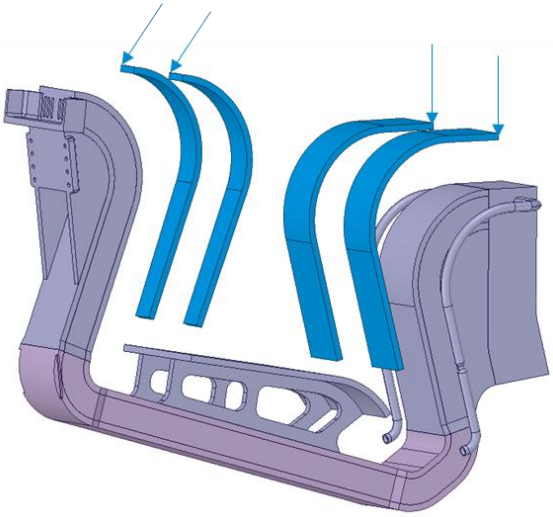

9. OT flanges and IT flanges are welded to the main body.

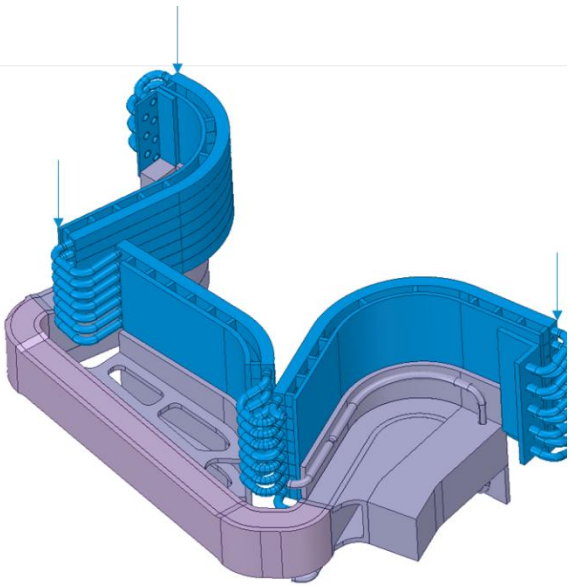

10. PFU sub-assembly is slid onto the main body. Target backplates are screwed to the flanges.

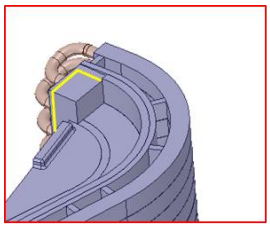

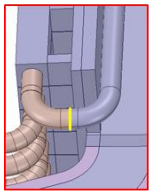

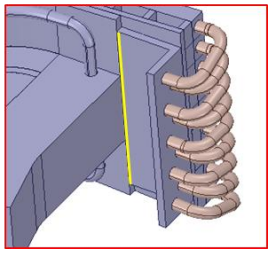

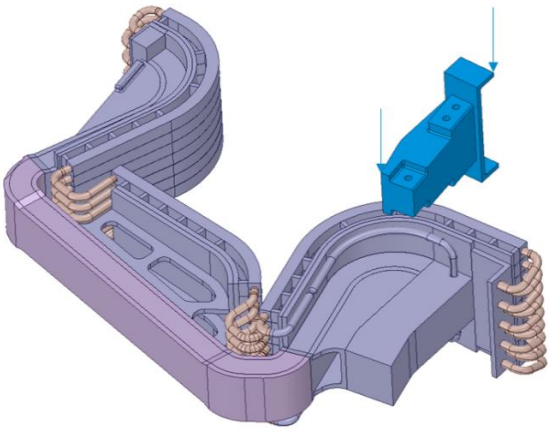

11. Welds should be performed at these locations after mounting the PFC assembly.

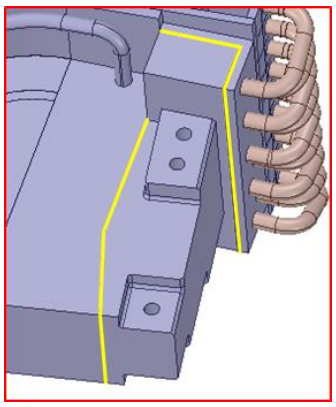

12. Inlet manifold is slid into position.

13. Welds should be performed at these locations after mounting the Inlet manifold.

Steps 11 and 13 present some critical issues, since the welds shown in figure should be performed after the PFC assembly has been put in place, and consequently after the last machining step. Under these conditions, the distortion introduced by the welding process could not be rectified by machining of the part. The necessity for this unorthodox procedure arises from a difficulty in welding the CuCrZr PFU pipes to the manifolds. The space constraints make it so that the connection can't be realized from the outside of the manifold, therefore access to the inside of the panel is necessary. The only way to allow this kind of access is to incorporate the manifold cover plates in the PFC assembly, and weld them to the manifold after the PFCs have been mounted on the CB.

The investigation of alternative assembly solutions for the manifolds is ongoing.

Originally, the flanges intended for bolting the back plates were fully curved and designed to exactly follow the back plate geometry, sharing the same curvature radii. However, following discussions with manufacturing companies during the market survey carried out for the DTT divertor cassette tender, it emerged that the required tolerance levels could not be reliably achieved over large curved surfaces. As a result, the design was revised and a faceted surface approach was adopte.

Therefore, after careful considerations it was decided to break down a manufacturing strategy through which the desirable tolerance values specified on the flange/cassette body

regions interfaced with the target back plates could be reached. In fact, the form tolerance foreseen on these surfaces is one order of magnitude tighter than what is realistically achievable after welding operations. Therefore, three main actions have been carried out on achieving this goal:

- Relax the form tolerance to align with achievable manufacturing capabilities post-welding (still on going)
- Allow for manual adjustment (fitting/shimming) on flat surfaces to meet final tolerance requirements.
- Do not allow adjustment on curved surfaces, as these are more difficult to control or modify post-process.

To meet the tolerance requirements, flat surfaces have been integrated into the design (Figure 42). These surfaces will be manufactured with tight tolerances and will serve as the sole interface between the back plate and the cassette flanges.

- All linear sections of the flanges and back plates will be fully toleranced.
- For the curved sections, a series of discrete flat pads—matching the number of bolted connections—will be created and manufactured with tight tolerances.

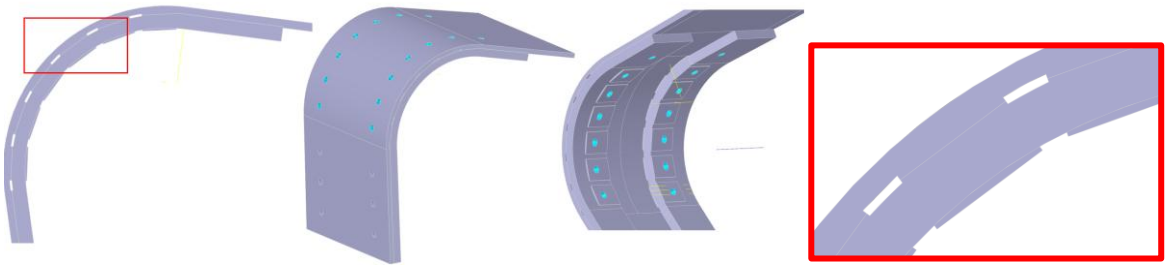

Figure 42 Faceted design for flange-back plates interfacing (figure shows the solution implemented on the OVT flange-back plate)

The offer a proper seating to the screw heads that will serve as connection between flanges and back plates, flat surfaces have been introduced into the design also on the lower region of the flanges.

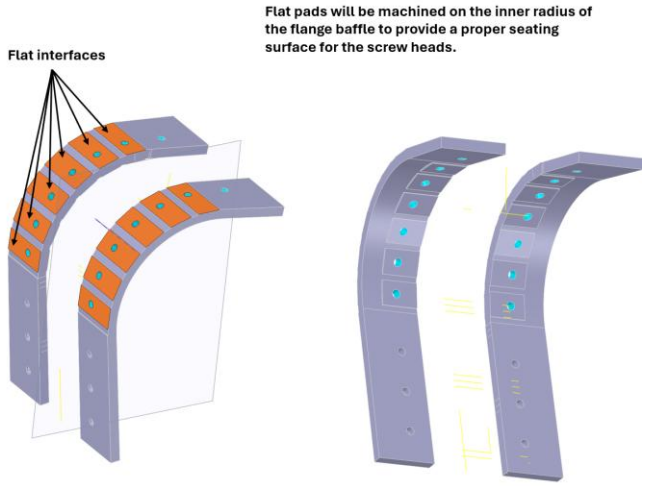

Figure 43 Seating surfaces for connection screws heads

A nominal gap has been set between the curved surface of the backplates and the curved surface of the interfaced flanges so that, even rough tolerancing of these surfaces won't affect critically the mounting between the two components.

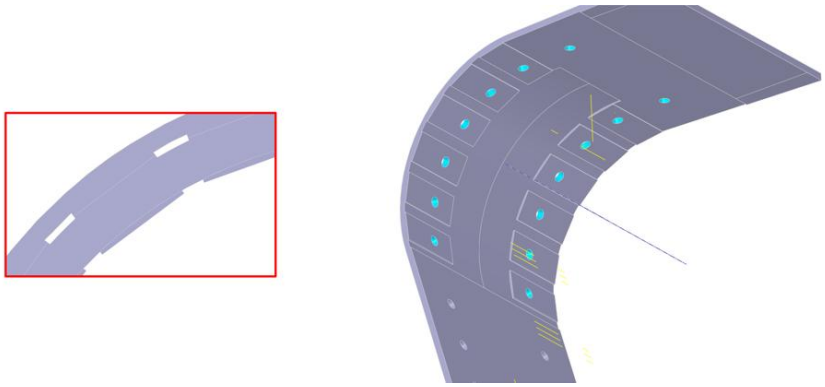

Figure 44 Faceted interfaces modeled on back plates side

3.4.2.2 Uncompressed configuration

The DTT divertor attachment system is based on a scaled-down version of the solution adopted in ITER. The divertor cassette acts as a spring compressed between the Nose and the Knuckle. The whole mechanism relies on an elastic deformation of the cassette to effectively impart a preload to the system, keeping the nose in contact with its socket as long as the radial component of the EM loads does not exceed the preload limit.

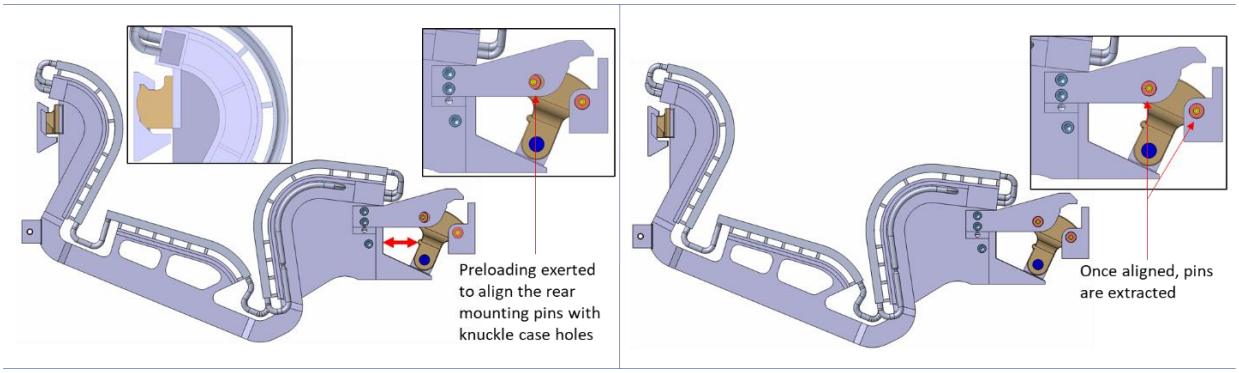

Figure 45 – Application of preload and locking of the knuckle system

Even when adjusting for the significant scale difference, the DTT cassette has a much lower stiffness compared to the ITER one, due to its much slimmer profile. For this reason, a significant deformation of the cassette (in the order of several mm) will be needed to impart a sufficient preload to the system.

This deformation needs to be accounted for in the manufacturing process, to ensure that the tight tolerances related to the positioning of the targets can be met after the installation of the divertor.

The placement of other interfaces, such as the connection points for RH systems and the feeding pipes should also account for the deformation of the cassette during preload, to avoid clashes or misalignments.

To this end, an uncompressed model of the cassette will be designed, such that after the preload phase the target profiles reach their nominal position. To obtain the undeformed configuration, starting from the nominal model, the cassette is constrained at the inboard and outboard and subjected to a set of external forces that are equal and opposite to those acting during the preload phase.

The system is subjected to its own dead weight (acting in the positive z direction) and a 20 kN force between cassette body and knuckle, that simulates the action of a mechanical jack.

The 20 kN force is applied using a preloaded spring, of very low stiffness, so as not to change the dynamics of the system.

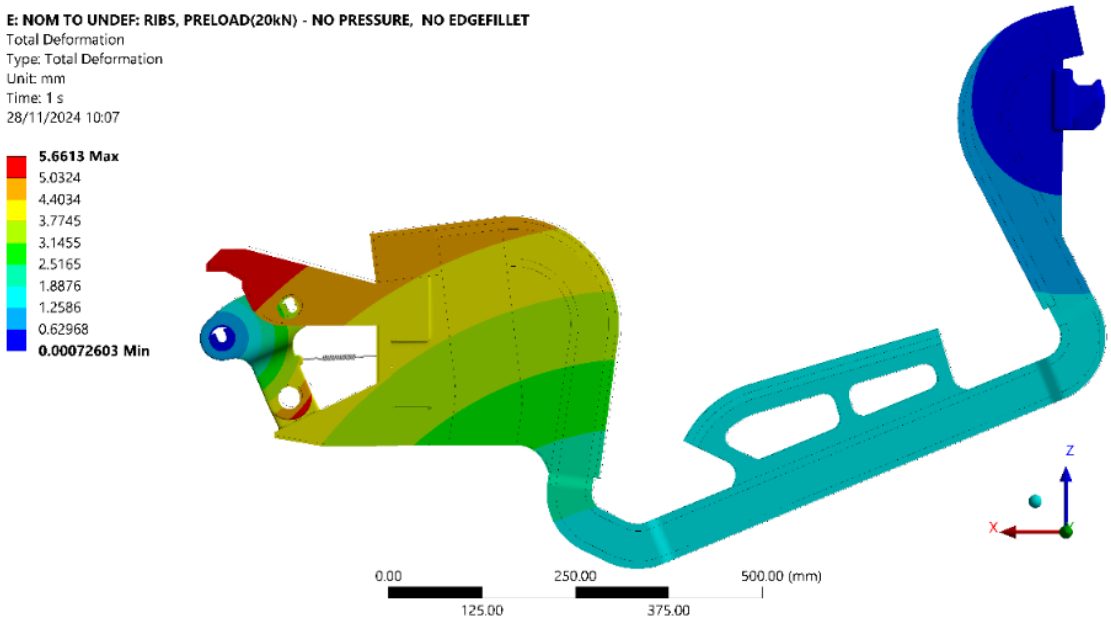

Figure 46 – Deformation of the cassette under inverse load

The undeformed geometry obtained as a result of the analysis shows a maximum displacement of 5.6 mm, localized at the outboard extremity of the divertor (Figure 46). The shape of each target remains nearly unchanged, and most of the strain is localized in the "elbows" of the cassette (Figure 47), which tend to open widening the horseshoe shape of the cassette.

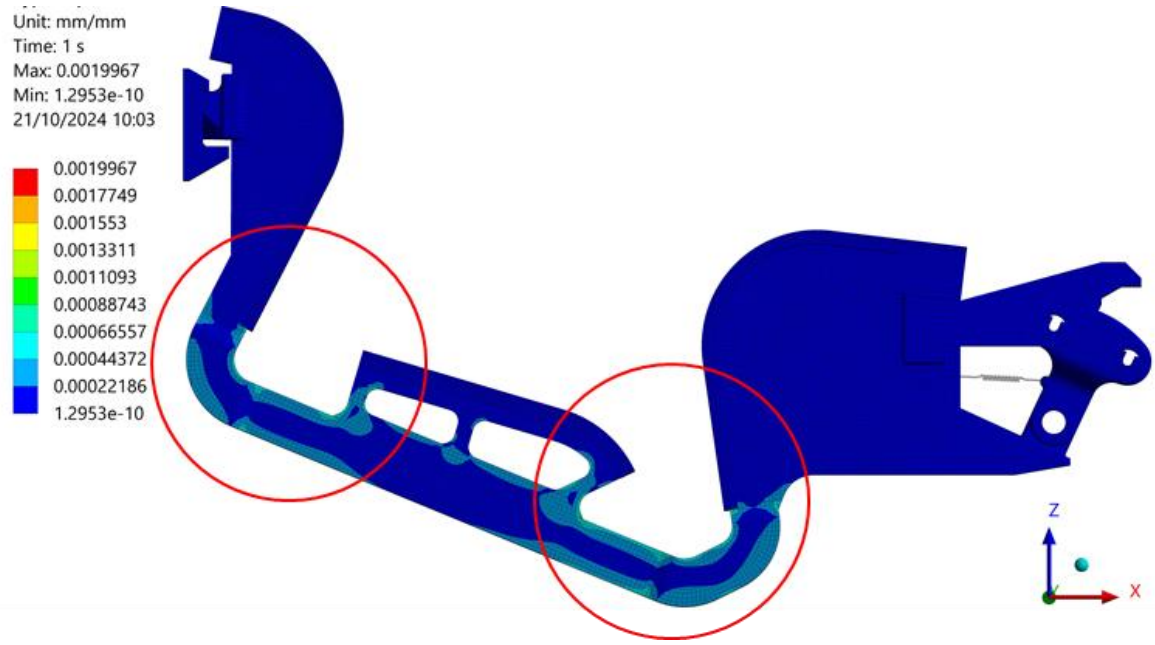

Figure 47 – Strain on the cassette after preload

The undeformed geometry obtained from the analysis must be translated in a model fit for manufacturing. For this reason, a CAD modelling step is necessary. Using a set of

geometrical references derived from the FEM analysis, a CAD model reproducing the undeformed configuration is generated. Since the positioning of the targets is a critical issue for the divertor, the new position of the targets is codified using a set of points on each of the target backplates.

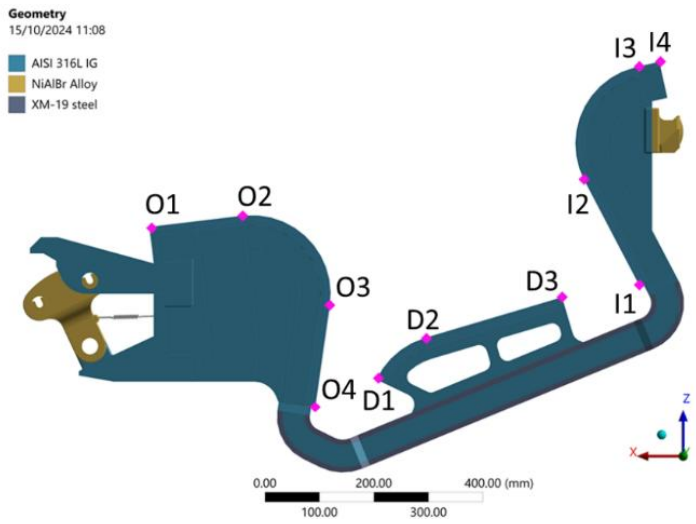

Figure 48 – Set of points used for reconstruction of the CAD model

The interface points between the cassette and the VV are taken as fixed points (namely, the center of the knuckle outboard pin and the center of the nose's hemispherical surface). The angle of the knuckle with respect to the vertical axis is also added to the references, to univocally determine the position of the other knuckle pins.

To verify the procedure, the uncompressed CAD model obtained is analysed under preload conditions, and the profile of the target backplates is compared to the target nominal position. As can be seen in Figure 49, the profiles of the deformed OVT and Dome follow the reference of the nominal configuration with an error <0.1 mm.

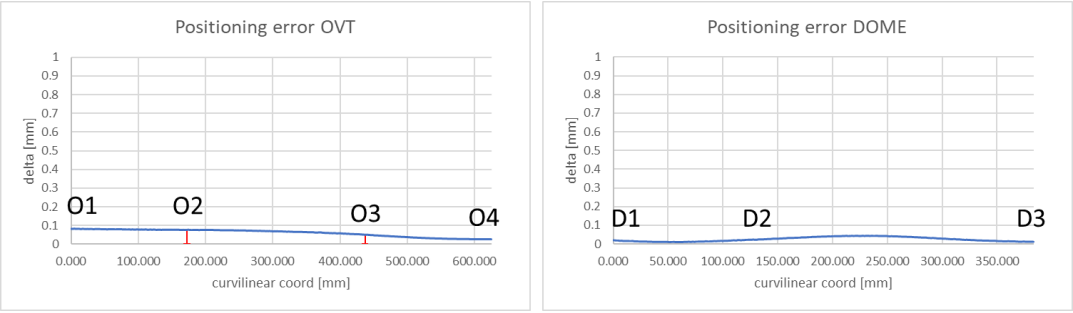

Figure 49 – Positioning error on OVT and DOME backplates

Higher values of the error, up to 1.3mm, can be observed on the IVT. This misalignment corresponds to an under-rotation of the IVT (0.3° ~ 0.4° short of the nominal position).

Through an iterative procedure, the discrepancy can be corrected in the cad model to achieve a better approximation.

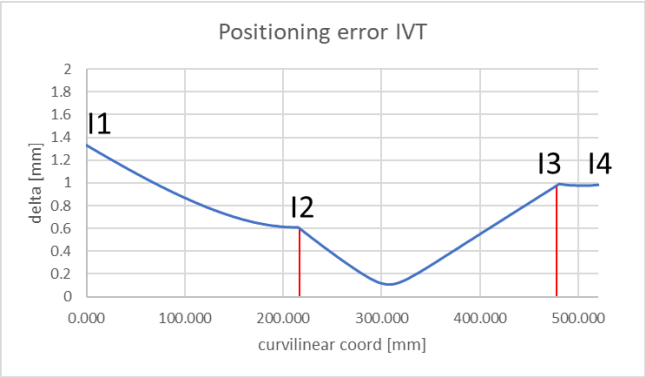

Figure 50 – Positioning error on IVT backplate

3.4.3 Fixation Systems

The DTT divertor fixation system plays a major role in ensuring the mechanical integrity and operational stability of the divertor during reactor operation [46]. Its primary function is to securely anchor the 54 divertor cassettes to the vacuum vessel, guaranteeing accurate positioning and structural stability throughout all operational phases of DTT.

The system is required to provide a reliable mechanical lock between each cassette and the vacuum vessel and to withstand significant electromagnetic loads, including those generated by disruption events. In addition, the fixation system must maintain the divertor alignment within the prescribed tolerances relative to the vacuum vessel, while accommodating thermal deformations and differential thermal expansion between the cassette and the supporting rails.

To ensure maintainability, full compatibility with remote handling systems is required for both installation and removal operations. Finally, the fixation system must guarantee continuous electrical contact among its components under all operational conditions. These requirements define the functional scope and design constraints of the divertor fixation system, which secures the cassettes to the toroidal rails welded to the vacuum vessel.

Before describing the design process that led to the actual DTT Divertor fixation system baseline, an overall description of the robotic tool dedicated to the handling of the divertor cassette is presented. The necessity for remote handling of the DTT divertor is fundamentally driven by the substantial neutron activation anticipated within the tokamak environment. Given a projected neutron rate ranging from $0.3 * 10^{17}$ for Advanced Tokamak scenarios to $1.3 * 10^{17}$ ns for H-mode extremes, the short and medium-term activation of in-vessel components mandates that all maintenance and replacement operations be executed remotely, thereby safeguarding personnel and minimizing their exposure [47].

This capability is further crucial for facilitating the testing of diverse divertor configurations, enabling the straightforward replacement of various cassette types to explore alternative magnetic configurations and power exhaust systems.

The comprehensive handling strategy for the DTT divertor is underpinned by a specialized Remote Maintenance System. This system encompasses dedicated equipment and a "Shielded and restricted area" specifically designated for repair operations and the temporary storage of radioactive waste, with the overarching aim of minimizing machine shutdown periods and maximizing machine availability. The DTT tokamak itself is meticulously

designed to accommodate these complex operations, featuring 18 sectors, with four, specifically sectors 1, 5, 10, and 15,earmarked for remote handling procedures. Each of these designated sectors is equipped with five ports, which serve as crucial conduits connecting the in-vessel environment to the out-vessel area [48].

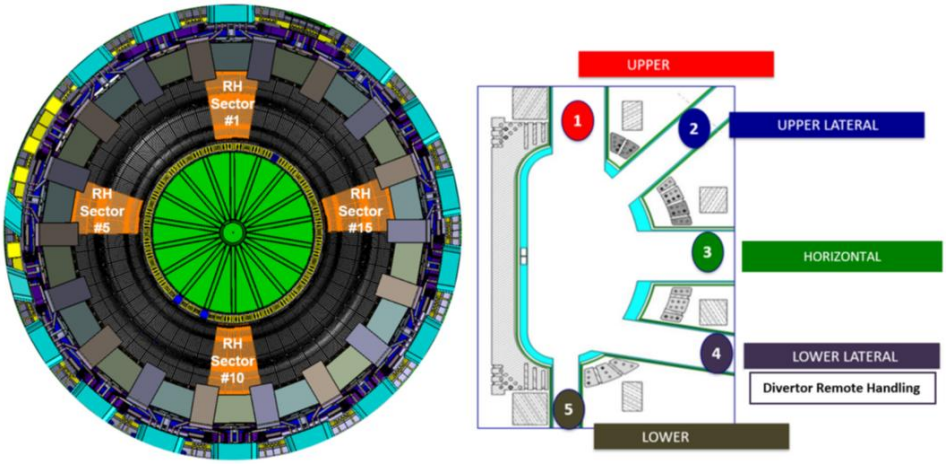

Figure 51 Remote Handling dedicated sectors and ports

At the core of the DTT divertor's remote handling system are two primary tele-operated robotic tools: the Cassette Multifunctional Mover (CMM) and the Cassette Toroidal Mover (CTM) [48]. The Cassette Multifunctional Mover is engineered for the critical task of precisely placing and removing divertor cassettes located in proximity to the designated remote handling ports, facilitating their ingress or egress from the vessel. This robot primarily manages cassettes positioned centrally and adjacently to the access ports Riccardi et al., 2023.

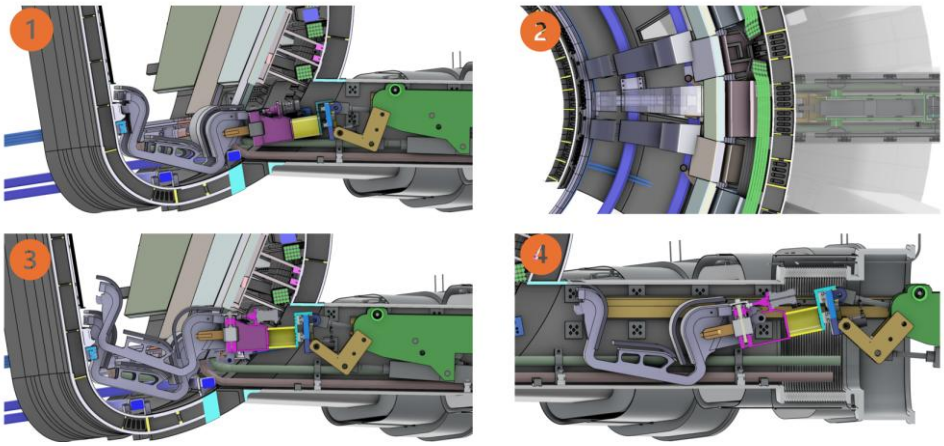

Figure 52 Four main frames of the simulation of right lateral cassette (second cassette right (SC-r)) removal by CMM in Case A (CMM – SC Grabbing Pose provided by CMM design team): 1) CMM grabs the SC-r; 2)

CMM toroidally moves the SC-r towards the sector's centre; 3) CMM lifts up the SC-r to make it pass over the Outboard Divertor Coil; 4) CMM extracts the SC-r through the duct.

The requirements for the divertor remote handling equipment are defined by the operational tasks to be performed and by the environmental constraints of the DTT device. The principal functions include handling of the divertor cassettes, locking and unlocking of the cassette fixation system, manipulation of the cassette cooling pipes, and the execution of auxiliary service operations. These activities must be carried out within the geometric constraints imposed by the vacuum vessel lower lateral port and the divertor remote handling casks, as well as under potentially demanding temperature and radiation conditions. These requirements have driven the development of the Cassette Multi-Manipulator (CMM) system, which provides the necessary capabilities for divertor maintenance operations. The CMM system consists of dedicated subsystems for cassette handling, fixation system actuation, cooling pipe manipulation, power and control, and visual inspection. The manipulators operate on radial rails installed in the access duct and casks, enabling controlled radial motion during in-vessel and transport operations

Generally, in tokamak devices, divertor cassettes must be preloaded to ensure stable mechanical coupling with the vacuum vessel during operation. This requirement arises from the inherent constraints of remote installation and removal procedures, which generally prevent the use of conventional bolted joints and the creation of fully hyperstatic connections between the divertor and the vessel.

As a result, preload is applied to maintain the divertor in a stable position under nominal operating conditions, during plasma transients, and in the presence of Lorentz forces generated by disruptions or Vertical Displacement Events. At the same time, the fixation system must accommodate differential thermal expansion between the divertor and the vacuum vessel without loss of contact or mechanical relaxation.

The preload strategy can be implemented through either flexible or rigid fixation concepts. In flexible systems, the preload is mainly absorbed by elastic elements within the fixation device, whereas in rigid systems the divertor structure itself is preloaded. The suitability of either approach strongly depends on the stiffness of the divertor cassette and on the distance between the preload application point and the zones most susceptible to bending. In devices such as DEMO or Volumetric Neutron Source (VNS) [49], where divertor cassettes exhibit

very high structural stiffness, flexible outboard fixation systems are adopted, allowing the fixation element to deform elastically during preloading.

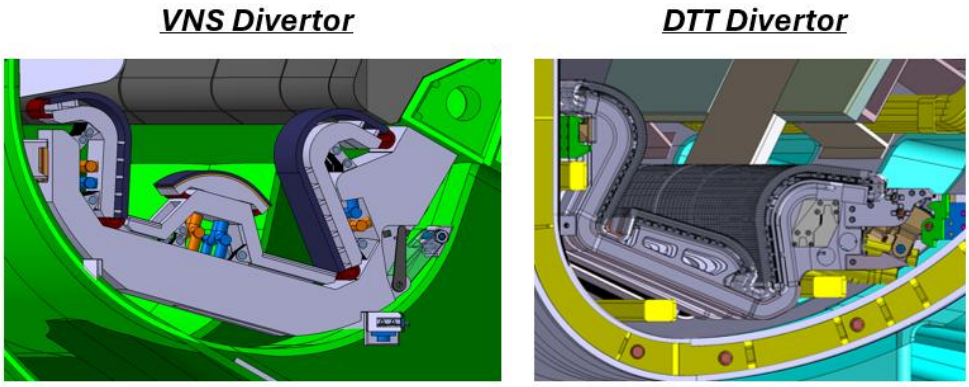

Figure 53 VNS and DTT Divertor- the bulky shape of VNS divertor would be too difficult to deform (with a reasonable amount of force)

During the first design iteration of the DTT divertor fixation system, several conceptual solutions were evaluated to identify the most suitable approach while ensuring compatibility with all remote handling procedures [50]. The knuckle mechanism was not initially considered due to its higher mechanical complexity. The three most promising alternatives investigated at this stage were the wedge-based fixation system, the spring pack fixation system, and the wishbone concept. The wishbone represents the baseline solution for DEMO [51] and VNS divertors, while the spring pack system emerged as a viable option during the conceptual design phase of the DEMO divertor. However, preliminary structural assessments highlighted that the relatively high flexibility of the DTT divertor cassette made the adoption of a flexible fixation system unsuitable. In the case of the wishbone concept, preload application led to bending deformation of the cassette itself, particularly around the outer elbow of the omega-shaped structure, rather than elastic deformation of the fixation element. This behavior would compromise both structural integrity and alignment, making it difficult to design a fixation system less rigid than the cassette while still capable of withstanding the severe electromagnetic loads expected during disruptions. Consequently, the wishbone solution was ruled out. The spring pack fixation system was also excluded from the set of feasible solutions. Its reliance on friction between the front interface of the spring pack and the outboard rail did not guarantee sufficient stability of the divertor in the outboard region. In addition, significant uncertainty exists regarding the long-term performance of metallic springs under neutron irradiation, as irradiation-induced

embrittlement and loss of elastic properties could severely degrade their functionality over the divertor lifetime.

Based on this assessment, the wedge-based fixation system was initially selected as the baseline solution for the DTT divertor fixation system. Following further design iterations and technical discussions among the teams involved in the conceptual development, the wedge concept was eventually replaced by a rigid knuckle-based fixation system, which provides a more robust and precise locking mechanism suitable for the DTT operational environment. Nevertheless, the wedge-based system was retained as a backup solution and developed in detail; its prototyping activities are discussed in 3.4.3.1.

The DTT divertor fixation system consists of three primary elements: the outboard fixation system (knuckle), the inboard fixation system (nose), and a lower stop Figure 55.

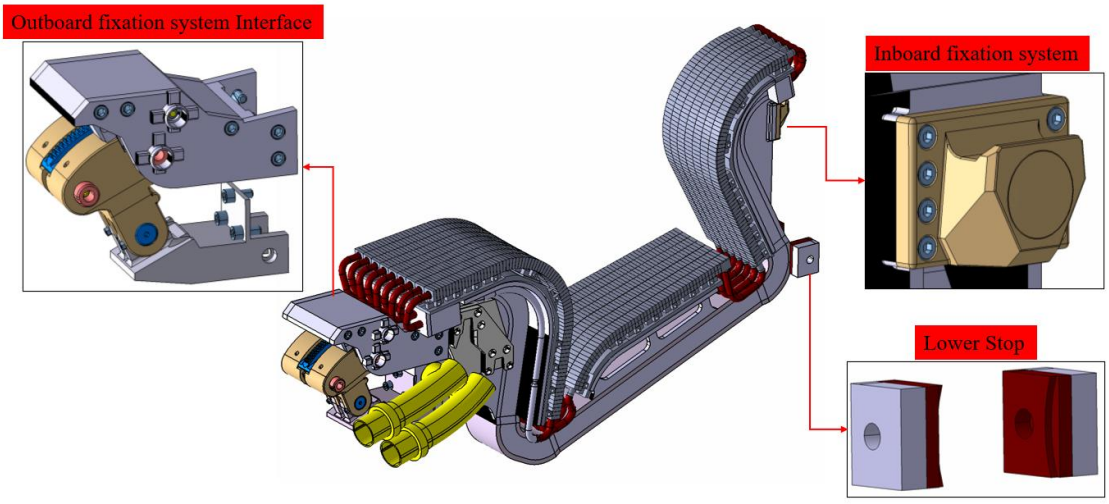

Figure 54 DTT Divertor Fixation System

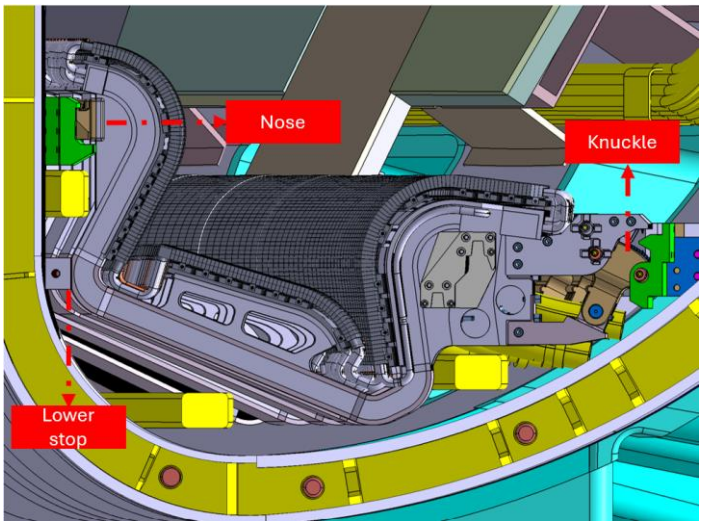

Figure 55 Fixation system components located in vessel

The knuckle system serves as the main outboard fixation mechanism, closely resembling the ITER knuckle configuration [53][54]Its design and operation are critical for securely locking the divertor cassette to the outer rail of the vacuum vessel. Key components of the first design iteration of knuckle are highlighted in Figure 56 [46]. Further into the document the updated and final knuckle design will be discussed, highlighting the process that led to the revision of the concept. It must be said that, also after the redesign, the key functions of the device were preserved.

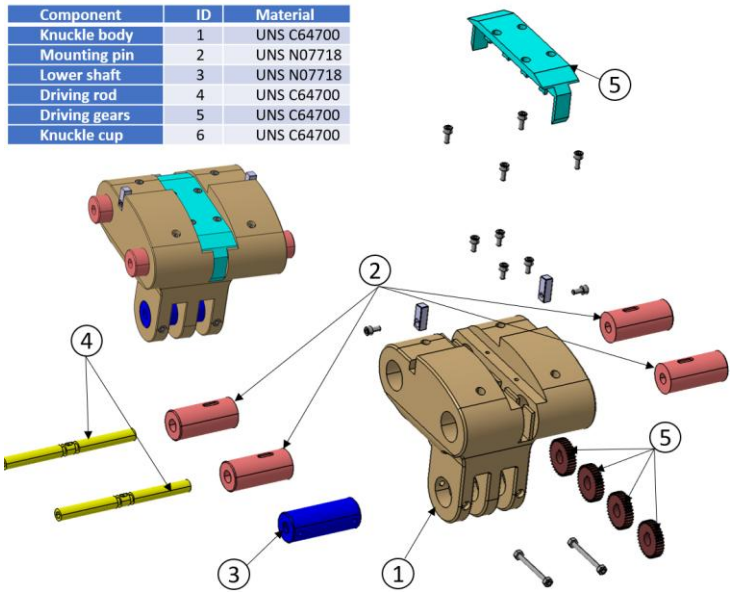

Figure 56 Knuckle first design iteration

These parts are primarily fabricated from Ni-AlBr steel alloy, selected for its anti-grip properties, high mechanical strength, and low friction coefficient. The mounting pins and the lower shaft, which are crucial for the engagement mechanism, are made of Inconel 718 due to their superior mechanical and thermal properties. The mounting pins are hollow and internally threaded and are screwed onto the driving rod. Rotation of the driving rod causes the pins to translate and engage with their corresponding mounting holes, thereby locking the cassette. The knuckle is interfaced on one side with the divertor cassette body and on the other side with the outboard rail (Figure 57).

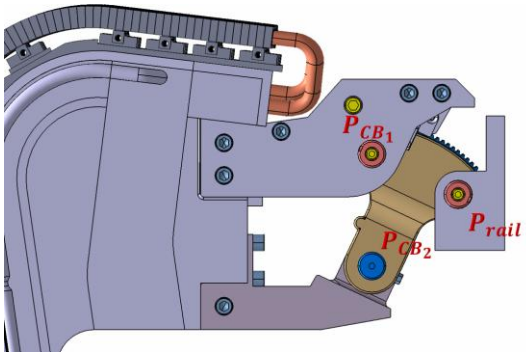

Figure 57 Knuckle anchoring points

In particular, it is connected to the cassette body at two distinct points. The lower connection, implemented by means of a shaft, allows relative rotation of the knuckle with respect to the lower axis. As a result, the knuckle is permanently mounted on the cassette through this lower shaft. This rotational capability is required because, as will be outlined later, in the late phase of the DTT machine a Cassette Toroidal Mover (CTM) will be introduced for the toroidal handling of the cassette. During toroidal handling, the CTM travels along the outboard and inboard rails, carrying the cassette to its correct toroidal position prior to installation. In this phase, the knuckle must be retracted and kept as close as possible to the cassette body in order to avoid collisions or potential interference with surrounding in-vessel components. For this reason, the knuckle is designed to retract into the cassette body during toroidal handling. Once the Cassette Toroidal Mover has positioned the cassette in its final toroidal location, an actuator on the Cassette Multifunctional Mover rotates the lower shaft together with the attached knuckle. The front part of the knuckle then mates with the vertical interface of the outboard rail. At this stage of the installation sequence, the second anchoring point between the knuckle and the cassette, as well as the anchoring to the outboard rail, is secured through the extraction of the mounting pins. The mounting pins are provided with an internal thread, which enables their extraction once the corresponding driving rods are rotated. In addition, the pins are machined with dedicated circumferential grooves that define the extraction end-stroke. Specifically, the terminal surface of each groove comes into contact with a mechanical stop screw, which prevents any further extraction once the correct deployed position of the pin has been reached, thereby ensuring a reliable and repeatable locking condition.

The actuation of the pins is achieved through a dedicated kinematic chain composed of a series of transmission gears. The rear driving rod, which is directly accessible by the Cassette Multifunctional Mover, is mechanically connected to a rear gear wheel. Upon actuation, this

rear gear transfers the motion to one or more intermediate gears, which in turn transmit the rotation to the front gear wheel. The front gear is keyed to the front driving rod. Thanks to this arrangement, the rotation of the rear driving rod alone is sufficient to simultaneously actuate both the rear and the front driving rods, allowing the extraction of both the rear and front mounting pins in a synchronized manner. The detailed description of this locking mechanism and its operational sequence will be provided in the following sections.

The interface between the knuckle and the cassette is designed to accommodate the knuckle during the retraction phase. In particular, the interface geometry allows the knuckle to rotate and retract close to the cassette body during toroidal handling, ensuring sufficient clearance with surrounding in-vessel components. In addition, the interface incorporates a front feature that is required to support the divertor on the outboard rail during the initial installation phase. This feature prevents the divertor from falling before the preload is effectively applied and before the mounting pins are engaged both with the outboard rail and with the secondary engagement point on the cassette. The design of this interface underwent several iterations, mainly driven by manufacturing requirements. Due to its complex geometry and the presence of multiple non-conventional functional features, the interface could not be manufactured as a single component. It was therefore subdivided into multiple parts, allowing feasible manufacturing processes while maintaining the required mechanical robustness of the system. The main functional features Figure 58 of the interface include the tooth required for the divertor parking position, the supports for the lower shaft that connects the interface to the knuckle in the lower region, the bore for housing the mounting pin, and a set of mechanical stops. These stops are positioned to ensure a well-defined and repeatable end-of-stroke condition, defining the end of the preload phase through a purely mechanical constraint. This solution avoids the need for position control or active feedback systems from robotic manipulators during installation.

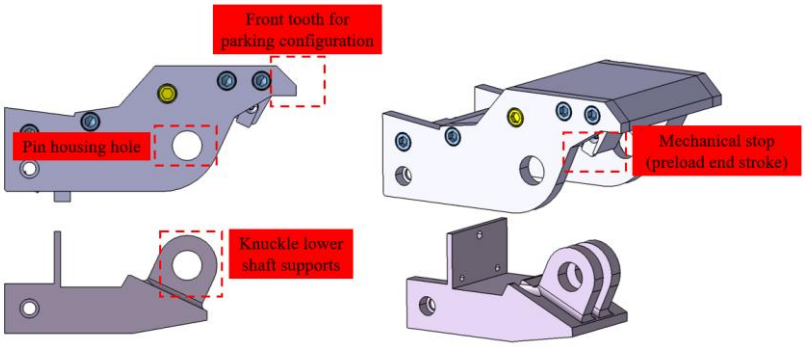

Figure 58 Knuckle case (knuckle cassette body interface) features

The nose Figure 59 functions as the inboard support for the cassette and features a hemispherical interface. This interface engages with a corresponding socket on the inboard rail during installation, ensuring accurate toroidal centering of the cassette once the divertor is positioned [54]. As for the knuckle body, the nose is manufactured from Ni-AlBr steel alloy, selected for its suitable mechanical properties and anti-gripping behavior [46]. The nose geometry incorporates several functional features. The hemispherical interface is required to provide self-centering capability during the installation phase, in which the nose is pushed into the inboard rail. A hook feature is integrated to prevent upward displacement of the nose, which could be induced during plasma disruptions that tend to pull or disengage the nose from the inboard rail. In addition, a 45-degree inclined interface is provided to allow controlled sliding of the nose along the inboard rail during the mounting phase. In the nominal configuration, only two interfaces are designed to be in effective contact with the mating surfaces of the inboard rail: the hemispherical interface and the inclined interface. A finite clearance of 1 mm is intentionally introduced between the hook and the corresponding surface of the rail, as well as between the vertical surfaces of the nose and those of the rail. This design choice is required because, during the preload phase, the nose undergoes a finite rotation induced by the deformation and bending of the inboard branch of the divertor as it is compressed. This motion results in a rotation of the nose about the axis of the hemispherical cap, which tends to reduce the clearance between the hook and the rail. Without the presence of these gaps, contact would occur during the preload phase, leading to excessive and unmanageable stress and to a highly over-constrained mechanical condition.

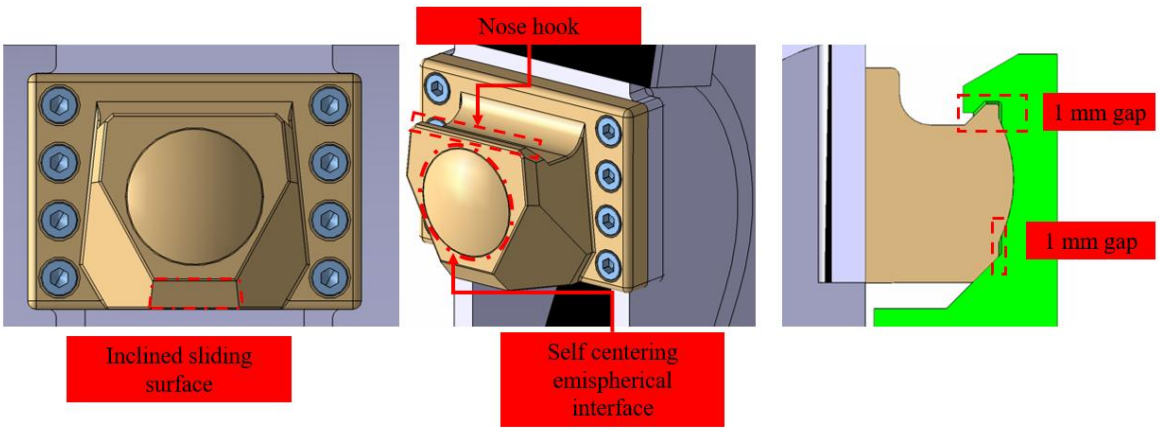

Figure 59 Nose features

An additional ***lower stop*** (Figure 60)is integrated on the inboard side. Its primary function is to prevent or mitigate toroidal displacement of the cassette during disruption events and to

reduce high stress concentrations on the nose resulting from large radial torques. The lower stop, as shown in Figure 55, is part of the vacuum vessel shell, meaning that is rigidly anchored to the vessel, while it is interfaced to the cassette by mean of two surfaces that, during operation are never in touch with the CB with a clearance of 1 mm per side. If a severe off normal event occurs (such as a sudden plasma disruption), the toroidal displacement of the inboard elbow is limited by the lower stop.

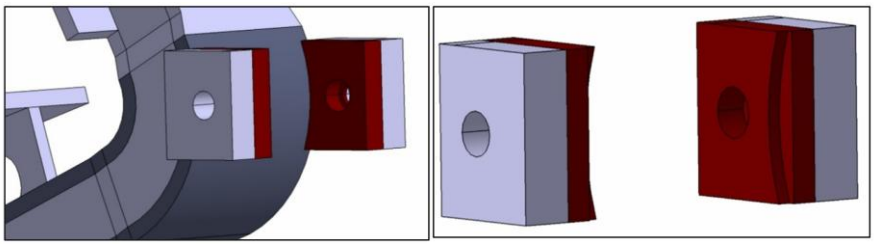

Figure 60 Lower stop

The divertor-vessel anchoring system has been designed to comply with all the remote handling required operations and tool, that have been developed in parallel. Following a detailed description of the mounting procedure of the lateral cassette [55] (left or right in the 20° sector shown in Figure 40).

- Phase 1 – Initial Positioning in Parking Configuration (Figure 61)

The divertor cassette installation sequence begins with the release of the cassette by CMM into the parking position. In this configuration, the outboard parking interface, defined by a dedicated feature on the knuckle case, rests on the outboard rail, while the lower surface of the hemispherical nose is supported by the inboard rail. At this stage, the knuckle mechanism is fully retracted and does not yet interface with the outboard rail. The cassette is therefore statically supported by gravity and rail contact, without any applied preload.

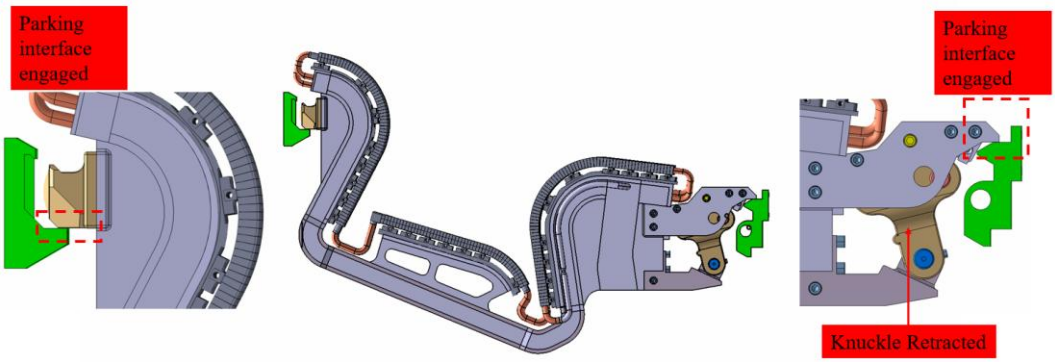

Figure 61 Divertor parking position

- Phase 2 – Knuckle Deployment and Outboard Rail Engagement (Figure 62)

Following stabilization in the parking position, the knuckle is actuated by the CMM and rotated towards the outboard rail. This motion brings the knuckle interface surface into contact with the corresponding vertical interface of the outboard rail. The actuation is performed through an internal mechanism integrated within the CMM, allowing controlled and precise engagement. At the end of this phase, the knuckle is mechanically coupled to the outboard rail, while the cassette remains free to translate rigidly along the radial direction.

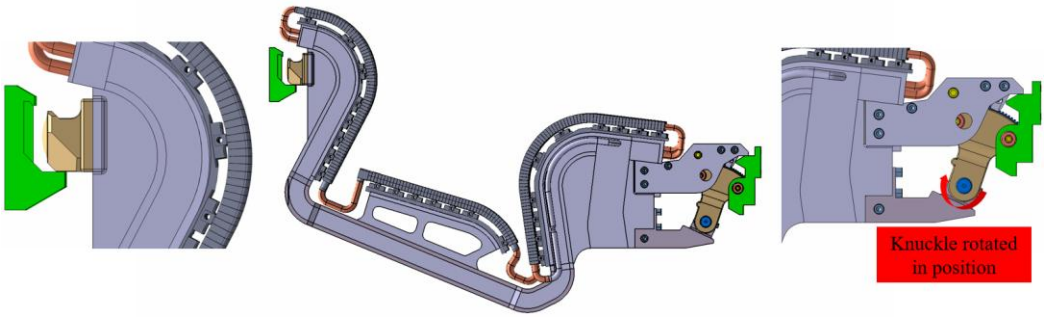

Figure 62 Knuckle extraction

- Phase 3 – Rigid Cassette Translation and Nose Engagement (Figure 63)

Subsequent actuation induces a rigid radial translation of the divertor cassette, driven by the relative displacement between the knuckle and the cassette body. During this motion, the hemispherical nose, located on the inboard side of the cassette, progressively approaches and finally engages with its corresponding spherical socket on the inboard rail. Once this engagement occurs, the toroidal position of the cassette is kinematically constrained, ensuring accurate centering. From this point onward, further relative displacement between the knuckle and the cassette can no longer result in rigid body motion.

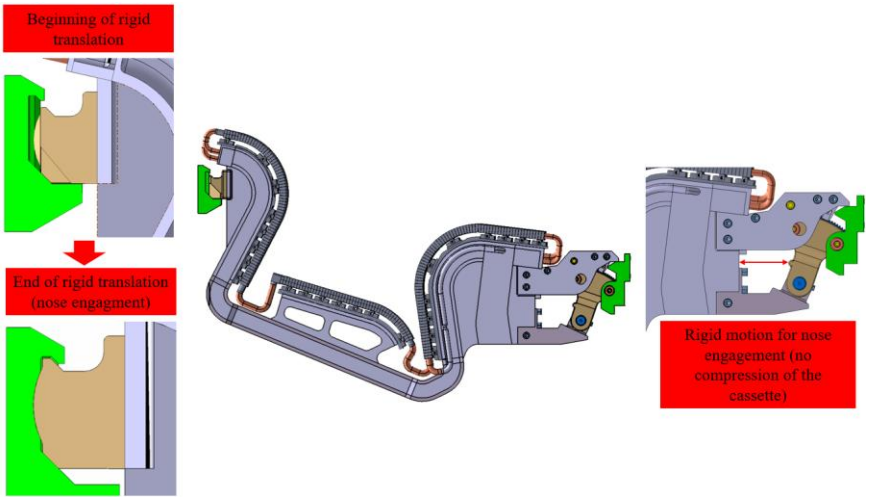

Figure 63 Divertor rigid displacement-nose engagement

- Phase 4 – Cassette Preloading through Knuckle Actuation

After the nose engagement, any additional actuation of the knuckle produces an elastic deformation of the cassette, initiating the preloading phase. An external mechanical jack interposed between the knuckle and the cassette, has been originaly identified as the tool to apply the required preload. However, this solution was abandoned due to the lack of sufficient integration space. As a result, the knuckle design was revised to incorporate an internal worm gear mechanism, enabling the generation of the necessary preload forces within the available envelope.During this phase, the rigid translation of the cassette ceases, and the applied displacement leads to radial precompression of the cassette structure.The preloading process continues until the axis of the knuckle pin is brought into precise alignment with the corresponding mounting hole on the cassette interface. This condition is ensured by the presence of the overmentioned mechanical stop, which limits the knuckle stroke and guarantees repeatable alignment. At this point, the required preload has been fully applied, and further actuation is mechanically prevented.

- Phase 6 – Locking Pin Actuation and Final Fixation (Figure 64)

Once alignment is achieved, the rear driving rod of the knuckle mechanism is actuated by the CMM. Through a gear-coupled system, this single actuation simultaneously extracts both the pin engaging the cassette interface, and the pin engaging the outboard rail interface. This synchronized motion locks the cassette securely in position, completing the installation sequence. The successful completion of the operation is confirmed by end-stroke detection and a characteristic increase in torque measured by the Torque Tool End Effector.

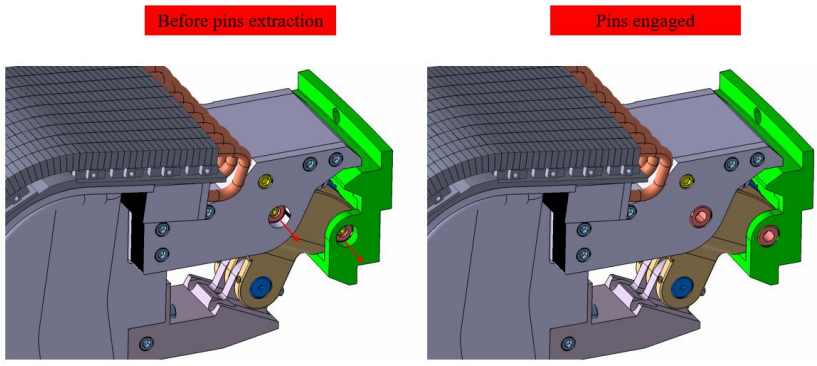

Figure 64 Pin extraction

A preload value of 20kN has been assessed throughout the structural verification process discussed in 5.1, leading to a maximum displacement of the outboard branch of the omega shape, of 5mm. As will be detailed in 3.4.2.2, after the preload the divertor must be as close as possible to the nominal configuration, in particular the target envelope must match the poloidal/toroidal nominal profile highest possible accuracy. To meet this requirement, the divertor must be manufactured in an **undeformed configuration prior to preload application**, such that, once the 20 kN preload is applied, the structure undergoes the expected 5 mm compression while simultaneously ensuring the correct **alignment of the knuckle pin with its hosting hole**.

Consequently, the **as-manufactured cassette body geometry** must intentionally differ from the nominal configuration in order to compensate for the preload-induced deformation. This design approach is discussed in detail in 3.4.2.2.

The mounting procedure will be different if considering the lateral cassette or the central one.

For the central divertor cassettes, the preloading action is achieved by actuating what is referred to as the **dummy rail**. This mechanism, supported by Central Cassette Outer Rail, employs a distinct preloading strategy outlined in [56].

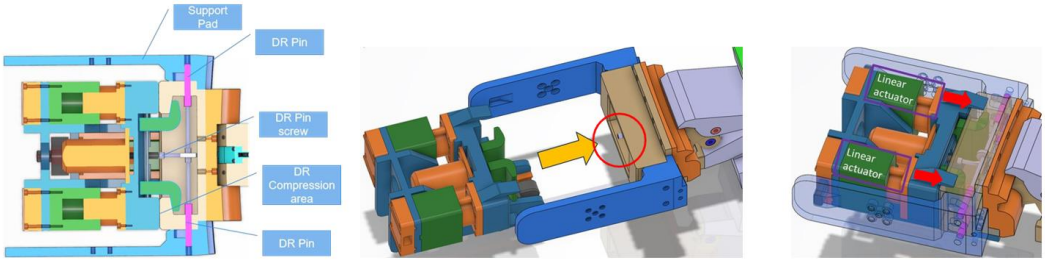

Figure 65 Central cassette coupled with dummy rail

The use of a fully integrated mechanical jack for the primary locking and engagement mechanism faced significant challenges. Crucially, the reactor environment strictly limits the use of **actively lubricated mechanisms** due to the vacuum and radiation fields. Furthermore, the inherent **lack of available space** between the knuckle and the cassette body posed a significant constraint for interposing a comprehensive mechanical jack system for primary engagement. These factors led to the re-evaluation of mechanical jack for the preloading. Consequently, the knuckle design evolved to the current **geared knuckle system**, responsible for the primary locking and unlocking of the divertor cassette. This

redesign was specifically driven by the spatial constraints identified. The preloading system was adjusted by incorporating a **rack and pinion mechanism** on the head of the knuckle, with preloading exerted through the rotation of a series of conical gears. Multiple design options were explored for this redesigned solution (Figure 66).

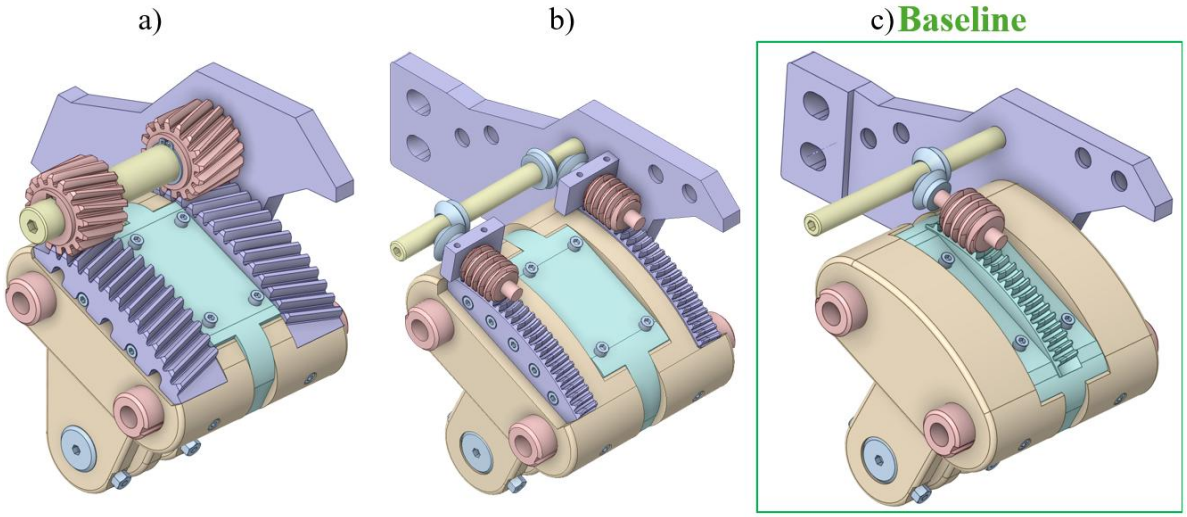

Figure 66 Geared Knuckle alternatives

Three geared knuckle configurations were analyzed, each characterized by different trade-offs in terms of actuation effort, robustness, and synchronization requirements.

- The first configuration (Figure 66-a) is mechanically simple, requiring fewer components and no gear train, which makes it easier to manufacture and inherently robust due to the single-tooth design. However, it is affected by retrograde motion unless additional blocking mechanisms are introduced, and it requires a relatively high actuation torque. Moreover, potential asynchronies between the left and right sides may lead to system failure.

- The second configuration (Figure 66-b) eliminates retrograde motion if the lead angle is properly designed with respect to the friction coefficient, while still allowing back-driving. It features a lower actuation torque and a higher number of teeth engaged, improving load distribution. Nevertheless, it remains sensitive to left–right synchronization errors, making accurate gear phasing essential to avoid failure.

- The third configuration (Figure 66-c) further reduces the risk of failure due to asynchronies by coupling the worm gear with a single conical gear. Like the second solution, it provides lower actuation torque, increased tooth engagement, and

suppression of retrograde motion when the lead angle is correctly dimensioned, while preserving back-driving capability. Overall, this configuration offers improved reliability at the cost of increased mechanical complexity

Ultimately, through analysis of their respective advantages and disadvantages, the baseline configuration was established using a single **worm** whose axial action was positioned approximately in the middle plane of the system.

This design choice aims to ensure symmetric behavior during the preloading process.The device is actuated through the shaft on which the conical gears are mounted and transfers the rotation to another conical gear that is rigidly coupled with the worm gear and shares the same rotation axis. Therefore, the action of the worm gear is transferred to the rack on the head of knuckle. Figure 67 shows an exploded view of the assembly with the respective BOM.

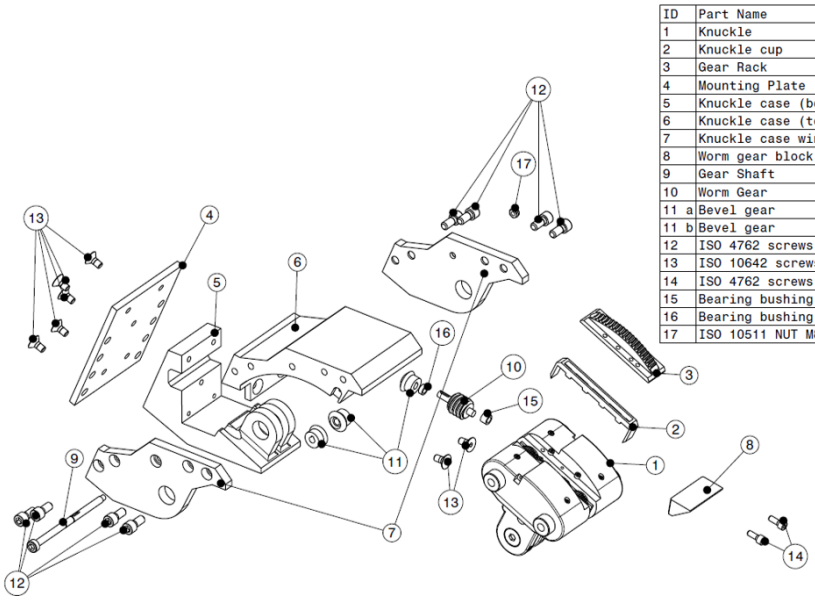

ID	Part Name	Quantity	Material
1	Knuckle		UNS C64700
2	Knuckle cup	1	AISI 316 L
3	Gear Rack	1	UNS C64700
4	Mounting Plate		AISI 316 L
5	Knuckle case (bottom)		AISI 316 L
6	Knuckle case (top)	1	AISI 316 L
7	Knuckle case wings	2	AISI 316 L
8	Worm gear block	1	AISI 316 L
9	Gear Shaft	1	AISI 316 L
10	Worm Gear	1	AISI 316 L
11 a	Bevel gear	1	AISI 316 L
11 b	Bevel gear	2	UNS C64700
12	ISO 4762 screws M12x25	8	Defined according to standard
13	ISO 10642 screws M10x20	7	Defined according to standard
14	ISO 4762 screws M8x20	2	Defined according to standard
15	Bearing bushing	1	UNS C64700
16	Bearing bushing	1	UNS C64700
17	ISO 10511 NUT M8	1	Defined according to standard

Figure 67 Geared Knuckle assy exploded view and BOM

The mounting procedure remains unchanged compared to the previously described sequence. The main difference lies in the fact that the entire preloading phase, including the initial rigid rotation of the knuckle to seat it on the outboard rail, the first rigid displacement of the cassette caused by the knuckle's pushing action, and the subsequent preloading itself, is now directly actuated by the rotation of the upper shaft mounting the first conical gear. The CMM will first actuate the gear train to apply the desired preload and then move to the pin region to extract the pins and insert them into the holes on the outboard rail. To relieve

the torque exerted by the CMM end effector (Figure 68), specially designed cross-shaped interfaces have been created and positioned precisely where the actuation of both the gear train shaft and the pins occurs.

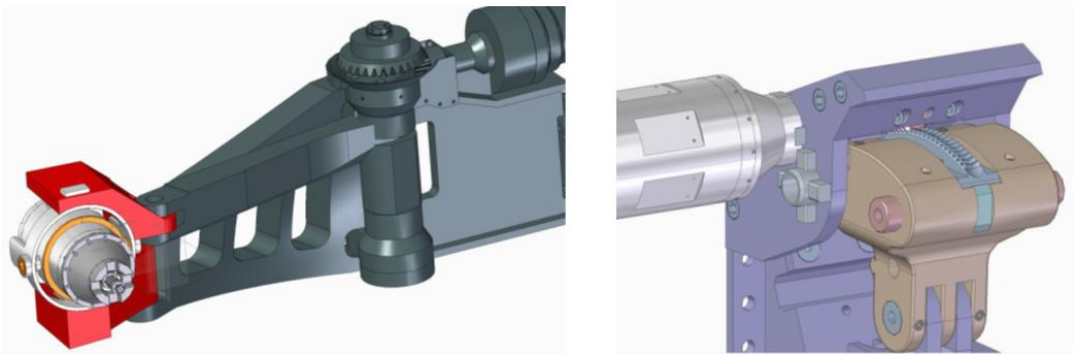

Figure 68 CMM end effector anchored for preloading

The preliminary dimensioning of the system has been carried out starting from the assumption that the torque needed on the shaft of knuckle equivalent to the 20kN preload is 1000 Nm. The 1000 Nm torque has been used as input for the dimensioning and all the relevant quantities have been evaluated accordingly. The principal DOF of the process were the axial module, the pressure angle and the lead angle.

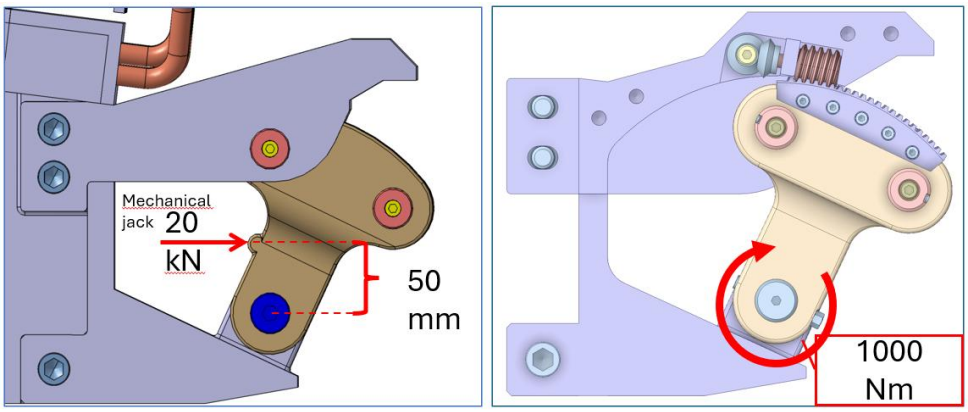

Figure 69 Necessary torque at knuckle shaft axis, equivalent to 20kN preload

The dimensioning of the worm gear fillets and rack teeth Figure 70 followed the ISO/TS 14521 standard. Considering the low speed rotation required during the preloading, the aspects related to fatigue and vibration of the parts in contact have been neglected. The screw lead angle has been set small enough to prevent retrograd motion. The high gear ratio will be advantageous since the torque applied at the conical gear axis, needed for the acutation , would be significantly lower than the 1000 Nm equivalento of 20kN preload. The final

design parameters, outcome of the preliminary structural/integration validation are shown in Table 7.

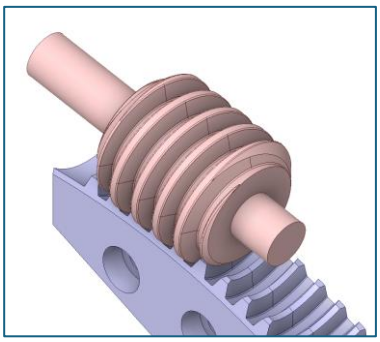

Figure 70 Paired wormgear-rack system

Table 7 Geared knuckle main parameters

Geometry and kinematics			
Parameter	Symbol	Value	Unit
Axial module	m	1.5	mm
Number of starts (worm)	z_1	1	–
Number of teeth (gear)	z_2	202	–
Center distance	a	164.25	mm
Nominal diameter (worm / gear)	d_n	25.5 / 303	mm
Root diameter (worm / gear)	d_f	21.75 / 299.25	mm
Tip diameter (worm / gear)	d_h	28.5 / 306	mm
Gear width	b	18	mm
Lead angle	ψ	3.37	deg
Gear ratio	i	**202**	–
Load and efficiency			
Parameter	Symbol	Value	Unit
Output torque	T_{out}	1000	Nm
Input torque	T_{in}	46.6	Nm

Tangential force (gear)	F_t	6601	N
Axial force (gear)	F_a	3652	N
Efficiency	η	0.106	–

Strength factors and safety

Parameter	Symbol	Value	Unit
Form factor	Y_f	1.10	–
Contact factor	Y_ε	0.50	–
Lead factor	Y_γ	1.00	–
Life factor	Y_{nl}	2.00	–
Tooth shear stress	τ_f	191	MPa
Allowable shear stress	τ_{fg}	256	MPa
Safety factor	SF	1.34	–

The details regarding the prototyping of the fixation system alternatives will be given in the next section.

3.4.3.1 DTT Divertor fixation system test rig prototyping

Before describing the two outboard fixation system alternatives, a brief premise on the objectives of the prototyping activity is provided. The fixation systems were prototyped in order to experimentally reproduce, as closely as possible, the functional behavior of the divertor fixation concept and to validate the assumptions adopted during the design and numerical assessment phases.The main objectives of the prototyping activity were the following:

- To demonstrate the correct functioning of the fixation systems once assembled, with particular attention to the synchronous extraction of the knuckle pins during operation.
- To verify the correct application of the preload through mechanical actuation. In the first prototyped configuration, the knuckle and the supporting frame were coupled to a mechanical jack system. Unlike the real divertor configuration, sufficient space was available in the test rig to accommodate a mechanical jack capable of applying the

target preload of 20 kN, allowing the preload application concept to be directly tested.

- To assess whether the reaction force at the nose after preload application matched the expected value. Based on numerical simulations and supporting hand calculations, this reaction force was predicted to be approximately 10 kN, and its experimental verification represented a key validation target for both fixation system concepts.
- To ensure that, for an equivalent preload level, the displacement field of the prototype was representative of that of the real divertor. To this end, the test rig frame was specifically designed to exhibit an equivalent stiffness to that of the actual divertor structure.

In order to achieve these objectives, the prototyping activity was also conceived as an experimental validation of both the preload level and the resulting structural response. To this end, piezoelectric sensors were planned to be used to measure the reaction force developing between the outboard rail and the supporting pad to which it is bolted. This measurement allowed a direct verification of the reaction force predicted by the numerical simulations.The management of the deformed and undeformed configurations was addressed through the use of calibrated shims interposed between the inboard rail and the supporting pad. By reducing the distance between the outboard rail and the inboard rail, a controlled misalignment was intentionally introduced. In order to restore the alignment between the knuckle pins and the corresponding holes on the cassette interface, it was necessary to apply a preload equal to the force associated with the imposed displacement. This behavior must match the numerical predictions, which indicated that the preload required to recover the alignment corresponded to the shortening imposed through the shims. The detailed technical drawings of the fixation system alternatives have been included in ***Annex E – DTT Divertor Fixation System Test Rig Technical Drawings***

3.4.3.1.1 Knuckle fixation system

Figure 71 shows the Test rig CAD model coupled with Knuckle fixation system. Figure 72 includes an exploded view of the Test rig-Knuckle system, comprehensive of the materials related to each component of the assembly.

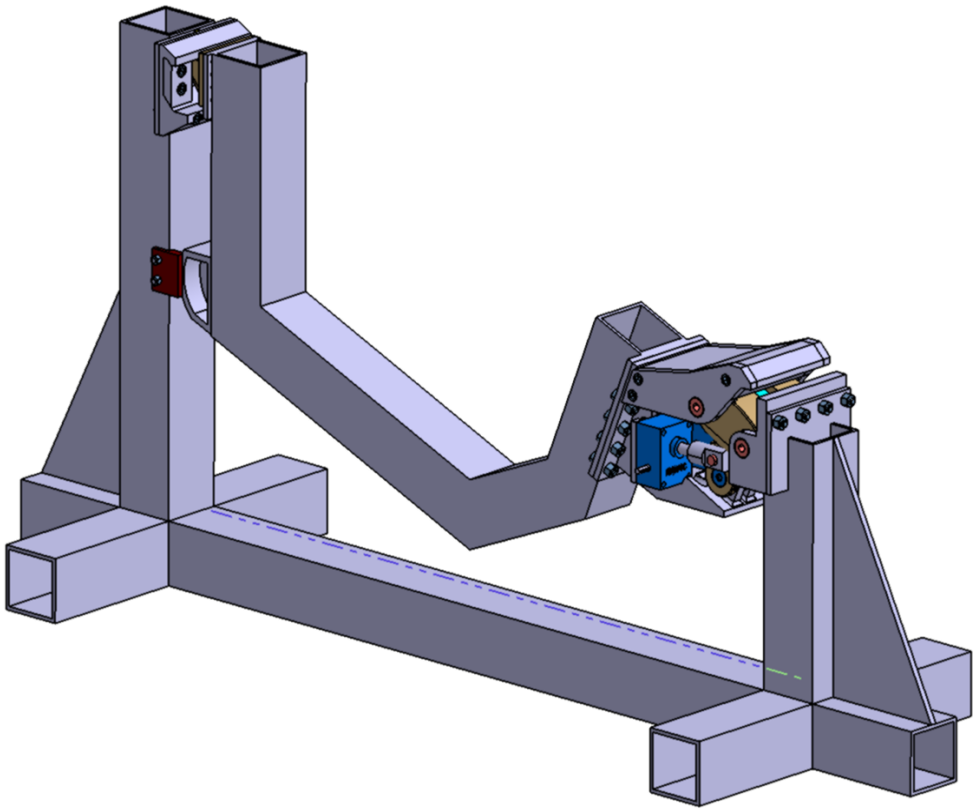

Figure 71 – Test rig CAD model coupled with Knuckle

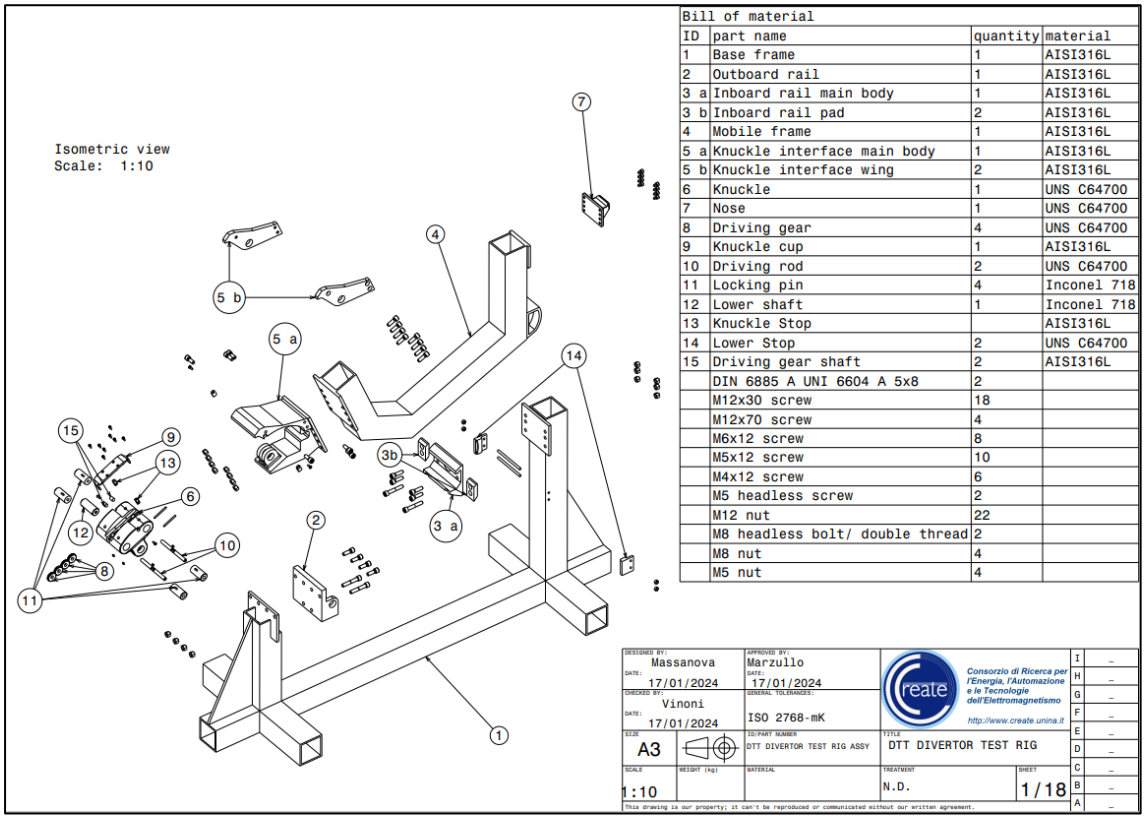

Figure 72 – Test rig-Knuckle exploded view

3.4.3.1.2 Wedges fixation system

Figure 73 shows the wedges alternative integrated on the Test rig. To be noted that the flange interface between both Knuckle case and wedges fixation system is the same, therefore they can be easily switched.

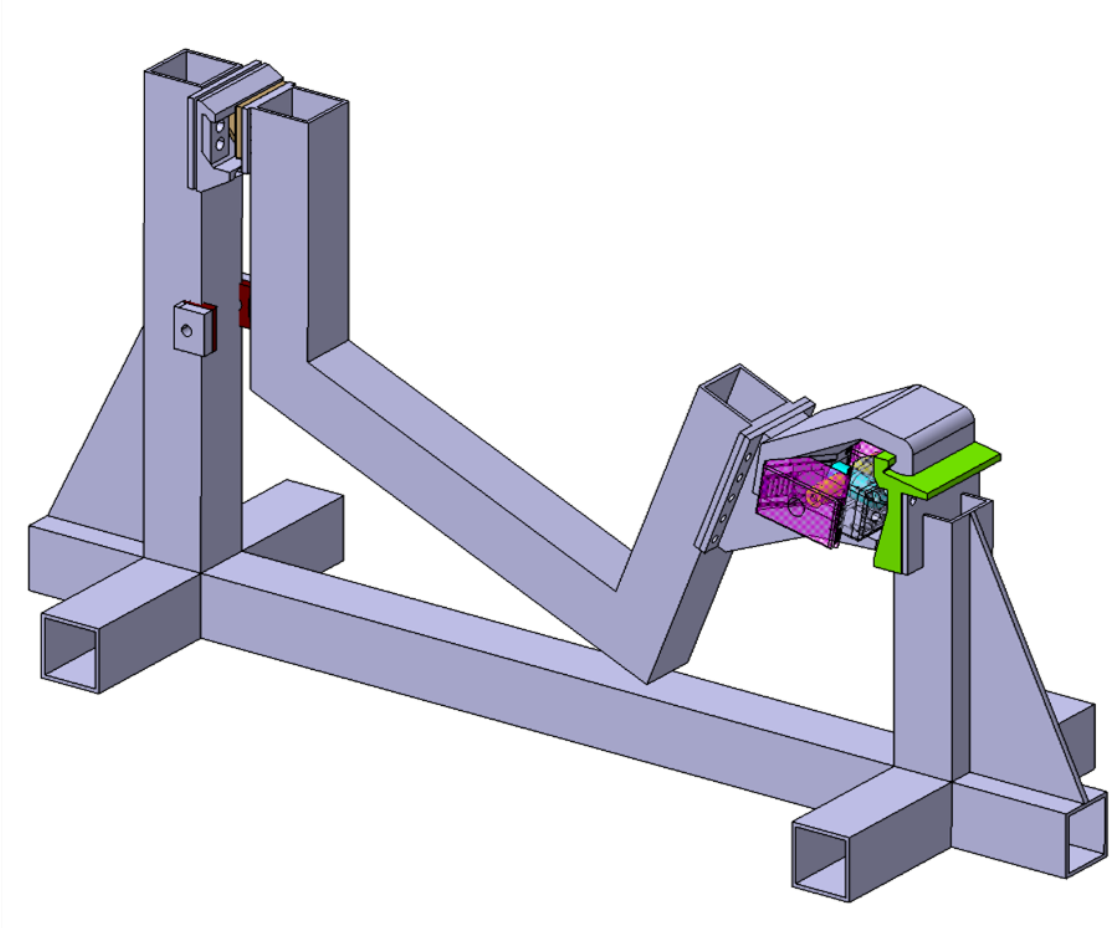

Figure 73 – Test rig CAD model coupled with wedges fixation system

The wedges fixation system represents an alternative fixation concept based on the use of a set of sliding components (wedges) that, through their relative motion, enable the application of the preload.

The system consists of two lateral wedges which, by means of dovetail interfaces, are engaged with both a rear wedge and a front wedge. The two lateral wedges are screwed onto the actuation screw; the rotation of this screw causes the lateral wedges to advance or retract, depending on the direction of rotation, as they are screwed in or out along the actuation screw itself. Figure 74 shows the wedges fixation system and its main components. The assembly is maintained together by a central shaft, which mechanically couples the relative motion of the front wedge with that of the actuation screw and, consequently, of the lateral wedges.

This configuration ensures a coordinated and stable motion of all moving components during the preload phase.

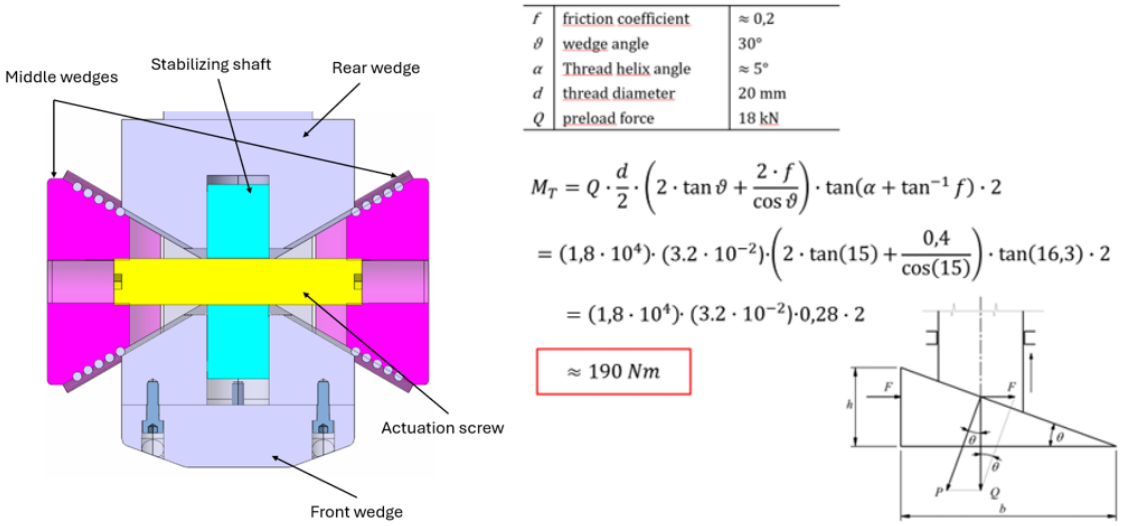

Figure 74 – Wedges fixation system section view

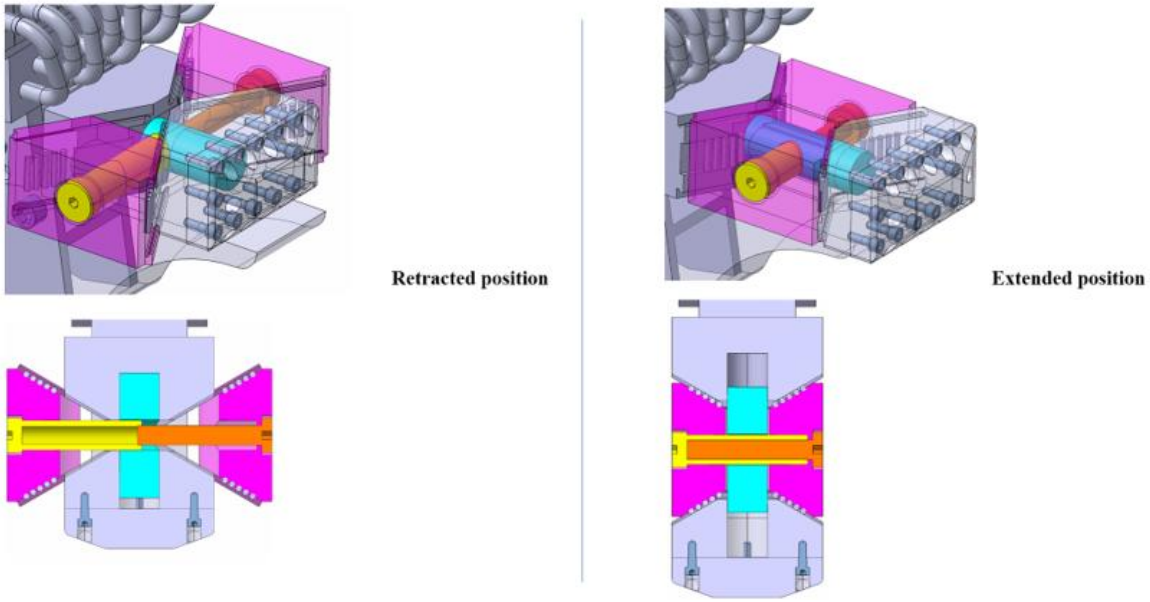

Figure 75 Wedges fixation system retracted and extended configuration

The wedges fixation system was conceived with the objective of providing increased flexibility during the preload application. Unlike the knuckle fixation system, where the preload level is uniquely determined by the geometric characteristics of the nose–knuckle interface and where the knuckle pins align with the corresponding holes only at a specific preload value (apart from component clearances), the wedges fixation system allows a certain degree of adjustability.As the wedges advance, they push against the outboard rail,

while a hook-shaped appendage at the head of the wedges progressively approaches its complementary dovetail feature on the outboard rail. A mechanical stop is reached only when this appendage comes into contact with the dovetail interface. Therefore, while a mechanical limit to the preload application does exist, it is not inherently associated with a single predefined preload value. Within the available clearance before contact is established, the preload can be regulated, allowing controlled adjustments of the cassette position.This characteristic is particularly advantageous in the presence of unavoidable manufacturing tolerances or assembly inaccuracies. If, following the preload application, the cassette were to be positioned outside the nominal tolerance range—resulting, for instance, in Plasma Facing Units (PFUs) being misaligned—the preload could be further increased or partially released to bring the cassette closer to its nominal configuration.A key design requirement of the wedges fixation system is the prevention of vertical detachment of the outboard section. This function is ensured by the hook-shaped appendage, which engages with the dovetail on the outboard rail. In order to preserve the desired preload flexibility, the hook was intentionally designed not to enter into perfect radial contact with the dovetail. Instead, a clearance margin was introduced to accommodate the intended positional adjustments while still guaranteeing vertical retention and structural safety.

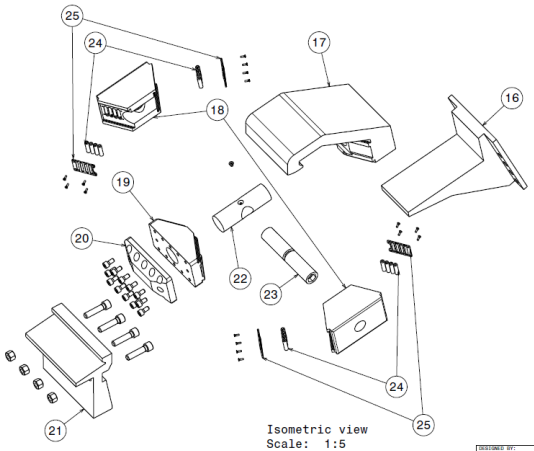

Bill of material			
ID	part name	quantity	material
16	Support pad	1	AISI316L
17	Rear wedge	1	AISI316L
18	Middle wedge	2	UNS C64700
19	Front wedge	1	AISI316L
20	Front wedge pad	1	UNS C64700
21	Outboard rail	1	AISI316L
22	Shaft	1	UNS C64700
23	Driving shaft	4	AISI316L
24	Roller	16	AISI316L
25	Roller pad	4	AISI316L
	M12x50 screw	4	
	M8x16 screw	12	
	M5x8 countersunk screw	1	
	M4x10 countersunk screw	16	
	M12 nut	4	

Figure 76 – Wedges mechanism exploded view

The manufacturing drawings of all the assembly and subsystems/components have been included in and.

3.4.3.1.3 Prototype hardware delivery

The prototype has been delivered in the second half of 2024. Figure 77 displays the divertor Test rig mounting the knuckle fixation system, while Figure 78 shows the test rig mounting the wedge mechanism at Laboratory of University of Trieste. Figure 79 includes few renderings of the knuckle fixation system in mounting configuration.

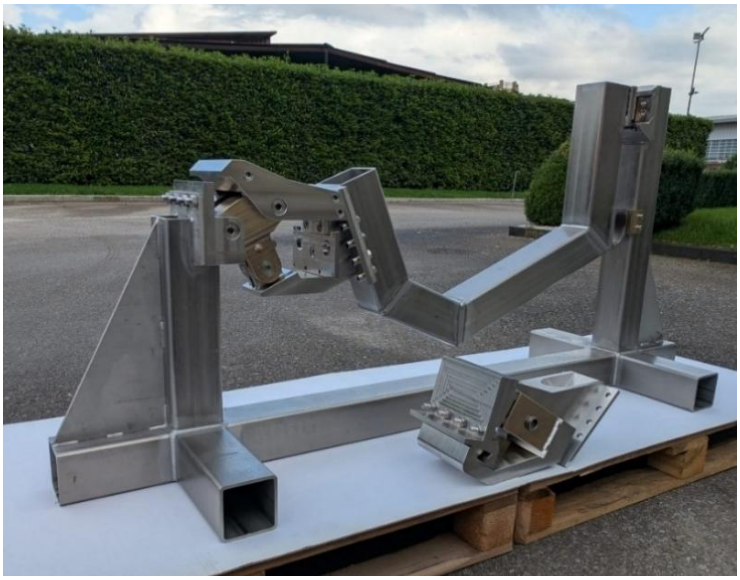

Figure 77 – DTT Divertor Test rig coupled with knuckle fixation system

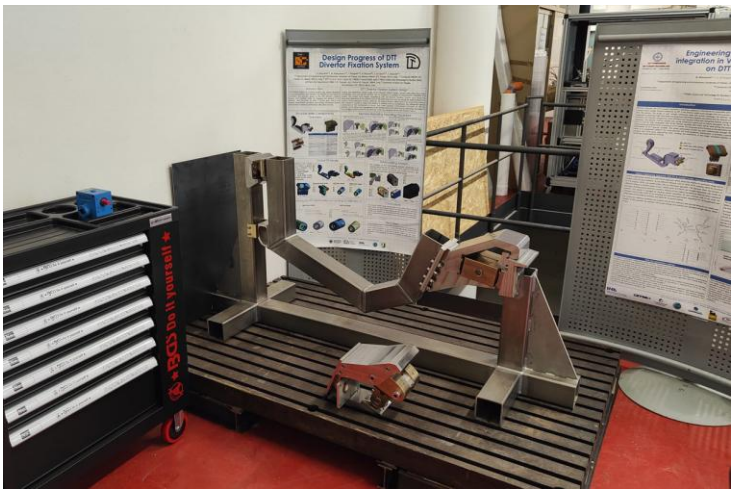

Figure 78 – DTT Divertor Test rig coupled with wedges fixation system

The hardware included:

- Mobile frame (dummy divertor)
- Base frame
- Knuckle fixation
- Wedges fixation systems

- Nose
- Outboard rail
- Inboard rail

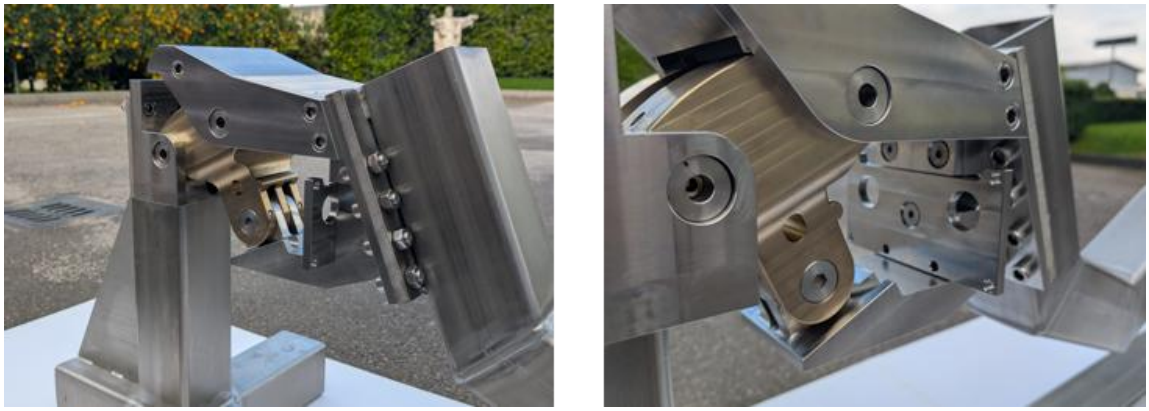

Figure 79 – Knuckle fixation system

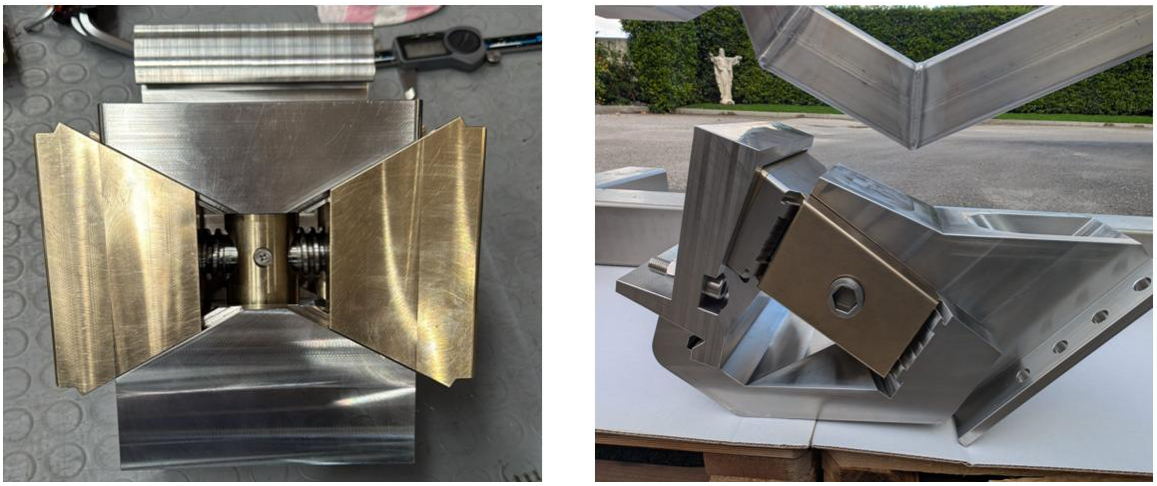

Figure 80 – Wedges fixation system

The geared knuckle device was prototyped and delivered by the end of 2025. As previously discussed, this system represents the baseline solution for the outboard fixation of the divertor and will be experimentally tested to verify that the mechanism operates as intended. The main challenge encountered during manufacturing concerned the accurate refinement of the rack gear integrated on top of the knuckle, which is essential to ensure smooth actuation and to prevent blockage or failure of the coupled worm gear–rack mechanism during the application of preload. A dedicated test campaign is planned for 2026 to validate the performance and reliability of the system.

Figure 81 Extracted and retracted geared knuckle

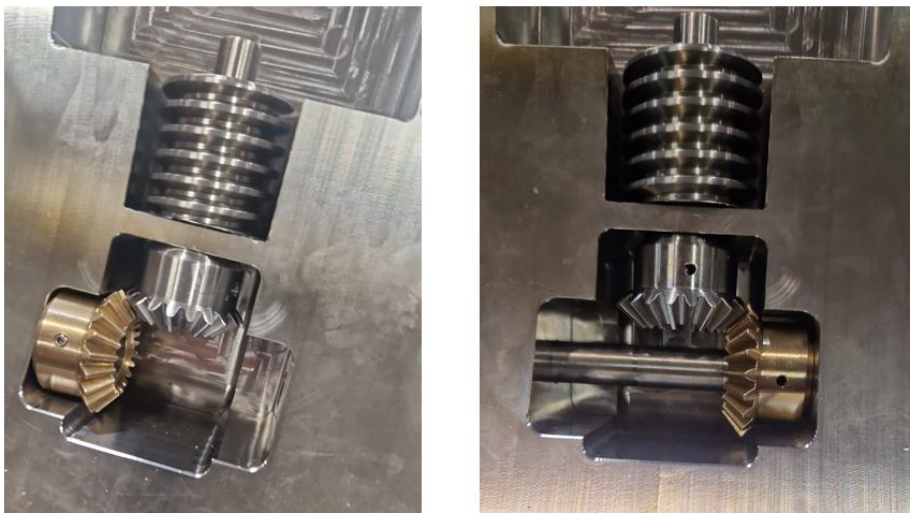

Figure 82 Conical gears-worm gear train

3.4.3.1.4 Acceptance tests

After the delivery of the prototype, some inspections and functional tests were carried out to evaluate the functionality of the Test rig.

The tests performed included:

1. Assembly of the knuckle system – the whole device has been dismantled and reassembled to verify that the components interfaced properly to each other.
2. Assembly of the wedges system – the wedges mechanism has been dismounted and assembled for scratches for the same purpose of point 1
3. Functional test of the Knuckle system-extraction of the mounting pins through the actuation of the driving rods.
4. Functional tests of wedges fixation system – displacement of the wedges through the actuation of the driving screw

In the following paragraphs each acceptance test will be discussed in detail.

The knuckle system was delivered already attached to the test frame. Some difficulties were encountered during the disengagement and removal of the system, due to some tolerance issues that were not detected during the first assembly.

- **Incomplete retraction of locking pins:** During the disengagement procedure, the locking pins were not able to completely retract inside the knuckle body. A recovery procedure had to be implemented to disassemble the system, namely:
    i. Decoupling of the fixation system from the mobile frame by removing the 8 bolts of the flange
    ii. Decoupling of the outboard rail from the support frame by removing the 6 bolts of the outboard pad
    iii. Removal of the 4 screws limiting the excursion of the pins
    iv. Complete extraction of the pins and driving rods

After complete disassembly of the knuckle system, the issue was found to be an out-of-tolerance conical shape of the cylindrical holes in which the pins slide. Early detection of this issue would have been possible either by more thorough metrological inspections or by a better-defined assembly plan.

While testing the retraction of the pins, one of the driving rods was damaged (cracked in correspondence of the hexagonal socket. Even though the main cause is to be found in the dimensional issue with the pins, the final design of the driving rods should also be informed by this failure, in particular a future design revision should consider a reinforced driving rod, with a larger diameter or an alternative design of the connection point for the actuator.

- **Incorrect dimensions of pins stop:** The top of the pins presents a groove that functions as a end stroke to prevent the pin from falling. Due to a discrepancy in the technical drawings, the groove was manufactured 3mm shorter than needed and had to be sent back to the manufacturer to be machined again.
- **Design of the lower shaft:** The threaded bars that lock the lower shaft in place in the knuckle body were designed in such a way that properly tightening the two nuts is impossible, due to the lack of clearance around the nuts themselves. Removal of the threaded bars is challenging for the same reason. In a future design revision, a different system should be considered to lock the rotational and axial movement. Moreover, the “small gap” tolerance indication (H7-g6) resulted in an excessive interference between the parts, which caused a non-negligible amount of friction during operations.

- **Tight fit of the gear train closure cup:** In disassembling the knuckle, some difficulties were experienced in removing the closure plate that seals the gear train. Warping of the part made it difficult to remove, therefore wider gaps should be included in a future redesign. An entirely different design could also be conceived.

At current stage, all the identified issues has been fixed and the system is correctly performing his function.

The wedge system was delivered already assembled but separate from the frames. The movement was first tested on its own, before mounting it to the frame.

- **High friction:** Small misalignments of the two wedges paired with high contact friction of the screw made the system hard to operate. For this reason, the system was disassembled, in order to check the coupling of the single parts. After some break-in, the parts fitted together in a smoother way and operation of the system was easier.
- **Missing end stops:** Since no end stops were foreseen in the wedge system, the wedges can be disengaged by over-rotating the screw. In future iterations of the design, such a feature should be added.
- **Complex assembly procedure:** Assembly of the four wedges requires perfect alignment of multiple parts. The assembly plan should be revised in order to facilitate this operation (for example splitting the wedges in two halves that get screwed together or providing a pilot hole to facilitate the dovetail insertion.
- **Clamped rolling elements:** The rolling elements included to reduce friction between the wedge's surfaces were clamped by their own closure plates and could not roll. The issue was provisionally solved by loosening the screws of each plate in order to give more clearance to the rollers, but the necessity of these elements should be assessed, along with proper assignment of tolerances.

After the first few preload attempts using the wedge system, it was observed that the inboard branch of the support structure is more flexible than originally anticipated. According to the FEA conducted during the design phase, the expected displacement of the dummy divertor (mobile frame) under preload should have been approximately 5 mm. However, during the tests, part of the deformation was instead absorbed by the taller branch of the frame (about 2mm), revealing a behavior that contradicts the initial FEM analysis.

To address this discrepancy, a recovery procedure has been devised. It involves stiffening the flexible branch by installing a reinforcement bracket between it and a thin metal sheet, which rests against a structural wall of the building housing the prototype. This solution aims to increase the overall rigidity of the frame and better distribute the preload forces in accordance with the original design assumptions.

Tolerance issues: Geometrical inspection of the mobile frame revealed warping of the part. The horseshoe shape that should have lied all in one plane had instead some twist such that the axis of the first and last pipe were on different planes. This issue was evidenced when testing the engagement of the system, by the lateral motion of the mobile frame, which self-aligned in a skewed position.

Even more noticeably, the lower stop interfaces did not match the lower stop position by several millimeters on the side.

To avoid such alignment issues, clearer tolerance indications should be given, and the addition of centering pins for the inboard and outboard fixation system interfaces.

A possible solution could also be to manufacture the lower stop with a slanted profile, so that it is self-aligning. Though such a precaution could introduce a deformation (and therefore stress) in the cassette during the mounting operation.

The following high-level requirements are shared by both systems and must be verified:

- Assessment of the Preload Action Applied During Assembly
- Evaluation of Deformation Induced on the Dummy Frame After Assembly
- Measurement of Key Reference Areas Relevant for Potential Divertor Target Positioning
- Characterization of Stress Acting on the Most Critical Components (mainly Hertzian contact stress on the hemispherical nose surface – optional)
- Characterization of Electrical Continuity Between Divertor and Rail (i.e., Vessel Connection)
- Preload assessment during assembly

To evaluate the preload applied during assembly, the following tools have been purchased or are planned to be acquired:

- Torque Wrench: Used during assembly to estimate the preload. Although the measurement will be approximate, it provides a qualitative indication of the applied torque.
- Load Cell: To be placed in a strategic position to accurately measure the preload force. The test plan includes installing the load cell between the inboard rail and the pad resting on the base frame. At the current stage, a set of "FelxifFoce load sensors" has been purchased (https://www.tekscan.com/flexiforce-loadforce-sensors-and-systems) to be placed at the inboard rail. A market survey is also ongoing to identify alternative suitable solutions that meets both measurement requirements and the tight geometric constraints of the prototype.

3.4.3.1.5 Deformation evaluation after assembly

To assess deformation induced on the dummy frame, the following equipment has already been acquired:

- Laser Distance Meters: With an accuracy of 0.01 mm, used for high-precision dimensional checks.
- 3-Plane Laser Level Used to verify the flatness of critical planar features on the prototype before and after preload is applied.

To be noted that the testing procedure is still in early stage and further investigation – both in terms of tools and strategies to be used – will be done in the next future.

- Dimensional and Positional inspection of Reference Zones

Specific reference zones on the prototype must be measured to verify their suitability for positioning divertor targets. The same laser tools mentioned above will be used to carry out these checks, focusing on repeatability and positional accuracy.

- Stress Characterization on Critical Components (Optional)
    - Stress analysis may be conducted on the most mechanically stressed areas, primarily focusing on:
    - Hertzian contact stresses on the hemispherical nose surface.
    - Instrumentation and methodologies for this optional task are still under evaluation.

- Electrical Continuity Verification
    - Tests will be performed to ensure proper electrical continuity between the divertor and the rail, which is essential for grounding and system integration. The methodology and instrumentation for this task will be defined in a later phase.
- Testing under relevant load conditions
    - While preloaded, the prototype should be tested under load conditions representative of the forces and moments acting on the divertor during disruptions. The engineering aspects of this phase will be further developed in the next period to provide meaningful insights into whether the preload is sufficient to maintain structural integrity during off-normal events such as disruptions.

3.4.4 Pipes stumps

Figure 83, shows the **pipe stumps** that shall be pre welded on the divertor and later connected to the pipes running along the entire duct. The pipes are not welded during the initial installation phase; instead, welding is performed only after the installation of the corresponding cassette, once the final alignment between the pipes and the pipe stumps has been achieved.

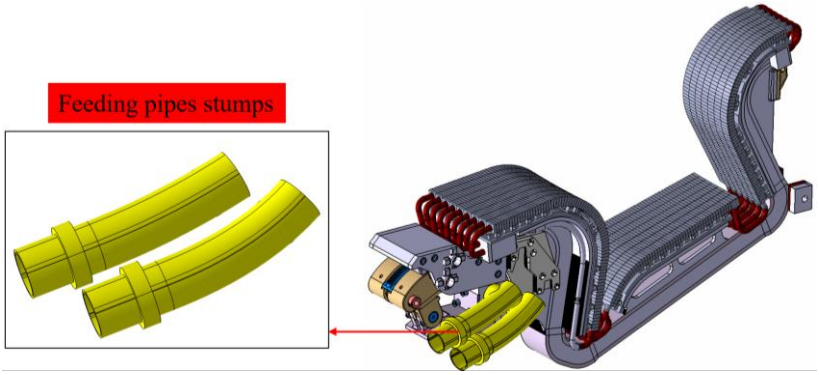

Figure 83 Lateral cassette pipe stumps

The pipes run continuously along the duct and terminate at the port interface, where they are connected to the pipe stumps, as illustrated in Figure 84. The configuration of the pipe stumps is therefore required to be fully coherent with the routing and positioning of the pipes inside the duct, ensuring proper alignment and accessibility for the remote handling tools.

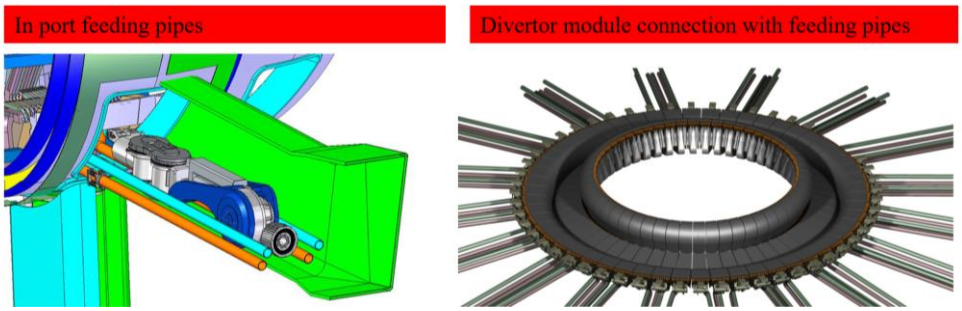

Figure 84 In duct divertor feeding pipes routing

The pipes are characterized by an outer diameter of 60 mm and a wall thickness of 3 mm. This geometry has been defined to satisfy two main requirements:

- to guarantee structural integrity and tightness under the operational pressure of 5 MPa;
- to allow the internal passage of the remote handling cutting and welding tool, which operates from inside the pipe bore.

Welding operations are performed by means of a remote orbital welding unit, shown in Figure 85, which executes a full circumferential weld between the pipe stumps and the corresponding pipes.

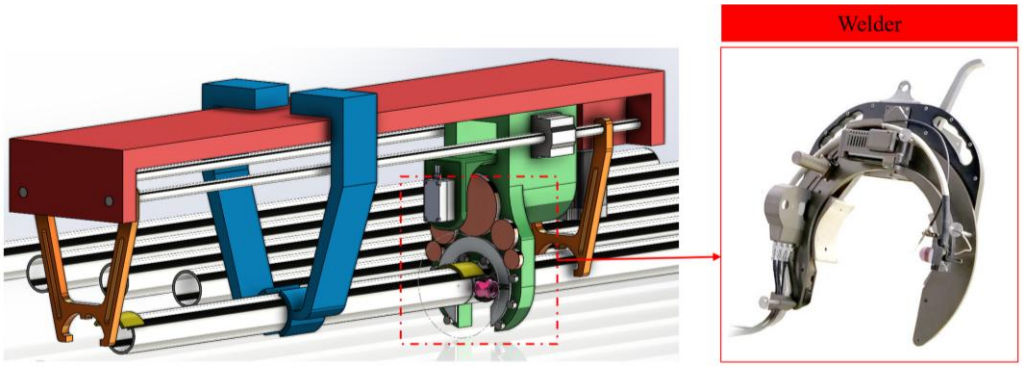

Figure 85 Welding tool

The orbital welding system is designed to operate internally and remotely, ensuring repeatable and controlled weld quality in a confined environment. References to the welding system and its design constraints can be found in [57].

At the current stage, the cutting tool has not yet been fully designed; however, it is already assumed that it will also operate internally. Consequently, the selected pipe diameter represents a compromise between pressure resistance requirements and the need to accommodate an internal cutting tool capable of performing the required operations without interference

3.4.5 CMM grasping interface

During the transport of a divertor module, the CMM end effector couples with a dedicated **grasping interface (**Figure 86) to handle and carry the entire assembly into the duct, where the module is finally positioned in its parking location [55].The CMM grasping interface is based on a relatively simple and robust design. It consists of a socketed plate manufactured in AISI 316L stainless steel, which is welded or bolted to the divertor cassette side panel. The interface is installed on the right side of the left cassette and on the opposite side of the right cassette, ensuring symmetry and compatibility with the transport sequence. From a functional standpoint, the interface is composed of two distinct parts: a flat plate, directly interfacing with the divertor cassette body; a socketed, thicker plate, designed to mate with the CMM end effector during handling operations. The definition of the connection strategy between the grasping interface and the cassette is still an open design issue. Both bolted and welded solutions are currently under evaluation, each presenting specific advantages and

drawbacks. In particular, the cassette side panel is designed to contain cooling water and therefore must remain fully watertight. To avoid weakening the panel by introducing threaded holes, a possible solution foresees the manufacturing of the panel with an additional metal overlayer, allowing the creation of threaded holes dedicated to hosting the screw shanks. Conversely, a welded connection would eliminate the need for mechanical fasteners but could introduce a significant heat input, potentially leading to local distortions of the cassette structure. This trade-off will be further analysed and resolved in future design phases.The primary requirements for the CMM grasping interface are:

- structural robustness, necessary to withstand the full dead weight of the divertor cassette while it is transported in a cantilevered configuration;
- tight socket tolerances, required to ensure a precise and repeatable coupling with the CMM end effector, avoiding both excessive clearance and interference during engagement.

The CMM end effector, also shown in Figure 86, features two dedicated engagement pins, which are designed to accurately match the sockets of the grasping interface, providing a secure and stable mechanical coupling throughout the transport and positioning operations.

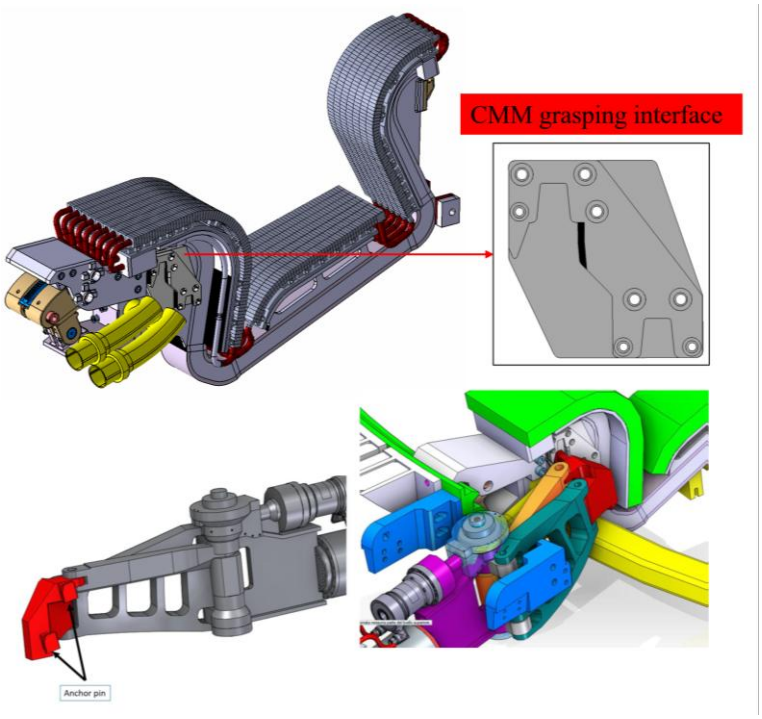

Figure 86 CMM grasping interface

3.4.6 Diagnostic interfaces

The design of the divertor **diagnostics interface** is currently at a purely conceptual stage. At this phase, no detailed mechanical solution has been defined yet; however, Table 8 provides an overview of all the diagnostic systems that are foreseen to be integrated on the divertor (Figure 87).

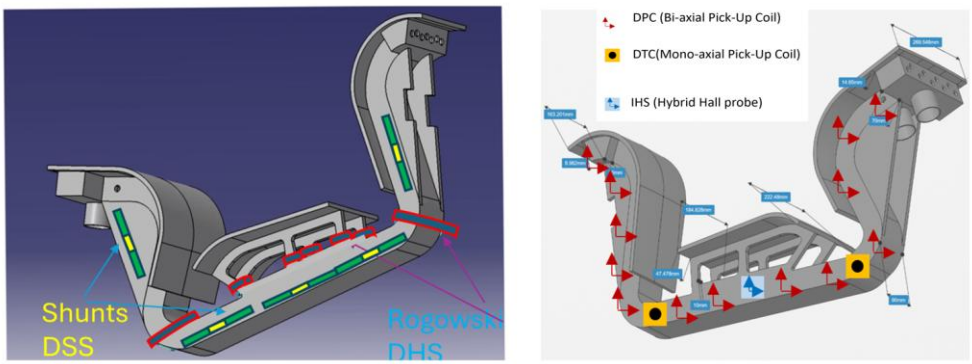

Figure 87 Identified location for divertor diagnostic

The proposed interface methodology is based on the adoption of a dedicated structural frame, which will be welded directly onto the divertor structure. All diagnostic components will be mounted onto this frame, which will therefore represent the primary mechanical interface between the divertor and the diagnostic systems.The welding strategy foresees the use of localized (spot) welds, in order to limit the heat input transferred to the cassette structure. This approach is intended to minimize the risk of residual stress generation and to avoid excessive distortions of the divertor cassette resulting from thermal effects.

As a consequence, the frame must be designed to be fully compatible with the integration envelopes and spatial constraints imposed by the surrounding components and by the overall divertor geometry. Particular attention shall be paid to avoid any interference with adjacent systems and to ensure accessibility for installation, inspection and possible maintenance operations.In addition, all diagnostic components must be positioned in the shadow of the PFUs (Plasma Facing Units). This requirement is essential in order to protect the diagnostics from direct plasma interaction, reducing thermal loads and radiation exposure and ensuring the integrity and operational reliability of the diagnostic systems.Further refinement of the interface design, including structural definition, detailed integration layouts and attachment solutions, will be addressed in future design phases, once the diagnostics requirements and boundary conditions are further consolidated.

Table 8 Embedded divertor diagnostics

Sensor	Nr x Sector	Total Sensors	Nr. Cables	Sector
DPC (divertor bi-axial pick upcoils)	13 x 4	52	104	1,5,10,15
DTC (divertor monoaxial pick-up coils)	2 x 4	8	16	1,5,10,15
IHS (Hybrid Hall sensors)	3 x 4	12	12	1,5,10,15
DHS (diverotr Halo sensors – partial Rogowski coils)	8 x 4	32	32	1,5,10,15
DSS (divertor shunt sensors)	4 x 4 minimum*(4 x 7 maximum)*	16	16	1,5,10,15

4 JOREK crosscheck verification: benchmarking maxFEA results for DTT disruption simulation

4.1 Integrated Workflow for Electromagnetic Load Evaluation

The design process for a tokamak divertor, incorporates a methodical workflow for the comprehensive evaluation of EM loads, integrating physics simulations with engineering analyses:

1. **Identification of Demanding Disruption Scenarios:** The workflow commences with the identification and simulation of the most severe plasma disruption scenarios. For the DTT divertor, this initial step in evaluating electromagnetic loads involves a thorough understanding of plasma behavior during these transient events .

2. **Quantification of Disruption Parameters:** A critical phase involves using a 2D axisymmetric plasma equilibrium code, such as **MAXFEA, DINA, CREATE NL, CARIDDI** and many other codes widely used over the last few decades. For the DTT divertor design, MAXFEA has been instrumental in "evaluating main disruption parameters," including plasma motion and current. The code takes as input a 2D poloidal cross-section encompassing all metallic and non-metallic structures influencing plasma evolution, such as the Central Solenoid, Poloidal Field Coils, Vacuum Vessel, Divertor outline, and First Wall outline. MAXFEA is capable of simulating the time history of a full discharge and analyzing disruption growth times. Forces are calculated as volume integrals of the cross product of the toroidal current density with the poloidal magnetic field, providing an overview of forces on coils in equilibrium and transient conditions.

3. **Preparation of Input for 3D Electromagnetic Analysis:** The outputs from MAXFEA simulations, specifically the data pertaining to "plasma motion and current decay," in conjunction with estimated magnetic field variations and plasma current evolution, are then transformed into inputs for more detailed 3D electromagnetic analyses. This step translates the axisymmetric results into a format suitable for complex 3D geometries. The DTT divertor features 54 toroidally discontinuous modules; therefore, the material properties for the divertor within MAXFEA are set to represent air, as no net toroidal current can be driven in them during a disruption event.

4. **Execution of 3D Electromagnetic Analysis:** Subsequent to defining disruption parameters and plasma evolution, specialized 3D electromagnetic codes are employed to compute the actual EM loads on the intricate 3D components. Tools such as TYPHOON, EMAS, ANSYS, and ABAQUS are commonly used for this purpose. These codes simulate the induction of eddy currents in 3D structures and the resultant forces arising from their interaction with magnetic fields during disruptive events. This comprehensive analysis, often supplemented by further EM and mechanical stress assessments, is essential for ensuring the structural integrity of components under severe disruption scenarios.

5. **Integration with Structural Assessment:** The calculated electromagnetic loads serve as critical input for subsequent **structural assessment**. This step verifies that the divertor components can withstand the predicted mechanical stresses and maintain their structural integrity throughout their operational lifetime, thereby meeting stringent performance and safety criteria. The entire design process, from initial conceptualization to final detailed design, is inherently iterative, with ongoing refinement of geometry and material selection based on analytical feedback.

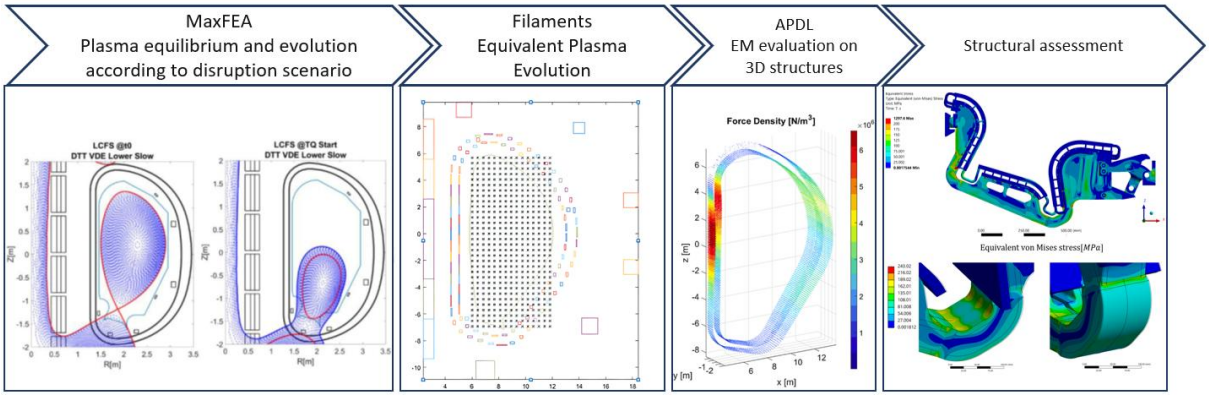

Figure 88 EM loads evaluation-structural verification integrated workflow

4.2 Disruption simulation and Electromagnetic Loads Evaluation

4.2.1 Background overview on disruption phenomena

In the following, the disruptive plasma phenomena relevant for the design and dimensioning of in-vessel components are introduced.

Plasma disruptions are sudden, large-scale instabilities in tokamak plasmas that lead to a rapid and complete loss of plasma confinement [59]. These events are a significant concern for fusion reactors due to the substantial thermal and structural loads they impose on machine components (Bandaru et al., 2024). Disruptions are typically characterized by distinct phases:

Phases of a Plasma Disruption

1. **Thermal Quench**: The thermal quench is the initial phase of a disruption, marked by a rapid and dramatic decrease in the plasma temperature. This can occur within a few milliseconds, with the plasma temperature dropping from approximately 10 keV to around 10 eV. This rapid cooling is primarily caused by non-linear interaction of large-scale magneto-fluid instabilities that lead to a stochastization of the magnetic field structure, causing thermal energy loss through parallel transport along open field lines. In the context of the EU DEMO, a thermal quench can release a significant amount of thermal energy (e.g., 1.3 GJ) in a very short timeframe, roughly 1 to 4 ms. This rapid loss of thermal energy results in substantial and potentially localized heat loads on plasma-facing components.
2. **Current Quench**: Following the thermal quench, the dramatic drop in plasma temperature significantly increases the plasma's electrical resistivity. This increased resistivity causes the plasma current to decay rapidly, marking the beginning of the current quench phase. The current quench duration is typically longer than the thermal quench, often lasting tens to hundreds of milliseconds. During the CQ, the decaying plasma current induces strong eddy currents and considerable electromagnetic forces in the surrounding conducting structures of the reactor. Simulating the current quench phase is crucial to predict asymmetric forces on the wall in mitigated disruptions.

Associated Phenomena and Consequences

- **Vertical Displacement Events**: VDEs are common occurrences in elongated tokamak plasmas, where control of vertical position is lost [60]. These events can either trigger

a thermal quench or occur after it [60]. As plasma moves and can contact limiting surfaces, it exacerbates the conditions leading to MHD activity and the onset of the TQ and CQ [60]. During a VDE, the electromagnetic loads due to eddy currents and halo currents can be substantial. For example, analyses using MAXFEA for the DTT vacuum vessel show peak vertical forces from eddy currents reaching approximately -8 MN, and from halo currents about -7.4 MN, with a total peak force of about -10.6 MN. Disruptions impose "substantial thermal loads on tokamak first-wall components and generate transient electromagnetic loads due to rapid magnetic field alterations caused by plasma displacement against the confinement field".

- **Runaway Electrons**: A critical consequence of the current quench is the generation of runaway electrons. As the plasma current rapidly decays, a strong toroidal electric field is induced. If this field is sufficiently strong, it can accelerate a small seed of electrons to relativistic energies, forming a beam that can carry a significant fraction of the pre-disruption plasma current. These high-energy runaway electrons pose a severe risk, as their localized impact can cause significant damage to plasma-facing components[61].
- **Halo Currents**: During the current quench phase, particularly during VDEs, halo currents can arise, circulating in the plasma edge and through the surrounding conducting structures. These currents contribute significantly to the electromagnetic loads and mechanical stresses on the tokamak's components. The DTT divertor fixation system is specifically designed to carry the maximum halo and eddy currents during Vertical Displacement Events.

Table 9 Disruption scenario categorization

Transport-dominated disruptions (energy loss dominated by parallel losses)		Radiative disruptions (energy loss dominated by radiation)
Major disruptions	Hot VDEs	
1. MHD instability	1. Loss of vertical control	1. Impurity injection
2. TQ	2. VDE	2. Radiative TQ
3. VDE	3. TQ (due to q_{95} drop)	3. CQ + cold VDE
4. CQ	4. CQ	
• Post-TQ temperatures ~several 10 s to 100 s of eV		• Post-TQ temperatures ~few to 10 s of eV
• Slow CQ → Large $I_p \Delta Z_{curr}$ and global wall forces		• Fast CQ → Local eddy current loads
• Localized thermal loads		• Distributed thermal loads
• Low q_{95} → Toroidally asymmetric forces and heat loads		• Large q_{95} → Expected toroidal symmetry

After the definition of 2D outline and 3D geometries the next step into the design is to evaluate the off normal loads acting on the Divertor geometries. The task is complex and, as already said involves different phisics branches but, generally the most demanding loads acting on an invesell compoents, besides the thermal one, are the electromagnetic loads induced on the metallic structures during the disruption of the plasma. As it appens for the design of a divertor tokamak several disruption cases must be addressed to ensure the structural integrity also under the most burdening events. One of the codes developed for engineering purposes that has been used to evaluate the main disruption parameters that, here again are reported, will be used as input for electromagnetic loads evaluation is MAXFEA.

The precise evaluation of electromagnetic loads on three-dimensional (3D) structures, such as the Divertor Tokamak Test facility's divertor, is an indispensable step in the design and validation of fusion reactor components. This workflow is particularly critical in the context of off-normal operational events, primarily plasma disruptions, which induce significant transient forces on conductive structures.

Fundamental Principles of Electromagnetic Load Generation

Electromagnetic loads originate from the interaction between induced currents within conductive materials and ambient magnetic fields. During normal tokamak operation, magnetic fields are designed to be stable, ensuring plasma confinement. However, during plasma disruption events, rapid alterations in plasma parameters, such as plasma current decay and positional shifts, lead to dynamic changes in the magnetic flux. These abrupt magnetic flux variations induce **eddy currents** in proximate metallic structures, including the vacuum vessel and divertor components. As elaborated in the user's current document, these "transient electromagnetic loads due to rapid magnetic field alterations caused by plasma displacement against the confinement field" and the consequent "generation of intense eddy currents in the divertor’s conductive components, which amplify transient electromagnetic forces and thereby increase mechanical stresses during vertical disruption events" are primary drivers of mechanical stress. The subsequent interaction of these induced eddy currents with the pre-existing strong magnetic fields generates substantial electromagnetic forces on the structural components.

Primary Sources of Electromagnetic Loads During Plasma Disruptions

Two specific phenomena significantly contribute to EM loads during plasma disruptions:

1. **Poloidal Field Variation:** The poloidal magnetic field is fundamental for plasma shaping, positioning, and stability within a tokamak, generated by both external poloidal field coils and the plasma's self-induced current. A "poloidal field variation" denotes a rapid and significant change in this magnetic field component. During a plasma disruption, events such as rapid plasma current quench or substantial vertical displacement can drastically alter the poloidal field distribution across the entire tokamak volume. These rapid variations are a potent source of induced eddy currents in surrounding metallic structures, which then experience considerable electromagnetic forces as they interact with the overall magnetic field. The poloidal field variation is a consequence of the interaction of the displacing plasma, carrying a toroidal current density , that while displacing generate a poloidal field that therefore interacts with the preexisting poloidal field generated by the poloidal field coils, the central solenoid and the other in vessel coil that contribute to the poloidal magnetic field configuration
2. **Halo Currents:** Halo currents are substantial radial currents that develop during specific types of plasma disruptions, notably Vertical Displacement Events. A VDE occurs when the plasma loses vertical stability and migrates towards the upper or lower boundaries of the vacuum vessel. Upon contact with the vessel walls, a resistive electrical connection is established, allowing a fraction of the toroidal plasma current (the "halo current") to flow into and through the plasma-facing components and other conductive structures before returning to the plasma. These halo currents constitute a major source of electromagnetic loads, particularly on components like the divertor fixation system, which must be engineered to "carry the maximum HALO and eddy currents during the Vertical Displacement Events" .

4.3 DTT data integration in Integrated Modeling and Analysis Suite (IMAS)

4.3.1 IMAS

The decision to populate IMAS with DTT data before initiating JOREK for disruption computation was a strategic choice, yielding benefits for both the DTT project and the wider ITER community.

For DTT, this approach provided a solid and unambiguous reference for its geometrical and dimensional characterization, as well as for various equilibrium scenarios [62]. By leveraging IMAS's machine-generic data dictionary and Interface Data Structures (IDS) (Figure 89), all DTT data would be consistently and unequivocally stored. This standardization ensures that subsequent analyses and simulations, including those related to disruptions, are founded on a single, easily accessible, and standardized source of truth.

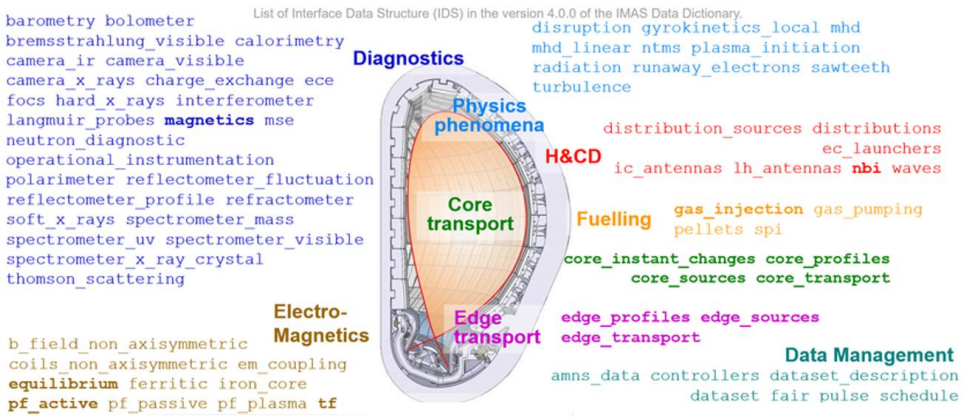

Figure 89 List of IDS in the versione 4.0.0 of the IMAS Data Dictionary

Indeed, the DTT scientific program specifically includes disruption studies in support of ITER [63]which would inherently benefit from such a standardized data foundation. Furthermore, the explicit requirement for JOREK to identify its necessary IDS before initialization directly links its computational needs to the IMAS framework.

Simultaneously, ITER benefited from this decision by promoting the use of IMAS beyond its immediate organization. IMAS is designed to be accessible to all ITER members as a key tool for scientific exploitation and serves as an efficient platform for multi-facility data analysis and multi-code integration. Its application to DTT helps solidify its role as a universal platform for fusion data management and integrated modeling within the broader fusion community.

The inclusion of disruption data computed with JOREK into IMAS further strengthens this integrated approach. IMAS, through its IDSs, facilitates data exchange between coupled codes and stores input and output data in a consistent format. Therefore, incorporating JOREK's disruption data into IMAS would ensure a non-equivocal and perfectly consistent storage with the initial DTT parameters, aligning with IMAS's goal of standardized data structures for managing tokamak fusion data.

While integrating data into IMAS before JOREK initialization may not have been strictly necessary in a technical sense, this systematic approach was of extreme utility. It guaranteed data integrity, facilitated collaboration, and ultimately contributed to more reliable and traceable results for the DTT disruption studies, all within a framework designed for the integrated modeling and analysis of fusion experiments.

ITER, as a large and complex international project, requires a systematic approach to managing the vast amount of data and various simulation codes involved in its design, operation, and research. IMAS addresses this need by providing a standardized environment that allows different research software packages and institutions to work together seamlessly.

Key reasons for IMAS's importance at ITER include:

- **Standardization**: IMAS, built upon a machine-generic data dictionary, acts as a key standardization tool, ensuring consistency across different experimental and simulated data.
- **Integration and Interoperability**: It enables the integration of diverse modeling and analysis codes, allowing for complex workflows and comprehensive simulations of plasma behavior and machine operation. This "on-the-fly code coupling" avoids the need for extensive code modification to accommodate varied input/output data formats.
- **Data Management and Sharing**: IMAS promotes Findability, Accessibility, Interoperability, and Reusability principles for scientific data, facilitating widespread sharing and collaboration among the scientific community.
- **Verification and Validation**: It provides a platform for verifying and validating models and data across different facilities, which is essential for ensuring the reliability of predictive simulations for ITER scenarios.

- **Plasma Operation and Research**: IMAS supports both routine plasma operations and advanced research activities on ITER, contributing to the assessment of ITER scenarios and requirements for future fusion pilot plants.

The advantages of using IMAS are significant for the fusion community:

- **Enhanced Collaboration**: By providing a common data structure and interface, IMAS streamlines collaboration between different research groups and institutions contributing to ITER.
- **Improved Efficiency**: It reduces the effort required for data conversion and code adaptation, accelerating the pace of research and analysis.
- **Comprehensive Understanding**: The integrated nature of IMAS allows for a more holistic understanding of tokamak plasmas by combining various physics models and experimental data.
- **Future-Proofing**: The framework is designed to be extensible, allowing for the integration of new codes and modules as research progresses and technology evolves.
- **Support for Control Systems**: IMAS data structures are leveraged by tools that facilitate the execution of complex transport solvers, indicating its role in supporting the development of advanced control systems for ITER.

How IMAS Works: Data Dictionary and Interface Data Structures

IMAS's functionality hinges on its standardized information architecture, primarily through its **Data Dictionary** and **Interface Data Structures**.

- **Data Dictionary**: The IMAS system is built upon a machine-generic data dictionary. This dictionary defines the nomenclature and structure of the data, ensuring consistency across all integrated components.
- **Interface Data Structures**: IDSs are well-defined, generalized data structures that act as standardized interfaces for information exchange between coupled codes. They contain physics definitions for various plasma parameters, including:
    - Machine description
    - Equilibrium

- Neoclassical transport and core sources
- Transport, impurities, and profiles

The workflow typically involves:

1. **Data Mapping**: Experimental data from various tokamaks are mapped into IMAS IDS format.
2. **Code Integration**: Physics components and numerical codes exchange data through these IDSs. This standardized interface enables "on-the-fly" code coupling, where codes can directly access input data from IMAS databases and save output back to them.
3. **Workflow Management**: Frameworks like OMFIT and the Kepler workflow manager orchestrate the execution of transport simulations, with information exchange mediated by IMAS data structures.
4. **Data Conversion**: Tools and description files, in conjunction with the data dictionary, are used to convert different types of source data into I/O operations under the standardized IMAS data model, facilitating software interaction.

The IMAS access layer currently operates at the Interface Data Structure level, enabling essential operations such as putting or getting data, performing time interpolations, and accessing single time slices of data. Concurrently, the architecture and functionalities for a longer-term access layer have been designed. This final product is intended to extend beyond IMAS usage, providing access to any ITER data. It will support operations based not only on the ITER Physics data model but also, for example, on the ITER CODAC data model through the same interface. The design is based on a client-server architecture and incorporates the data dictionary and data model correspondence previously described. This is a joint development with ITER CODAC that will eventually replace the current access layer prototype. The Access Layer has interfaces for Python, C++, Fortran, Java, Matlab.

4.3.2 Required IMAS ids for DTT JOREK disruption initialization

Before JOREK could be initialized, it was essential to identify the complete set of **Interface Data Structures (IDSs)** required to ensure that all necessary data were available for the accurate computation of **DTT disruptions**.

The IMAS access layer was compatible with python interface, that has been used to generate the codes through which all the required data have been specified in IMAS.

In particular, the following databases needed to be populated:

- **Machine Description (MD)**
- **Equilibrium**
- **Core Profiles (Neoclassical transport and core sources, impurities and profiles**
- **pf_active currents related to the reference equilibrium scenario**

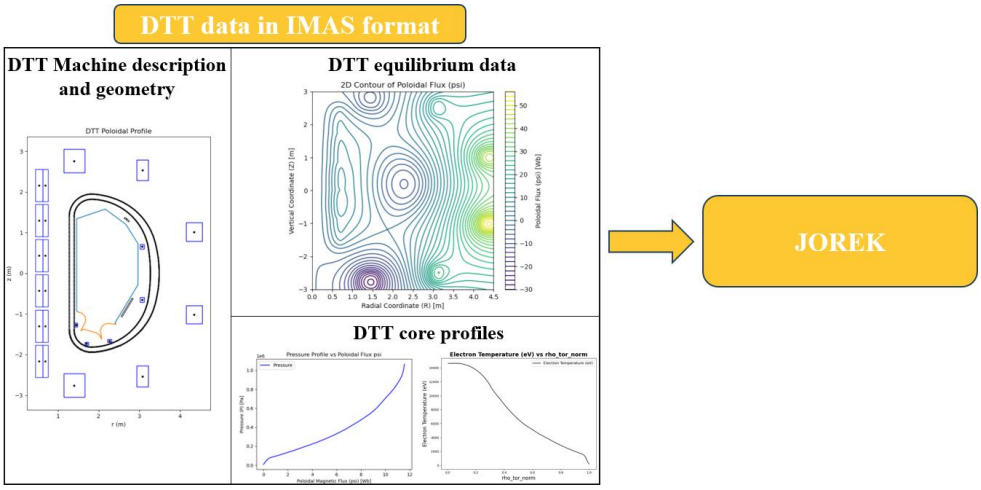

Figure 90 Required ids for JOREK initialization

4.3.3 Machine description (pf_active ids, pf_passive ids, wall ids)

The **DTT Machine Description (MD)** contains all the geometrical, dimensional, and descriptive characterizations of the tokamak. The MD database is extremely broad and can potentially include several types of information serving different purposes.

For the present application, only the information required for **JOREK initialization** is considered. In particular, the IDSs included in the Machine Description and relevant to this work are outlined below.

For this application, the informations included are divided respectively in:

- **pf_active:** Description of the axisymmetric active poloidal field (PF) coils and supplies; includes the limits of these systems; includes the forces on them; does not include non-axisymmetric coil systems.

- **pf_passive:** Description of the axisymmetric passive conductors, currents flowing in them. Electromagnetic simulations are expected to use only this IDS to describe passive conductors and their specific discretization, not the component-related IDS (e.g. wall) which are used to store e.g. the component machine description.
- **wall:** Description of the torus wall and its interaction with the plasma.

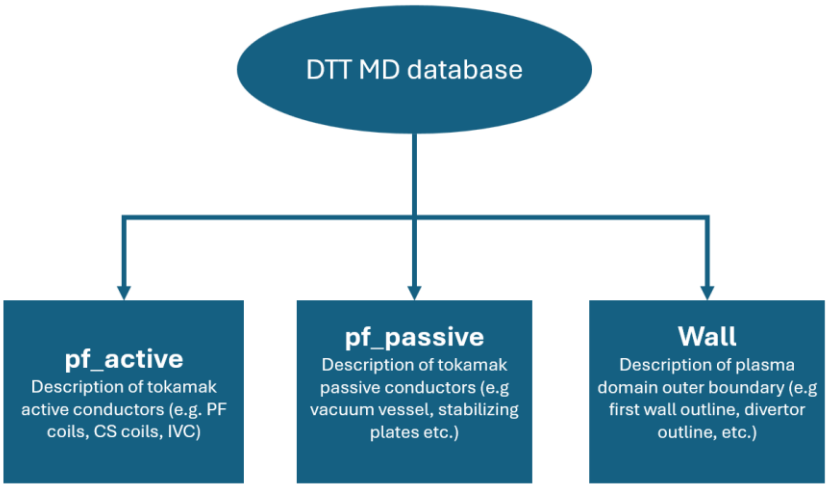

Figure 91

Generally speaking, ***pf_active*** ids can integrate a broad description of the axisymmetric active conductors of a machine, and it can includes a wide set of information related to several aspects of the system [65]. Table 53 in ***Annex B - DTT required data and IDS for JOREK initialization*** includes the identified minimum set of data required for disruption simulation purposes.

DTT coils system comprehends [66]:

- 12 Central Solenoid (CS) coils defining 6 independent circuits
- 6 independent Poloidal Field (PF) coils
- 3 independent divertor coils
- 2 independent invessel Vertical Stabilization (VS) coils

Table 10 reports the specified parameters of DTT coils layout, used to populate the pf_active ids.

It should be noted that within the *pf_active* infrastructure, each coil may consist of multiple elements.

These elements can, in principle, possess different geometrical configurations and formulations — for instance, rectangular, oblique (parallelogram-shaped), or annular geometries.

Furthermore, the elements belonging to the same coil can be connected either in series or in anti-series, depending on the circuit design requirements.

All DTT axisymmetric active conductors feature a rectangular cross section and can therefore be conveniently defined by specifying the coordinates of the rectangle's center (radial and vertical positions), together with the element's height, width, electrical resistivity, and number of turns.

In the present model, each coil has been represented by a single element, except for the Central Solenoid, which will be described in detail in the following section.

A zero-resistance value was assigned to all conductors.

Although the coils are superconducting and thus characterized by an extremely low but finite resistance, the assumption of perfect conductivity was an intentional simplification.

This approximation has been verified to have a negligible impact on the overall simulation results.

Table 10 DTT magnetic coil system coordinates, dimensions and number of turns

Coil ID	R [m]	Z [m]	DR [m]	DZ [m]	Turns	Resistance
CS3U_H	0.5349	2.1603	0.1788	0.7911	108	0
CS3U_L	0.6879	2.1603	0.1272	0.7911	162	0
CS2U_H	0.5349	1.2962	0.1788	0.7911	108	0
CS2U_L	0.6879	1.2962	0.1272	0.7911	162	0
CS1U_H	0.5349	0.432	0.1788	0.7911	108	0
CS1U_L	0.6879	0.432	0.1272	0.7911	162	0
CS1L_H	0.5349	-0.432	0.1788	0.7911	108	0

CS1L_L	0.6879	-0.432	0.1272	0.7911	162	0
CS2L_H	0.5349	-1.2962	0.1788	0.7911	108	0
CS2L_L	0.6879	-1.2962	0.1272	0.7911	162	0
CS3L_H	0.5349	-2.1603	0.1788	0.7911	108	0
CS3L_L	0.6879	-2.1603	0.1272	0.7911	162	0
PF1	1.4	2.76	0.51	0.5904	360	0
PF2	3.0795	2.534	0.279	0.5168	160	0
PF3	4.3511	1.015	0.3898	0.4522	196	0
PF4	4.3511	-1.015	0.3898	0.4522	196	0
PF5	3.0795	-2.534	0.279	0.5168	160	0
PF6	1.4	-2.76	0.51	0.5904	360	0

In Figure 92 is shown the poloidal profile of the coils geometry integrated in the the pf_active ids related to DTT MD description. The division of each Central Solenoid module [67] into two components serves to provide enhanced spatial resolution and flexibility in shaping the magnetic field, which is crucial for precise plasma handling:

- **High Field (H) Sub-module**: Positioned with a smaller major radius, this sub-module is located closer to the geometric axis of the Central Solenoid. Its proximity to the core plasma region allows it to generate a more intense and concentrated magnetic field. This characteristic is particularly valuable for contributing significantly to the overall toroidal magnetic flux and for influencing the plasma current profile in the central region, which is vital for achieving and maintaining stable plasma equilibria.
- **Low Field (L) Sub-module**: Conversely, this sub-module is situated at a larger major radius, further from the Central Solenoid axis. Its placement allows for a broader influence on the magnetic field distribution. While its individual field contribution might be comparatively less intense than that of the 'H' sub-module at the plasma core, its peripheral location offers greater leverage for fine-tuning the poloidal field configuration. This enables more precise control over plasma shape, position, and

vertical stability, particularly during dynamic events such as ramp-up, flat-top, and ramp-down phases, as well as during off-normal events like disruptions.

This architectural choice, to subdivide the Central Solenoid into spatially distinct 'High Field' and 'Low Field' components, represents a sophisticated engineering approach.

It allows for the independent control or differential powering of these segments, providing the DTT device with superior capabilities for magnetic field synthesis. Such granular control is indispensable for optimizing plasma performance, mitigating instabilities, and accurately modeling complex plasma dynamics through codes like JOREK. This detailed configuration of the active poloidal field system forms a critical input for numerical simulations, ensuring that the magnetic environment used in computational models faithfully represents the physical capabilities of the DTT device.

Therefore, each CS module has been defined in IMAS as a single coil composed by two elements sharing the same currents.

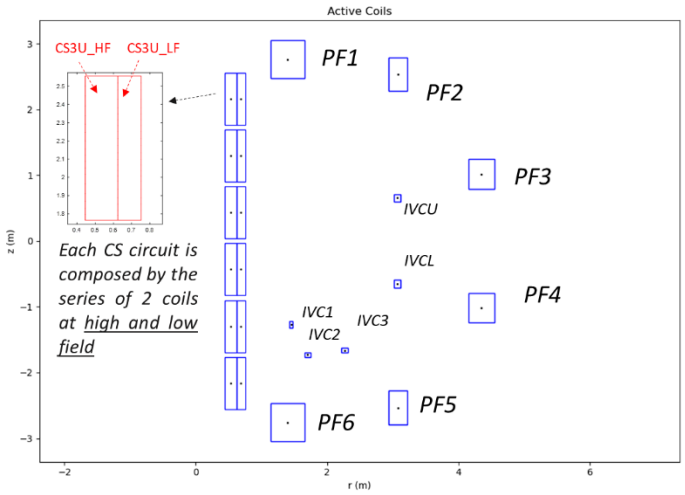

Figure 92 DTT magnetic coils poloidal profile integrated in IMAS

The ***pf_passive ids*** has been populated with the description of the inner and outer shell of the vacuum vessel as well as the stabilizing plates that will interact passively with the plasma [68].

The pf_passive Interface Data Structure within IMAS for the DTT project comprehensively describes the tokamak's passive conductive elements. These elements are critical for accurately simulating induced currents and the resulting electromagnetic forces during transient events

such as plasma disruptions and Vertical Displacement Events. The ids infrastructure is detailed in Table 56, included in ***Annex B - DTT required data and IDS for JOREK initialization***

The infrastructure detailed within the pf_passive IDS primarily includes the vacuum vessel and its associated components:

- **The Vacuum Vessel (VV) (**Figure 93**)**: the system composed of 18 individual vacuum vessel sectors. The DTT vacuum vessel features two stainless steel shells, each with a thickness of 1.5 cm.

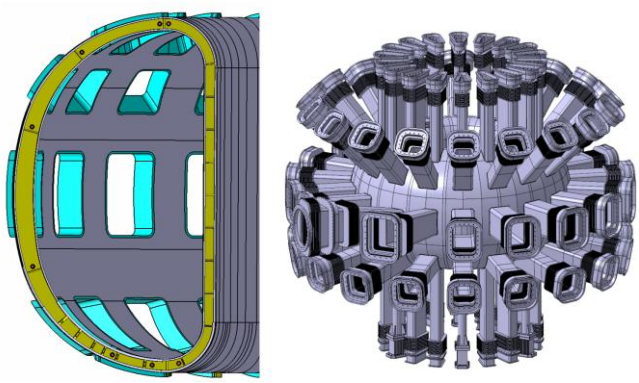

Figure 93 Vacuum Vessel and Ports CAD model

- **Stabilizing plates (SP) (**Figure 94**):** a large saddle coil installed inside the vacuum vessel. It consists of two loops made of copper on the upper and lower side of the vessel, which are connected by a bridge, so that the currents in the lower and upper part are anti-parallel and it only reacts to the net flux change of the plasma.

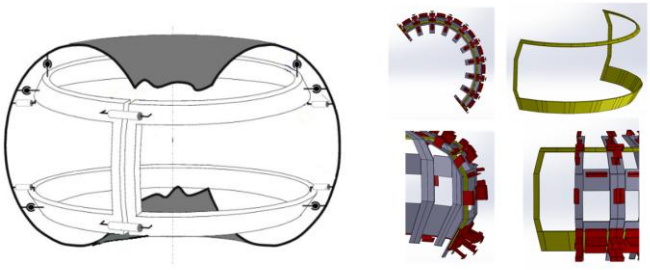

Figure 94 Stabilizing Plates CAD model

The pf_passive IDS is populated with geometric representations, specifically "loop (parallelograms) elements and rectangular elements," used to discretize these conductive

structures for electromagnetic simulations. Additionally, the system incorporates two stabilizing plates.To accurately simulate induced currents within the vessel and stabilizing plates, these continuous structures must be discretized into a network of resistive and inductive elements. The "loop (parallelograms) elements" mentioned can be characterized as *oblique elements* (Figure 95)due to their general quadrilateral shape, each requiring specific parameters for their definition:

- **Starting Point (r, z) Coordinates**: These coordinates define the initial spatial position of each element within the poloidal cross-section.
- **Alpha Angle (α)**: This angle specifies the orientation of the parallelogram with respect to the radial axis.
- **Beta Angle (β)**: This angle defines the orientation of the parallelogram with respect to the vertical axis. Together, the alpha and beta angles fully describe the element's angular disposition.
- **Length Alpha (l_a)**: This denotes the length of the parallelogram along the direction identified by the alpha angle.
- **Length Beta (l_b)**: This denotes the length of the parallelogram along the direction identified by the beta angle.

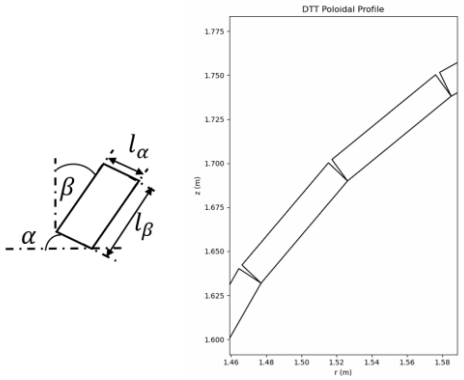

Figure 95 Example of pf_passive oblique loop

The most challenging aspect of the pf_passive integration was the creation of an appropriate discretization of the two vacuum vessel shells, ensuring compliance with the prescribed requirements on α, β, the length along α, and the length along β for each individual oblique element

The procedure was carried out starting from an ordered point discretization of both the vacuum vessel (VV) and the stabilizing plates (SP).

For the vacuum vessel, each elementary parallelogram was defined using three consecutive points. Consequently, the initial source file containing the VV point coordinates was sorted and filtered to form triplets of points organized as illustrated in (Figure 96). The line connecting the first and second points defines the β direction, while the line connecting the second and third points defines the α direction.

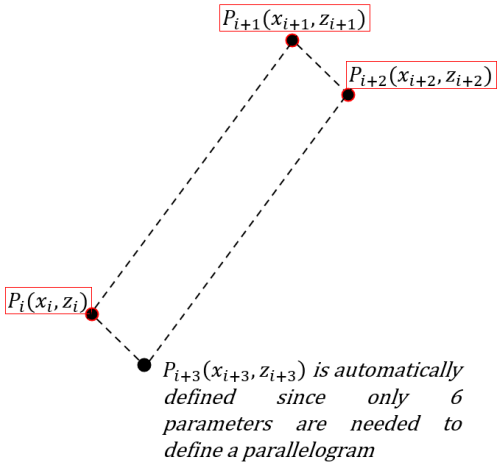

Figure 96 Example of a triplet of points defined to discretize the VV shells

Therefore a .py routine has been developed to compute, by iterating on the dataset of triplets, the parameters related to each loop (Routine for vessel loop discretization) included in ***Annex C - Python routines for DTT IMAS shot integration***

Basically, the procedure implements recursively the following equations (taking in account Figure 96 schematic):

$$l_\beta = \sqrt{[(x_{i+1} - x_i)^2 + (y_{i+1} - y_i)^2]}$$

$$l_\alpha = \sqrt{[(x_{i+2} - x_{i+1})^2 + (y_{i+2} - y_{i+1})^2]}$$

$$\beta = \tan^{-1}(y_{i+1} - y_i\,, x_{i+1} - x_i) - \pi/2$$

$$\alpha = \tan^{-1}(y_{i+2} - y_{+1i}\,, x_{i+2} - x_{i+1})$$

The discretization resulted in 212 loops including stabilizing plates (Figure 97). The stabilizing plates have been defined as a single loop, which is composed of two elements connected in series. In this configuration, the current flows with opposite signs within these elements. Figure 97 shows the poloidal profile discretization included in IMAS for inner/outer shell of the DTT VV and the SP.

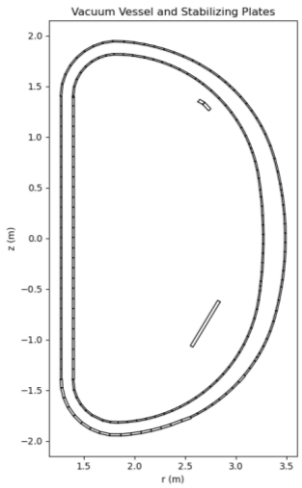

Figure 97 DTT VV and SP discretization integrated in IMAS

One other aspect to be addressed was the accurate determination of resistance for each discrete element.

For both the vessel and the stabilizing plates, the resistance of each discretized loop is calculated based on its material properties and geometric configuration. The general principle involves:

1. **Material Resistivity ($\boldsymbol{\rho_{mat}}$)**: This is an intrinsic electrical property of the conductive material, such as the stainless steel used for the DTT vacuum vessel and stabilizing plates.
2. **Length of Current Path ($\boldsymbol{L_{loop}}$)**: For each element, the effective length that the current traverses must be determined. This has been defined as the length of the circumference with a radius equal to the r coordinate of the loop. Therefore:

$$L_{loop} = 2\pi r_{loop}$$

3. **Cross-sectional Area ($\boldsymbol{A_{loop}}$)**: This is the area perpendicular to the direction of current flow through the element.

$$A_{loop} = l_b \cdot l_a \cdot \sin\left(\frac{\pi}{2} - \beta + \alpha\right)$$

The resistance (R_{loop}) for each segment is calculated as follows:

$$R_{loop} = \rho_{mat} * \frac{L_{loop}}{A_{loop}}$$

The total resistance of a stabilizing plate is the sum of the resistances of its two constituent elements due to their series connection.

The detailed inclusion of these geometric and resistive properties for each passive element within the pf_passive IDS ensures that simulation codes can accurately model the complex behavior of induced currents, their magnetic fields, and the resultant forces on DTT's passive structures during plasma operation and disruptive events.

The last ids related to the Machine Description is the ***wall***. As already said it includes a description of the outer boundary of the plasma domain [69]. The required data integrated in IMAS are outlined in Table 57 of ***Annex B - DTT required data and IDS for JOREK initialization***. In particular:

- 6 first wall panels (divided in inboard, top, outboard first wall)
- 3 divertor targets (Innet Target, Central Target, Outer Target)

To be noted that the defined outline shown in Figure 98 Wall outline including First Wall and Divertor is not toroidally continuous.

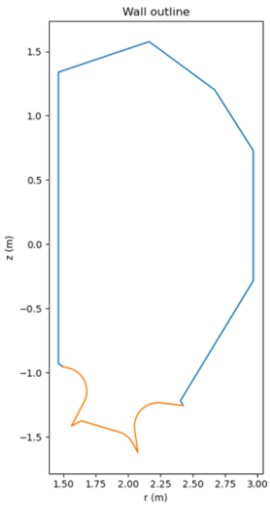

Figure 98 Wall outline including First Wall and Divertor shape

Figure 99 shows the DTT poloidal profile integrated in IMAS.

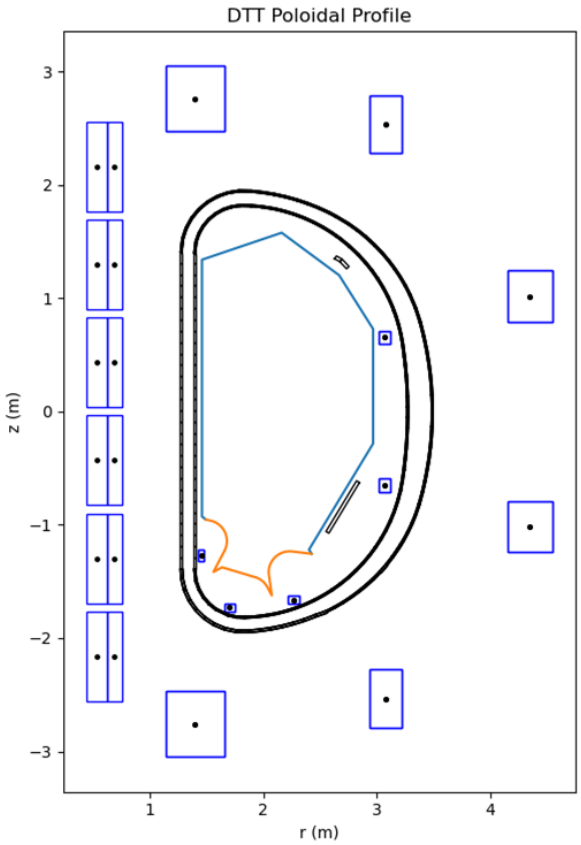

Figure 99 DTT poloidal profile integrated in IMAS

The IMAS shots outlined in Table 11 , are comprehensive of DTT Machine Description database.

Table 11 DTT Machine Description shots

DTT MD			
	pf_active	**pf_passive**	**wall**
Username	public	public	public
Database	DTT_MD	DTT_MD	DTT_MD
Shot	111002	115006	116001
run	1	1	1

The complete routine coded to integrate the DTT MD data has been included in *Full routine for DTT IMAS Machine Description integration* part of ***Annex C - Python routines for DTT IMAS shot integration***

4.3.4 Equilibrium ids

Within the IMAS data model, the *equilibrium IDS* encapsulates all quantities necessary to describe the magnetic configuration of the plasma and its global macroscopic parameters at a given time [70]. To ensure a consistent representation of the DTT magnetic equilibrium, each relevant field of the IDS must be properly populated with data extracted from a reference EQDSK file. The principal groups and substructures involved in this process are detailed in Table 54 of ***Annex B - DTT required data and IDS for JOREK initialization***. At the top level, the **equilibrium.ids_properties** group contains metadata related to the dataset definition, including the IMAS schema version (version_put.data_dictionary, version_put.access_layer, and version_put.access_layer_language), and the flag homogeneous_time, indicating whether time slices share a uniform temporal basis. The **equilibrium.vacuum_toroidal_field** group defines the magnetic field configuration in vacuum conditions, specifically the reference major radius ($r0$) and the corresponding toroidal magnetic field amplitude (b0). For each **time slice** in the IDS (equilibrium.time_slice[]), three main categories of data are populated:

- **Global quantities (global_quantities)**, including the total plasma current (ip), the poloidal magnetic flux at the magnetic axis and at the plasma boundary (psi_axis, psi_boundary), and the spatial coordinates of the magnetic axis (magnetic_axis.r, magnetic_axis.z).
- **One-dimensional profiles (profiles_1d)**, describing quantities as functions of the normalized poloidal flux, such as the pressure profile (pressure), the poloidal current function (f), their derivatives with respect to ψ (dpressure_dpsi, f_df_dpsi), the safety factor (q), and the normalized toroidal flux coordinate (rho_tor_norm).
- **Two-dimensional profiles (profiles_2d)**, which map the poloidal magnetic flux distribution over the computational grid defined by (grid.dim1, grid.dim2, r, z, and psi).

Each time slice is associated with a specific time stamp (equilibrium.time_slice[].time), and the temporal evolution of the equilibrium is referenced in the global time vector (equilibrium.time).

The population of the *equilibrium* and *core_profiles* Interface Data Structures (IDS) within the IMAS framework for the DTT project relied on the definition of a consistent and physically meaningful reference magnetic equilibrium. To this end, it was first necessary to select an

appropriate **reference EQDSK file**, which represents the numerical solution of the Grad–Shafranov equation for a given plasma configuration [71]. The EQDSK provides a self-consistent magnetic equilibrium that serves as the foundation for defining the global plasma parameters, magnetic geometry, and flux-surface-related quantities used in the IMAS data hierarchy. Although the overall structure of the EQDSK format is well defined, several variants exist, reflecting differences in coordinate conventions, units, and the definition of flux functions adopted by different equilibrium reconstruction or transport codes. Broadly, EQDSK files can be classified into:

- **Standard EFIT or "G-EQDSK" files**, which contain the complete two-dimensional magnetic flux distribution (PSIRZ) together with pressure, current, and safety factor profiles tabulated on a uniform ψ grid. This format is commonly used for code coupling within IMAS, JINTRAC [72]., and other integrated modeling environments.
- **"A-EQDSK" or "L-EQDSK" formats**, which may include additional metadata (e.g., coil current definitions, limiter geometry, or diagnostic constraints) or alternative normalization schemes for the flux coordinates.
- **Transport-code specific variants**, adapted for use with simulation tools such as JOREK, DINA [73]or CREATE, which require consistent normalization and sign conventions for magnetic flux and current definitions.

Because the sign and scaling of quantities such as the poloidal flux ψ, toroidal field B_t, and plasma current I_p can differ between implementations, a **COCOS (COordinate COnventionS)** system was introduced to provide a unified reference framework [74]. Each COCOS index, ranging from 1 to 21, specifies the adopted conventions for:

- the orientation of the cylindrical coordinate system (R,ϕ,Z)(R, \phi, Z)(R,ϕ,Z),
- the sign of the toroidal magnetic field and plasma current,
- the definition of the poloidal flux ψ (increasing or decreasing from axis to boundary), and
- the reference used for the safety factor $q(\psi)$.

Table 12 a) Coordinate conventions for each COCOS index. COCOS ≤ 8 refers to ψ divided by (2π) and thus with $e_{B_p} = 0$ while COCOS ≥ 11 refers to full poloidal flux with $e_{B_p} = 1$. Otherwise COCOS = i and COCOS = 10 + i have the same coordinate conventions. The cylindrical (with the related $\sigma_{R\phi Z}$ value) and poloidal (with $\sigma_{\rho\theta\phi}$) right-handed coordinate systems are given as well. b) The indications in this subtable (last three columns) are assumingI_p and B_0 positive in the related coordinate system, that is in the direction of the related ϕ.

COCOS	e_{B_p}	σ_{B_p}	***Cylindrical (R, ϕ, Z)***	***Poloidal (ρ, θ, ϕ)***	$\sigma_{\rho\theta\phi}$	***ϕ from top***	***θ from front***	***ψref***	***sign(q)***	***sign(dψ/dψ)***
1/11	0/1	+1	(R, ϕ, Z)	+1 (ρ, θ, ϕ)	+1	cnt-clockwise	clockwise	increasing	+1	-1
2/12	0/1	+1	(R, Z, ϕ)	-1 (ρ, θ, ϕ)	+1	clockwise	cnt-clockwise	increasing	+1	-1
3/13	0/1	-1	(R, ϕ, Z)	+1 (ρ, ϕ, θ)	-1	cnt-clockwise	cnt-clockwise	decreasing	-1	+1
4/14	0/1	-1	(R, Z, ϕ)	-1 (ρ, ϕ, θ)	-1	clockwise	clockwise	decreasing	-1	+1
5/15	0/1	+1	(R, ϕ, Z)	+1 (ρ, ϕ, θ)	-1	cnt-clockwise	cnt-clockwise	increasing	-1	-1
6/16	0/1	+1	(R, Z, ϕ)	-1 (ρ, ϕ, θ)	-1	clockwise	clockwise	increasing	-1	-1
7/17	0/1	-1	(R, ϕ, Z)	+1 (ρ, θ, ϕ)	+1	cnt-clockwise	clockwise	decreasing	+1	+1
8/18	0/1	-1	(R, Z, ϕ)	-1 (ρ, θ, ϕ)	+1	clockwise	cnt-clockwise	decreasing	+1	+1

In this work, the equilibrium data were first loaded in IMAS following **COCOS 11 convention** (since most of equilibrium codes already coupled with IMAS, such as DINA require COCOS11 formatting) and then have been converted in **COCOS8** required to be **compatible with the JOREK MHD code**. Therefore, the EQDSK used to populate the IMAS *equilibrium IDS* was selected and verified to conform to **COCOS = 11**, ensuring that the orientation of the toroidal field, current, and flux functions is consistent between EFIT, IMAS, and JOREK. Using a COCOS11-compliant equilibrium guarantees that quantities such as *q(ψ)* and the poloidal flux gradients maintain the correct physical sign and normalization when imported into the IMAS

data structures and subsequently used for disruption evolution simulations.In particular for COCOS11 convention follows:

$$q = \frac{1}{(2\pi)^{(1-e_{B_P})}} \frac{d\phi_{tor}}{d\psi_{ref}}$$

An **EQDSK file** contains all the information required to describe the two-dimensional axisymmetric magnetic equilibrium of a tokamak plasma. In particular, it typically includes all the parameters reported in Table 13.

Table 13 Main variables contained in an EQDSK file, including grid geometry, magnetic flux data, flux-surface quantities, and plasma boundary definitions.

Variable	Description	Units / Notes
CASE	Identification of character string	-
NW, NH	Number of grid points in R and Z directions	-
RDIM, ZDIM	Dimensions of computational box	m
RLEFT, ZMID	Lower-left corner R and vertical center Z of the grid	m
RMAXIS, ZMAXIS	Radial and vertical coordinates of magnetic axis	m
SIMAG, SIBRY	Poloidal flux at magnetic axis and plasma boundary	Weber/rad
RCENTR, BCENTR	Reference radius and vacuum toroidal magnetic field at RCENTR	m, T
CURRENT	Total plasma current	A
FPOL(ψ)	Poloidal current function ($F = R\,B_t$)	m·T
PRES(ψ)	Plasma pressure on uniform flux grid	N/m²
FFPRIM(ψ)	Derivative of $F \cdot F'(\psi)$	(m·T)² / (Weber/rad)
PPRIME(ψ)	Derivative of pressure with respect to ψ	(N/m²) / (Weber/rad)
PSIRZ(R, Z)	Poloidal magnetic flux on rectangular grid	Weber/rad
QPSI(ψ)	Safety factor profile on uniform flux grid	-
NBBBS	Number of plasma boundary points	-

LIMITR	Number of limiter contour points	-
RBBBS(i), ZBBBS(i)	Coordinates of LCFS boundary points	m
RLIM(i), ZLIM(i)	Coordinates of limiter contour	m
JT(R, ψ)	Toroidal current density, computed as $J_T = R \cdot P'(\psi) + F \cdot F'(\psi)/R$	A/m²

For the DTT case, the reference EQDSK corresponds to a **Single Null magnetic configuration** under **full power operating conditions**, characterized by a plasma current of **5.5 MA** and a **toroidal magnetic field of 6 T** at the plasma magnetic axis [75].

This configuration was selected because it represents a critical operational state for the study of disruption phenomena, particularly those impacting the divertor region. The equilibrium corresponds to the **end of the flat-top phase (t = 43s)** of the 2024 Single Null scenario (**Equil_DTT_v16_Ipl_5d5MA_betap_0d65_li_0d8_t_at_43s_COCOS11**).

As already the **equilibrium IDS** was populated by importing the full set of macroscopic and geometric quantities extracted from the EQDSK file.

These include the total plasma current, poloidal beta, internal inductance, and the magnetic flux values at both the axis and the boundary.

The geometric definition comprises the major and minor radii, the coordinates of the magnetic axis and X-point, and the poloidal contour of the plasma boundary.

In addition, shape descriptors such as elongation (κ) and triangularity (δ) were derived from the boundary geometry to provide a comprehensive description of the plasma cross-section.

Table 14 includes the main 0-dimensional parameters related to the scenario, integrated in the equilibrium ids.

Table 14 0D Parameters related to the full power SN reference scenario(note that the included parameters are related to the end of the flat top at 43s)

Time	**13,75s**	**16s**	**43s**	**51s**
Ipl [MA]	5,50	5,50	**5,50**	5,50
Betapol	0,10	0,65	0,65	0,10

Separatrix at 43 s

Li	0,80	0,80	0,80	0,80
Boundary flux [Vs]	2,97	2,21	-3,89	-4,38
Axis flux [Vs]	13,19	12,52	6,41	5,87
Rpl [m]	2,17	2,23	2,24	2,19
Zpl [m]	0,17	0,18	0,18	0,18
Raxis - node [m]	2,23	2,28	2,29	2,23
Zaxis - node [m]	0,18	0,19	0,20	0,20
Rbound - node [m]	1,88	1,86	1,87	1,87
Zbound - node [m]	-1,18	-1,17	-1,18	-1,18
R [m]	2,19	2,19	2,20	2,20
a [m]	0,70	0,70	0,70	0,71
Btor_tot at Major Radius [T]	-6,19	-5,96	-5,95	-6,17
Btor at Magnetic Axis [T]	-6,08	-5,72	**-5,72**	-6,09
q_95	-2,76	-2,88	-2,81	-2,68
elongation (k)	1,79	1,79	1,81	1,79
k_95	1,66	1,65	1,68	1,66
Triangularity (Delta)	0,40	0,44	0,36	0,28
Delta_95	0,29	0,32	0,26	0,19
Perimeter [m]	6,16	6,18	6,19	6,19
Volume [m^3]	34,26	34,16	34,70	35,13

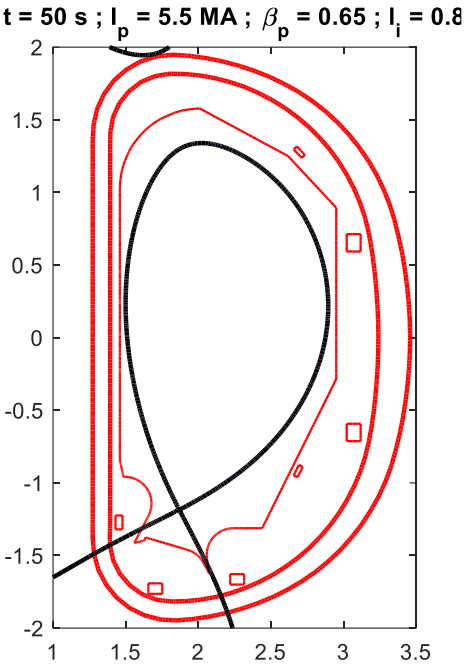

Since the filled equilibrium ids includes many 1D and 2D parameters, for simplification purposes, only the most relevant quantities have been here graphically reported. The IMAS shot related to the integrated data will be provided further in the document.

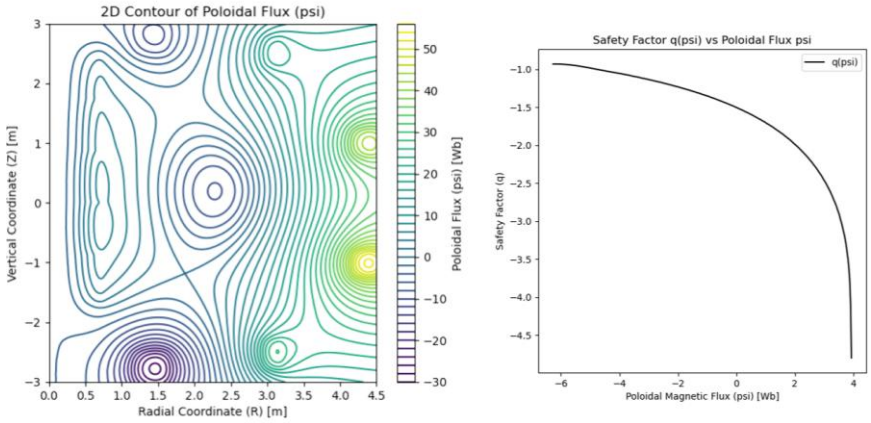

Figure 100 left) 2D Contour of poloidal flux on the set grid); right) q_{95} vs poloidal flux

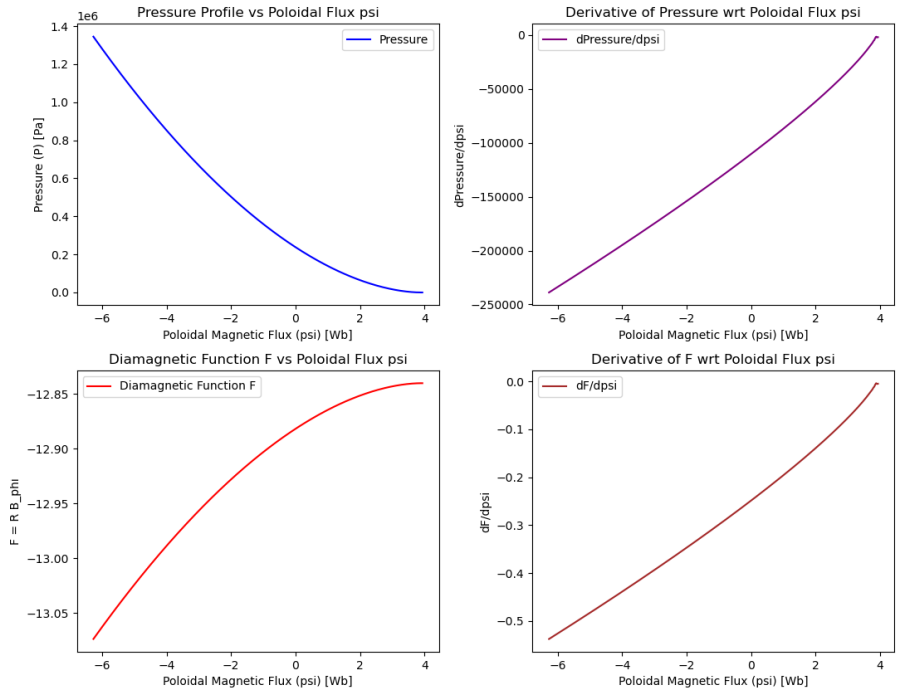

Figure 101 Main 1D quantities related to the end of the flat top of the reference SN scenario at full power (5.5 MA and 6T)

4.3.5 Core_profile ids

Table 55 included in ***Annex B - DTT required data and IDS for JOREK initialization***, reports the core_profiles ids infrastructure, Since no officially integrated scenarios were available in the official DTT database (Alfresco) that consistently coupled magnetic equilibrium and core profile data, the core_profiles IDS had to be constructed manually to ensure internal consistency. A JINTRAC simulation output was used as a reference for the plasma core profiles; however, this dataset was not directly associated with the same magnetic equilibrium

described by the reference EQDSK file. It was therefore necessary to reconcile these datasets to obtain a coherent integrated scenario. In this process, the electron density (n_e) from the JINTRAC simulation was interpolated onto the normalized poloidal flux grid (ψ_{norm})derived from the reference equilibrium (EQDSK at 43 s). This re-mapping ensured that the density profile was expressed consistently with equilibrium geometry. Based on this interpolated density, the electron temperature (T_e) and average ion temperature (T_i) were then evaluated through the pressure balance relationship:

$$assuming\ T_e = T_i \ \rightarrow\ p_{equilibrium} = n_{e_{interpolated}}(T_e + T_i) \cong 2\ T_e\ n_e$$

The following equations describe the interpolation method adopted in this case. The method is automatically implemented by the intrepid function (SciPy function).

$$f_k(x) = \begin{cases} y_i + \dfrac{y_{i+1} - y_i}{x_{i+1} - x_i}\ (x - x_i), & x_i \le x \le x_{i+1} \\ (linear\ extrapolation), & otherwise \end{cases}$$

For each pair of neighboring points (x_i, y_i) and (x_{i+1}, y_{i+1}). For values of x outside the original range, say $x < x_0$ or $x > x_N$, the function extrapolates linearly using the slope of the nearest segment:

$$f_k(x) = \begin{cases} y_0 + \dfrac{y_1 - y_0}{x_1 - x_0}\ (x - x_0), & x < x_0 \\ y_N + \dfrac{y_N - y_{N-1}}{x_N - x_{N-1}}\ (x - x_0), & x > x_0 \end{cases}$$

This ensures all profiles are defined consistently on the same radial grid. Assuming $\psi_{norm_{JINTRAC}} = \psi_{norm,0}, \psi_{norm,i}, \psi_{norm,i+1} \dots \dots \psi_{norm,N}$ as independent variable from which construct the piecewise-linear function, and $\psi_{eq} = \psi$ as argument to find the interpolated values of ne_{new}, it follows:

$$n_{e,new} = \begin{cases} n_{e,i} + \dfrac{n_{e,i+1} - n_{e,i}}{\psi_{norm,i+1} - \psi_{norm,i}}\left(\psi_{eq,norm} - \psi_{norm,i}\right) \\ n_{e,0} + \dfrac{n_{e,1} - n_{e,0}}{\psi_{norm,1} - \psi_{norm,0}}\left(\psi_{eq,norm} - \psi_{norm,0}\right) \\ n_{e,N} + \dfrac{n_{e,N} - n_{e,N-1}}{\psi_{norm,N} - \psi_{norm,N-1}}\left(\psi_{eq,norm} - \psi_{norm,N}\right) \end{cases}$$

As can be seen in the original profiles from the JINTRAC simulation (Figure 102, Figure 103), the main characteristics of H-mode confinement were present. However, since the pressure profile associated with the equilibrium did not feature a pedestal (being derived from a scenario not coupled with transport phenomena), using this pressure to derive the temperature, caused the pedestal to be lost in both the electron density and temperature profiles. This, however, does not affect the disruption simulation.

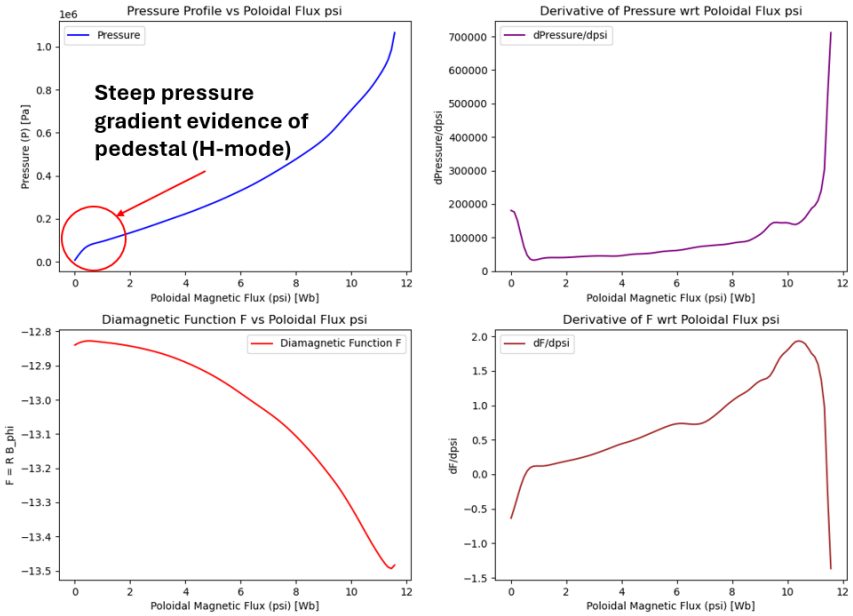

Figure 102 JINTRAC original profiles (pressure profile features the pedestal evidence of H-mode confinement)

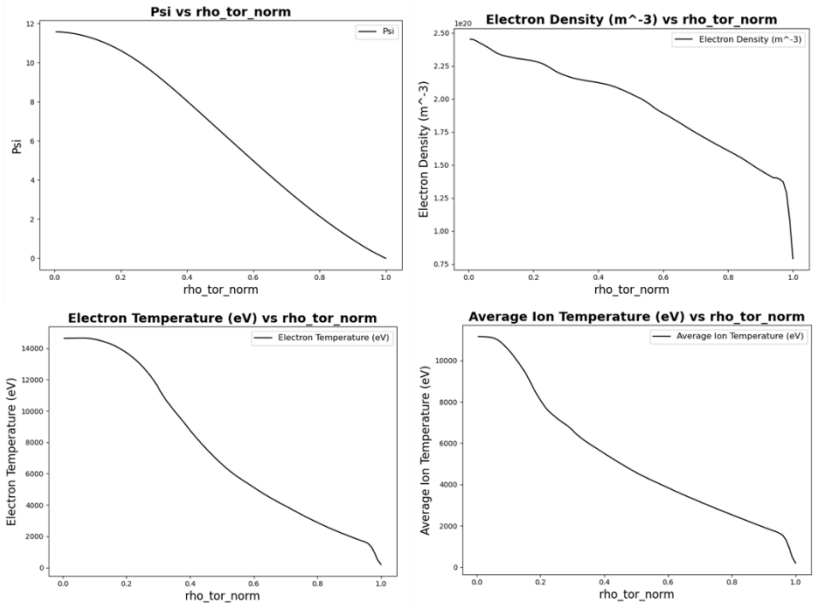

Figure 103 JINTRAC psi, electron temperature, ion temperature, electron density vs ρ_{norm}

Figure 104 shows the main core_profiles integrated into the ids.

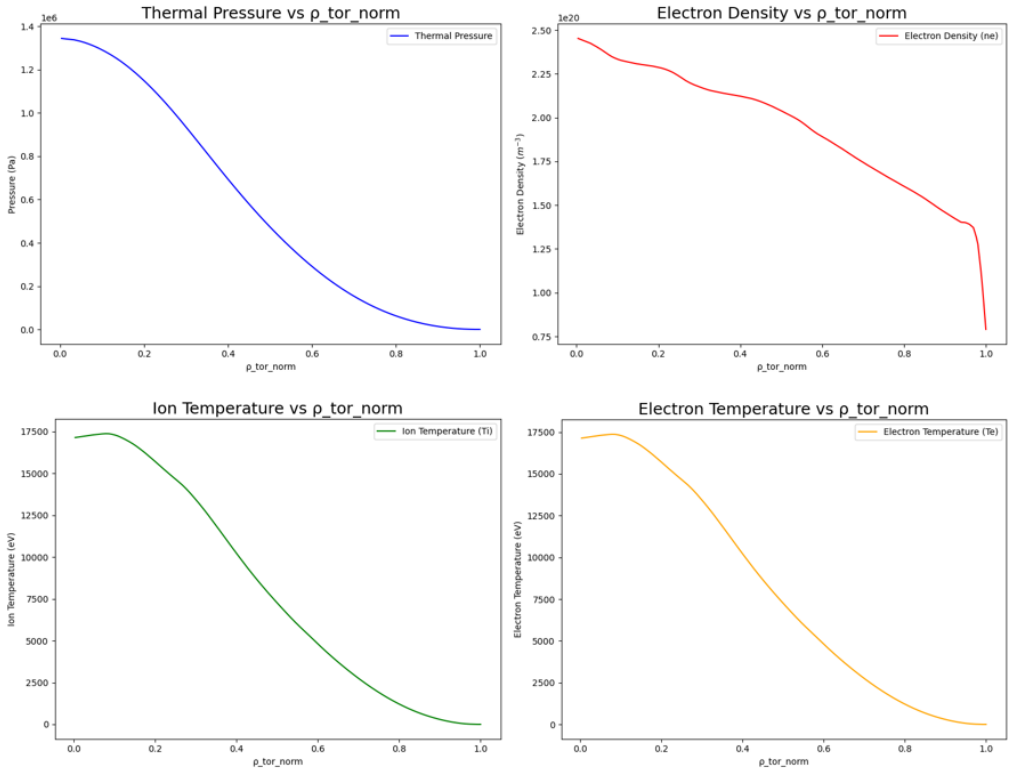

Figure 104 Main integrated core_profiles, consistent with equilibrium ids

4.3.6 Pf_active ids including current

Lastly, the pf_active ids, including the current related to the equilibrium, has been integrated.

Table 15 SN Full power scenario, coil currents and turns

Coil ID	Turns	Current turn [kA]	Total current [MA]
CS3U [kA]	108	-23,53	-2.54
CS2U [kA]	162	-24,36	-3.95
CS1U [kA]	108	-30,74	-3.32
CS1L [kA]	162	-33,78	-5.47
CS2L [kA]	108	-27,21	-2.94
CS3L [kA]	162	-2,45	-0.40

PF1 [kA]	108	10,64	1.15
PF2 [kA]	162	-10,46	-1.69
PF3 [kA]	108	-9,98	-1.08
PF4 [kA]	162	-13,22	-2.14
PF5 [kA]	108	-15,86	-1.71
PF6 [kA]	162	23,68	3.84

4.3.7 DTT populated IMAS shots

In Table 16 are reported the official DTT shot integrated in IMAS.

The routine developed for populating the DTT IMAS integrated equilibrium scenario has been included in *Full routine for DTT IMAS integrated equilibrium scenario integration* in ***Annex C - Python routines for DTT IMAS shot integration.***

The code employs dedicated routines, namely **read_eqdks** and **read_JINTRAC_DATA**, which are responsible for reading and formatting the quantities contained in the EQDSK files according to their sequential structure and in the JINTRAC output files, respectively. The extracted data are first stored in a library and subsequently retrieved by the main script, where they are used as input to populate the IDS structures.

Table 16 DTT IMAS official databases

<table>
<tr><th colspan="2">DTT_MD Database</th><th colspan="2">DTT Database</th></tr>
<tr><td>pf_active</td><td>user: public
shot: 111002
run: 1</td><td rowspan="3">Equilibrium ids+ core_profiles ids + pf_active ids (with currents related to the scenario)</td><td>user: public</td></tr>
<tr><td>pf_passive</td><td>user: public
Shot: 115006
run: 1</td><td>shot: 100004</td></tr>
<tr><td>wall</td><td>user: public
shot: 116001
run: 1</td><td>run: 1</td></tr>
</table>

4.4 JOREK background

JOREK is a massively parallel, fully implicit non-linear **extended magnetohydrodynamic (MHD)** simulation code designed to model large-scale instabilities in tokamak plasmas with realistic X-point geometry. The code solves a set of reduced or full MHD equations that evolve the magnetic field, plasma flow, density, and temperature in time [76].

A key feature of JOREK is its use of **flux-surface-aligned Bézier finite elements** for the discretization in the poloidal plane, combined with a **toroidal Fourier representation**, which allows it to accurately resolve edge and scrape-off-layer dynamics while limiting computational cost [77]. Temporal advancement is performed using a **fully implicit time-stepping scheme**, which efficiently handles the stiff multi-time-scale nature of MHD phenomena, ranging from fast Alfvénic dynamics to slower resistive processes. The code incorporates anisotropic parallel heat conduction, resistive and two-fluid effects, neoclassical terms, neutral and impurity models, and optional coupling to resistive walls via the **STARWALL** code for free-boundary simulations [78].

Initial plasma equilibria are obtained from a built-in **Grad–Shafranov solver**, ensuring that the discrete state satisfies force balance before non-linear evolution begins. JOREK has been successfully applied to study **edge-localized modes (ELMs)**, **disruptions and runaway electrons**, **vertical displacement events (VDEs)**, and various **ELM control techniques** such as resonant magnetic perturbations, pellet injection, and magnetic kicks, making it one of the leading computational tools for predictive tokamak stability studies.

The cylindrical coordinate system used in JOREK, (R, Z, ϕ) is related to Cartesian coordinates (x, y, z) through the transformations $x = R\cos(\phi)$, $y = -R\sin(\phi)$ and $z = Z$. With this definition, the toroidal angle ϕ increases in the clockwise direction when the plasma is viewed from above. Following the conventions defined in reference, this choice corresponds to a COCOS scheme with index 8. The Bézier finite elements implemented in JOREK are constructed in an isoparametric manner, meaning that the geometric coordinates $R$and Z are represented using the same Bézier basis functions as the physical variables. As a result, each element naturally introduces a local coordinate system (s, t, ϕ) [76].

JOREK incorporates an internal Grad–Shafranov (GS) equilibrium solver that relies on the same finite-element grid and variable representation as the subsequent nonlinear MHD

simulations. This ensures that the initial state used for the time evolution satisfies the force-balance condition at the discrete level, preventing artificial transients at the beginning of the calculation. The code is capable of computing equilibria with a fixed plasma boundary, or, when coupled to the STARWALL resistive-wall model, fully free-boundary equilibria (see section 2.9).

To compute an equilibrium, the solver requires prescribed profiles of the plasma pressure (provided separately as temperature and density, as these values are needed later for the initial condition setup) and the function FF'. These profiles are specified as functions of the normalized poloidal magnetic flux, $\psi_N = (\psi - \psi_{axis})/(\psi_{bnd} - \psi_{axis})$ given either analytically or through numerical tables. Here, ψ_{axis} and ψ_{bnd} represent the poloidal flux values at the magnetic axis and at the plasma boundary, respectively. Additionally, the boundary values of ψ on the computational domain must be supplied, typically as a list of (R, Z, ψ) points or, for simpler cases, through coefficients of analytic flux moments [76]. These inputs can be imported from standard sources such as *geqdsk* files or equilibria produced by the CLISTE code.

The Grad–Shafranov equation is then solved iteratively, either through Picard or Newton methods, until the desired accuracy is reached. After this first solution, the resulting flux surfaces are generally used to construct a new, flux-aligned finite-element grid. The GS equation is then solved again on the updated grid, yielding the fully consistent initial state for the MHD time integration.

Once the equilibrium is obtained, all physical fields are initialized coherently. The poloidal flux ψ is taken directly from the GS solution, and the toroidal current density is computed from this flux using the definition of the current operator. Temperature and density are assigned according to the prescribed profiles. Velocity-related quantities, namely the stream function, vorticity and parallel velocity—are initialized to zero unless a background rotation profile is imposed. If sheath boundary conditions are applied, the parallel velocity at divertor plates is set to the ion sound speed.

Therefore, in this application, the required parameters/profiles to initialize JOREK have been defined starting from the DTT scenario included in IMAS.

The MHD model in JOREK is formulated through a set of normalized equations that describe the evolution of the magnetic potential (A), mean velocity (V), total density ρ, and total pressure (p). The normalization procedure uses the central mass density ρ_0 and the vacuum permeability μ_0, such that μ_0 does not appear explicitly in the normalized equations. Time is normalized by a factor $\tau_{norm} = \sqrt{\mu_0\ \rho_0}$, which typically approximates the Alfvén time $\tau_A = a\frac{\sqrt{\mu_0\rho_0}}{B_0}$. Total pressure and mass density are normalized byμ_0 and ρ_0 respectively.

The core normalized governing equations are:

1. **Magnetic Potential Evolution**:

$$\frac{\partial \boldsymbol{A}}{\partial t} = -\boldsymbol{E} - \nabla\phi$$

   Here, E represents the electric field and ϕ is the electrostatic potential. In the JOREK full MHD model, the Weyl gauge, $\phi = 0$, is typically employed.

2. **Momentum Equation**:

$$\rho\frac{\partial \boldsymbol{V}}{\partial t} = -\rho\,\boldsymbol{V}\cdot\nabla\boldsymbol{V} - \nabla p + \boldsymbol{J}\times\boldsymbol{B} + \nabla\cdot\underline{\tau} + \boldsymbol{S_V}$$

   This equation describes the conservation of momentum, encompassing convective terms, the pressure gradient, the Lorentz force $J \times B$, the viscous stress tensor $\underline{\tau}$, and a momentum source term $\boldsymbol{S_V}$.

3. **Continuity Equation**:

$$\frac{\partial \rho}{\partial t} = -\nabla\cdot(\rho\boldsymbol{V}) + \nabla\cdot\left(\underline{\boldsymbol{D}}\nabla\rho\right) + S_\rho$$

   This equation governs the evolution of plasma density, accounting for convective transport, particle diffusion $\nabla\rho$, and a particle source term S_ρ.

4. **Pressure Equation**:

$$\frac{\partial p}{\partial t} = -\boldsymbol{V}\cdot\nabla p - \gamma p\nabla\cdot\boldsymbol{V} + \nabla\cdot\left(\underline{k}\nabla T\right) + (\gamma-1)\underline{\tau}\colon\nabla\boldsymbol{V} + S_p$$

This equation details the evolution of total pressure, incorporating convective transport, compressional heating/cooling (where γ is the ratio of specific heats, usually $5/3$), anisotropic heat diffusion ($\underline{k}\nabla T$), viscous heating, and a pressure source term S_p. The total pressure is defined using the ideal gas law as $p = p_e + p_i = \rho T$(with μ_0 eliminated due to normalization). This total pressure is the sum of the ion and electron pressures. In some models, it is assumed that the electron and ion pressures each constitute half of the total pressure, for instance when computing diamagnetic terms. The model extension further detailed in, however, allows the electron and ion temperatures to be evolved as separate variables.

5. The magnetic field vector $\boldsymbol{B}$ and the current density vector $\boldsymbol{J}$ are defined as:

$$\boldsymbol{B} = F\nabla\phi + \nabla \times \boldsymbol{A} \text{ and } J = \nabla \times \boldsymbol{B}$$

The toroidal flux function $F(\psi) = RB_\phi$ is often taken from the initial Grad-Shafranov equilibrium. The electric field E is determined by a generalized Ohm's law that incorporates resistivity and drift-ordered (diamagnetic) terms:

$$\boldsymbol{E} = -\boldsymbol{V} \times \boldsymbol{B} + \eta(J - J_*) + F_0 \frac{\delta^*}{\rho}(\nabla_\perp p_i - \nabla_{||}\, p_e)$$

The resistivity η follows a Spitzer temperature dependence:

$$\eta = \eta_0 \cdot \left(\frac{T}{T_0}\right)^{-\frac{3}{2}}$$

$$\delta^* = \frac{m_{ion}}{eF_0\sqrt{\mu_0\rho_0}}$$

where η_0 is a constant parameter, T_0 is the initial plasma core temperature, m_{ion} is the ion mass, and e is the elementary charge. The constant $F_0 = R_0 B_{\phi_0}$is defined as the major radius at the geometric centre times the vacuum toroidal field.

These equations represent the core of JOREK MHD model. A much more comprehensive description of the JOREK governing equations and model is detailed in.

JOREK's capability for free boundary simulations is facilitated by its coupling with the STARWALL code. STARWALL is designed to discretize conducting structures, such as tokamak walls, using triangles under a thin-wall approximation.

The interaction between the plasma and the resistive wall is handled by applying a **natural boundary condition** at the edge of the JOREK computational domain, which replaces traditional Dirichlet boundary conditions.

The coupling mechanism involves STARWALL calculating **response matrices** that describe the magnetic field generated by currents in the conducting structures. These matrices are then utilized within JOREK.

The evolution of the wall currents themselves is determined by **resistor–inductor circuit equations** applied to each discretized wall element. This entire coupling process is **fully implicit**, ensuring consistency between the evolving plasma dynamics and the induced wall currents. This integrated framework allows for a flexible choice of either fixed or free boundary conditions for individual toroidal harmonics, providing comprehensive modeling capabilities for plasma-wall interactions.

The spatial discretization in JOREK relies on a mixed numerical representation of the plasma domain, in which the poloidal (R, Z) plane is discretized with **two–dimensional Bézier finite elements**, while the toroidal direction ϕ is treated through a **real Fourier expansion**. This formulation is particularly suited for tokamak geometries, where the magnetic configuration is predominantly axisymmetric and where strong gradients and transport structures are often aligned with magnetic flux surfaces. Bézier finite elements provide high-order continuity and geometric flexibility, allowing an accurate description of the plasma region, including separatrices, X-points, private flux regions and scrape–off layer domains. Different initial mesh layouts may be employed depending on the physical configuration, such as rectangular grids, simple polar grids, or polar grids with a rectangular central region, which are often used to obtain an initial equilibrium before constructing a flux-surface-aligned grid for higher numerical accuracy.

In the toroidal direction, all physical variables are expanded into cosine and sine Fourier components, and the number of retained harmonics is controlled by the parameter.n_{tor}.

Because the $n = 0$ mode contains only a cosine term, n_{tor} is required to be an odd integer. The code also allows the specification of a toroidal periodicity factor n_{period}, which enforces symmetry over a fraction $1/n_{period}$ of the full toroidal domain. In this case, only the harmonics $n = k \cdot n_{period}$ are included in the expansion, reducing the computational cost in configurations that naturally exhibit a repeated toroidal pattern. A more comprehensive overview of JOREK model is reported in [76].

4.5 DTT STARWALL-JOREK model building

Therefore, the first step was to reconstruct the STARWALL model and the FEM grid starting from the DTT IMAS data. Figure 105 shows:

- The STARWALL model including all the active and passive conductors, consistent with the integrated pf_active and pf_passive ids.
- The FEM grid defines the plasma domain, with its outer boundary located close to the IMAS wall outline. Due to the specific mathematical formulation of the finite-element grid, constructing an outer boundary that perfectly matches the DTT IMAS wall would be extremely difficult and time-consuming. Moreover, for the purposes of this work, the slight increase in simulation accuracy obtained with a more realistic boundary would not justify the effort required to implement it

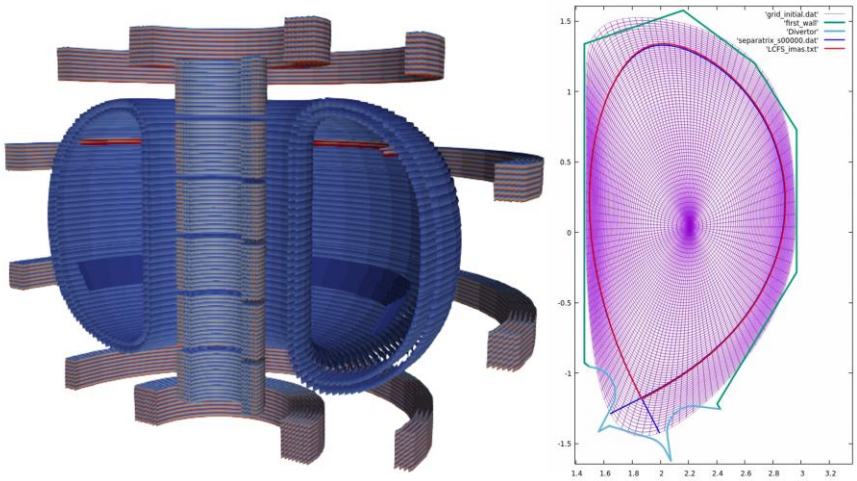

Figure 105 DTT STARWALL model (left)-FE grid and Separatrix computed through free boundary equilibrium with JOREK and LCFS integrated in IMAS (right)

All the JOREK required profiles have been directly translated from the IMAS ids, with automatic routine.

Therefore, the reference scenario used for JOREK was the Single Null at full power integrated in IMAS. The computed free boundary equilibrium results were in very good agreement with the IMAS integrated data. As proof of that, figure shows the overlapping between the separatrix result of the free boundary equilibrium and the Last Close Flux Surface (LCFS) integrated in IMAS (Figure 105).

4.6 DTT JOREK unmitigated disruption

The first disruption scenario computed was an unmitigated Downward Vertical Displacement Event (DVDE).

The general inputs for the disruption evolution were:

- Plasma pulled downward by setting an impulsive $5\ ms$ $200\ A$ overcurrent on the PF6
- Thermal quench triggered once q_{95} reaches a value of 2 (meaningful from the physic point of view) [79].

Therefore, after setting the input conditions for the disruption evolution, the scenario resulted in a unmitigated DVDE with a τ_{CQ} (current quench time) of roughly $50\ ms$.

Figure 106 includes the overtime evolution of the total thermal energy content of the plasma. It can be clearly seen that the total thermal energy drops once the q_{95} reaches the value of 2 (Thermal Quench).

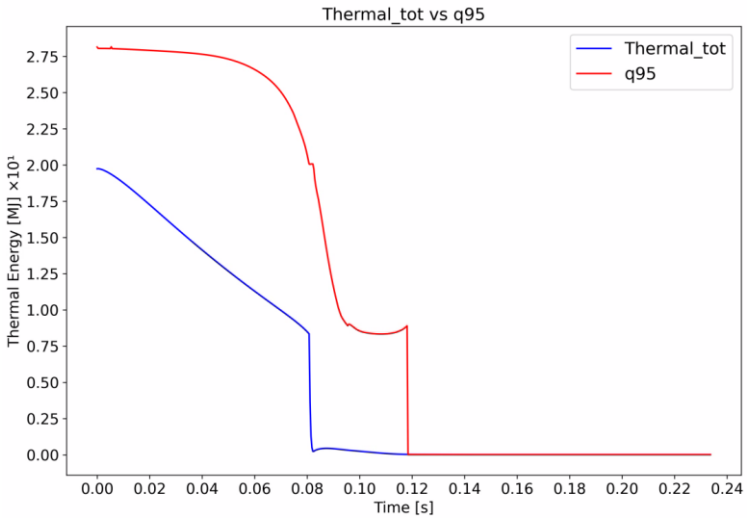

Figure 106 Unmitigated DVDE total thermal energy and q_{95}

Figure 107 shows the overtime evolution of the 2D electron temperature, until the thermal quench happens ($82\ ms$).

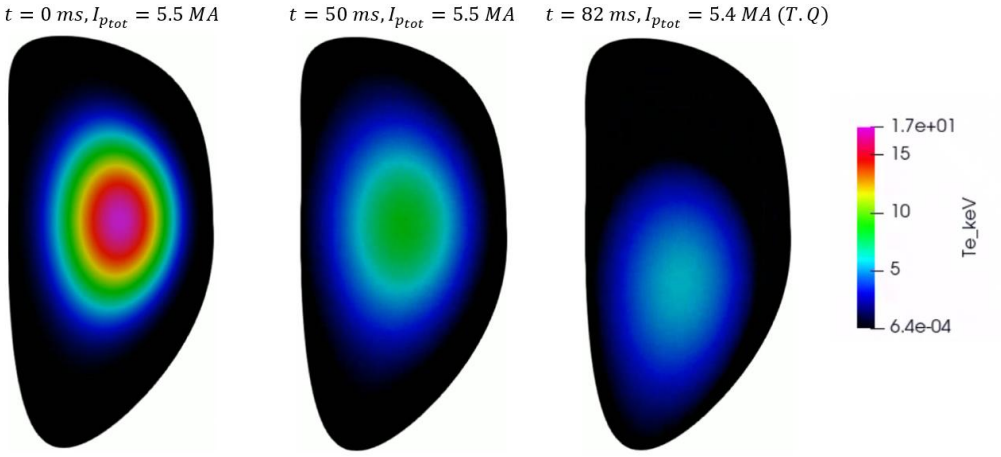

Figure 107 Unmitigated DVDE 2D contour of temperature evolution

Figure 108 shows the toroidal current density (J_{tor}) evolution and as can be seen from the contour, at the thermal quench, the current spreads from the core of the plasma to the scrape of layer (SOL), determining the generation of HALO currents on the wall [60].

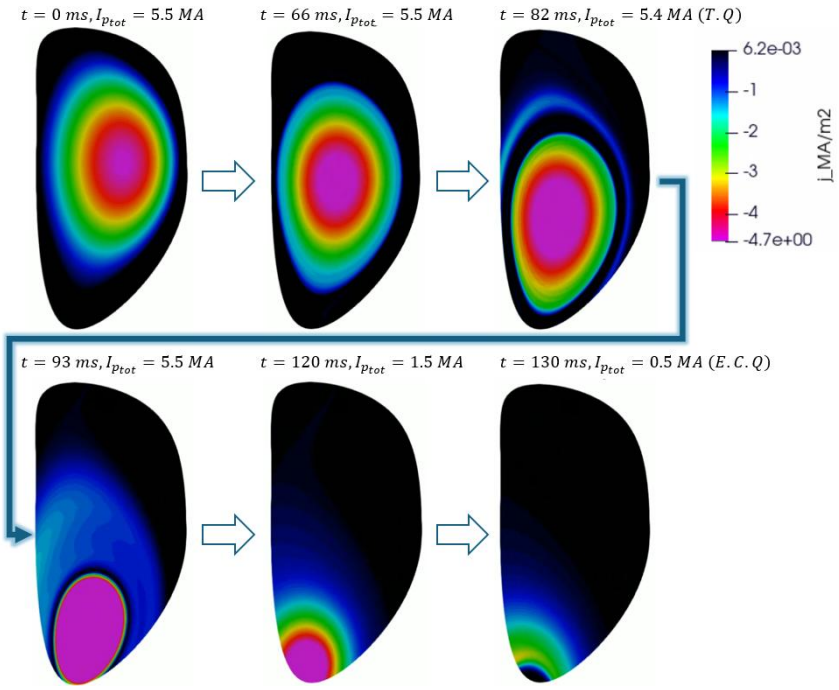

Figure 108 Unmitigated DVDE 2D contour of toroidal current density evolution

Figure 109 reports the evolution of the radial and vertical position of both the magnetic axis and the current center. Around $120\ ms$, the vertical coordinate of the magnetic axis appears to

drift upward; however, this behavior has no physical meaning. After this time, no plasma remains in the domain, and the model therefore attempts to locate the minimum of the poloidal magnetic flux, normally associated with the magnetic axis, somewhere else.

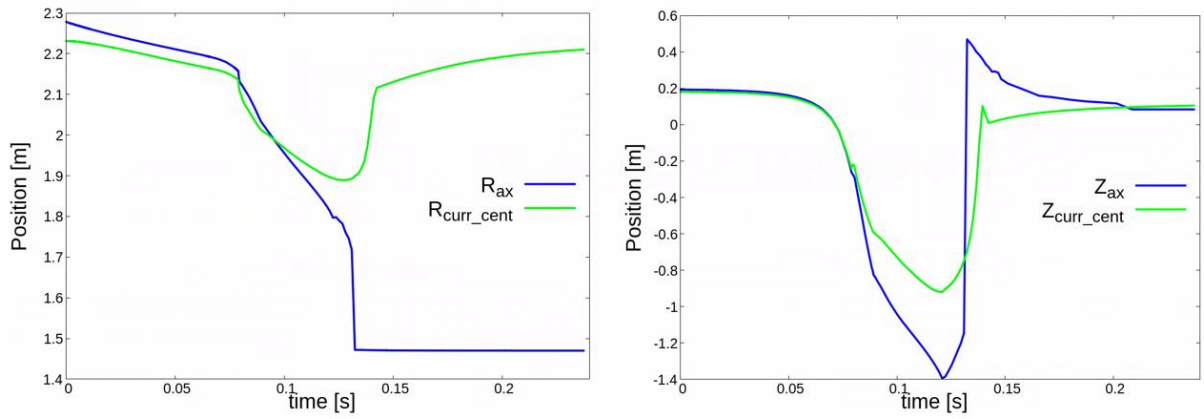

Figure 109 Unmitigated DVDE Radial and vertical position of the magnetic axis and the current center

As said, the disruption was characterized by a current quench lasting 50 ms. The current quench time τ_{CQ} is defined according to the ITER disruption characterization as a linear extrapolation of τ^{80-20} ,time of the plasma current decay from 80% to 20% of Ip before TQ [80].Therefore $\tau_{CQ} = 1.67 \cdot \tau^{80-20}$. Figure 110 shows the profile of total plasma current and HALO current. The HALO reaches a peak of $\cong 3\ MA$ that is roughly 55% of the total plasma current before the thermal quench and is entirely reasonable as max amount [81].

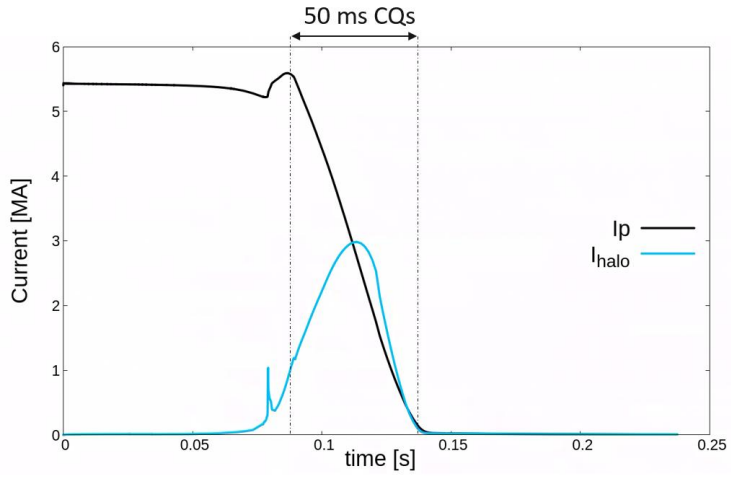

Figure 110 Unmitigated DVDE Total plasma current and HALO current profiles

4.7 DTT JOREK mitigated disruptions

4.7.1 Mitigated UVDE

An additional step was taken by simulating a mitigated disruption, even though the initial operational phase of the DTT machine does not include any active Disruption Mitigation System (DMS), either via Massive Gas Injection (MGI) or Shattered Pellet Injection (SPI) [82]. While future stages of DTT will certainly explore disruption mitigation, for design purposes a mitigated disruption poses a significantly lower challenge compared to an unmitigated event, both in terms of heat fluxes and electromagnetic loads on the structure [83]. Nonetheless, the effort to simulate a mitigated disruption with JOREK was carried out in order to further validate the DTT JOREK model and to allow a direct comparison with the previously described unmitigated disruption case.

Mitigation techniques, such as impurity injection, fundamentally alter the energy dissipation mechanisms during a disruption, thereby reducing thermal loads and redistributing them more evenly.

Unmitigated Disruptions:

[1] **High and Localized Thermal Loads**: The thermal energy is primarily deposited in a highly localized manner, leading to very high heat fluxes on limited areas of plasma-facing components. This is especially true if the fraction of radiated energy is low [60].

- **High Post-TQ Temperatures**: Plasma temperatures can remain elevated (several tens to hundreds of eV) post-TQ, increasing the potential for significant heat deposition [60].
- **Strong Electromagnetic Forces**: Slow current quenches in unmitigated scenarios lead to larger vertical displacement and electromagnetic forces due to halo and eddy currents, as well as toroidally asymmetric forces [60].

Mitigated Disruptions:

- **Distributed Thermal Loads**: Impurity injection, such as with Neon, rapidly cools the plasma through radiation, leading to a high radiation fraction [85]. This distributes the thermal energy more broadly throughout the vacuum vessel, reducing localized heat

fluxes. The goal is to achieve a uniform deposition onto the plasma facing components of the pre-TQ thermal energy Hoelzl et al., 2021.

- **Lower Post-TQ Temperatures**: Mitigated disruptions typically result in post-TQ temperatures that are significantly lower (a few to tens of eV) [85].
- **Reduced and More Symmetric Electromagnetic Forces**: The low temperatures induced by impurities lead to resistive current diffusion, which broadens the current profile, increases , and promotes toroidal symmetry [85]. This reduces halo currents and improves toroidal symmetry, preventing the formation of modes that lead to sideways forces. A faster current quench time (if optimized) can minimize both eddy and halo currents [85]

In summary, mitigation aims to transform a scenario of intense, localized, and potentially damaging energy deposition into one where energy is radiated and dissipated over a larger volume and time, thereby protecting the integrity of the tokamak's critical components [86]

In this simulation, Neon impurity injection was employed as a mitigation technique. The **Neon impurity density** was set to and introduces as uniform value of $10^{20}m^{-3}$ the simulation grid. The thermal quench was specifically triggered at the very beginning of the simulation, set to occur when the safety factor (q_{95})dropped below a value significantly greater than two, effectively ensuring an early onset.

To actively control the plasma's position, as done for the unmitigated case, a overcurrent kick was specified on the PF6 coil current, intended to drive the plasma downwards. However, despite this active control effort, the disruption ultimately resulted in an upward displacement. This occurred because the rapid plasma evolution and displacement, triggered by the impurity injection, proceeded on a timescale much shorter than the penetration time of the magnetic perturbation from the PF6 coils through the resistive vessel structures. The vessel effectively shielded the plasma from the magnetic kick; the magnetic field perturbation could not reach the plasma with sufficient strength and speed to counteract its swift upward motion. Thus, the scenario resulted in a mitigated Upward Vertical Displacement Event (UVDE). The characteristic resistive time scale of the vessel, which can be around 500 ms for ITER-like parameters Hoelzl et al., 2021, was substantially longer than the plasma's inherent displacement timescale, rendering the PF6 kick ineffective in achieving the desired downward control.

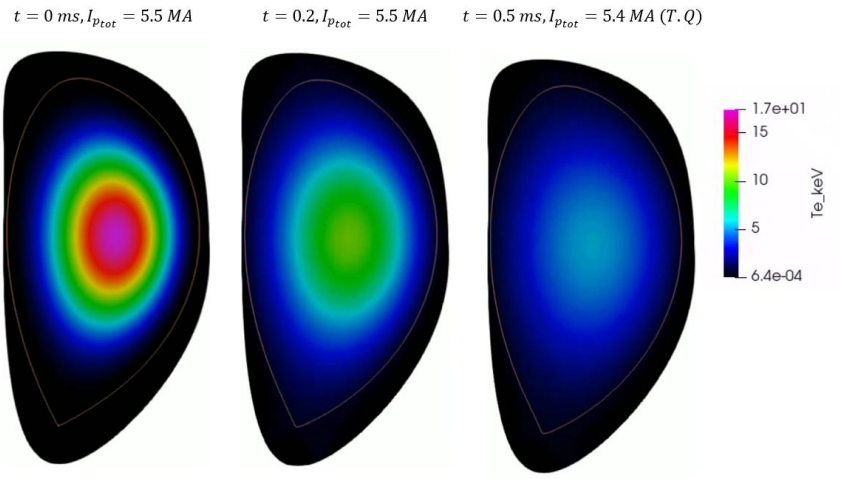

Figure 111Mitigated UVDE 2D contour of the electron temperature

Figure 112 shows the evolution of the current density on the grid. As can be clearly seen, the time scale evolution (both for current and displacement of the plasma) is much smaller compared to the unmitigated case (Figure 114).

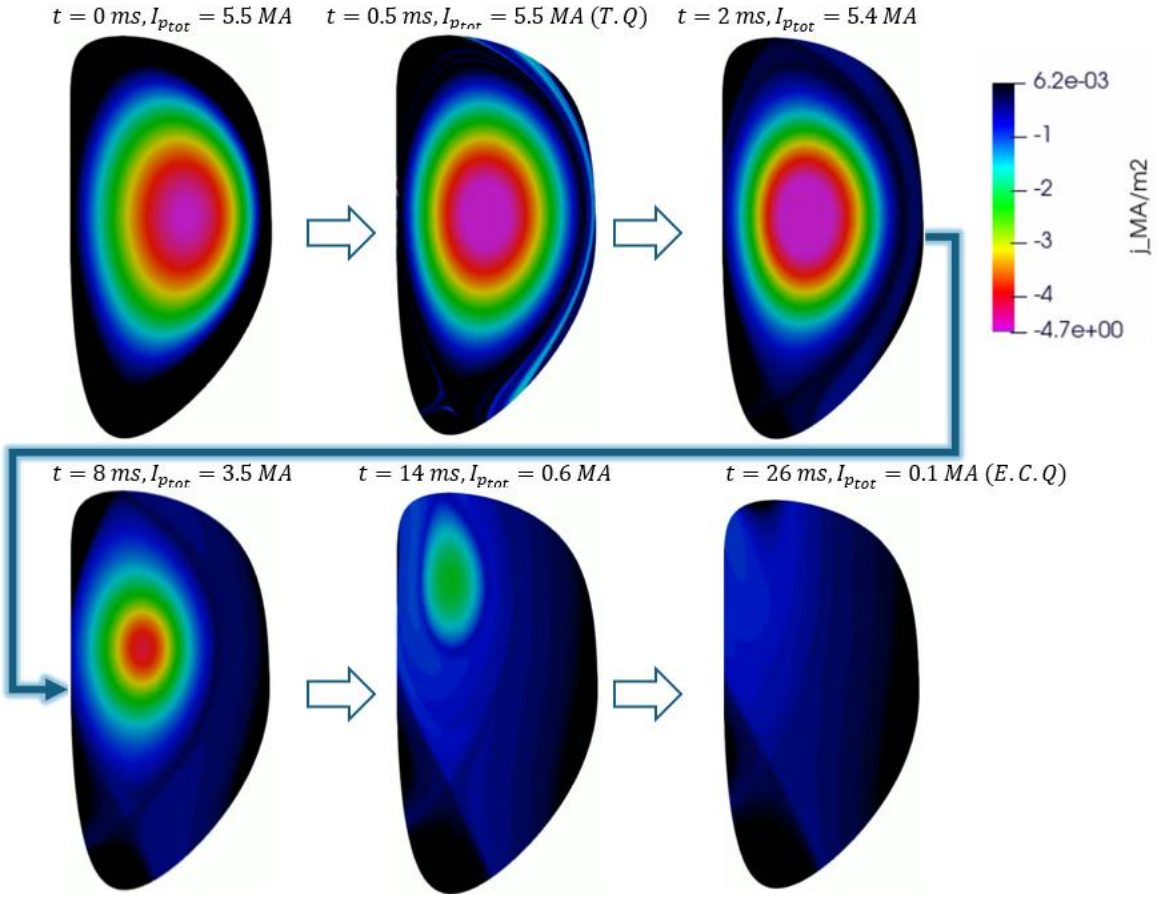

Figure 112 Mitigated UVDE 2D contour of the toroidal current density (J_t) (it's clear that the time scale of the event is much smaller if compared to the unmitigated case)

Figure 113 includes the main global quantities associated with the event. As expected, the HALO current is lower than in the unmitigated case, since the current quench occurs very rapidly while the plasma is still far from the walls (Figure 115). It should be noted that the observed peak in HALO current of 1.6 MA is a direct consequence of the thermal quench. Its physical relevance remains uncertain and is likely just a numerical artifact consistent with the simulation model rather than a meaningful physical effect.

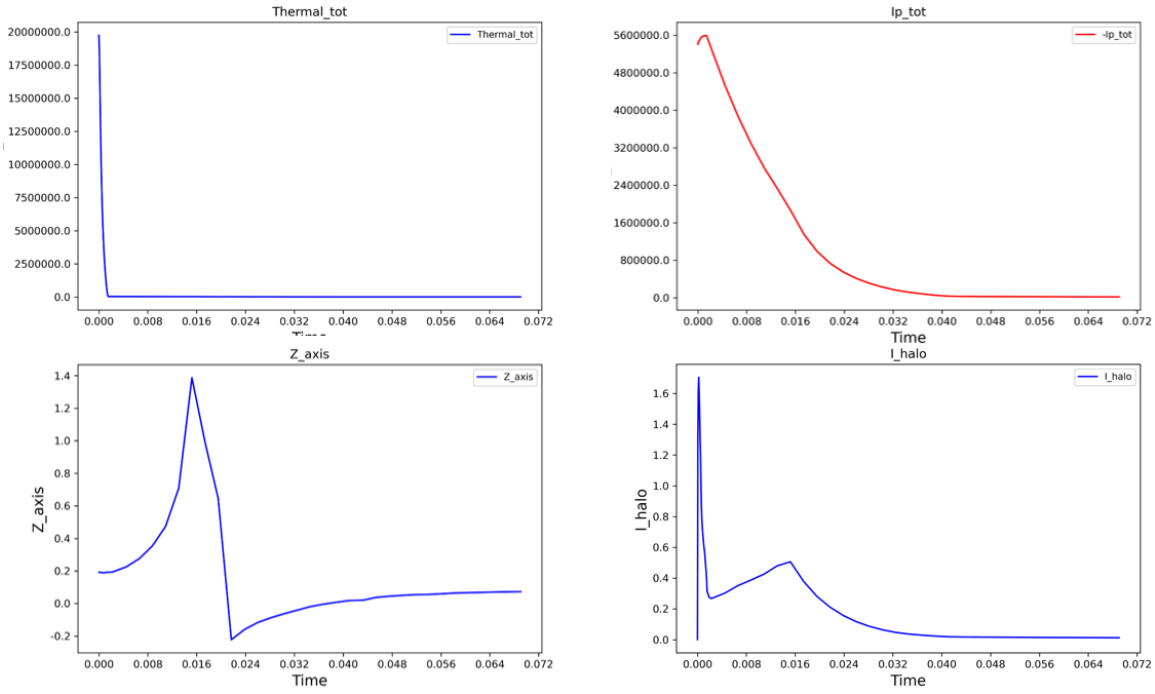

Figure 113 Mitigated UVDE main plasma global quantities

The disruption was characterized by a current quench of roughtly 24 ms, as expected lower than the current quench duration predicted with JOREK for the unmitigated scenario.

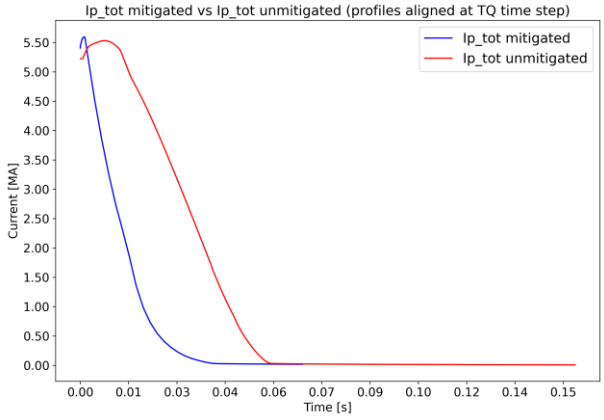

Figure 114 Unmitigated DVDE-mitigated UVDE total plasma current comparison

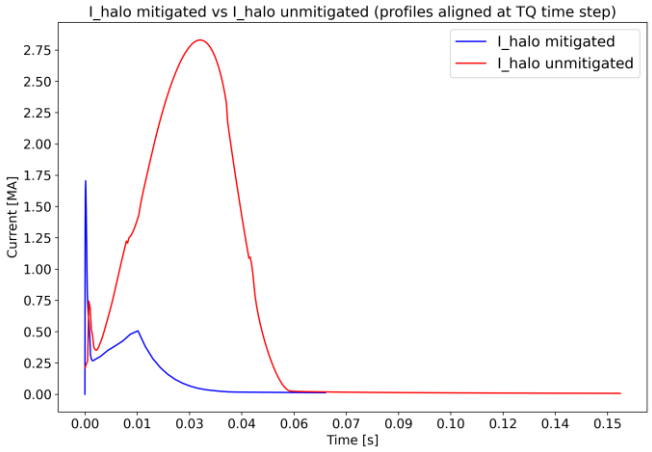

Figure 115 Unmitigated DVDE-mitigated UVDE halo current comparison

In this case, the comparison between plasma current and HALO current is of limited significance, since the unmitigated disruption corresponds to a downward event whereas the mitigated one is upward. The next case to be analyzed will be the mitigated downward disruption.

4.7.2 Mitigated DVDE

To effectively simulate a downward disruption and circumvent the timescale issue previously encountered with the vessel's shielding effect, the analysis was initiated from a specific time instant within an unmitigated disruption scenario. At this chosen starting point, the plasma was already significantly displaced downwards.

This pre-displaced state served as the new initial condition for the mitigated downward disruption simulation. Consistent with previous mitigation attempts, a $10^{20} m^{-3}$ Neon impurity density of was introduced, and the thermal quench was induced immediately at the onset of this simulated event (Figure 119).

From Figure 116, it can be seen that the disruption is downward; in fact, the magnetic axis shifts progressively downward, then returns to a position determined by the code but with no physical significance, since, as previously highlighted, the code searches for the minimum poloidal magnetic flux point (relative to the plasma magnetic axis) at around 100 ms, but the plasma is no longer present. Therefore, the vertical position is simply the result of a numerical solution, not a physical one

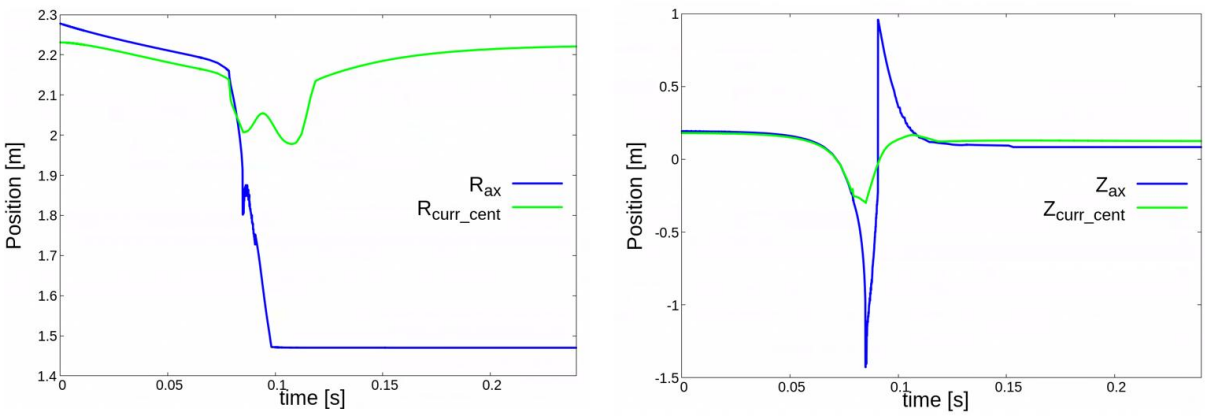

Figure 116 Mitigated DVDE radial and vertical position of the plasma magnetic axis and current center

When comparing the total plasma current evolution with that observed during the computed unmitigated downward Vertical Displacement Event, the current quench duration in the mitigated case is shorter, approximately 20 ms (Figure 122). As you can see, differently from the upward scenario, since at the starting point the plasma was alredy displaced downward, the thermal quench occurs while the plasma is closer to the wall (Figure 117).

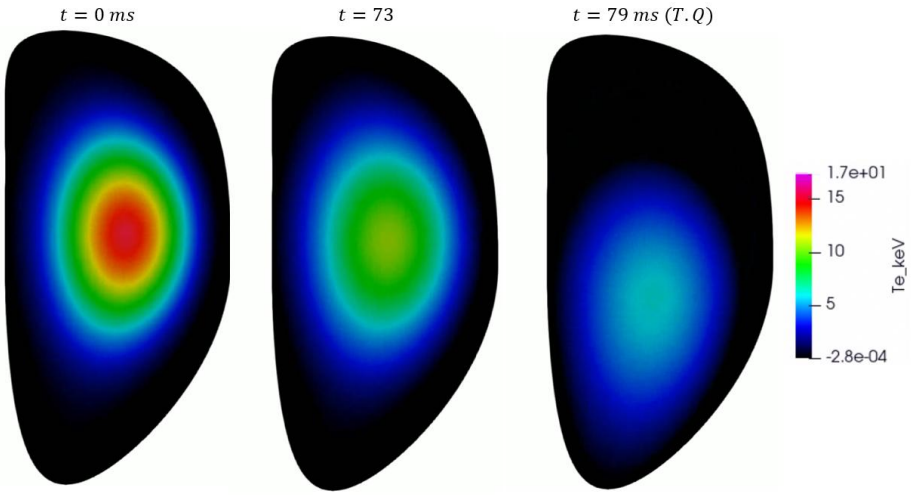

Figure 117 Mitigated DVDE 2D contour of the electron temperature

Unmitigated disruptions typically exhibit longer and less controlled current decay. The faster termination of the current quench in the mitigated case is linked to the low temperatures produced by radiating impurities, which increase resistive current diffusion and accelerate plasma current decay.

In Figure 118 is shown the evolution of the plasma toroidal current density during the event.

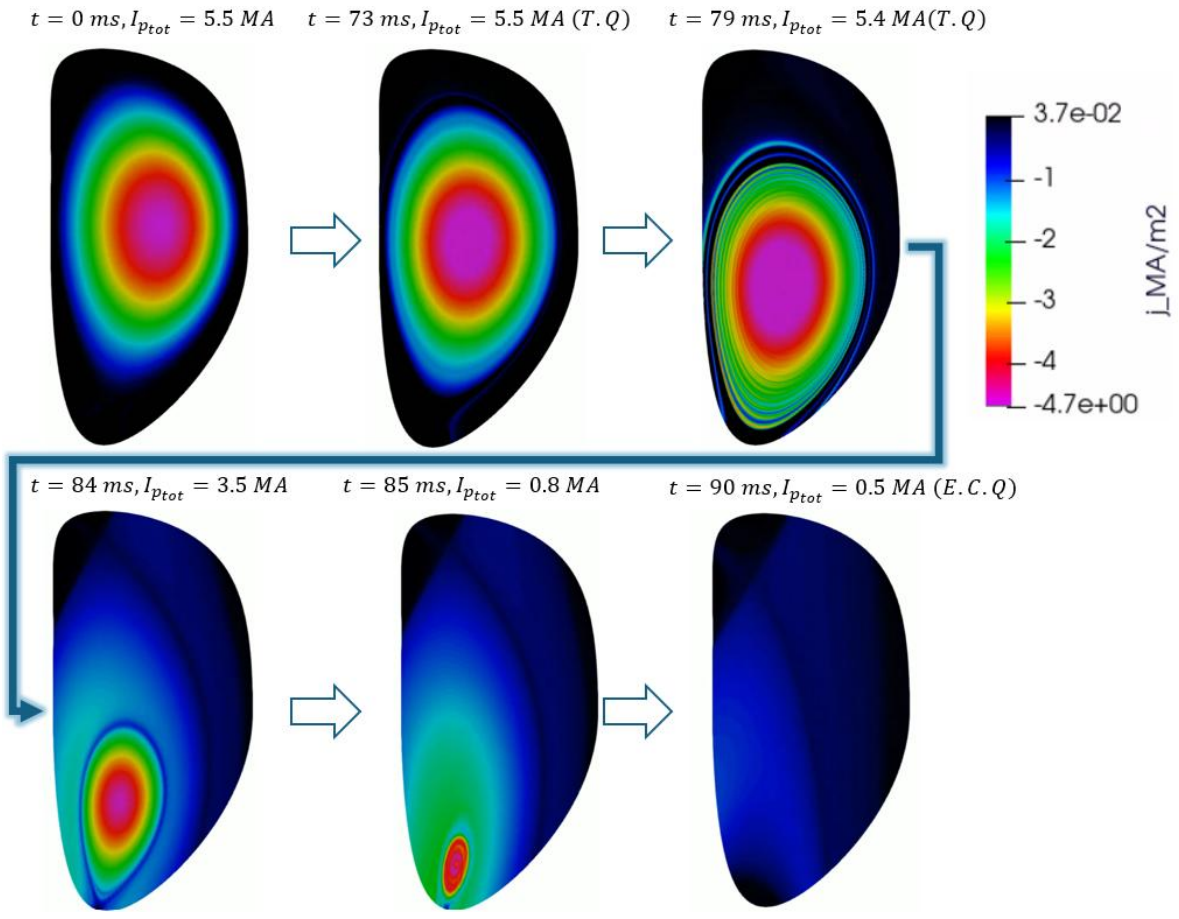

Figure 118 Mitigated DVDE 2D contour of the toroidal current density (J_t)

The total halo current is also reduced in the mitigated downward disruption. In this simulation, a peak halo current of about $1.2\ MA$ is observed, compared to roughly $3\ MA$ in typical unmitigated events (Figure 122).

This reduction is associated with impurity injection, which leads to low temperatures and resistive current diffusion beyond the Last Closed Flux Surface. This process increases the safety factor without requiring MHD activity and supports improved toroidal symmetry (Figure 120) [79].

By broadening the halo region and promoting toroidal symmetry, impurity-based mitigation contributes to a decrease in poloidal halo currents and lowers the likelihood of asymmetric loads. Simulations with JOREK suggest that the ITER Disruption Mitigation System may reduce halo-current-related electromagnetic loads by more than a factor of two compared to their maximum potential values [87] [76].

These findings indicate that an optimized mitigation strategy, even when initiated from a pre-displaced plasma state to address intrinsic timescale limits, can reduce the overall severity of plasma disruptions [89].

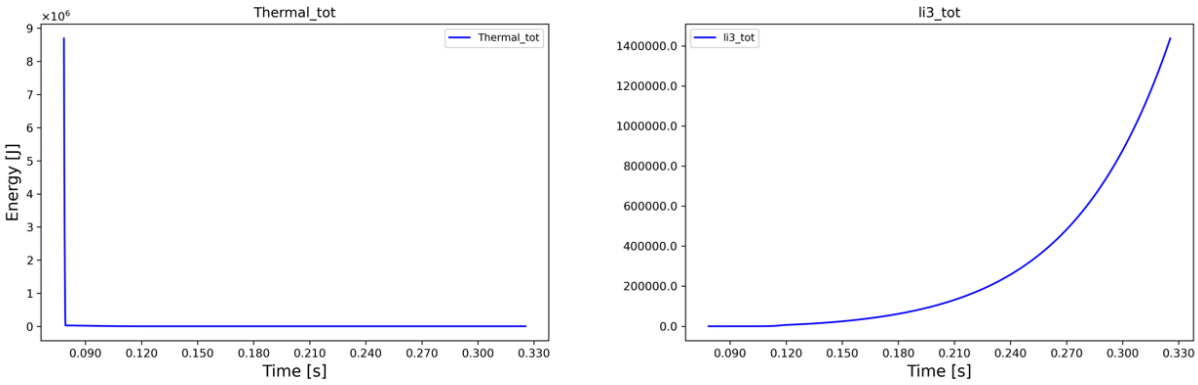

Figure 119 Mitigated DVDE plasma total thermal energy and internal inductance

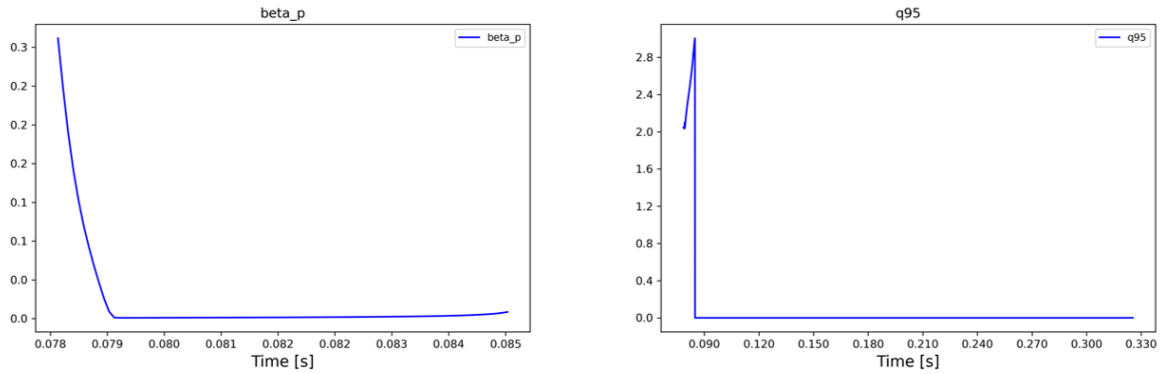

Figure 120 Mitigated DVDE poloidal beta and edge safety factor

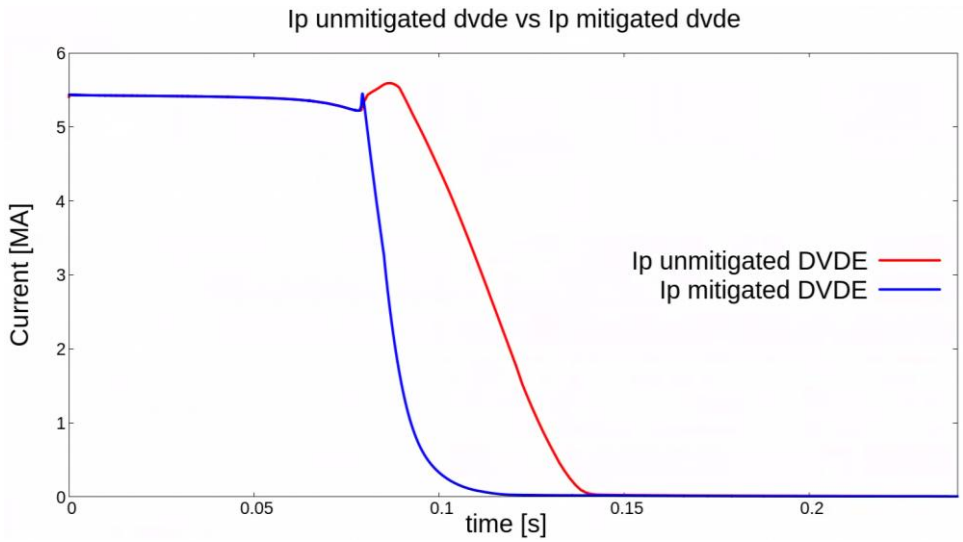

Figure 121 Unmitigated DVDE-Mitigated DVDE total plasma current comparison

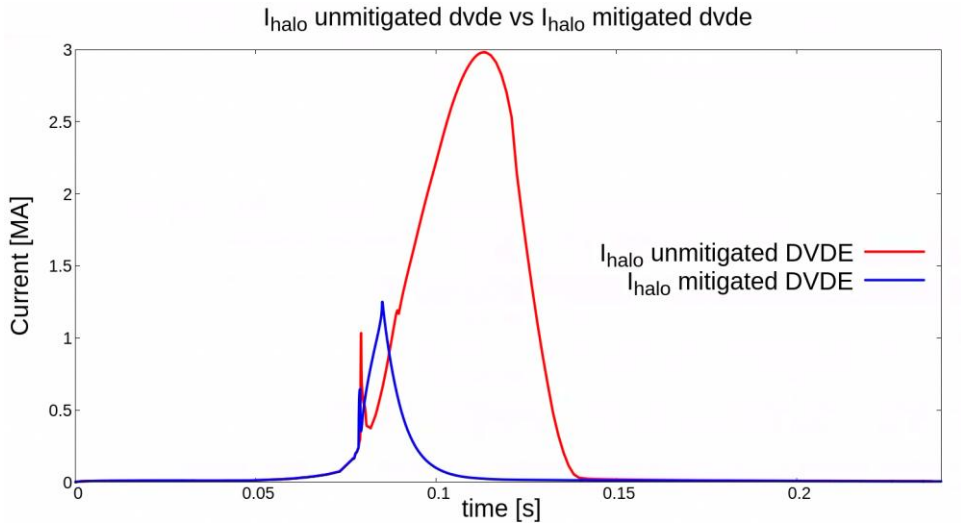

Figure 122 Unmitigated DVDE-Mitigated DVDE halo current comparison

4.8 JOREK – maxFEA Unmitigated Downward Vertical Displacement Event results comparison

The work performed with JOREK, as mentioned several times, was aimed at validating the disruption simulations carried out with maxFEA, whose results were subsequently used as input for electromagnetic simulations of the Lorentz forces acting on the DTT divertor during the most critical disruption events. In particular, JOREK was used to benchmark global quantities such as total plasma current, halo current, plasma magnetic axis displacement, and poloidal beta, all obtained from maxFEA . The whole workflow for DTT maxFEA disruption simulation is omitted and details about the code framework can be found in [88].S

Regarding both heat flux and electromagnetic force distribution, the unmitigated scenarios are the most demanding. Focusing on the divertor, downward events are particularly challenging, as the plasma interaction is concentrated near the divertor while still carrying a significant amount of energy. To validate maxFEA disruptions, the same reference scenario ((Figure 123) Single Null at full power : $I_p = 5.5MA, B_{T_{axis}} = 6\ T$) was used as the starting point for both codes, and a downward disruption was simulated with maxFEA. The main parameters were thoroughly discussed during the analysis of the DTT data integration into IMAS and were reported in Table 14.

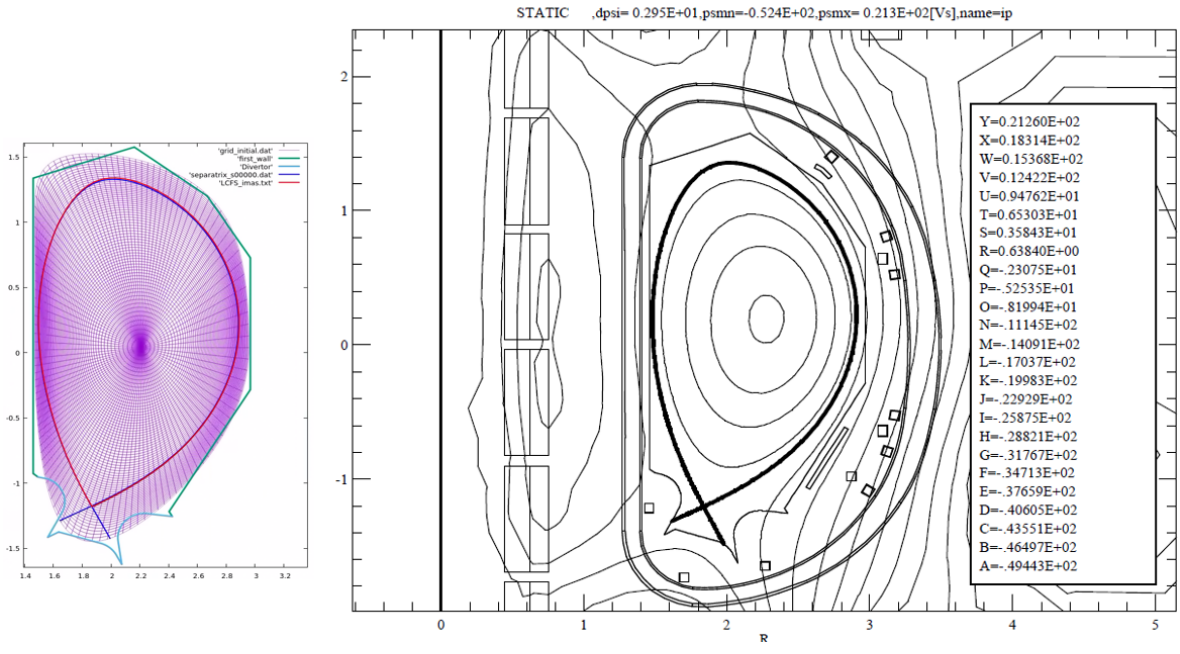

Figure 123 (left)Reference JOREK equilibrium LCFS – (right) Reference LCFS maxFEA equilibrium

To reproduce the same plasma displacement timescale—especially before the thermal quench—the overcurrent kick applied to the lower PF (PF6), consistent with the JOREK setup, had to be increased to $600\ A$, since $200\ A$ (set as current kick to run the JOREK unmitigated DVDE) resulted in a plasma drift toward the wall that was too slow.

The maxFEA simulation produced a downward event with a current quench timescale (τ_{CQ}) of $50\ ms$, fully consistent with JOREK predictions. The thermal quench trigger was imposed once q_{95} reached 2, as in JOREK. Additionally, since halo currents in maxFEA can be activated at a chosen moment during the plasma evolution, they were set to begin flowing into the wall once the plasma reached a limiter configuration. The total plasma current profiles show excellent agreement both in terms of timescale and absolute values, demonstrating the reliability of the maxFEA simulations (Figure 124).

It should be noted once again that JOREK provides highly predictive and extremely accurate results, thanks to the wide range of physics phenomena included in the code. In contrast, maxFEA offers fast and robust estimates of the main electromagnetic quantities, although its solver does not fully account for all the transport processes involved in plasma evolution. Nevertheless, the overlay of the profiles confirms once more that the assumptions and results obtained with maxFEA can be considered accurate with respect to the plasma's global quantities.

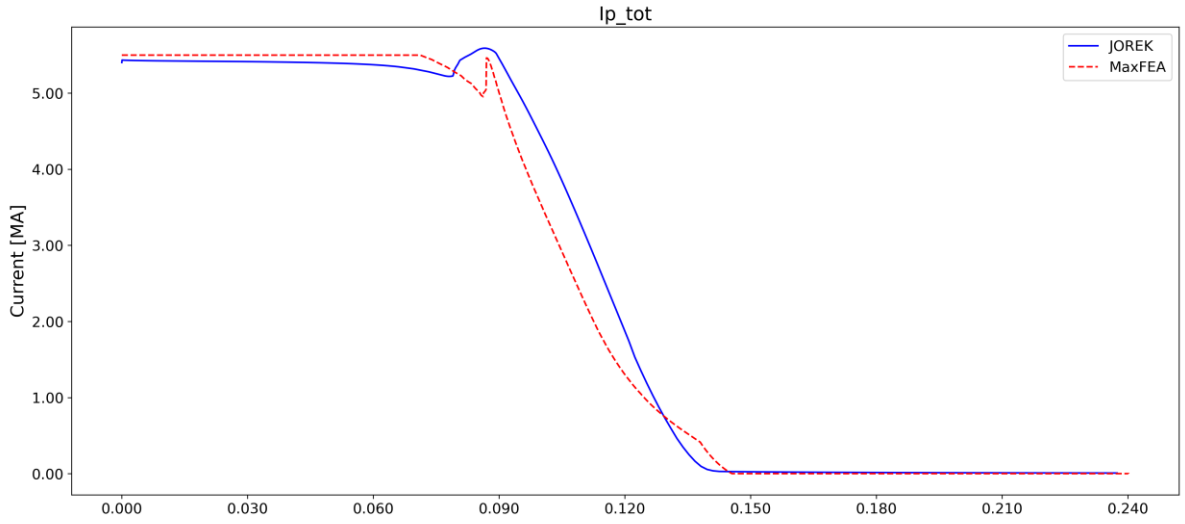

Figure 124 Total toroidal plasma current comparison between maxFEA and JOREK unmitigated DVDE

The same applies to the halo current: the curves from both codes are very close to each other. It should be noted that, in the case of maxFEA, the halo current exhibits a sudden increase due to the specific settings applied during the analysis.

As previously mentioned, the halo current was set to start flowing once the plasma reaches a limiter configuration, while it is completely neglected beforehand. In both simulations, the halo current peak consistently reaches approximately 3 MA, corresponding to roughly 55% of the total plasma current prior to the thermal quench.

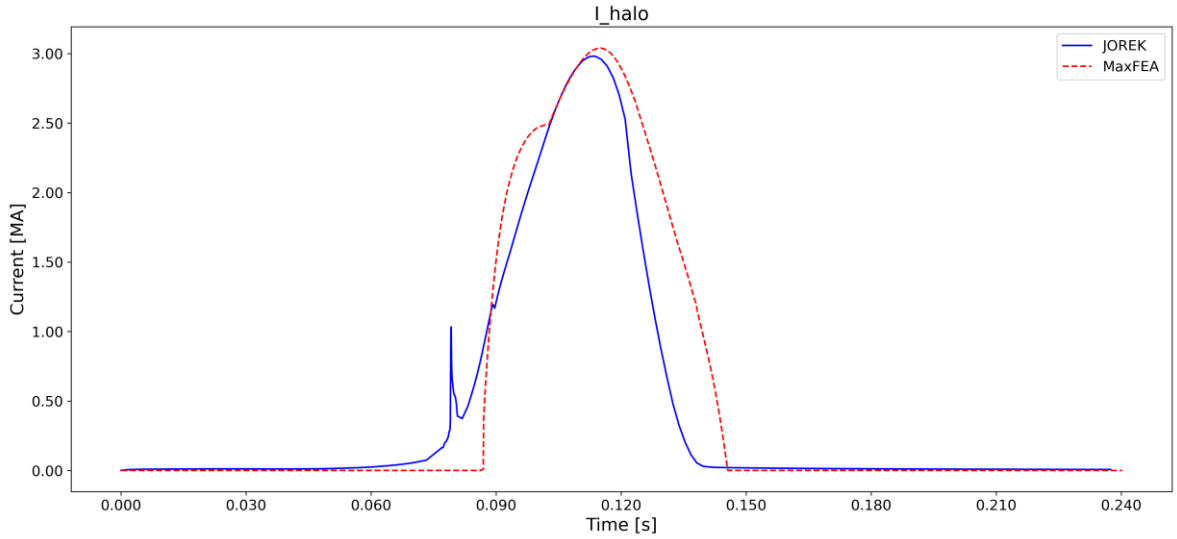

Figure 125 Halo current comparison between maxFEA and JOREK unmitigated DVDE

Very good agreement is also observed in the time evolution of the vertical and radial coordinates of the plasma magnetic axis (Figure 126), as well as for the safety factor q_{95} (Figure 127). The only notable discrepancy concerns the internal inductance, which differs significantly between the simulations.

This difference could be related to the distinct formulations used by the two codes to compute the internal inductance li_3, or it may arise from the fact that the internal inductance reported by maxFEA during post-processing could be defined differently from that in JOREK. The comparison between these quantities is included in.

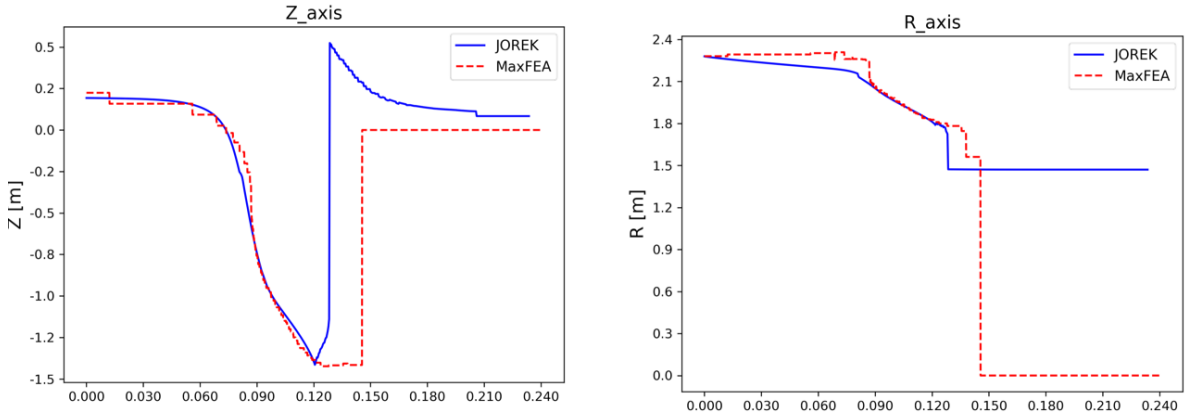

Figure 126 JOREK-maxFEA unmitigated DVDE R_{axis} and Z_{axis} comparison

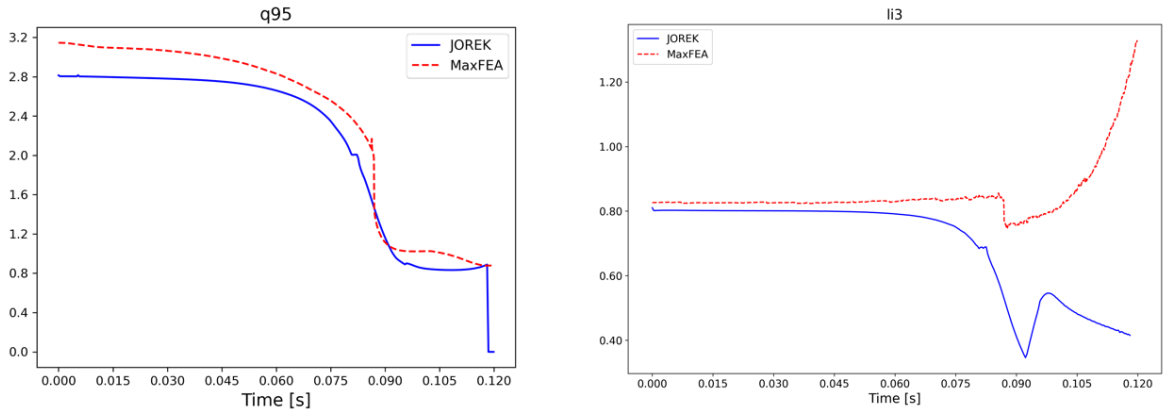

Figure 127 JOREK-maxFEA unmitigated DVDE q_{95} and li_3 comparison

5 DTT Divertor Cassette Body structural verification

5.1 Preload assessment

Before delving deep into the analysis details, a premise is necessary. The preloading role is complex and involves several engineering and physical aspects. Said that, for its determination, in this work three aspects have been taken in account:

- The preload must counteract the effect of the EM loads induced by loss of plasma confinement
- The preload has to ensure that, under each load configurations (in particular during major VDE) the engagement of the divertor and its supporting structures is guaranteed.
- The preload has to compensate the effects of different thermal expansion between vessel and divertor

Therefore, considering the time history load (EM forces resultants on CB and forces resultants on VTs and Dome(Figure 128)) of a slow DVDE ($40\ ms$), several trials have been done to understand which preload value could be more effective for the mentioned purposes.

Figure 128 EM forces resultants on Divertor Cassette body(left) and PFCs (right) induced by $40\ ms$ *major DVDE*

In particular the force reaction of the contact between nose and inboard rail, along the preload direction has been investigated. The preload value which ensured that the force reaction component of the nose along the preload direction was always opposite to the preload during the whole analysis time (and therefore the nose keeps contact with the inboard rail) was $20\ kN$. Therefore, the described analysis is related to a preload of $20\ kN$, which is the actual baseline value. The results in term of nose force reaction are reported in this section.

A dummy knuckle pin has been modeled to properly simulate knuckle engagement on the divertor cassette body after the preloading phase.

In fact, the preloading force induces on the cassette body a maximum directional displacement (due to the compression/bending of the structure) which has been estimated to be of $4.8\ mm$ using a preload value of $20\ kN$.

To properly simulate the preloading phase, in SpaceClaim, the distance between inboard and outboard rail has been reduced by this value.

During this procedure, the divertor cassette has been constrained to the supporting structures in accordance to the expected kinematic. Therefore, the geometry used as starting point for the analysis, had the dummy pin not aligned with their mounting holes as can be seen in Figure 129. Once the preload action is exerted (through a joint load which will be described later) the pins align and the contact imposed between them and their holes activates.

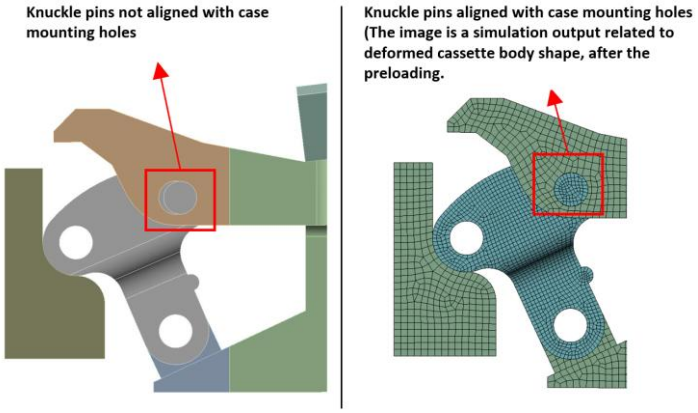

Figure 129 Knuckle pins not aligned (left picture); Knuckle pins aligned (right picture

The forces resultants have been applied as nodal forces, therefore the moments with respect to the center of the machine are not coincident with the moment of the EM force distribution output of the EM analysis (since in our case the forces are uniformly distributed between the nodes).

Anyway, the order of magnitude of the moments generated by the forces set on the structural nodes is absolutely equal to the order of magnitude of the moments generated by the real EM force distribution (with respect to the origin of the machine) and so are their signs.

Figure 130 shows the time plot of the X force reaction (preload direction) of the frictional contact between nose and inboard rail.

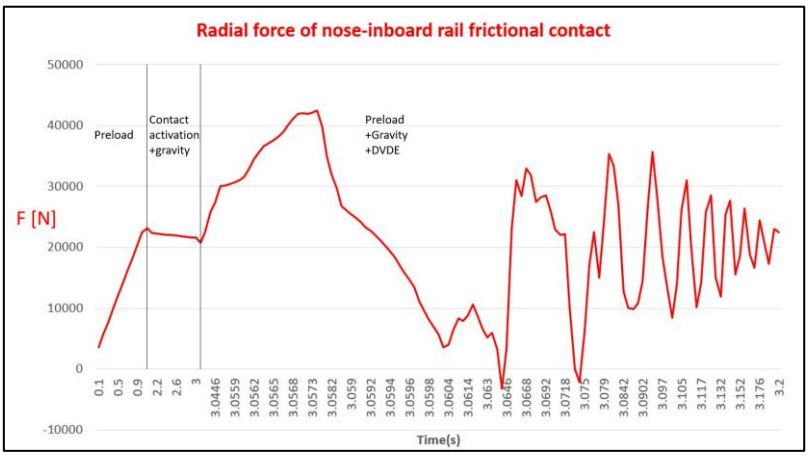

Figure 130 $F(x)$(radial) nose constraint reaction

As can be seen, just during few instants of time the force reactions is slightly below zero. This result should not be misleading. In fact, although in those few instants of time the reaction has the same sign of the preload, the nose does not disengage thanks to the action of the hook which features.

In Figure 131 is shown the trend of the force reactions on the revolute joint imposed between knuckle outer hole and the inboard rail holes.

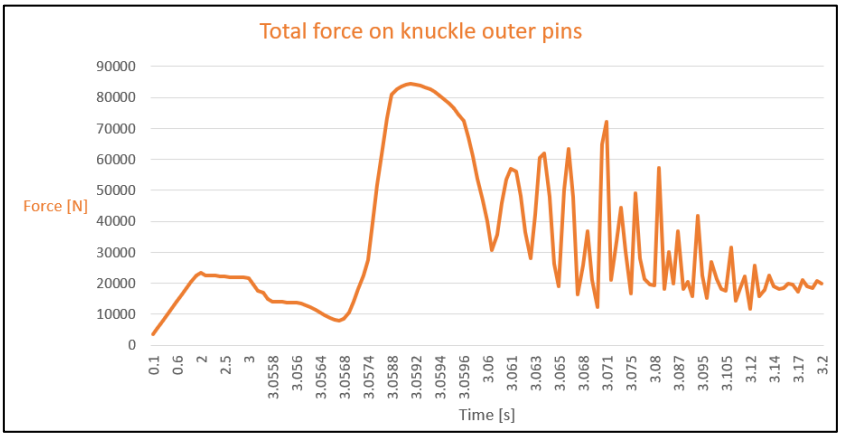

Figure 131 Knuckle outer pin total constraint force (joint reaction)

In the next analysis which will be presented, the reaction forces acting on knuckle pins are reported. These are higher than the overtime maximum value of 85340 N which occurs during the dynamic analysis described in this section. This is due to the constraining conditions of the

divertor used for the analysis presented in section 3.2 and also to the methodology used to apply the EM loads. Moreover, the effect of the preload seems to mitigate the constraint reaction acting on knuckle pin due to the EM loads. Therefore, the verification in section 3.2 (in which a lower preload value has been used) is more conservative and has been used for the dimensioning and verification of knuckle pins.

5.2 Structural assessment against operating and off normal conditions

5.2.1 Scope of the assessment

The structural verification of the divertor cassette body has been carried out using a 3D Finite Element Analysis (FEA) model, which provides sufficient spatial resolution and degrees of freedom to capture the mechanical behavior of the system under the defined load cases. The analysis has been carried out using Ansys Worbench 2024 R2 software.

The engineering model is designed to support the global assessment of the DTT Divertor Cassette body. As such, it is suitable for evaluating overall global structural behavior, but not for detailed analysis in regions of stress concentration or for capturing local responses. The type of analysis adopted is non-linear static analysis, which is consistent with the problem requirements. Non-linearity accounts for contact interactions (frictional and revolute), material behavior under large displacements, and preload conditions. This is adequate given the absence of transient dynamic phenomena in the current scope. Fatigue, dynamic, and ratcheting analyses are not included, as this analysis strictly focuses on static verification under operating conditions and worst-case disruption.

The verification carried out, from the results point of view, is focused on the assessment of the linearized stress in critical regions by defining Stress Classification Lines to probe the linearized stress occurring there. During the discussions of the results a detailed description of displacement, stress contour and linearized stress will be done.The scope of the present analysis is limited to a static structural assessment under the prescribed load conditions. The objective is to evaluate the primary stress response of the component, ensuring compliance with the allowable limits defined in SDC-IC.

The following assessment types are considered or excluded as follows:

- Static Assessment: ✓ Included — Primary stress evaluation under defined mechanical and pressure loads.

- Ratcheting Assessment: ✕ Excluded — Cyclic loading effects and progressive plastic deformation over repeated load cycles are not considered in this analysis.
- Fatigue Assessment: ✕ Excluded — Fatigue life evaluation due to repeated or fluctuating loads is outside the current scope.
- Dynamic Assessment: ✕ Excluded — Effects from transient, shock, or vibration loads are not included in this verification.
- Buckling assessment: ✕ Excluded — Effects from transient, shock, or vibration loads are not included in this verification.

5.2.2 Geometry included in simulation

The objective of the structural analysis performed on the DTT divertor cassette body is to assess its mechanical integrity under both nominal operating conditions and off-normal scenarios. The reference geometry used as input for the simulation encompasses the full assembly of subsystems that constitute the DTT divertor.

It is important to emphasize that the Plasma Facing Components (PFCs), the supports of the Plasma Facing Units (PFUs) to the back plates, the back plates of the PFCs, and the attachment systems connecting the cassette to the vacuum vessel—fall outside the direct scope of this structural assessment. Nevertheless, these elements have been retained in the simulation model to capture the comprehensive structural response of the assembly.

This modeling choice is aimed at preserving the fidelity of the analysis by preventing artifacts or inaccuracies that might arise from excessive simplification of the physical system. The geometry input of the simulation is shown in Figure 135. All the components included are consistent with the geometry used as input for the EM analysis. As already said, the DTT machine comprises 54 divertor cassettes, each anchored to the vacuum vessel via inboard and outboard fixation systems.

On the inboard side, a lower stop is included to prevent or mitigate toroidal displacement of the cassette during disruption events (Figure 132). It must be said that the divertor geometry included into the simulation is in its undeformed configuration, meaning that the knuckle interface holes and knuckle pins are not aligned yet.

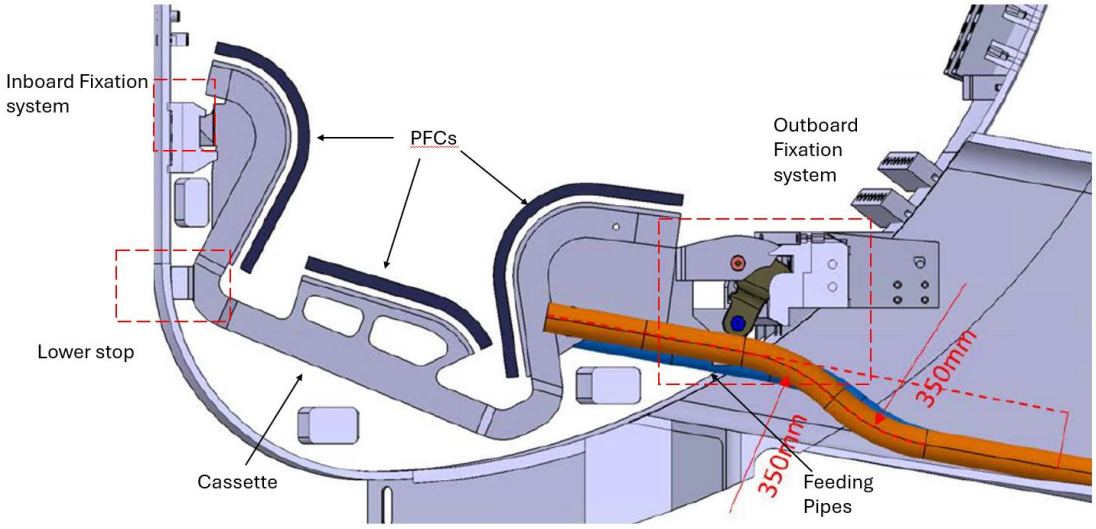

Figure 132 DTT divertor module and its interfaces

The interface system includes feeding pipes that supply cooling water to the cassettes, passing through the port where each cassette is installed. The starting point of the simulation is a single module of the DTT divertor cassette. This approach is justified by the fact that the DTT divertor system is not toroidally continuous: a minimum toroidal gap of 8 mm exists between adjacent cassettes (in proximity to the PFU lateral surfaces).

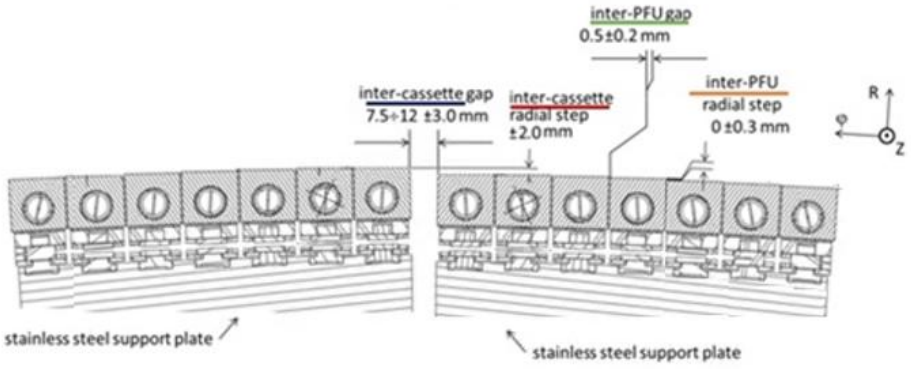

Figure 133 Minimum gap between two adjacent divertor modules

As a result, analyzing a standalone module under the most demanding load conditions is sufficient to characterize the mechanical behavior of the divertor cassette body. The interaction between adjacent cassettes is negligible due to the non-zero gap. It is important to note, however, that the 8 mm gap must never be closed — any contact between adjacent cassettes is undesirable. While this issue is not addressed in the present analysis, it is considered of

significant importance and should be investigated separately. Below are the reasons for excluding certain interface components from the present verification analysis:

- Vacuum vessel model excluded. The rationale about this choice will be soon detailed.
- The feeding pipes have been excluded from the model because they are connected through bellows, which accommodate thermal expansion and provide flexibility along both the pipe axis and the radial direction. As a result, they do not transfer any significant load to the divertor cassette

Other interfaces, such as the CMM interface, have been excluded as they do not contribute to the structural response of the system under either normal operating conditions or off-normal events. It is important to note that the thermal map applied in the final step of the structural analysis (See Loads) is derived from a steady-state thermal simulation, which considers the heat flux incident on the exposed surfaces of the cassette body. The thermal interaction between the Plasma Facing Units (PFUs) and the cassette body has been deliberately excluded from this assessment. This exclusion is justified, firstly, by the fact that such interaction falls outside the scope of the present structural verification, and more critically, by its primary relevance to the dedicated PFU design process.

Furthermore, it is assumed that the thermal decoupling between the PFU and the cassette body is physically sound under normal operating conditions. Specifically, the high velocity of the cooling water circulating within both the PFU cooling pipes and the internal channels machined into the cassette body ensures extremely efficient heat removal. As a result, the thermal gradient across each monoblock becomes negligible, and the temperature field stabilizes near the cooling water temperature within a short distance from the plasma-exposed surface—typically within the midsection of the PFU pipe.

Consequently, the supports of the PFUs, as well as the underlying structural elements of the cassette body, are assumed to remain thermally unaffected by the plasma interaction and the intense heat flux absorbed by the PFUs. This assumption allows the structural assessment to proceed without incorporating complex thermal coupling effects that would otherwise introduce minimal influence on the cassette body's mechanical response. Moreover, the differential thermal expansion between vessel and divertor has been neglected as well since both structures have the same temperature during normal operating conditions and baking,

furthermore they are mainly composed by the same material (except for the XM-19 steel employed for the central core of the cassette body shell). To further detail the issue, a preliminary check on the significance of an eventual loss of preload due to different thermal expansion is here reported. Taking in account an overall length of the divertor along the preload direction (Knuckle outer pin-Nose semispherical interface) of $L = 1200\ mm$, same assumed between inboard and outboard rail and considering the extreme case in which the whole divertor is made by XM-19 while the vessel is in 316L as well as the extreme case of baking condition consequent to the larger $\Delta T_{baking} = 250°C$ then it follows that:

$$\Delta l_{div} = \alpha_{XM-19} * \Delta T_{baking} * L_{tot} = 15.2 * 10^{-6} * 250 * 1200 = 4.56\ mm$$

$$\Delta l_{vv} = \alpha_{AISI316L} * \Delta T_{baking} * L_{tot} = 15.7 * 10^{-6} * 250 * 1200 = 4.7\ mm$$

$$\delta_{u_{div-vv}} = 0.14\ mm$$

The action exerted during the preloading phase displaces the outboard branch of the divertor of roughly 5 mm, therefore the stiffness along the preload direction can be estimated as follows:

$$K_{div} = \frac{Preload}{displacement\ along\ preload\ dir.} \cong \frac{20kN}{5\ mm} = 4\frac{kN}{mm}$$

Therefore, the loss of preload due to the relative displacement induced by the differential thermal expansion is:

$$\Delta Preload = K_{div} * \delta_{div-vv} = 800\ N$$

The engineering model integrates all the screwed connections included into the CAD model (Figure 134).

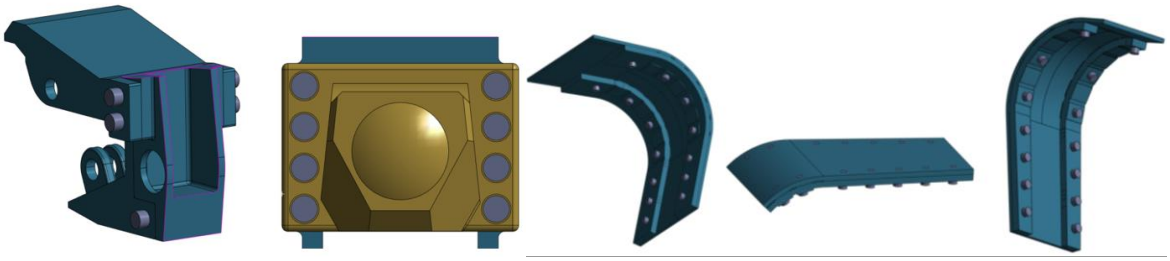

Figure 134 Bolted connections between knuckle case and cassette body;bolted connections between nose and cassette body -bolted connections between flanges and targets back plates (right)

Table 17 Sub systems integrated in the engineering model

Sub system	Level of definition in current simulation
Knuckle and embedded components	FE model includes knuckle body and a dummy pin (interfaced with knuckle case)
Nose	FE model consistent with the input geometry
Knuckle housing case	FE model consistent with the input geometry
Knuckle-Knuckle housing case bolted connections	FE model consistent with the input geometry
Nose bolted connections	FE model consistent with the input geometry
PFU	-----
PFU back plate supports	FE model consistent with EM model for interpolation accuracy purpose
Back plates bolted connections	FE model consistent with the input geometry

The native geometry for the engineering model building, was derived from the CAD geometry with only minor defeaturing; therefore, the CAD dimensions have been directly preserved in the simulation model.

As can be seen from Figure 135, the dimensions of the engineering model are identical to those of the original input CAD model.

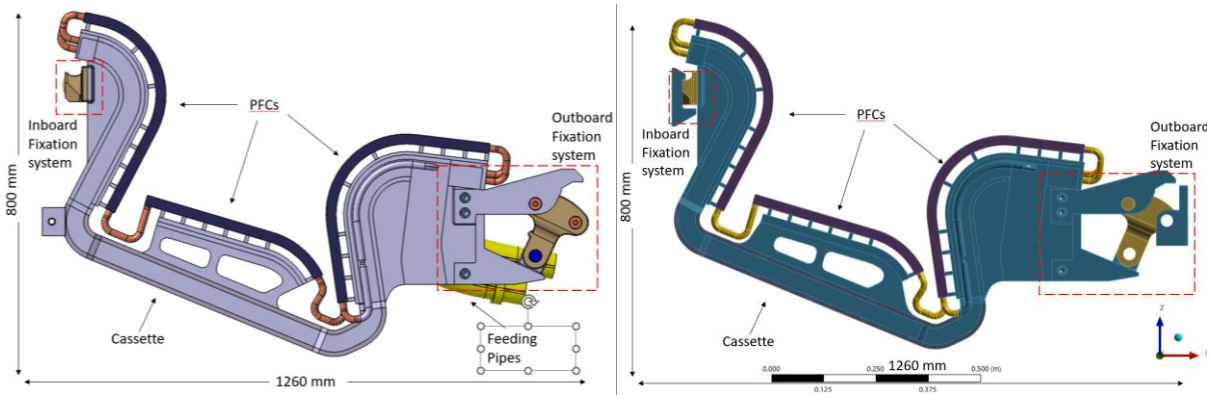

Figure 135 DTT divertor CAD model, input for FEA vs Defeatured geometry included into the simulation

The design subject to verification is illustrated in Figure 136, providing a detailed view of its internal layout. As described in the divertor cassette body is a stainless-steel box structure, approximately 1.2m long, 0.8m high and 0.3m wide at the widest point. The mass of one cassette is approximately 80 kg. The welded structure is made of 316L(N) and XM-19 plates and forged and machined parts. Component geometrical symmetry minimizes toroidal

distortions during manufacture and operation. The cooling circuit has also been arranged in such a way as to provide symmetric cooling, thus minimizing the thermal stresses and distortions in the DIV-CB.

Several sections can be identified on the cassette, namely:

- **Main body**, spanning most of the length of the DIV-CB, and featuring the main coolant channels,
- **Inlet and Outlet manifolds,** which interface with the primary divertor cooling loop via the pipe stubs,
- **Outboard distributor manifold,** which distributes the coolant flow to PFUs,
- **Inboard collector manifold**, which gathers the coolant from the PFUs and channels it into the return circuit
- **The Inboard stiffening ribs and Nose pad,** responsible for the connection to the Inboard Fixation System,
- **The Outboard fixation system interface,** responsible for the connection to the Outboard Fixation System,
- **The PFC supports** which provide the bolted connection for the PFCs assembly,
- **The OVT returning pipes**, which connect the first and last PFUs of the OVT to the Outlet manifold

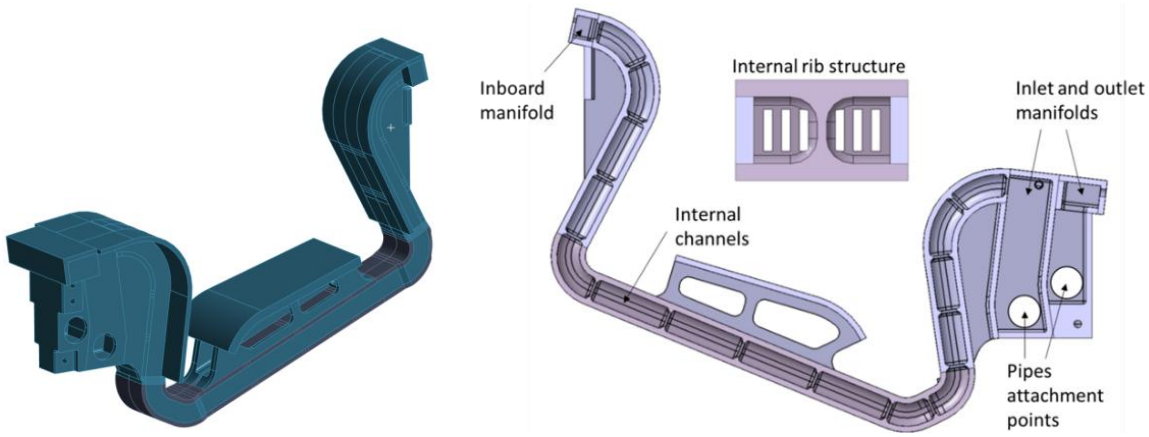

Figure 136 DTT divertor cassette body subject to verification process- Section of the DTT divertor cassette body

5.3 Engineering Model building

5.3.1 Mesh

The meshing strategy was designed to ensure element quality and accuracy across the model. Higher-order 3D elements with quadratic shape functions were used throughout, primarily hexahedral and tetrahedral types. Most of the components were meshed using the sweep method to maintain regularity, while automatic meshing was applied to certain complex regions to avoid distortion, particularly in thin sections. A minimum of two elements was ensured through the thickness of each body.

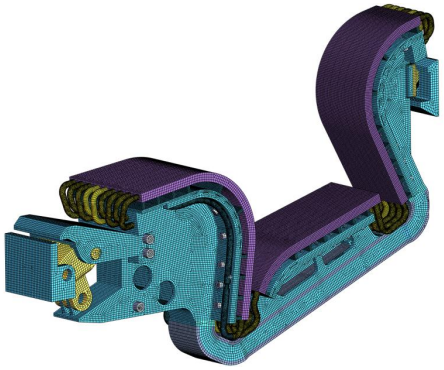

Figure 137 – Structural mesh

Below are a few choices followed to mesh the model:

- SOLID 186 (20 nodes) with quadratic shape function formulation used for the hexahedral element generation
- Majority of bodies meshed with sweep method to enhance mesh regularity
- Automatic method used for few PFU pipes to prevent highly distorted elements in the thickness
- At least two elements in the thickness of each body.

The discretized model catches with good approximation all the features included into the starting geometry, in particular, the minimum element size adopted in the model is such that, all over the mesh, at least two elements are placed into the thickness of each component.

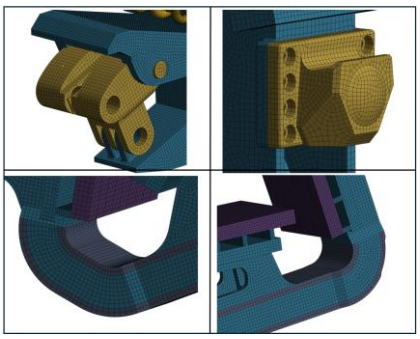

Figure 138 Region of major interest (high stress foreseen, contact definition etc.)

As can be seen in Figure 138 the mesh in the regions of interest has good quality even though, in particular on the nose is not refined enough to catch the local stress intensification or to address the stress due to Hertzian pressure on the edges.

The mesh of monoblock , and monoblock support, in adherence with the input geometry is simplified, the reason behind this choice is twofold:

- To ensure optimal interpolation on the PFC assembly, the geometry used in the engineering model is identical to that employed in the electromagnetic (EM) analysis. This includes a simplified representation of the PFU and its supports. As illustrated in Figure 139, a detailed model of the PFU support structure exists; however, the version used in the simulation is only a representative simplification and consistent with the EM model used for EM loads computation.
- Since the PFU supports are outside the scope of this study, there was no need to validate a fully detailed model. Nonetheless, the inclusion of a more detailed geometry and the corresponding connection definitions for the PFU supports could, to some extent, influence the verification results.

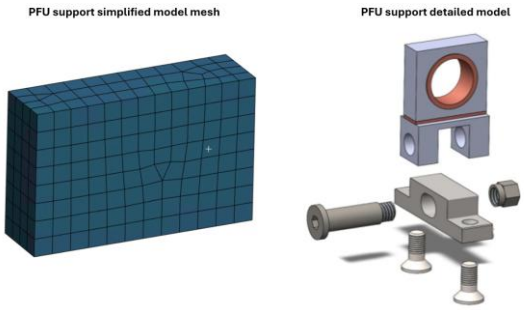

Figure 139 Detailed PFU support model

As can be seen in Figure 140 , few errors have been detected in some of the generated elements.

SUMMARIZE SHAPE TESTING FOR ALL SELECTED ELEMENTS

<<<<<< SHAPE TESTING SUMMARY >>>>>>
<<<<<< FOR ALL SELECTED ELEMENTS >>>>>>

| Element count 629843 MESH200 |

Test	Number tested	Warning count	Error count	Warn+Err %
Aspect Ratio	629843	6868	0	1.09 %
Parallel Deviation	434388	537	0	0.12 %
Maximum Angle	629843	3018	0	0.48 %
Jacobian Ratio	629843	25	2	0.00 %
Warping Factor	434388	7477	32	1.73 %
Any	629843	16284	34	2.59 %

Figure 140 Ansys Mechanical APDL element shape testing summary

This occurrence is not of major concern since the elements affected by errors are far from critical regions of interest for stress classification. None of them is intersected by the path defined for stress classification lines.

In Figure 141 and Figure 142 are reported the main metrics of the mesh.

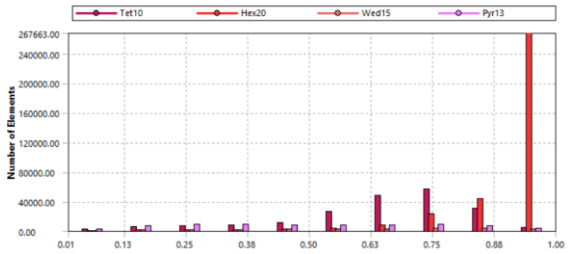

Figure 141 - Mesh element quality metrics

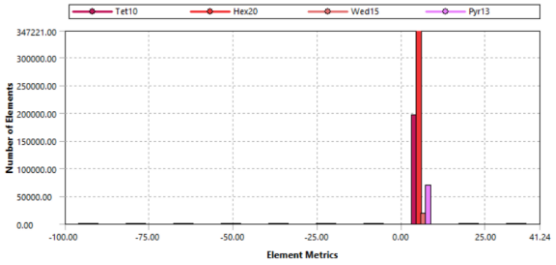

Figure 142 - Element jacobian ratio

5.3.2 Materials

The material properties are herein outlined. Figure 143 shows the geometry included in the simulation and the reference materials of each sub system.

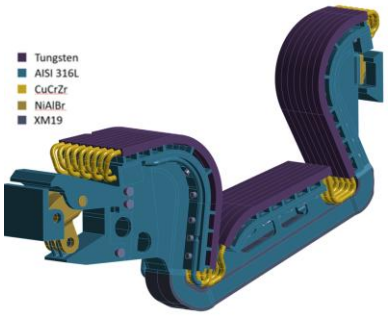

Component	Material
Knuckle Main Body	NiAlBr Alloy
CB Outboard Inboard branches	AISI 316 L IG
Nose	NiAlBr Alloy
Elbows+CB Central Body	XM19

Figure 143 Defeatured geometry included in simulation and related materials

For each included material, the meaningful set of physical properties (mechanical and thermal) has been included in Ansys Workbench analysis engineering data. It is supposed that the strain of the components is such that all the materials included stay in the linear elastic field (even

though large displacement option have been set on). All the defined materials were assumed to be isotropic.

5.3.3 Connections and boundary conditions

A comprehensive set of **frictional contacts** has been introduced in the model in order to realistically capture all possible relative sliding phenomena between components, even in the presence of bolted or pinned connections. Although several parts are mechanically connected through bolts, pins, or shared topology, frictional interactions were systematically introduced wherever relative motion could potentially occur under load. The friction coefficient has been adjusted to vacuum conditions according to [91]. In particular, the following frictional contact interfaces were defined:

- **Nose – Inboard rail interface**Frictional contacts were imposed between the nose lateral and bearing surfaces and the corresponding inboard rail surfaces (Figure 144). These contacts govern the load transfer mechanism between the divertor cassette and the rail system and allow for limited relative sliding under load.

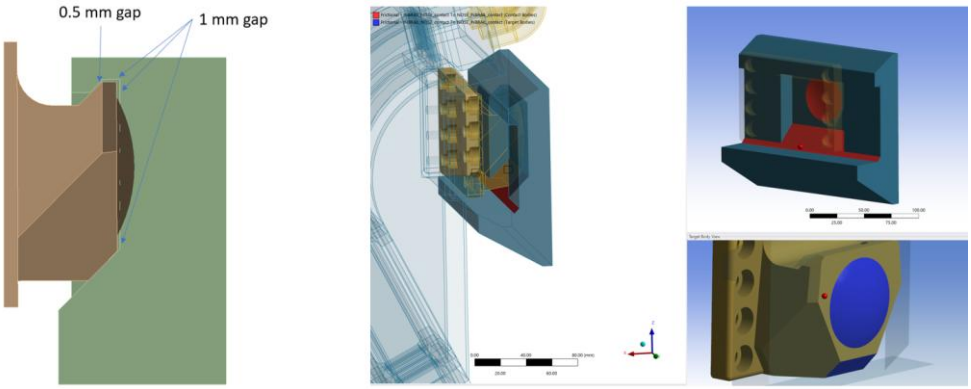

Figure 144 Frictional contacts between nose and inboard rail

- **Nose – Cassette body interface**Additional frictional contacts were introduced between the nose and the interfacing surfaces of the cassette body, wherever direct contact occurs during assembly or operation (Figure 145). This choice allows the model to capture possible micro-sliding effects and contact pressure redistribution at the nose–cassette interface.

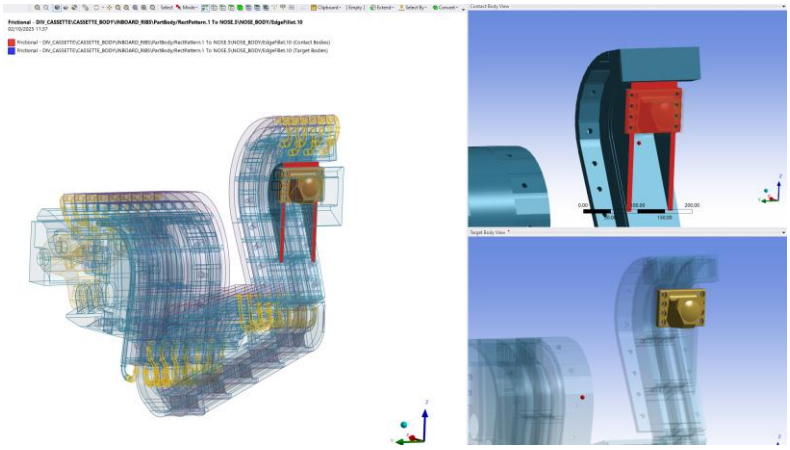

Figure 145 Frictional contacts between nose and cassette body nose pad

- **Knuckle – Knuckle case interface**Frictional contacts were imposed between the lateral surfaces of the knuckle and the corresponding lateral surfaces of the knuckle case (Figure 146). These contacts enable a realistic representation of the knuckle constraint mechanism, allowing for relative motion limited by friction rather than enforcing an artificially rigid behavior.

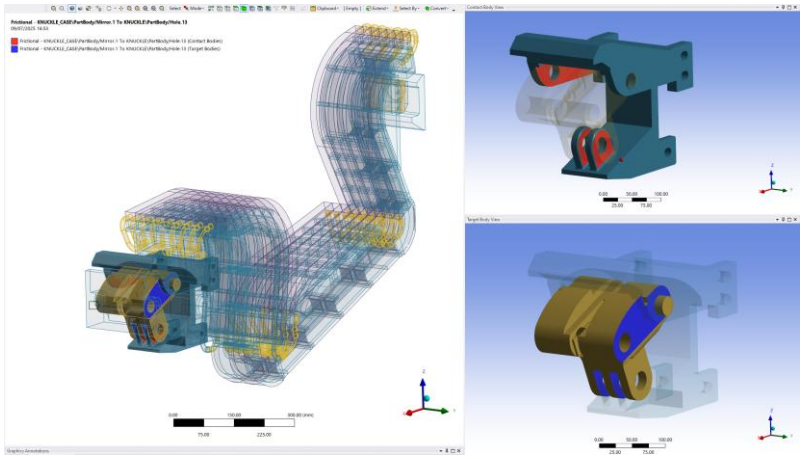

Figure 146 Frictional contact between knuckle lateral surfaces – knuckle case lateral surfaces

The surfaces paired into the following contacts formulation have been included in *Frictional contacts part* of ***Annex D – Set of contacts for structural assessment***.

- **Knuckle interface – Cassette body surfaces**Frictional contacts were defined between the knuckle interface surfaces and the corresponding interfaced surfaces on the cassette body. Even though these components are part of the same load path and are connected

through mechanical joints, the frictional formulation ensures that any potential relative sliding under preload or operational loads is correctly captured.

- **Dummy pins – Knuckle case holes**A frictional contact was imposed between the dummy pins and the knuckle case holes they interface with (Figure 147). Due to the initial misalignment between the knuckle pins and their mounting holes in the input geometry (Figure 146, left), this contact set was **activated only after the preload step**. This strategy allowed the preload force to be applied and subsequently deactivated in the following analysis steps, while ensuring that the divertor assembly retained its prestressed configuration once the pins were fully aligned (Figure 146, right).

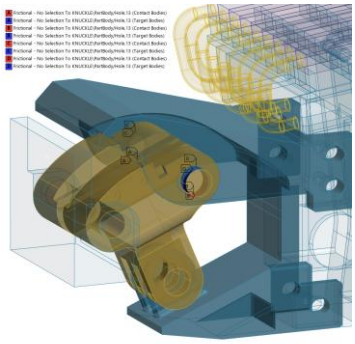

Figure 147 Frictional contact between knuckle dummy pins and knuckle case

As said, the analysis input geometry had the knuckle pins not aligned with their mounting holes as can be seen in Figure 148. Therefore, the contact set between the dummy pins and the holes has been activated only after the preload, so that the preload force could be deactivated through the next steps of the analysis while the divertor would keep its prestressed configuration.

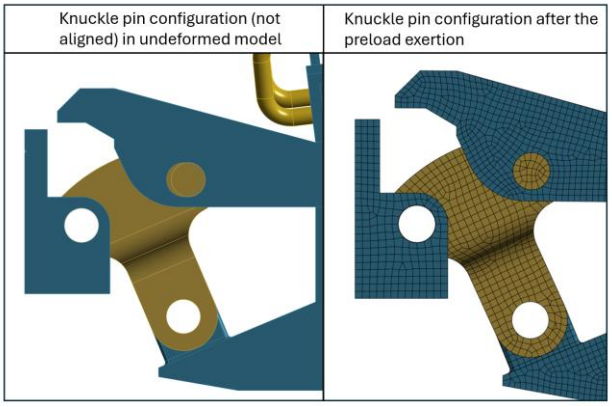

Figure 148 Knuckle pins not aligned (left picture); Knuckle pins aligned (right picture)

- **Flange faceted surfaces – Back plate interfaces** Frictional contacts were introduced between the faceted contact surfaces of the flanges and the corresponding contact surfaces on the back plates, where contact occurs. These interfaces, extensively discussed in 3.4.2, play a key role in load transfer and contact pressure distribution and therefore required an explicit frictional formulation.

The modeling of the **solid bolted connections** followed a standard and well-established approach (Figure 149):

- A **frictional contact** was imposed between the underside of the bolt head (or nut, where applicable) and the supporting surface, allowing load transfer through friction and contact pressure.
- A **bonded contact** was imposed between the bolt shank and the threaded portion of the hole in the back plate, representing the engaged thread region and preventing relative motion in this zone.

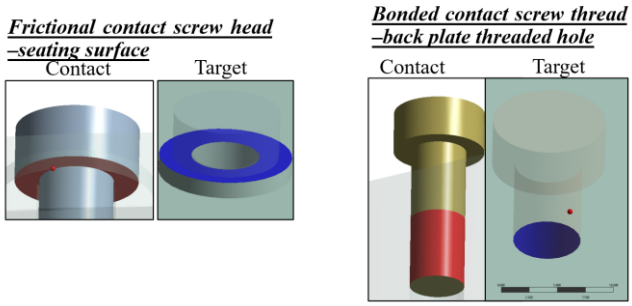

Figure 149 Frictional contact between screw head and seting surface (left)- Bonded contact between bolt thread and back plate threaded hole

This canonical formulation ensures a realistic representation of bolt preload effects, load transfer mechanisms, and stiffness contributions without introducing unnecessary modeling complexity. Figure 150 shows the components of the cassette body, whose elements share topology. All cassette components that are intended to be welded together in the actual assembly were modeled using a *shared topology* approach. This modeling choice ensures that, during the meshing phase, nodal continuity is enforced across adjacent bodies, resulting in the same mesh nodes being shared at the interfaces between different parts.

As a consequence, the welded regions are represented by a fully continuous structural domain, without the need to explicitly model weld beads or introduce bonded contact definitions. This

approach guarantees full displacement compatibility and stress transfer between the connected bodies, providing an accurate representation of the structural behavior of the welded cassette assembly. These choices are direct implications of the assembly strategy outlined in 3.4.2.1.

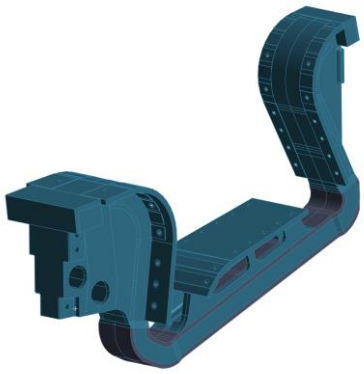

Figure 150 Cassette body components sharing topology

The imposed frictional contacts detailes are reported in Table 18.

Table 18 Summary of frictional contacts set

Contact region	**Target region**	**Friction coefficient**	**Rationale for friction coefficients**
Inboard rail	Nose	0.2	[91]
Knuckle case lateral surfaces	Knuckle lateral surfaces	0.2	
Knuckle case pin holes surfaces	Knuckle pin surfaces	0.2	
Cassette body nose pad	Nose	0.9	
Cassette body interface	Knuckle case surfaces	0.9	
IVT screws heads	IVT back plate	0.2	
OVT screws heads	OVT back plate	0.2	
Dome screws heads	Dome back plate	0.2	

Bonded contacts were introduced to model the interaction between components that are welded or rigidly connected in the real assembly but do not fall within the scope of the structural verification of the cassette body. In these cases, the interaction was deliberately simplified in order to reduce model complexity while preserving the correct load transfer path.In particular, bonded contacts were imposed between the PFU supports and the corresponding back plates. Although these components are bolted together in the real configuration, neither the back plates nor the PFU supports were included in the verification scope; therefore, their interaction was modeled as fully bonded.Bonded contacts were also defined between the PFUs and their respective supports, representing their rigid mechanical coupling without allowing relative motion. Finally, bonded contact formulations were introduced between the curved sections of the feeding pipes and the cassette body manifolds, as well as between the curved sections of the feeding pipes and the PFU inlet regions. These connections were modeled as bonded to represent welded or rigid connections and to ensure continuity in load transfer, without explicitly modeling the detailed joint geometry. The surfaces paired into the set bonded contacts formulation have been included in *Bonded contacts* of ***Annex D – Set of contacts for structural assessment***. The contact-target region of the overmentioned connections are reported in Table 19Table 19.

Table 19 Summary of bonded contacts set

Contact region	**Target region**
Lower surfaces of IVT/DOME/OVT PFU supports	IVT/DOME/OVT back plate
Upper surfaces of IVT/DOME/OVT PFU supports	IVT/DOME/OVT monoblocks lower surfaces
Upper IVT pipes	IVT monoblocks, inner manifold
Upper OVT pipes	OVT monoblocks, outer manifold
Lower inner pipes	IVT monoblocks, DOME monoblocks
Lower outer pipes	OVT monoblocks, DOME monoblocks

In Table 20 are outlined the initial conditions of the contacts. To be noted that in the contact regions between knuckle pins and knuckle case holes (orange in Table 20) a large amount of gap/penetration was detected. This was already foreseen since the contact surfaces at the

beginning of the simulation are wide far from each other and get in touch once the preload is exerted.

Table 20 Contacts initial conditions

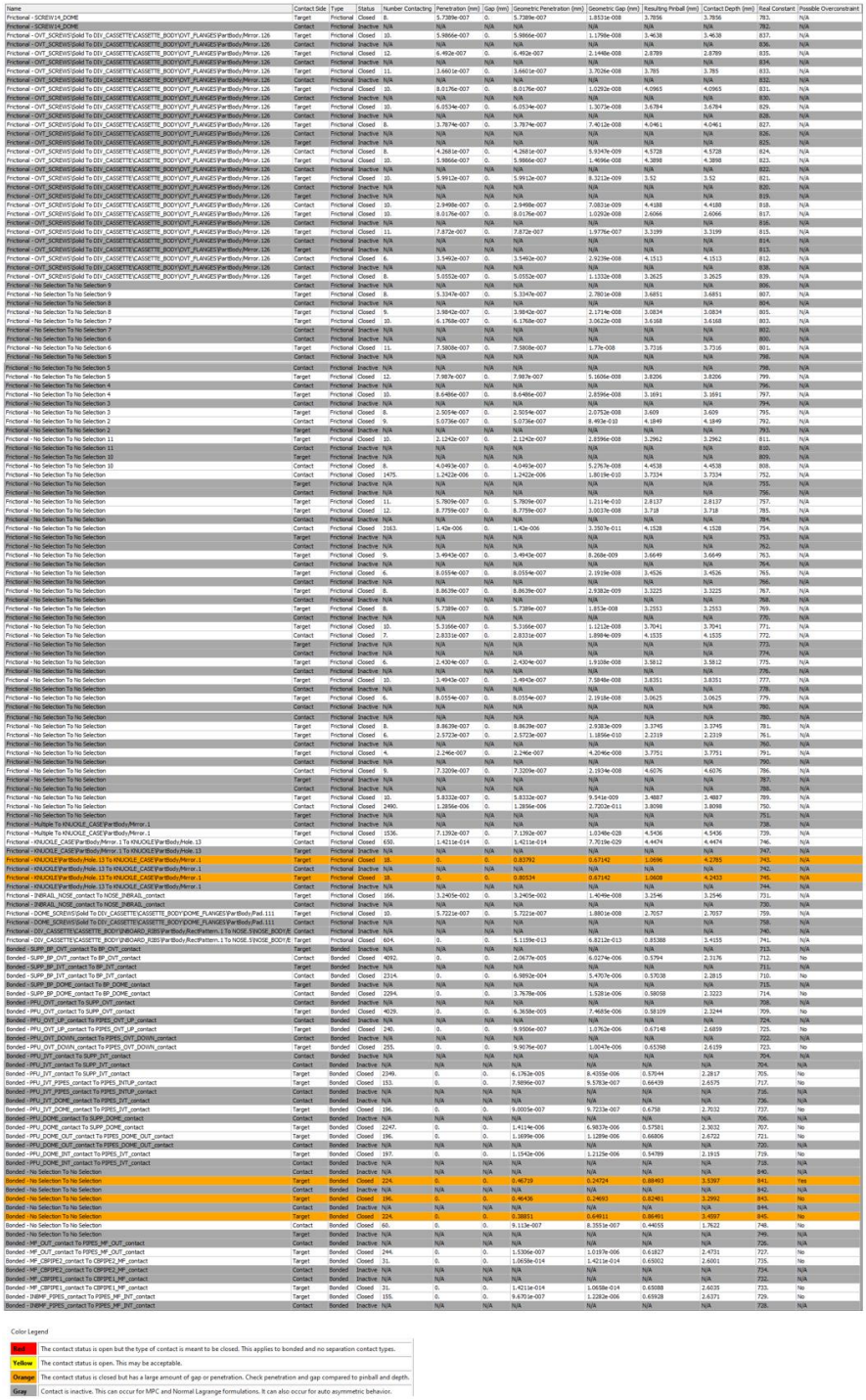

Name	Contact Side	Type	Status	Number Contacting	Penetration (mm)	Gap (mm)	Geometric Penetration (mm)	Geometric Gap (mm)	Resulting Pinball (mm)	Contact Depth (mm)	Real Constant	Possible Overconstraint
Frictional - SCREW14_DOME	Target	Frictional	Closed	8.	5.7389e-007	0.	5.7389e-007	1.8531e-008	3.7856	3.7856	783.	N/A
Frictional - SCREW14_DOME	Contact	Frictional	Inactive	N/A	N/A	N/A	N/A	N/A	N/A	N/A	783.	N/A
Frictional - OVT_SCREWS/Gold To DIV_CASSETTE\CASSETTE_BODY\OVT_FLANGES\PartBody/Mirror.126	Target	Frictional	Closed	10.	5.9866e-007	0.	5.9866e-007	1.1798e-008	3.4638	3.4638	837.	N/A
Frictional - OVT_SCREWS/Gold To DIV_CASSETTE\CASSETTE_BODY\OVT_FLANGES\PartBody/Mirror.126	Contact	Frictional	Inactive	N/A	N/A	N/A	N/A	N/A	N/A	N/A	836.	N/A
Frictional - OVT_SCREWS/Gold To DIV_CASSETTE\CASSETTE_BODY\OVT_FLANGES\PartBody/Mirror.126	Target	Frictional	Closed	12.	6.492e-007	0.	6.492e-007	2.1448e-008	2.8789	2.8789	835.	N/A
Frictional - OVT_SCREWS/Gold To DIV_CASSETTE\CASSETTE_BODY\OVT_FLANGES\PartBody/Mirror.126	Contact	Frictional	Inactive	N/A	N/A	N/A	N/A	N/A	N/A	N/A	834.	N/A
Frictional - OVT_SCREWS/Gold To DIV_CASSETTE\CASSETTE_BODY\OVT_FLANGES\PartBody/Mirror.126	Target	Frictional	Closed	11.	3.6601e-007	0.	3.6601e-007	3.7026e-008	3.785	3.785	833.	N/A
Frictional - OVT_SCREWS/Gold To DIV_CASSETTE\CASSETTE_BODY\OVT_FLANGES\PartBody/Mirror.126	Contact	Frictional	Inactive	N/A	N/A	N/A	N/A	N/A	N/A	N/A	832.	N/A
Frictional - OVT_SCREWS/Gold To DIV_CASSETTE\CASSETTE_BODY\OVT_FLANGES\PartBody/Mirror.126	Target	Frictional	Closed	10.	8.0176e-007	0.	8.0176e-007	1.0292e-008	4.0965	4.0965	831.	N/A
Frictional - OVT_SCREWS/Gold To DIV_CASSETTE\CASSETTE_BODY\OVT_FLANGES\PartBody/Mirror.126	Contact	Frictional	Inactive	N/A	N/A	N/A	N/A	N/A	N/A	N/A	830.	N/A
Frictional - OVT_SCREWS/Gold To DIV_CASSETTE\CASSETTE_BODY\OVT_FLANGES\PartBody/Mirror.126	Target	Frictional	Closed	10.	6.0534e-007	0.	6.0534e-007	1.3073e-008	3.6784	3.6784	829.	N/A
Frictional - OVT_SCREWS/Gold To DIV_CASSETTE\CASSETTE_BODY\OVT_FLANGES\PartBody/Mirror.126	Contact	Frictional	Inactive	N/A	N/A	N/A	N/A	N/A	N/A	N/A	828.	N/A
Frictional - OVT_SCREWS/Gold To DIV_CASSETTE\CASSETTE_BODY\OVT_FLANGES\PartBody/Mirror.126	Target	Frictional	Closed	8.	3.7874e-007	0.	3.7874e-007	7.4112e-008	4.0461	4.0461	827.	N/A
Frictional - OVT_SCREWS/Gold To DIV_CASSETTE\CASSETTE_BODY\OVT_FLANGES\PartBody/Mirror.126	Contact	Frictional	Inactive	N/A	N/A	N/A	N/A	N/A	N/A	N/A	826.	N/A
Frictional - OVT_SCREWS/Gold To DIV_CASSETTE\CASSETTE_BODY\OVT_FLANGES\PartBody/Mirror.126	Target	Frictional	Inactive	N/A	N/A	N/A	N/A	N/A	N/A	N/A	825.	N/A
Frictional - OVT_SCREWS/Gold To DIV_CASSETTE\CASSETTE_BODY\OVT_FLANGES\PartBody/Mirror.126	Contact	Frictional	Closed	8.	4.2681e-007	0.	4.2681e-007	5.9347e-009	4.5728	4.5728	824.	N/A
Frictional - OVT_SCREWS/Gold To DIV_CASSETTE\CASSETTE_BODY\OVT_FLANGES\PartBody/Mirror.126	Target	Frictional	Closed	10.	5.9866e-007	0.	5.9866e-007	1.4696e-008	4.3898	4.3898	823.	N/A
Frictional - OVT_SCREWS/Gold To DIV_CASSETTE\CASSETTE_BODY\OVT_FLANGES\PartBody/Mirror.126	Contact	Frictional	Inactive	N/A	N/A	N/A	N/A	N/A	N/A	N/A	822.	N/A
Frictional - OVT_SCREWS/Gold To DIV_CASSETTE\CASSETTE_BODY\OVT_FLANGES\PartBody/Mirror.126	Target	Frictional	Closed	10.	5.9912e-007	0.	5.9912e-007	8.3212e-009	3.52	3.52	821.	N/A
Frictional - OVT_SCREWS/Gold To DIV_CASSETTE\CASSETTE_BODY\OVT_FLANGES\PartBody/Mirror.126	Contact	Frictional	Inactive	N/A	N/A	N/A	N/A	N/A	N/A	N/A	820.	N/A
Frictional - OVT_SCREWS/Gold To DIV_CASSETTE\CASSETTE_BODY\OVT_FLANGES\PartBody/Mirror.126	Target	Frictional	Inactive	N/A	N/A	N/A	N/A	N/A	N/A	N/A	819.	N/A
Frictional - OVT_SCREWS/Gold To DIV_CASSETTE\CASSETTE_BODY\OVT_FLANGES\PartBody/Mirror.126	Contact	Frictional	Closed	10.	2.9498e-007	0.	2.9498e-007	7.0821e-009	4.4188	4.4188	818.	N/A
Frictional - OVT_SCREWS/Gold To DIV_CASSETTE\CASSETTE_BODY\OVT_FLANGES\PartBody/Mirror.126	Target	Frictional	Closed	10.	8.0176e-007	0.	8.0176e-007	1.0292e-008	2.6066	2.6066	817.	N/A
Frictional - OVT_SCREWS/Gold To DIV_CASSETTE\CASSETTE_BODY\OVT_FLANGES\PartBody/Mirror.126	Contact	Frictional	Inactive	N/A	N/A	N/A	N/A	N/A	N/A	N/A	816.	N/A
Frictional - OVT_SCREWS/Gold To DIV_CASSETTE\CASSETTE_BODY\OVT_FLANGES\PartBody/Mirror.126	Target	Frictional	Closed	11.	7.872e-007	0.	7.872e-007	1.9776e-007	3.3199	3.3199	815.	N/A
Frictional - OVT_SCREWS/Gold To DIV_CASSETTE\CASSETTE_BODY\OVT_FLANGES\PartBody/Mirror.126	Contact	Frictional	Inactive	N/A	N/A	N/A	N/A	N/A	N/A	N/A	814.	N/A
Frictional - OVT_SCREWS/Gold To DIV_CASSETTE\CASSETTE_BODY\OVT_FLANGES\PartBody/Mirror.126	Target	Frictional	Inactive	N/A	N/A	N/A	N/A	N/A	N/A	N/A	813.	N/A
Frictional - OVT_SCREWS/Gold To DIV_CASSETTE\CASSETTE_BODY\OVT_FLANGES\PartBody/Mirror.126	Contact	Frictional	Closed	6.	3.5492e-007	0.	3.5492e-007	2.9239e-008	4.1513	4.1513	812.	N/A
Frictional - OVT_SCREWS/Gold To DIV_CASSETTE\CASSETTE_BODY\OVT_FLANGES\PartBody/Mirror.126	Contact	Frictional	Inactive	N/A	N/A	N/A	N/A	N/A	N/A	N/A	836.	N/A
Frictional - OVT_SCREWS/Gold To DIV_CASSETTE\CASSETTE_BODY\OVT_FLANGES\PartBody/Mirror.126	Target	Frictional	Closed	8.	5.0552e-007	0.	5.0552e-007	1.1332e-008	3.2625	3.2625	839.	N/A
Frictional - No Selection To No Selection 9	Contact	Frictional	Inactive	N/A	N/A	N/A	N/A	N/A	N/A	N/A	806.	N/A
Frictional - No Selection To No Selection 9	Target	Frictional	Closed	8.	5.3347e-007	0.	5.3347e-007	2.7801e-008	3.6851	3.6851	807.	N/A
Frictional - No Selection To No Selection 8	Contact	Frictional	Inactive	N/A	N/A	N/A	N/A	N/A	N/A	N/A	804.	N/A
Frictional - No Selection To No Selection 8	Target	Frictional	Closed	9.	3.9842e-007	0.	3.9842e-007	2.1714e-008	3.0834	3.0834	805.	N/A
Frictional - No Selection To No Selection 7	Target	Frictional	Closed	10.	6.1768e-007	0.	6.1768e-007	3.0622e-008	3.6168	3.6168	803.	N/A
Frictional - No Selection To No Selection 7	Contact	Frictional	Inactive	N/A	N/A	N/A	N/A	N/A	N/A	N/A	802.	N/A
Frictional - No Selection To No Selection 6	Contact	Frictional	Inactive	N/A	N/A	N/A	N/A	N/A	N/A	N/A	800.	N/A
Frictional - No Selection To No Selection 6	Target	Frictional	Closed	11.	7.5808e-007	0.	7.5808e-007	1.77e-008	3.7316	3.7316	801.	N/A
Frictional - No Selection To No Selection 5	Contact	Frictional	Inactive	N/A	N/A	N/A	N/A	N/A	N/A	N/A	798.	N/A
Frictional - No Selection To No Selection 5	Contact	Frictional	Inactive	N/A	N/A	N/A	N/A	N/A	N/A	N/A	798.	N/A
Frictional - No Selection To No Selection 5	Target	Frictional	Closed	12.	7.987e-007	0.	7.987e-007	5.1606e-008	3.8206	3.8206	799.	N/A
Frictional - No Selection To No Selection 4	Contact	Frictional	Inactive	N/A	N/A	N/A	N/A	N/A	N/A	N/A	796.	N/A
Frictional - No Selection To No Selection 4	Target	Frictional	Closed	10.	8.6486e-007	0.	8.6486e-007	2.8596e-008	3.1691	3.1691	797.	N/A
Frictional - No Selection To No Selection 3	Contact	Frictional	Inactive	N/A	N/A	N/A	N/A	N/A	N/A	N/A	794.	N/A
Frictional - No Selection To No Selection 3	Target	Frictional	Closed	8.	2.5054e-007	0.	2.5054e-007	2.0752e-008	3.609	3.609	795.	N/A
Frictional - No Selection To No Selection 2	Contact	Frictional	Closed	9.	5.0736e-007	0.	5.0736e-007	8.493e-010	4.1849	4.1849	792.	N/A
Frictional - No Selection To No Selection 2	Target	Frictional	Inactive	N/A	N/A	N/A	N/A	N/A	N/A	N/A	793.	N/A
Frictional - No Selection To No Selection 11	Target	Frictional	Closed	10.	2.1242e-007	0.	2.1242e-007	2.8596e-008	3.2962	3.2962	811.	N/A
Frictional - No Selection To No Selection 11	Contact	Frictional	Inactive	N/A	N/A	N/A	N/A	N/A	N/A	N/A	810.	N/A
Frictional - No Selection To No Selection 10	Target	Frictional	Inactive	N/A	N/A	N/A	N/A	N/A	N/A	N/A	809.	N/A
Frictional - No Selection To No Selection 10	Contact	Frictional	Closed	8.	4.0403e-007	0.	4.0403e-007	5.2767e-008	4.4538	4.4538	808.	N/A
Frictional - No Selection To No Selection	Contact	Frictional	Closed	1475.	1.2422e-006	0.	1.2422e-006	1.8019e-010	3.7334	3.7334	752.	N/A
Frictional - No Selection To No Selection	Target	Frictional	Inactive	N/A	N/A	N/A	N/A	N/A	N/A	N/A	753.	N/A
Frictional - No Selection To No Selection	Contact	Frictional	Inactive	N/A	N/A	N/A	N/A	N/A	N/A	N/A	756.	N/A
Frictional - No Selection To No Selection	Target	Frictional	Closed	11.	5.7809e-007	0.	5.7809e-007	1.2114e-010	2.8137	2.8137	757.	N/A
Frictional - No Selection To No Selection	Target	Frictional	Closed	12.	8.7759e-007	0.	8.7759e-007	3.0037e-008	3.718	3.718	781.	N/A
Frictional - No Selection To No Selection	Contact	Frictional	Inactive	N/A	N/A	N/A	N/A	N/A	N/A	N/A	784.	N/A
Frictional - No Selection To No Selection	Contact	Frictional	Closed	3163.	1.42e-006	0.	1.42e-006	3.3507e-011	4.1528	4.1528	754.	N/A
Frictional - No Selection To No Selection	Target	Frictional	Inactive	N/A	N/A	N/A	N/A	N/A	N/A	N/A	753.	N/A
Frictional - No Selection To No Selection	Contact	Frictional	Inactive	N/A	N/A	N/A	N/A	N/A	N/A	N/A	752.	N/A
Frictional - No Selection To No Selection	Target	Frictional	Closed	9.	3.4943e-007	0.	3.4943e-007	8.268e-009	3.6649	3.6649	763.	N/A
Frictional - No Selection To No Selection	Contact	Frictional	Inactive	N/A	N/A	N/A	N/A	N/A	N/A	N/A	764.	N/A
Frictional - No Selection To No Selection	Target	Frictional	Closed	6.	8.0554e-007	0.	8.0554e-007	2.1919e-008	3.4526	3.4526	765.	N/A
Frictional - No Selection To No Selection	Contact	Frictional	Inactive	N/A	N/A	N/A	N/A	N/A	N/A	N/A	766.	N/A
Frictional - No Selection To No Selection	Target	Frictional	Closed	8.	8.8639e-007	0.	8.8639e-007	2.9382e-009	3.3225	3.3225	767.	N/A
Frictional - No Selection To No Selection	Contact	Frictional	Inactive	N/A	N/A	N/A	N/A	N/A	N/A	N/A	768.	N/A
Frictional - No Selection To No Selection	Target	Frictional	Closed	8.	5.7389e-007	0.	5.7389e-007	1.853e-008	3.2553	3.2553	769.	N/A
Frictional - No Selection To No Selection	Contact	Frictional	Inactive	N/A	N/A	N/A	N/A	N/A	N/A	N/A	770.	N/A
Frictional - No Selection To No Selection	Target	Frictional	Closed	10.	5.3166e-007	0.	5.3166e-007	1.1212e-008	3.7041	3.7041	771.	N/A
Frictional - No Selection To No Selection	Contact	Frictional	Closed	7.	2.8331e-007	0.	2.8331e-007	1.8984e-009	4.1535	4.1535	772.	N/A
Frictional - No Selection To No Selection	Target	Frictional	Inactive	N/A	N/A	N/A	N/A	N/A	N/A	N/A	773.	N/A
Frictional - No Selection To No Selection	Contact	Frictional	Inactive	N/A	N/A	N/A	N/A	N/A	N/A	N/A	774.	N/A
Frictional - No Selection To No Selection	Target	Frictional	Closed	6.	2.4304e-007	0.	2.4304e-007	1.9108e-008	3.5812	3.5812	775.	N/A
Frictional - No Selection To No Selection	Contact	Frictional	Inactive	N/A	N/A	N/A	N/A	N/A	N/A	N/A	776.	N/A
Frictional - No Selection To No Selection	Target	Frictional	Closed	10.	3.4943e-007	0.	3.4943e-007	7.5848e-008	3.8351	3.8351	777.	N/A
Frictional - No Selection To No Selection	Contact	Frictional	Inactive	N/A	N/A	N/A	N/A	N/A	N/A	N/A	778.	N/A
Frictional - No Selection To No Selection	Target	Frictional	Closed	6.	8.0554e-007	0.	8.0554e-007	2.1918e-008	3.0625	3.0625	779.	N/A
Frictional - No Selection To No Selection	Contact	Frictional	Inactive	N/A	N/A	N/A	N/A	N/A	N/A	N/A	780.	N/A
Frictional - No Selection To No Selection	Contact	Frictional	Inactive	N/A	N/A	N/A	N/A	N/A	N/A	N/A	780.	N/A
Frictional - No Selection To No Selection	Target	Frictional	Closed	8.	8.8639e-007	0.	8.8639e-007	2.9383e-009	3.3745	3.3745	781.	N/A
Frictional - No Selection To No Selection	Target	Frictional	Closed	6.	2.5723e-007	0.	2.5723e-007	1.1856e-010	2.2319	2.2319	761.	N/A
Frictional - No Selection To No Selection	Contact	Frictional	Inactive	N/A	N/A	N/A	N/A	N/A	N/A	N/A	760.	N/A
Frictional - No Selection To No Selection	Target	Frictional	Closed	4.	2.296e-007	0.	2.296e-007	4.2046e-008	3.7751	3.7751	791.	N/A
Frictional - No Selection To No Selection	Contact	Frictional	Inactive	N/A	N/A	N/A	N/A	N/A	N/A	N/A	790.	N/A
Frictional - No Selection To No Selection	Contact	Frictional	Closed	9.	7.3209e-007	0.	7.3209e-007	2.1934e-008	4.6076	4.6076	786.	N/A
Frictional - No Selection To No Selection	Target	Frictional	Inactive	N/A	N/A	N/A	N/A	N/A	N/A	N/A	787.	N/A
Frictional - No Selection To No Selection	Contact	Frictional	Inactive	N/A	N/A	N/A	N/A	N/A	N/A	N/A	788.	N/A
Frictional - No Selection To No Selection	Target	Frictional	Closed	10.	5.8332e-007	0.	5.8332e-007	9.541e-009	3.4887	3.4887	789.	N/A
Frictional - No Selection To No Selection	Contact	Frictional	Closed	2490.	1.2856e-006	0.	1.2856e-006	2.7222e-011	3.8098	3.8098	750.	N/A
Frictional - No Selection To No Selection	Target	Frictional	Inactive	N/A	N/A	N/A	N/A	N/A	N/A	N/A	751.	N/A
Frictional - Multiple To KNUCKLE_CASE\PartBody/Mirror.1	Contact	Frictional	Inactive	N/A	N/A	N/A	N/A	N/A	N/A	N/A	738.	N/A
Frictional - Multiple To KNUCKLE_CASE\PartBody/Mirror.1	Target	Frictional	Closed	1536.	7.1392e-007	0.	7.1392e-007	1.0348e-028	4.5436	4.5436	739.	N/A
Frictional - KNUCKLE_CASE\PartBody/Mirror.1 To KNUCKLE\PartBody/Hole.13	Contact	Frictional	Closed	650.	1.4211e-014	0.	1.4211e-014	7.7019e-029	4.4474	4.4474	746.	N/A
Frictional - KNUCKLE\PartBody/Mirror.13 To KNUCKLE_CASE\PartBody/Hole.13	Target	Frictional	Inactive	N/A	N/A	N/A	N/A	N/A	N/A	N/A	747.	N/A
Frictional - KNUCKLE\PartBody/Hole.13 To KNUCKLE_CASE\PartBody/Mirror.1	Target	Frictional	Closed	18.	0.	0.	0.83792	0.67142	1.0696	4.2785	743.	N/A
Frictional - KNUCKLE\PartBody/Hole.13 To KNUCKLE_CASE\PartBody/Mirror.1	Contact	Frictional	Inactive	N/A	N/A	N/A	N/A	N/A	N/A	N/A	742.	N/A
Frictional - KNUCKLE\PartBody/Hole.13 To KNUCKLE_CASE\PartBody/Mirror.1	Contact	Frictional	Closed	18.	0.	0.	0.80534	0.67142	1.0608	4.2433	745.	N/A
Frictional - KNUCKLE\PartBody/Hole.13 To KNUCKLE_CASE\PartBody/Mirror.1	Contact	Frictional	Inactive	N/A	N/A	N/A	N/A	N/A	N/A	N/A	744.	N/A
Frictional - INBRAID_NOSE_contact To NOSE_INBRAID_contact	Target	Frictional	Closed	166.	3.2405e-002	0.	3.2405e-002	1.4049e-008	3.2546	3.2546	731.	N/A
Frictional - INBRAID_NOSE_contact To NOSE_INBRAID_contact	Contact	Frictional	Inactive	N/A	N/A	N/A	N/A	N/A	N/A	N/A	730.	N/A
Frictional - DOME_SCREWS/Gold To DIV_CASSETTE\CASSETTE_BODY\DOME_FLANGES\PartBody/Pad.111	Target	Frictional	Closed	10.	5.7221e-007	0.	5.7221e-007	1.8801e-008	2.7057	2.7057	759.	N/A
Frictional - DOME_SCREWS/Gold To DIV_CASSETTE\CASSETTE_BODY\DOME_FLANGES\PartBody/Pad.111	Contact	Frictional	Inactive	N/A	N/A	N/A	N/A	N/A	N/A	N/A	758.	N/A
Frictional - DIV_CASSETTE\CASSETTE_BODY\INBOARD_RIBS\PartBody/RectPattern..1 To NOSE_SI\NOSE_BODY/E	Contact	Frictional	Inactive	N/A	N/A	N/A	N/A	N/A	N/A	N/A	740.	N/A
Frictional - DIV_CASSETTE\CASSETTE_BODY\INBOARD_RIBS\PartBody/RectPattern..1 To NOSE_SI\NOSE_BODY/E	Target	Frictional	Closed	604.	0.	0.	5.1159e-013	6.8212e-013	0.85388	3.4155	741.	N/A
Bonded - SUPP_BP_OVT_contact To BP_OVT_contact	Target	Bonded	Inactive	N/A	N/A	N/A	N/A	N/A	N/A	N/A	712.	N/A
Bonded - SUPP_BP_OVT_contact To BP_OVT_contact	Contact	Bonded	Closed	4092.	0.	0.	2.0677e-005	6.0274e-006	0.5794	2.3176	712.	No
Bonded - SUPP_BP_IVT_contact To BP_IVT_contact	Target	Bonded	Inactive	N/A	N/A	N/A	N/A	N/A	N/A	N/A	711.	N/A
Bonded - SUPP_BP_IVT_contact To BP_IVT_contact	Contact	Bonded	Closed	2314.	0.	0.	6.9892e-004	5.4707e-006	0.57038	2.2815	710.	No
Bonded - SUPP_BP_DOME_contact To BP_DOME_contact	Target	Bonded	Inactive	N/A	N/A	N/A	N/A	N/A	N/A	N/A	715.	N/A
Bonded - SUPP_BP_DOME_contact To BP_DOME_contact	Contact	Bonded	Closed	2294.	0.	0.	3.767e-006	1.5281e-006	0.58058	2.3223	714.	No
Bonded - PFU_OVT_contact To SUPP_OVT_contact	Target	Bonded	Inactive	N/A	N/A	N/A	N/A	N/A	N/A	N/A	708.	N/A
Bonded - PFU_OVT_contact To SUPP_OVT_contact	Contact	Bonded	Closed	4029.	0.	0.	6.3658e-005	7.4685e-006	0.58109	2.3244	709.	No
Bonded - PFU_OVT_UP_contact To PIPES_OVT_UP_contact	Contact	Bonded	Inactive	N/A	N/A	N/A	N/A	N/A	N/A	N/A	724.	N/A
Bonded - PFU_OVT_UP_contact To PIPES_OVT_UP_contact	Target	Bonded	Closed	240.	0.	0.	9.9506e-007	1.0782e-006	0.67148	2.6859	725.	No
Bonded - PFU_OVT_DOWN_contact To PIPES_OVT_DOWN_contact	Contact	Bonded	Inactive	N/A	N/A	N/A	N/A	N/A	N/A	N/A	722.	N/A
Bonded - PFU_OVT_DOWN_contact To PIPES_OVT_DOWN_contact	Target	Bonded	Closed	255.	0.	0.	9.9076e-007	1.0047e-006	0.65398	2.6159	723.	No
Bonded - PFU_IVT_contact To SUPP_IVT_contact	Contact	Bonded	Inactive	N/A	N/A	N/A	N/A	N/A	N/A	N/A	704.	N/A
Bonded - PFU_IVT_contact To SUPP_IVT_contact	Contact	Bonded	Inactive	N/A	N/A	N/A	N/A	N/A	N/A	N/A	704.	N/A
Bonded - PFU_IVT_contact To SUPP_IVT_contact	Target	Bonded	Closed	2349.	0.	0.	6.1762e-005	8.4355e-006	0.57044	2.2817	705.	No
Bonded - PFU_IVT_PIPES_contact To PIPES_INTUP_contact	Target	Bonded	Closed	153.	0.	0.	7.9896e-007	9.5763e-007	0.66439	2.6575	717.	No
Bonded - PFU_IVT_PIPES_contact To PIPES_INTUP_contact	Contact	Bonded	Inactive	N/A	N/A	N/A	N/A	N/A	N/A	N/A	716.	N/A
Bonded - PFU_IVT_DOME_contact To PIPES_IVT_contact	Contact	Bonded	Inactive	N/A	N/A	N/A	N/A	N/A	N/A	N/A	726.	N/A
Bonded - PFU_IVT_DOME_contact To PIPES_IVT_contact	Target	Bonded	Closed	196.	0.	0.	9.0015e-007	9.7223e-007	0.6758	2.7032	727.	No
Bonded - PFU_DOME_contact To SUPP_DOME_contact	Contact	Bonded	Inactive	N/A	N/A	N/A	N/A	N/A	N/A	N/A	706.	N/A
Bonded - PFU_DOME_contact To SUPP_DOME_contact	Target	Bonded	Closed	2247.	0.	0.	1.4114e-006	6.9837e-006	0.57581	2.3032	707.	No
Bonded - PFU_DOME_OUT_contact To PIPES_DOME_OUT_contact	Target	Bonded	Closed	196.	0.	0.	1.1899e-006	1.1289e-006	0.66806	2.6722	721.	No
Bonded - PFU_DOME_OUT_contact To PIPES_DOME_OUT_contact	Contact	Bonded	Inactive	N/A	N/A	N/A	N/A	N/A	N/A	N/A	720.	N/A
Bonded - PFU_DOME_INT_contact To PIPES_IVT_contact	Target	Bonded	Closed	197.	0.	0.	1.1542e-006	1.2125e-006	0.54789	2.1915	719.	No
Bonded - PFU_DOME_INT_contact To PIPES_IVT_contact	Contact	Bonded	Inactive	N/A	N/A	N/A	N/A	N/A	N/A	N/A	718.	N/A
Bonded - No Selection To No Selection	Contact	Bonded	Inactive	N/A	N/A	N/A	N/A	N/A	N/A	N/A	840.	N/A
Bonded - No Selection To No Selection	Target	Bonded	Closed	224.	0.	0.	0.46719	0.24724	0.88493	3.5397	841.	Yes
Bonded - No Selection To No Selection	Contact	Bonded	Inactive	N/A	N/A	N/A	N/A	N/A	N/A	N/A	842.	N/A
Bonded - No Selection To No Selection	Target	Bonded	Closed	196.	0.	0.	0.46436	0.24693	0.82481	3.2992	843.	No
Bonded - No Selection To No Selection	Contact	Bonded	Inactive	N/A	N/A	N/A	N/A	N/A	N/A	N/A	844.	N/A
Bonded - No Selection To No Selection	Target	Bonded	Closed	224.	0.	0.	0.38851	0.64911	0.86491	3.4597	845.	No
Bonded - No Selection To No Selection	Contact	Bonded	Closed	60.	0.	0.	9.113e-007	8.3551e-007	0.44055	1.7622	748.	No
Bonded - No Selection To No Selection	Contact	Bonded	Inactive	N/A	N/A	N/A	N/A	N/A	N/A	N/A	749.	N/A
Bonded - MF_OUT_contact To PIPES_MF_OUT_contact	Contact	Bonded	Inactive	N/A	N/A	N/A	N/A	N/A	N/A	N/A	726.	N/A
Bonded - MF_OUT_contact To PIPES_MF_OUT_contact	Target	Bonded	Closed	244.	0.	0.	1.5306e-007	1.0197e-006	0.61827	2.4731	727.	No
Bonded - MF_CSP1PE2_contact To CSP1PE2_MF_contact	Target	Bonded	Closed	31.	0.	0.	1.0658e-014	1.421e-014	0.65002	2.6001	735.	No
Bonded - MF_CSP1PE2_contact To CSP1PE2_MF_contact	Contact	Bonded	Inactive	N/A	N/A	N/A	N/A	N/A	N/A	N/A	734.	N/A
Bonded - MF_CSP1PE1_contact To CSP1PE1_MF_contact	Contact	Bonded	Inactive	N/A	N/A	N/A	N/A	N/A	N/A	N/A	732.	N/A
Bonded - MF_CSP1PE1_contact To CSP1PE1_MF_contact	Target	Bonded	Closed	21.	0.	0.	1.4211e-014	1.0658e-014	0.65088	2.6035	733.	No
Bonded - INBMF_PIPES_contact To PIPES_MF_INT_contact	Target	Bonded	Closed	155.	0.	0.	9.670e-007	1.2282e-006	0.65928	2.6371	729.	No
Bonded - INBMF_PIPES_contact To PIPES_MF_INT_contact	Contact	Bonded	Inactive	N/A	N/A	N/A	N/A	N/A	N/A	N/A	728.	N/A

Color Legend

Red	The contact status is open but the type of contact is meant to be closed. This applies to bonded and no separation contact types.
Yellow	The contact status is open. This may be acceptable.
Orange	The contact status is closed but has a large amount of gap or penetration. Check penetration and gap compared to pinball and depth.
Gray	Contact is inactive. This can occur for MPC and Normal Lagrange formulations. It can also occur for auto asymmetric behavior.

Figure 151 shows the graphic visualization of the constrained equations resulting from the contacts set.

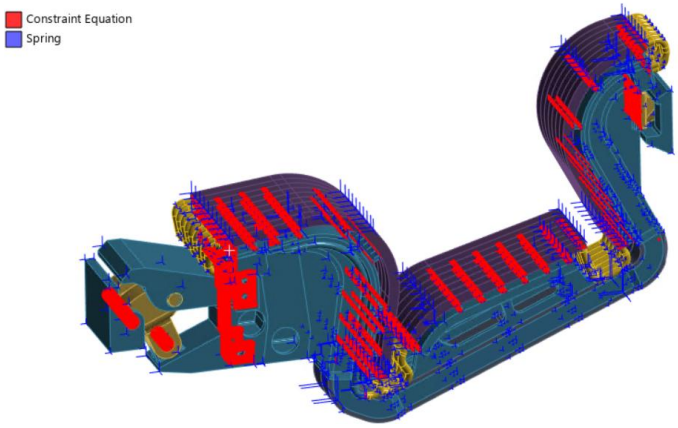

Figure 151 Graphic visualization of constraint equations generated for imposed bonded contacts and joints

Two **joints** have been set into the analysis. In particular, the knuckle lower shaft behavior has been replaced with a revolute joint between knuckle lower shaft holes and the equivalent holes on the knuckle case. The imposed joint formulation constr aints all the DOF with exception of the relative rotation around the Z axis (Figure 152). Similarly, the knuckle outer pin-outboard rail relative motion , has been replaced by a revolute joint, leaving free only the rotation around the Z axis of the joint coordinate system (Figure 152)

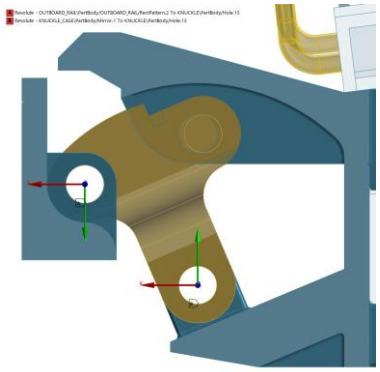

Figure 152 Revolute joints set between knuckle outer pin holes-outboard rail holes, knuckle winding shaft holes-knuckle case winding shaft holes

As detailed in 5.2.2, the differential thermal expansion between vessel and divertor has been neglected since both structures have the same temperature during normal operating conditions and baking, furthermore they are mainly composed by the same material.

Consequently, the inboard and outboard rail surfaces welded to the vessel have been fully constrained in the analysis using fixed supports Figure 153. This approach does not consider any differential thermal expansion between the rails and the divertor, which could otherwise be introduced as a displacement condition on the rail geometry. However, as previously mentioned, the preload loss resulting from such thermal expansion is negligible. Therefore, applying fixed support is a conservative assumption, likely overestimating the stress on the divertor. In practice, the actual stress will be slightly lower due to the vessel's thermal expansion at the rail locations, while on the other hand there will be a loss of preload. The lower stop has been simulated through a compression only support (Figure 153).

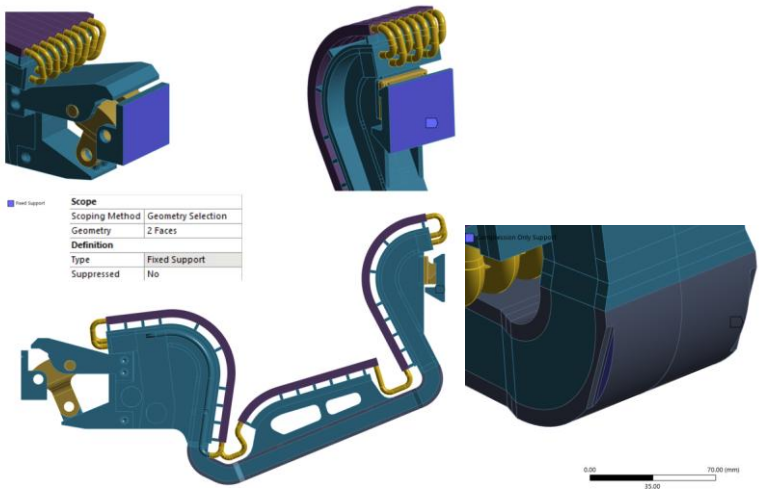

Figure 153 - Fixed supports set on inboard rail and nose- Compression only support to simulate the lower stop

5.3.4 Loads step definition

The loads included into the simulation are here outlined. The loads acting on DTT Divertor are reported and detailed in [92].

The loads included in the simulation are summarized in Table 21. The table reports the loads cumulatively applied at each step of the analysis, specifying the type of load as primary or secondary, as well as the assigned load category.

It is worth noting that, while the divertor preload (Steps 2) is generally considered a secondary load, as it does not contribute to the global equilibrium of the system but rather induces internal stresses within the structure, in this analysis it has been **treated as a primary load**. This choice was made to adopt a conservative approach, ensuring that the effects of the preload are fully accounted for in the structural verification.

Regarding the disruption load, although it would reasonably be classified as a Category 3 load, it has been treated as an operational load in the simulation. This conservative choice allows the disruption to be considered on the same footing as other operational loads, ensuring that the structural assessment captures the most critical load conditions safely.

Table 21 – Load steps

Step	Active load (Cumulative)	Type of load	Category
1	Bolt pretension (locked after the first step)	2S	1
2	20kN preload	1S	1
3	Knuckle pin contact activation	-	-
4	Knuckle pin contact activation	-	-
5	Dead weight	1S	1
6	Dead weight + 5 MPa nominal operating pressure	1S	1
7	EM loads force distribution application	1S	1
8	Map of temperature	2S	1

Seismic loads were deliberately excluded from the structural simulation. The acceleration magnitudes reported in the seismic spectra (see [inserire riferimento]) were significantly lower than those associated with other operational and non-operational loads. Therefore, the seismic loads were considered negligible in comparison and were not included in the analysis, allowing the focus to remain on the dominant loading conditions affecting the divertor.

- **Bolt pretension (STEP 1)**

The pretension action applied to the bolts was referred, as is customary in this type of analysis, to the smooth shank of the bolt. Being the portion of the bolt free to deform, the smooth shank is the region where the pretension force is effectively applied (as discussed in the section on contact definitions). Figure 154 illustrates both the location and the schematic representation of the pretension applied to the bolts.The bolts themselves were modeled as high-strength steel, grade A70. The pretension values reported in Table 22 were selected in accordance with the

relevant standard, ensuring that the applied forces remain within the allowable range for the chosen material while achieving the desired preload.

It should be noted that the chosen pretension values are necessary to maintain a proper compression of the flanged surfaces throughout the analysis.

Specifically, the preload ensures that the back plates on their respective faceted surfaces, the knuckle interface on the cassette, and the nose on the cassette remain sufficiently preloaded even under disruptive events.

This prevents any detachment of the aforementioned surfaces and guarantees continuous contact throughout the most critical loading conditions.

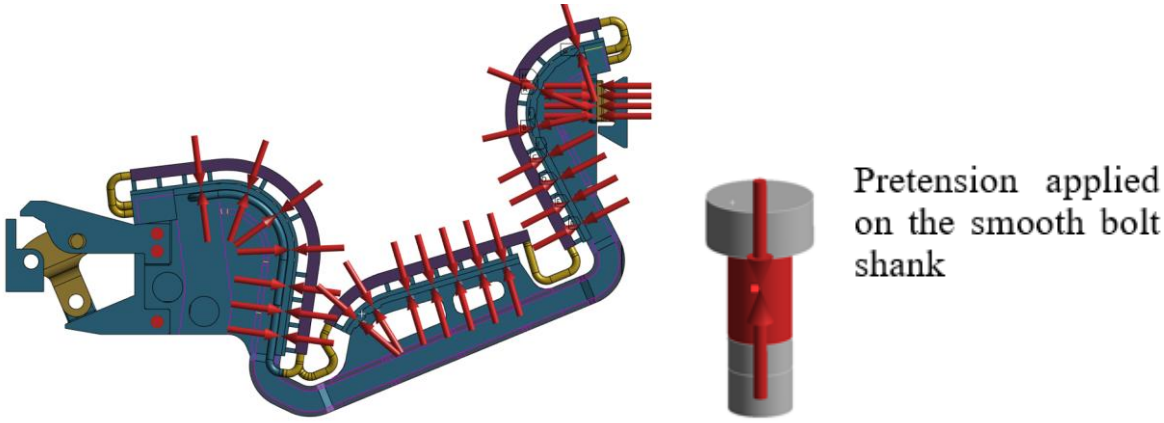

Figure 154 Bolt pretension application

Table 22 Bolts dimension and applied preload

Bolted Connection	**Pretension (kN)**	**Dimension**
IVT back plate - flanges	21.3	M10
Dome back plate - flanges	21.3	M10
OVT back plate - flanges	21.3	M10
Nose – cassette body	17	M8
Knuckle case – cassette body	44	M12

- **Preload (STEP 2)**

The preload is applied through forces exerted on appropriately defined construction surfaces that replicate the interface between the mechanical jack and the cassette (Figure 155). The evaluation of the preload magnitude has already been detailed in a previous section. As described in the section on the fixation system, in reality the mechanical jack has been replaced by the knuckle-geared system. Therefore, in the actual assembly, the preload is applied through the action of the worm gear on the head of the knuckle.In the simulation, the preload is instead applied at the knuckle–cassette interface, on the surfaces that were originally designated for the application of the preload by the mechanical jack. Although this does not exactly replicate the real preload path, it does not affect the validity of the analysis, since the knuckle-geared system has been designed to exert an action equivalent to the 20 kN preload applied by the mechanical jack. Consequently, the two actions can be considered equivalent for the purpose of the structural verification of the cassette body.

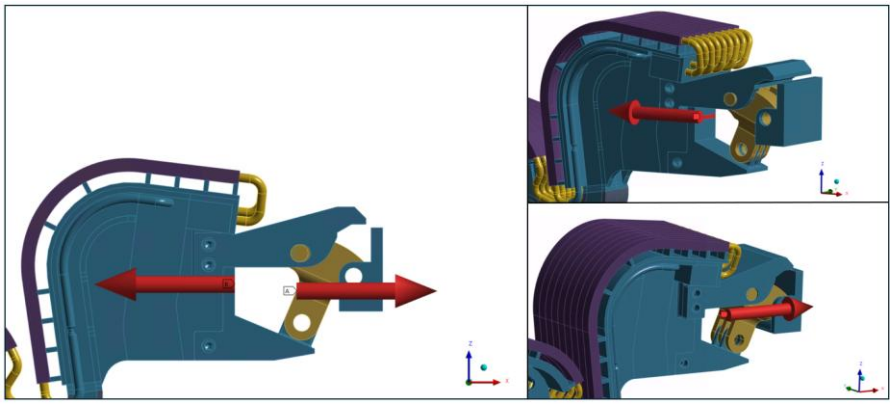

Figure 155 Preload applied on knuckle case-knuckle surfaces

- **Knucle pins contact activation (STEP 3-STEP 4)**

Once the preload action was applied, it was subsequently deactivated, and at the same time the contact between the knuckle pins and the corresponding holes on the cassette interface was activated. In this way, the preload is no longer maintained as an externally applied force acting on construction surfaces; instead, the cassette is brought into its preloaded configuration and mechanically locked in that state through the activation of the pin–hole contact. This modeling strategy accurately reflects the real assembly procedure, in which the preload is applied during

installation and then retained by the mechanical engagement of the knuckle pins, rather than by a continuously applied external force

- **Dead weight (STEP 5)**

The dead weight of the divertor assembly was activated only after the knuckle pin–cassette interface contact had been fully established. Without the activation of this contact, the cassette–knuckle kinematic chain would have remained partially unconstrained, with the possibility of rotation about the axis defined by the hole on the outboard rail. This condition would have led to an ill-defined constraint system and, consequently, to a lack of convergence of the analysis.By activating the pin–hole contact prior to the application of the dead weight, this issue was effectively avoided, ensuring a stable mechanical configuration and a convergent solution.

- **Pressure (STEP 6)**

Before discussing the application of the operating pressure, a clarification is required. The divertor cassette cooling system is a closed circuit; therefore, under normal operating conditions, the internal pressure is naturally balanced. In the present simulation, however, only the holes corresponding to the feeding pipe stubs were modeled, while the full geometry of the feeding pipe system was not included.

As a consequence, the feeding pipe holes represent open pressure surfaces. In the real system, these interfaces would be closed by the feeding pipes, and an equivalent counter-pressure would act on the opposite side of the holes, balancing the hydraulic forces. Since this counteracting pressure is not inherently present in the model, an unbalanced force arises due to the missing closure of the pipe interfaces.

This force imbalance is therefore a modeling artifact associated with the simplified representation of the cooling system and must be properly accounted for in the analysis. The estimation of the resulting unbalanced force is detailed in the following section.

Therefore, a normal operating pressure of 5 MPa has been applied to the inner surfaces exposed to cooling water flow, highlighted in red in Figure 156. The pressure is defined as acting normal

to the application surfaces, accurately representing the hydraulic loading conditions during operation (see [92]).

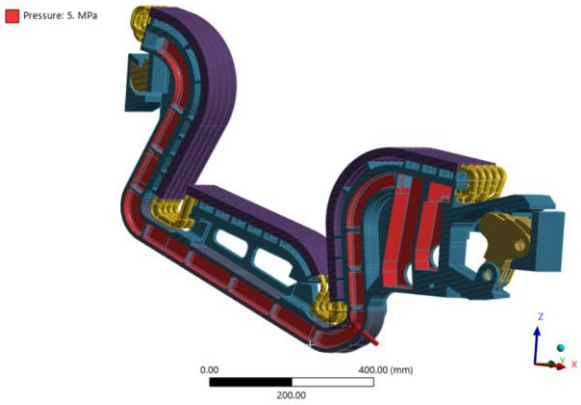

Figure 156 Surfaces subjected to normal operating pressure

- **EM load distribution (STEP 7)**

DTT has access to an extensive database of plasma disruption scenarios and many more have been computed through MAXFEA and other dedicated codes. Among these, the most relevant scenarios for in-vessel components, such as the divertor, include slow downward and slow upward disruptions with a current quench duration of 40 ms, as well as fast downward and fast upward disruptions with a current quench duration of 4 ms (see Figure 157). These scenarios have been systematically used over the past years to support the iterative design process of the DTT in-vessel components, in particular the inner vertical target.

Class of event	CQ [ms]	TQ init event	Halo onset	Axi-sim halo factor	Ip at TQ [MA]	Eddy max on VV - during CQ [MN]	Fz max on VV (Eddy+Halo) - during CQ [MN]
UVDE FAST	~4	@q95=2	@q95=2	~0.16	5.5	~5.29	~3.33
UVDE SLOW	~40	@q95=2	@q95=2	~0.29	5.5	~3.60	~6.77
DVDE FAST	~4	@q95=2	@q95=2	~0.50	5.5	~5.16	~-5.44
DVDE SLOW	~40	@q95=2	@q95=2	~0.60	5.5	~3.46	~-13.10

Figure 157 - Disruptive event classification

As discussed in the section dedicated to the benchmarking of MAXFEA disruption analyses against JOREK simulations, the slow downward disruption has been identified as the most critical scenario for the divertor.

Form Figure 158 to Figure 161 the comparisons of the electromagnetic load resultants acting on the whole divertor and on its main subcomponents are reported. Both Lorentz force

resultants and moment resultants with respect to the machine center are shown, comparing the fast downward and slow downward disruption scenarios. In addition, Table 23, summarizes the peak values of the force and moment resultants for the considered cases. Based on these peak values, the slow downward disruption clearly emerges as the most severe loading condition.It is worth noting that this type of comparison, based solely on global force and moment resultants, may in some cases be misleading. Disruption scenarios characterized by higher global electromagnetic resultants are not necessarily more severe from a structural standpoint than scenarios with lower overall resultants. This is due to the complex and non-intuitive nature of electromagnetic load distributions and the associated load transfer mechanisms. Localized peaks of electromagnetic forces may occur and be partially or fully counterbalanced by forces of opposite sign acting in other regions of the structure, leading to reduced global resultants while still inducing high local stresses.To avoid misinterpretation in the identification of the most critical disruption scenario, a double check was performed by running the structural analysis considering both the fast downward and slow downward electromagnetic load distributions. As expected, the slow downward disruption proved to be the most demanding condition for the divertor. This outcome is consistent with the strong interaction of halo currents with the divertor structure during the current quench phase and with the higher magnitude of halo currents associated with this disruption scenario

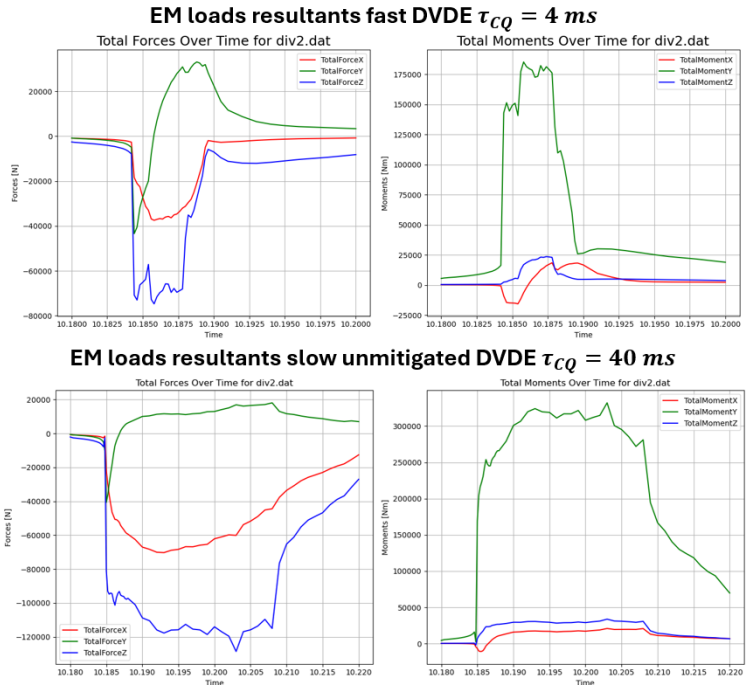

Figure 158 Divertor EM loads resultant comparison (fast-slow disruptive event)

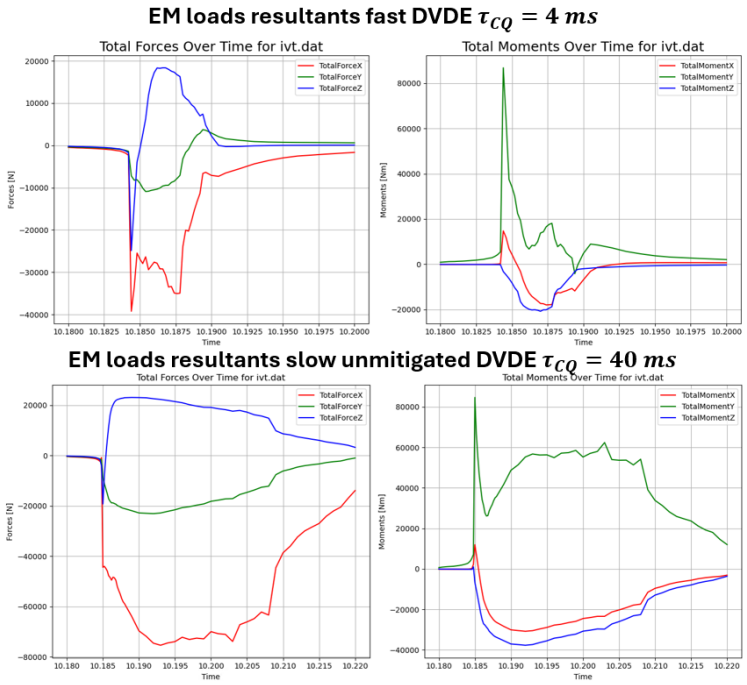

Figure 159 IVT EM loads resultant comparison (fast-slow disruptive event)

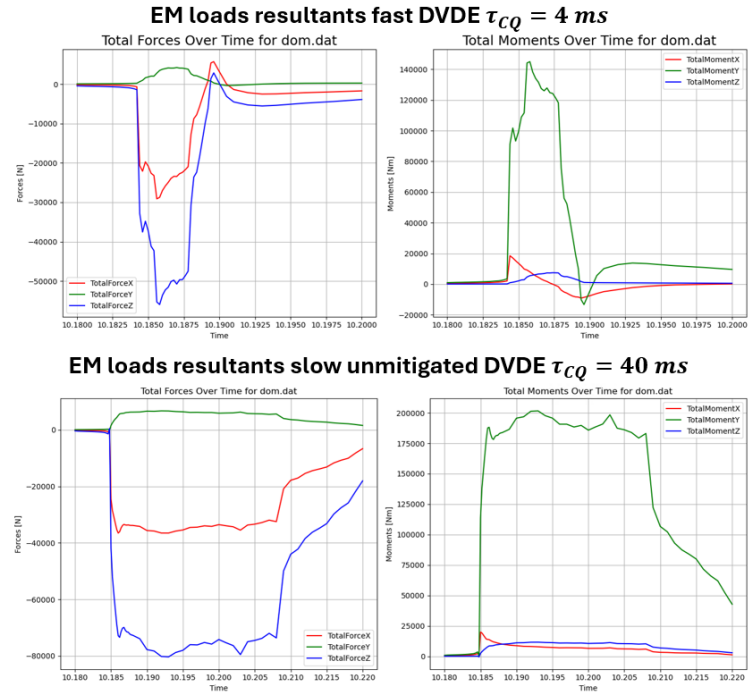

Figure 160 DOME EM loads resultants comparison (fast-slow disruptive event)

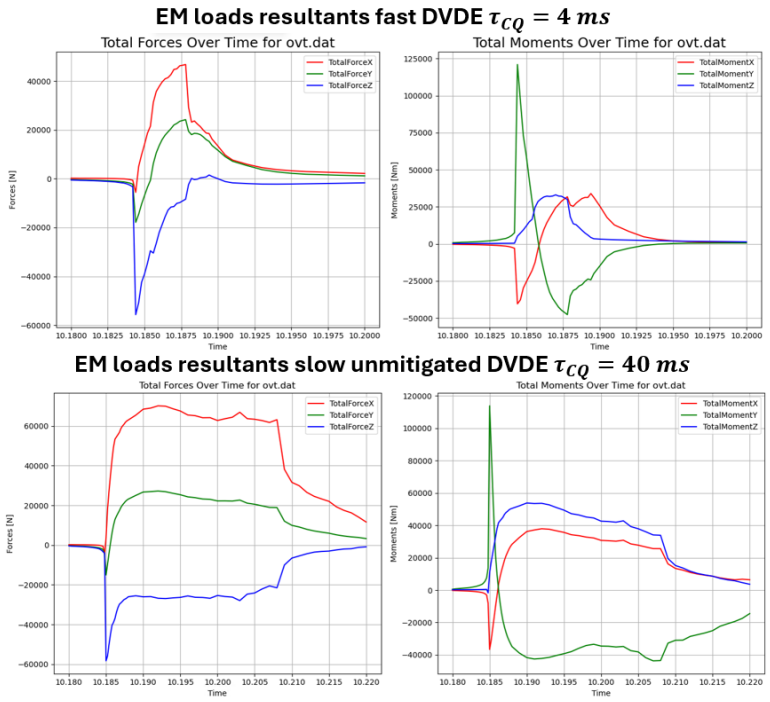

Figure 161 OVT EM loads resultants comparison (fast-slow disruptive event)

Table 23 Comparison EM force and moment resultants of fast and slow disruptive event

EM resultants	***fast 4 ms CQ***	***slow 40ms CQ***
$\lvert F_{x_{max}}\ (kN)\rvert$	37	70
$\lvert F_{y_{max}}(kN)\rvert$	43	17
$\lvert F_{z_{max}}\ (kN)\rvert$	75	128
$\lvert M_{x_{max}}\ (kN * \mathrm{m})\rvert$	18	20
$\lvert M_{y_{max}}\ (kN * \mathrm{m})\rvert$	185	332
$\lvert M_{z_{max}}\ (kN * \mathrm{m})\rvert$	23	34
$F_{tot}\ (kN)$	94	145
$M_{tot}\ (kN * m)$	187	334

Therefore, the EM loads related to a slow Hot Downward VDE with a Current Quench duration of 40 ms have been used as input for the structural assessment performed on the current design. he disruption is triggered at the End of the Flat Top of a SN scenario at full power (5.5MA and 6T at the magnetic axis).

The load distribution related to the most critical time step has been interpolated on the structural mesh.A python routine has been generated to evaluate, from the shared EM loads data, the input loads for the structural assessment.

Input:

- .dat files related to EM force densities overtime on each DIV component

Output:

- .csv of forces on elements centroid acting on each DIV component
- Time step related to most burdening loads overtime (whole div structure considered)
- .csv of forces on elements centroid of each DIV component in the most critical time-step
- Forces and moments resultants calculation and plot

As can be seen in Figure 163 at 10.203 s the higher global vertical force resultant and consequentially toroidal moment resultant occur. Therefore, it has been identified as the most critical time step. Through the .py routine mentioned above, the force distribution at 10.203s has been extracted and used as input for the simulation. Figure 162, shows the interpolated vectorial Lorentz force field acting on the divertor

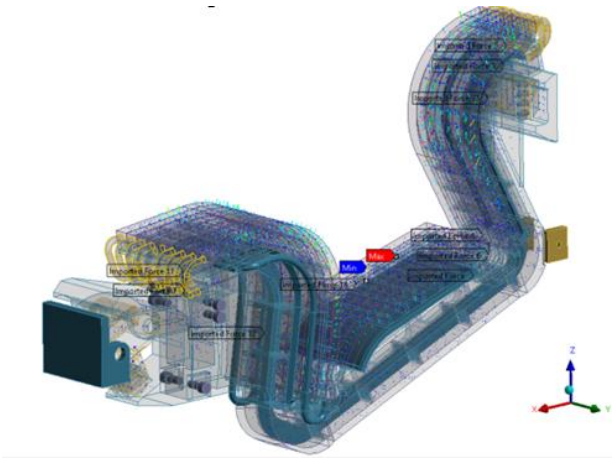

Figure 162 EM force distribution map imported on divertor structural model

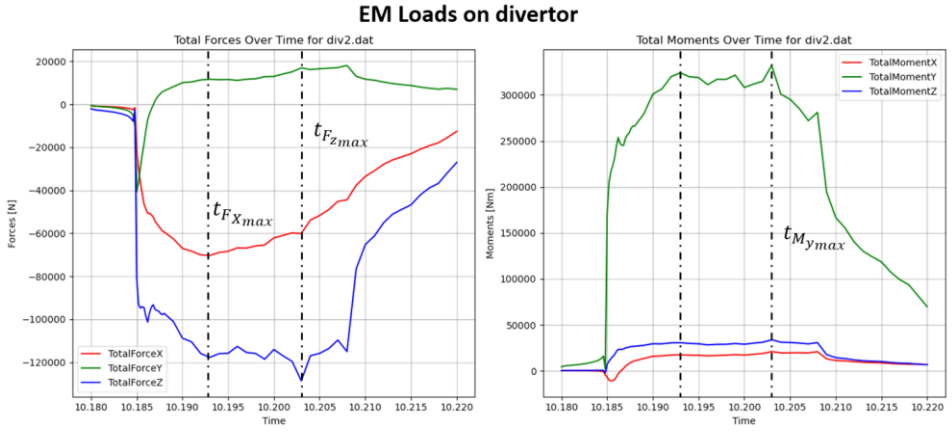

Figure 163 – Force and moment resultants overtime (slow DVDE with 40 ms current quench duration)

Although the time instant of 10.203 s was chosen for the simulation (as previously explained), another time point—closer to the Thermal Quench phase of the disruption and corresponding to the peak of the radial force (Fx in Figure 163)—was also analyzed.The justification for selecting 10.203 s lies in the fact that the stress induced in the structure at the time of the highest radial forces was less severe than that caused by the highest vertical resultant force.

- **Temperature distribution (STEP 8)**

It is important to note that the thermal map applied in the final step of the structural analysis is derived from a steady-state thermal simulation, which considers the heat flux incident on the exposed surfaces of the cassette body (Figure 165), an initial temperature of 60 °C and a temperature of the inner shell surfaces directly interfaced with the cooling water, of 60 °C .

The heat fluxes have been applied following the map shown in (Figure 164), the map refers to the heat flux on the PFC outline, and on the pipes placed above the elbows of the cassette.

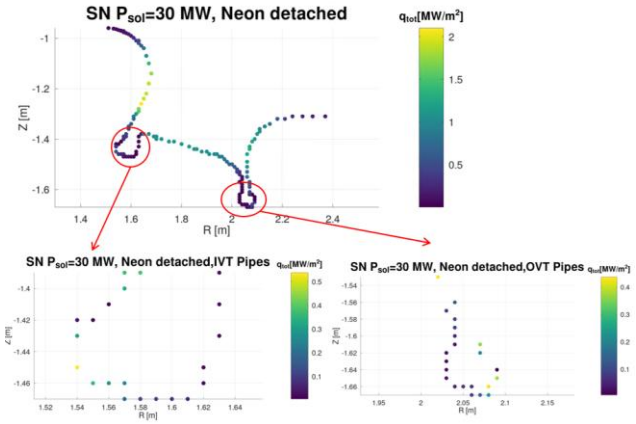

Figure 164 Heat flux map on PFC and pipes centerlines

To be conservative a heat flux value of 0.1 W/m^2 has been imposed uniformly on the underlying surfaces of the elbows, even though in reality the shadows of the pipes on the elbow's surfaces should be considered.

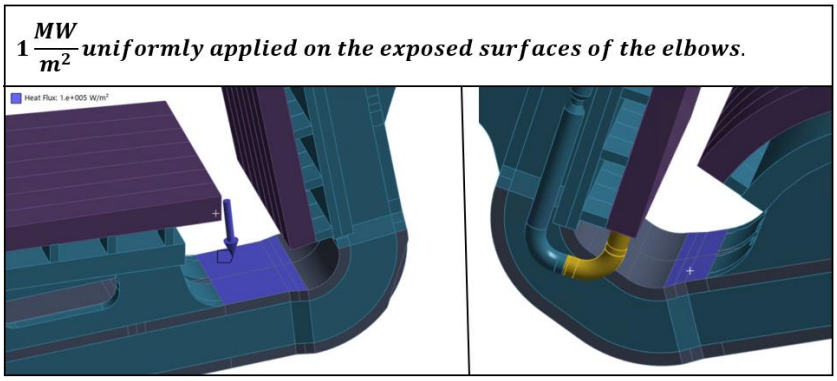

Figure 165 Elbow's surfaces affected by direct heat flux

The thermal interaction between the Plasma Facing Units (PFUs) and the cassette body has been deliberately excluded from this assessment.This exclusion is justified, firstly, by the fact that such interaction falls outside the scope of the present structural verification, and more critically, by its primary relevance to the dedicated PFU design process.Furthermore, it is assumed that the thermal decoupling between the PFU and the cassette body is physically sound under normal operating conditions.Specifically, the high velocity of the cooling water circulating within both the PFU cooling pipes and the internal channels machined into the cassette body ensures extremely efficient heat removal.As a result, the thermal gradient across each monoblock becomes negligible, and the temperature field stabilizes near the cooling water temperature within a short distance from the plasma-exposed surface—typically within the midsection of the PFU pipe.Consequently, the supports of the PFUs, as well as the underlying structural elements of the cassette body, are assumed to remain thermally unaffected by the plasma interaction and the intense heat flux absorbed by the PFUs.This assumption allows the structural assessment to proceed without incorporating complex thermal coupling effects that would otherwise introduce minimal influence on the cassette body's mechanical response.Figure 166 shows the temperature contour result of the steady state simulation, the whole cassette body reaches 60 °C of temperature with the exception of the elbows where the temperature goes up to 160 °C. The thermal map has been therefore imported from the steady state analysis block to the static structural for the verification.

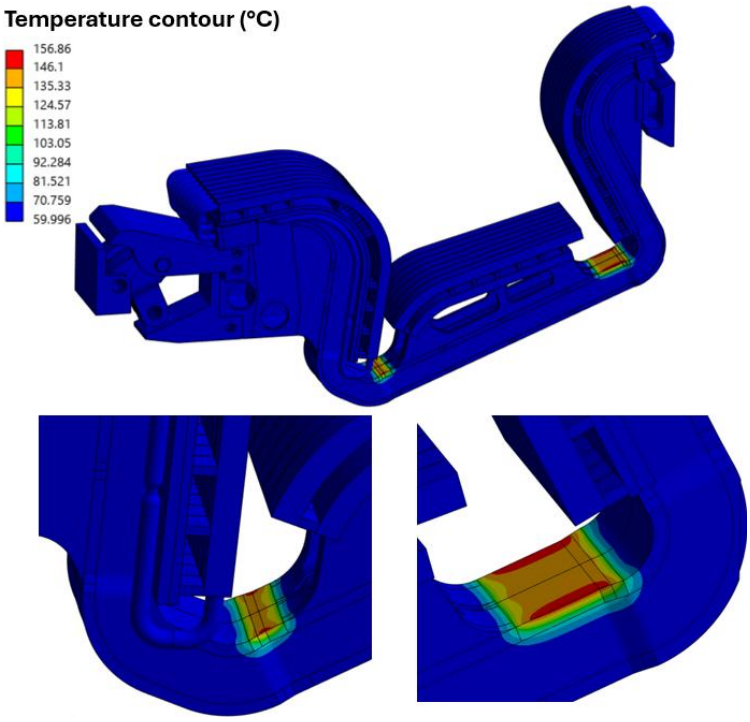

Figure 166 Thermal map result of the thermal steady state simulation

5.3.5 Slow DVDE scenario EM load distribution interpolation

A suited .py routine has been generated to compare the force and moment resultants of the force distribution interpolated on the structural mesh and the source EM force distribution. The check has been done considering both the whole divertor (Figure 167) and each one of its main sub systems (Figure 168).

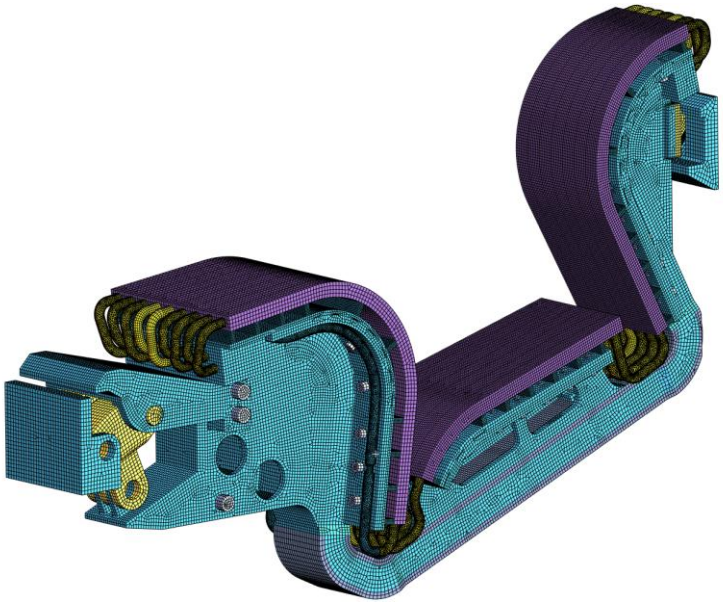

Figure 167 Divertor mesh

Since the most relevant loads are related to the PFCs and to the main shell of the divertor cassette body, herein only the comparative checks done on those sub systems are shown.

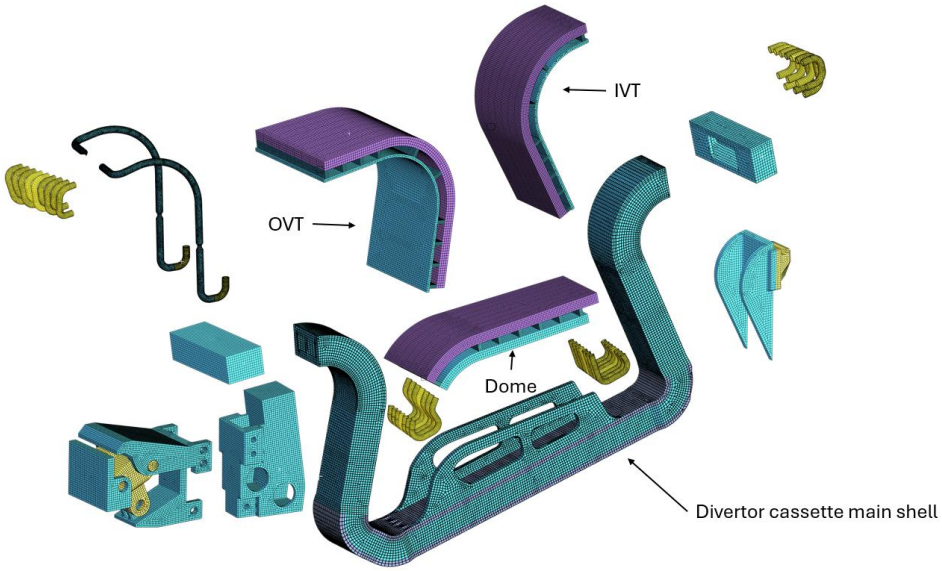

Figure 168 Divertor FEM subsystems

Table 24,Table 25,Table 26,Table 27, Table 28, include the results of the check. The moments are computed considering the origin of the Global Coordinate System as pole.

Table 24 - Force and moment resultants comparison between force distribution on structural mesh and source EM on whole divertor

Divertor			
Component	**Source_EM**	**Interpolated**	**Percentage_Error (%)**
ForceX [N]	-60117.90767	-56044.80765	-6.77518593
ForceY [N]	16929.89756	15007.75298	-11.35355117
ForceZ [N]	-128634.2963	-115695.9662	-10.05822749
MomentX [N*mm]	20887.84439	18710.89865	-10.42206987
MomentY [N*mm]	332055.0229	301055.1285	-9.33577036
MomentZ [N*mm]	33772.09987	30446.61076	-9.846853219
Force_Total [N*mm]	142994.9875	129428.7824	-9.487189283
Moment_Total [N*mm]	334420.9847	303168.7389	-9.345180852

Table 25 Force and moment resultants comparison between force distribution on structural mesh and source EM on Inner vertical target (PFU + PFU supports+IVT back plate)

Inner vertical target			
Component	**Source**	**Interpolated**	**Percentage_Error (%)**
ForceX [N]	-73846.17821	-72799.14131	1.417861997
ForceY [N]	-17115.77957	-16963.18357	0.89155154
ForceZ [N]	17641.51862	17558.9567	-0.467997774
MomentX [N*mm]	77829.50036	76783.99269	-1.343330821
MomentY [N*mm]	-23419.25787	-23096.57758	1.377841658
MomentZ [N*mm]	62357.08505	61149.25491	-1.936957348
Force_Total [N*mm]	-29714.88499	-29351.47528	1.222988755
Moment_Total [N*mm]	72937.24758	71653.27887	-1.760374503

Table 26 Force and moment resultants comparison between force distribution on structural mesh and source EM on Outer vertical target (PFU + PFU supports+OVT back plate)

Central target			
Component	**Source**	**Interpolated**	**Percentage_Error (%)**
ForceX [N]	-35482.4432	-35618.68854	-0.383979587
ForceY [N]	6298.148359	6138.963306	-2.527489739
ForceZ [N]	-79539.22686	-78981.77011	0.700857642
MomentX [N*mm]	87322.15674	86859.06892	-0.530321098
MomentY [N*mm]	6.936602072	6.733387388	-2.929599842
MomentZ [N*mm]	198.4497266	197.6448675	-0.405573281
Force_Total [N*mm]	11.26685369	11.02061813	-2.185486478
Moment_Total [N*mm]	198.8903025	198.0663681	-0.414265723

Table 27 Force and moment resultants comparison between force distribution on structural mesh and source EM on central target (PFU + PFU supports+IVT back plate)

Outer Vertical Target			
Component	**Source**	**Interpolated**	**Percentage_Error (%)**
ForceX [N]	66889.23292	66752.63896	-0.204209188
ForceY [N]	22672.4357	22648.39965	-0.106014427
ForceZ [N]	-27942.02127	-28040.38099	-0.352013642
MomentX [N*mm]	75953.70546	75862.55849	-0.120003324
MomentY [N*mm]	30.76868385	30.72529954	-0.141001499
MomentZ [N*mm]	-34.79759142	-34.34599042	1.29779383
Force_Total [N*mm]	42.75993416	42.80669298	0.109351943
Moment_Total [N*mm]	63.13474673	62.89756795	-0.375670743

Table 28 Force and moment resultants comparison between force distribution on structural mesh and source EM on Cassette body main shell

Cassette Body			
Component	**Source**	**Interpolated**	**Percentage_Error (%)**
ForceX [N]	-8655.635841	-10181.00221	-17.62281131
ForceY [N]	5.653352626	-471.1212049	-
ForceZ [N]	-7114.70089	-6276.229192	11.78505901
MomentX [N*mm]	11204.42022	11969.36983	6.827212759
MomentY [N*mm]	-141.733423	-838.9673353	-
MomentZ [N*mm]	28079.40913	29029.6524	3.384128445
Force_Total [N*mm]	815.4460644	-20.92988189	-
Moment_Total [N*mm]	28091.60476	29041.78064	3.382419388

The loads interpolated on the cassette body are the one affected by the highest inaccuracy.The reason behind the discrepancy between the resultants of the input source loads and the interpolated one is twofold:

- The structural mesh matches the CAD geometry with major accuracy if compared to the EM one, and is way finer, therefore the interpolation has to be done considering a load transfer between a certain number of source points to a set of target points extremely wider.
- The Electromagnetic mesh in few regions, particularly the surrounding of the attachment systems, doesn't match the geometry and moreover few regions of the EM mesh include geometry out of the CAD bounding box used as input for the simulation (and also for the EM calculation). This geometry discrepancy affects mainly the central shell of the cassette body and the attachment systems both because the needed simplifications for the EM calculations and also for the further modifications that the cassette has been subject previously the sharing of the EM loads distributions. As can be seen in **Error! Reference source not found.**the interpolation error is way higher on t he cassette (this event appens actually also because the loads on the cassette are lower if compared to the load acting on the PFC).

Differently the computed errors on the structural mesh of the PFCs are very low since the simulation geometry/mesh is very close to the mesh used for the EM calculations.

5.3.6 Solutions options and procedure

The solution has been carried out activating time spring. Weak springs are typically added to prevent rigid body motion in under-constrained models. Their stiffness is chosen to be several orders of magnitude smaller than that of the actual system, so they do not influence the physical behavior of the structure. As a result, the simulation results remain unaffected, provided the model is otherwise well-defined. The weak springs only serve as a numerical stabilization aid and not as a source of significant structural stiffness or load path. In particular where frictional contacts have been defined, the weak springs definition will help in this ways:

- Frictional contacts are nonlinear and may behave like loosely connected or initially open interfaces. This can cause instability or "floating" parts in the absence of sufficient constraint.
- Weak springs prevent uncontrolled rigid body motion before contact is fully established, giving the solver a stable starting point.

They allow the solver to detect contact more easily by keeping parts close enough for contact detection, especially in models with gaps or no initial contact pressure

Although introduced as a safety measure, the weak spring option could have been avoided, since the analysis was also completed successfully without its activation. The analysis is divided into 6 steps as already discussed in Loads . The definition of sub steps within each time step has been left program-controlled. Based on prior experience, various sub stepping strategies have been tested — involving both increases and decreases in the number of sub steps per time increment. It is important not to be misled by the presence of a time parameter, as the analysis is not dynamic. However, ANSYS Mechanical, even in static structural analyses, when non linearity must be accounted, employs a cumulative load application across time steps using the Newton-Raphson iteration method. For this reason, sub step definition is critical to avoid abrupt load increases that could result in non-convergence. That said, the program-controlled time stepping was ultimately adopted, as it produced results consistent with those obtained using manual stepping, while also reducing overall simulation time. In ANSYS Workbench, when substepping is set to "Program Controlled" for a nonlinear analysis, the

solver employs an adaptive implicit integration scheme—typically based on the Newmark method, which is conditionally stable in nonlinear cases—automatically adjusting time step sizes to maintain numerical stability and ensure convergence based on the degree of nonlinearity and solution behavior. The solver type has been left program controlled. Based on the defined model, ANSYS Workbench automatically determines and applies the most appropriate solver setting to ensure reliable and efficient analysis. A Direct Sparse solver has been used; the reason behind this choice (made automatically by Mechanical APDL) is that:

- Elements using u-P formulation (typically used in incompressible materials or advanced contact).
- Or MPC184 elements with Lagrangian multipliers (used for constraints like joints or couplings).

These elements require the direct solver due to their numerical complexity and convergence needs. ANSYS automatically overrode the solver setting to ensure stability.

The total mass of the engineering model is slightly higher than that of the CAD model. This increase is primarily due to geometric simplifications, such as the removal of internal 15 mm diameter holes within the PFC finger tiles and the omission of internal pipe geometries.

These features, present in the CAD model, were excluded from the engineering model to maintain consistency with the Electromagnetic model and to improve interpolation results. Despite these changes, the center of mass remains very close to that of the original CAD geometry, and the resulting mass distribution remains reasonable. The simplifications are considered conservative and do not compromise the reliability of the structural analysis.

The occurrence of a slightly higher engineering model total mass, is conservative in terms of stress and displacement predictions, as a higher mass generally leads to increased inertial and structural loads. This discrepancy arises primarily due to modeling simplifications.

In the CAD model, each PFC finger tile (represented as a set of aligned monoblocks) includes an internal 15 mm diameter hole running along the centerline of the finger's length, making it a hollow geometry. However, in the engineering model, this internal hole has been removed in all PFC fingers.

This modification was made for two reasons: To ensure consistency with the EM (Engineering Model), which does not include internal hollow features. To improve load interpolation and structural behavior under applied loads, by simplifying the mesh and avoiding numerical instabilities associated with thin-walled features.

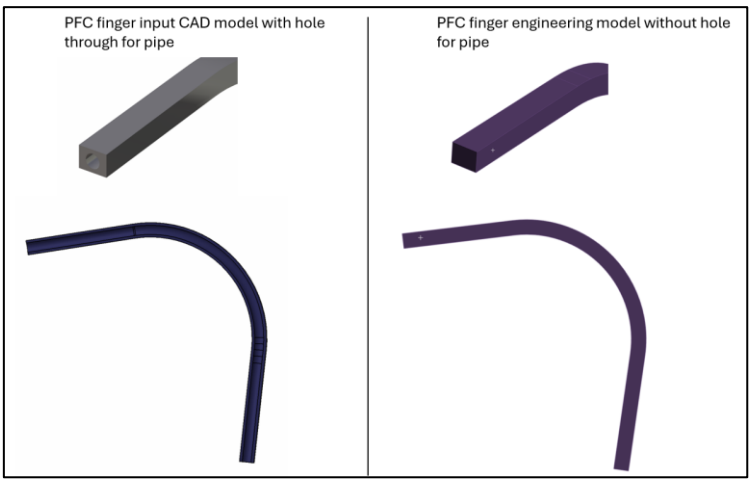

Figure 169 CAD model PFC finger – Engineering model PFC finger (i.e. OVT in figure)

Additionally, while the CAD model includes internal pipe geometries running through each individual finger, these have also been omitted in the engineering model to remain aligned with the EM model approach, which does not account for internal pipework within the PFC fingers.

As shown in the comparison between the inner cross-sections of the CAD and engineering PFC models, these simplifications contribute to the observed increase in mass but do not negatively impact the structural integrity or the conservative nature of the analysis.

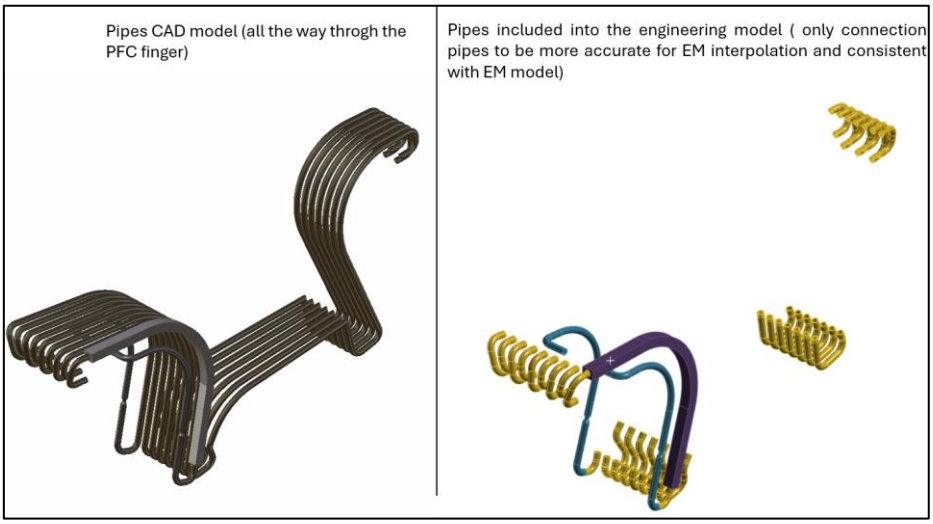

Figure 170 CAD model PFU pipes – Engineering model PFU pipes

Table 29 reports the mass and the center of mass coordinates for Divertor CAD and engineering model and as can be seen the differences are low and reasonable.

Table 29 Comparison between mass and center of mass coordinate of CAD model and engineering model

	Mass (kg)	X (m)	Y(m)	Z(m)
DIV CAD model	303	2.015	0.003	-1.373
DIV Engineering model	323	2.002	-0.006	-1.370
Δ (m)	20	0.013	0.063	0.003

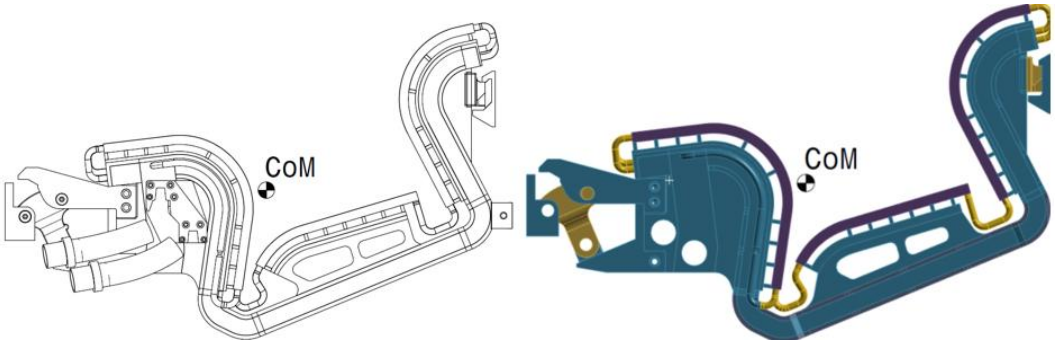

Figure 171 (Right)CAD model Center of Mass position-(Left) Engineering model center of mass position

Before discussing the constraint reactions a premise is needed. Since the Divertor cassette cooling system is closed, the pressure should be naturally balanced. If the simulation considers only the holes of the feeding pipes (Figure 172)—excluding the full geometry of the feeding pipe system—then these holes must be closed and an equivalent pressure to the internal water pressure must be applied. Otherwise, the lack of closure would result in a net force due to the missing counter-pressure. In a physically pressurized system, a counter-pressure would normally act on the opposite side of the holes, balancing the force. Without this, an imbalance occurs, resulting in a net lateral force in the direction of the applied pressure.

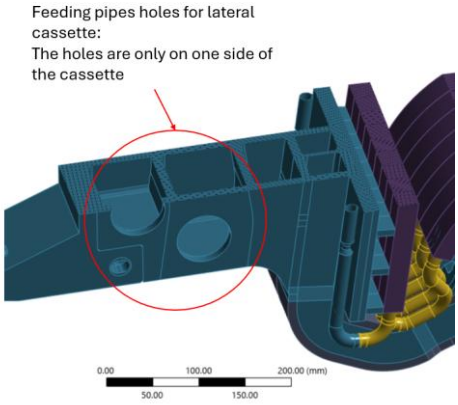

Figure 172 Section view of engineering model highlighting the feeding pipes holes only on one side

To estimate the magnitude of this unbalanced force:

- Parameters:
  - Pressure: $P = 5\,MPa = 5 * 10^6\,Pa$
  - Hole diameter: $d = 0.06\,m$
  - Number of holes: 2

Area of a single circular surface:

$$A = \pi * \left(\frac{d}{2}\right)^2 = \pi * (0.03)^2 \approx 0.002827\,m^2$$

Force on one hole surface:

$$F = P * A = 5 * 10^6 * 0.002827 \approx 14{,}135\,N$$

Total unbalanced force (2 holes):

$$F_{net} = 2 \times 14{,}135 = 28{,}270\,N\ (approximately\ 28.3\,kN)$$

Table 30, *Table 31*, *Table 32*,

Table 33 report the reaction forces at the fixed supports and at the compression-only support at each time step. Additionally, provide the reaction induced by each individual load by calculating the difference between the reactions in the step where the load is applied and the reactions at the previous step. In Step 4, both the dead weight and the pressure load are applied simultaneously, making it difficult to isolate their individual contributions to the support reactions. However, it is important to note that, aside from the previously evaluated 28 kN of reaction force due to pressure imbalance, the pressure does not significantly influence the total reaction over the entire boundary system. Therefore, the vertical reaction component observed in Step 4 is primarily attributed to the self-weight of the structure. That said, due to the particular geometry of the divertor, the pressure load tends to induce an opening effect: it pushes the outboard branch of the cassette outward and the inboard branch inward. This deformation can contribute to additional vertical reaction forces required to maintain equilibrium.

Table 30 Force reactions on fixed supports

STEP	Active load	Fx (N)	Fy (N)	Fz (N)	Ftot (N)
1.	Preload	-4.39	-3.09	0.07	5.37
2.	Preload	-4.39	-2.74	0.07	5.18
3.	Preload	-4.11	-15.05	0.08	15.60
4.	Preload + DW + Pressure	-5146.20	24654.00	4314.20	25552.00
5.	Preload + DW + Pressure + EM loads	50935.00	6294.70	119980.00	130490.00
6.	Preload + DW + Pressure + EM loads + Thermal distribution	50936.00	6314.70	119980.00	130500.00

Table 31 Force reactions on compression only support (lower stop)

STEP	Active load	Fx (N)	Fy (N)	Fz (N)	Ftot (N)
1.	Preload	0.01	18.00	0.00	18.00
2.	Preload	0.00	6.90	0.00	6.90
3.	Preload	0.01	14.46	0.00	14.46
4.	Preload + DW + Pressure	6.64	3591.80	-0.43	3591.80
5.	Preload + DW + Pressure + EM loads	22.46	7091.10	1.00	7091.20
6.	Preload + DW + Pressure + EM loads + Thermal distribution	21.37	6982.20	0.98	6982.30

Table 32 Force reaction on fixed supports due to isolated load contribution

STEP	Isolated load for reaction computation	Fx (N)	Fy (N)	Fz (N)	Ftot (N)
1.	Preload	-4.39	-3.09	0.07	5.37
2.	Preload	0.00	0.35	0.00	0.35
3.	Preload	0.28	-12.31	0.01	12.31
4.	Preload + DW + Pressure	-5142.09	24669.05	4314.12	25565.88
5.	Preload + DW + Pressure + EM loads	56081.20	-18359.30	115665.80	129848.90
6.	Preload + DW + Pressure + EM loads + Thermal distribution	1.00	20.00	0.00	20.02

Table 33 Force reaction on compression only supports due to isolated load contribution

STEP	Isolated load for reaction computation	Fx (N)	Fy (N)	Fz (N)	Ftot (N)
1.	Preload	0.01	18.00	0.00	18.00
2.	Preload	-0.01	-11.10	0.00	11.10
3.	Preload	0.00	7.57	0.00	7.57
4.	Preload + DW + Pressure	6.63	3577.34	-0.43	3577.35
5.	Preload + DW + Pressure + EM loads	15.82	3499.30	1.43	3499.34
6.	Preload + DW + Pressure + EM loads + Thermal distribution	-1.09	-108.90	-0.02	108.91

Table *34* reports the total force reactions, obtained by summing the reactions from all probed boundary condition points. As can be clearly seen, the value of Fy, induced by the pressure unbalance, at Step 4 matches the previously calculated value, while the value of vertical reaction (net with the pressure effect that tens to open the divertor) is very close to the weight load equal to $\cong \mathbf{3170}\ \boldsymbol{N}$.Furthermore, the force reactions at Step 5, which are induced by the

electromagnetic loads, are equal in magnitude and opposite in direction to the resultant of the EM force distribution interpolated over the divertor, as referenced in

Table 35.

Table 34 Total force reactions (fixed supports + compression only)

STEP	Isolated load for reaction computation	Fx (N)	Fy (N)	Fz (N)	Ftot (N)
1.	Preload	-4.38	14.91	0.07	15.54
2.	Preload	-0.01	-10.75	0.00	10.75
3.	Preload	0.28	-4.74	0.01	4.75
4.	Preload + DW + Pressure	-5135.46	28246.39	4313.69	29031.70
5.	Preload + DW + Pressure + EM loads	-56097.02	-14860.00	115667.23	129408.67
6.	Preload + DW + Pressure + EM loads + Thermal distribution	-0.09	-88.90	-0.02	88.90

Table 35 Force and moment resultants acting on divertor (Reference pole (0,0,0) of GCS)

COMPONENT	
$\boldsymbol{F_x}$ $[\boldsymbol{N}]$	-56044.81
$\boldsymbol{F_y}$ $[\boldsymbol{N}]$	15007.75
$\boldsymbol{F_z}$ $[\boldsymbol{N}]$	-115695.97
$\boldsymbol{M_x}$ $[\boldsymbol{N \cdot mm}]$	18710.90
$\boldsymbol{M_y}$ $[\boldsymbol{N \cdot mm}]$	301055.13
$\boldsymbol{M_z}$ $[\boldsymbol{N \cdot mm}]$	30446.61
$\boldsymbol{F_{tot}}$ $[\boldsymbol{N}]$	129428.78
$\boldsymbol{M_{tot}}$ $[\boldsymbol{N \cdot mm}]$	303168.74

5.3.7 Displacement results

STEP 4 Preload + Pin contacts activation

The displacement observed during the preload phase is primarily a bending of the outer branch of the cassette around its outer elbow, resulting in movement along the X and Z directions (Figure 174).The direction of the displacement in the step is therefore consistent with the applied preload. Knuckle, during the preload application undergoes a rigid rotation, that's why in Figure 173 the color bands of X displacement of knuckle body and knuckle case are opposite, this is how the component should move.After the preloading (STEP1) and once activated the contact between pin and knuckle case holes, the contact surfaces are properly in touch and the contact works as expected.

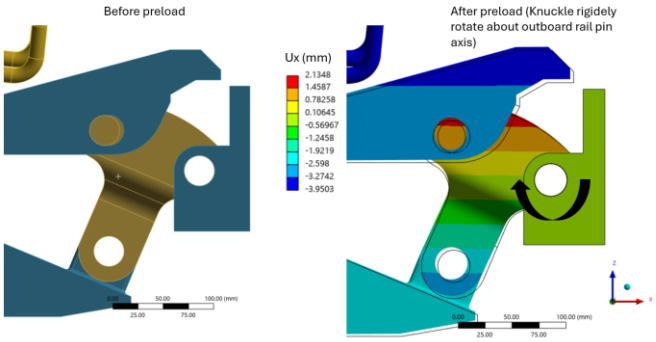

Figure 173 Knuckle rigid rotation about outboard rail pin axis during preload

The total displacement is a combination of vertical and radial components. It reaches an approximate maximum of 5 mm on the top part of the knuckle case, which is consistent with expectations, and the displacement is smooth and continuous in region of interest such as elbows highlighted in Figure 175.

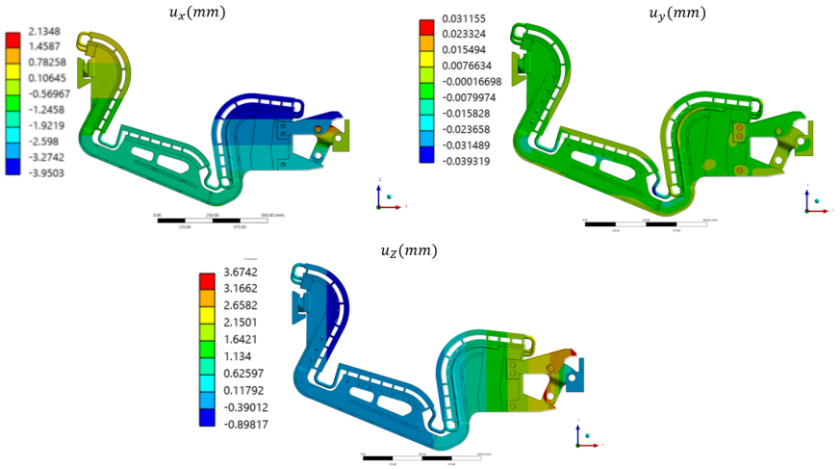

Figure 174 u_x, u_y, u_z displacement at step 4 (Preload + Pin contacts activation)

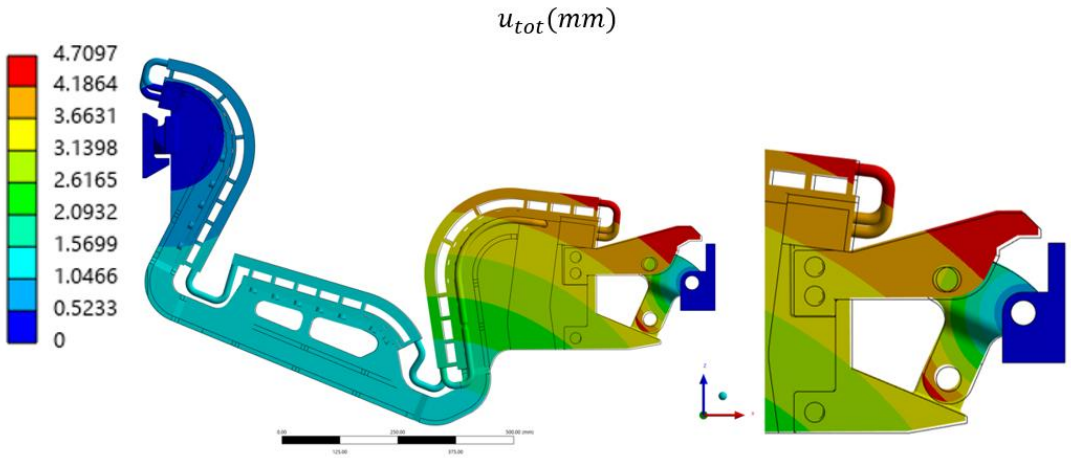

Figure 175 Total displacement at step 4 (Preload + Pin contacts activation)

STEP 5 Preload + Pin contacts activation + Dead Weight

As anticipated, the applied pressure—being unbalanced due to the omission of pressure on the end closures of the feeding pipe holes—induces a displacement of approximately 0.6 mm along the negative Y-axis. This displacement results from a net force of 28 kN acting in the same direction, which arises from the missing counter-pressure on the hole closures. This effect does not reflect the actual physical behavior of the system and represents a significant deviation between the simulated response and the expected real-world conditions.

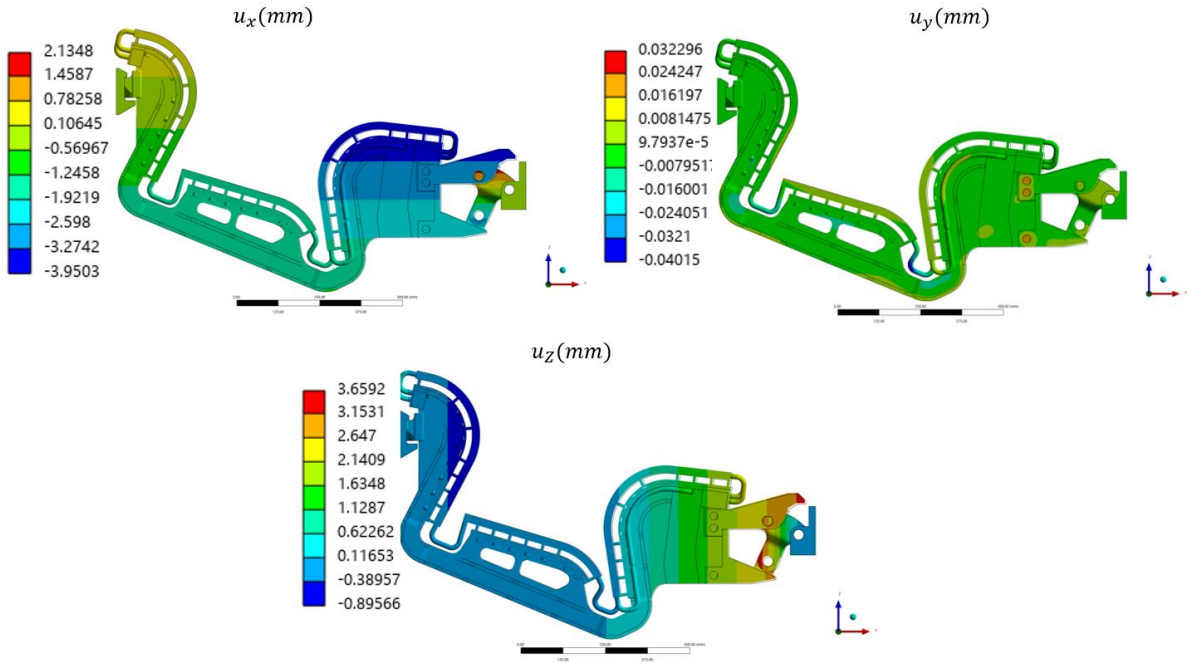

Figure 176 u_x, u_y, u_z displacement at step 5 (Preload + Pin contacts activation + Dead Weight)

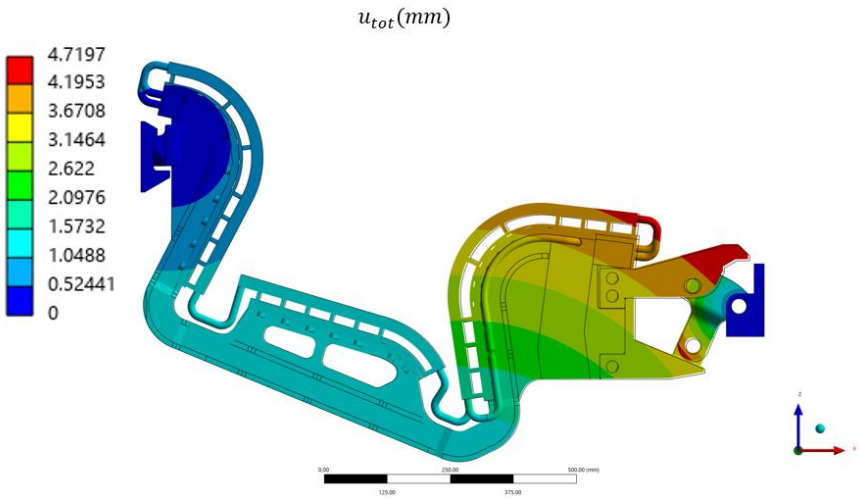

Figure 177 Total displacement at step 5 (Preload + Pin contacts activation + Dead Weight)

STEP 7 Preload + Pin contacts activation + Dead Weight + Pressure + EM loads

The lateral displacement does not exceed 1 mm, which is a positive result, since, as discussed previously, the minimum gap between two adjacent cassette PFUs is 8 mm. Therefore, the requirement that the sum of the absolute displacements between two cassettes must remain within this 8 mm limit is satisfied—at least for this disruption case. The displacement field is consistent with intuition since as can be seen in the contour plot with magnified scale of 18:1 the outboard and inboard branch of the cassette undergo opposite toroidal displacement (See Figure *179*). This is in line with the vertical positive torque, resultant of the EM load distribution that, as direct outcome, generate a tilt of the cassette around the vertical axis (running roughly in its center of mass). Moreover, the strong vertical force resultant of the EM interaction during the downward event, pushes the whole divertor down as expected.

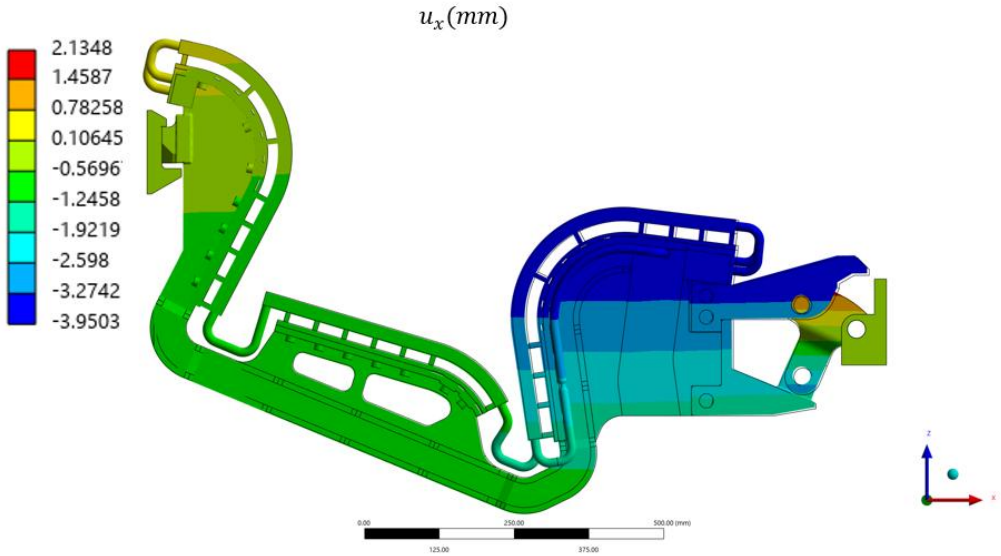

Figure 178 X displacement at step 7 (Preload + Pin contacts activation +Dead Weight + Pressure + EM loads)

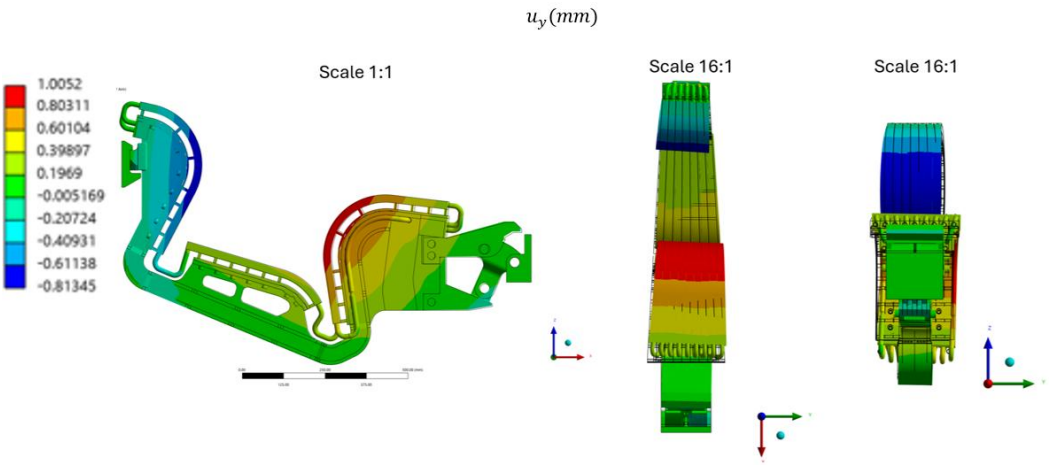

Figure 179 Y displacement at step 7 (Preload + Pin contacts activation + Dead Weight + Pressure + EM loads)

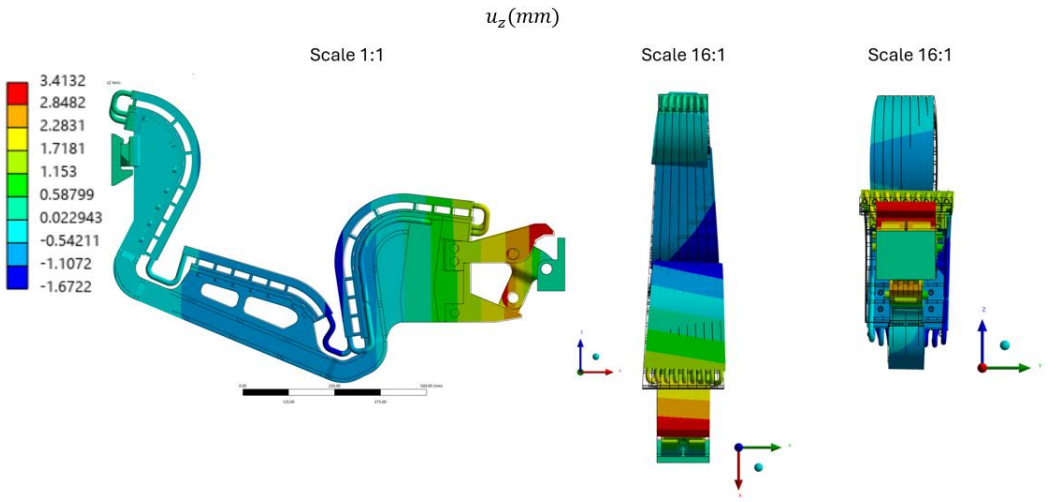

Figure 180 Z displacement at step 7 (Preload + Pin contacts activation + Dead Weight + Pressure + EM loads)

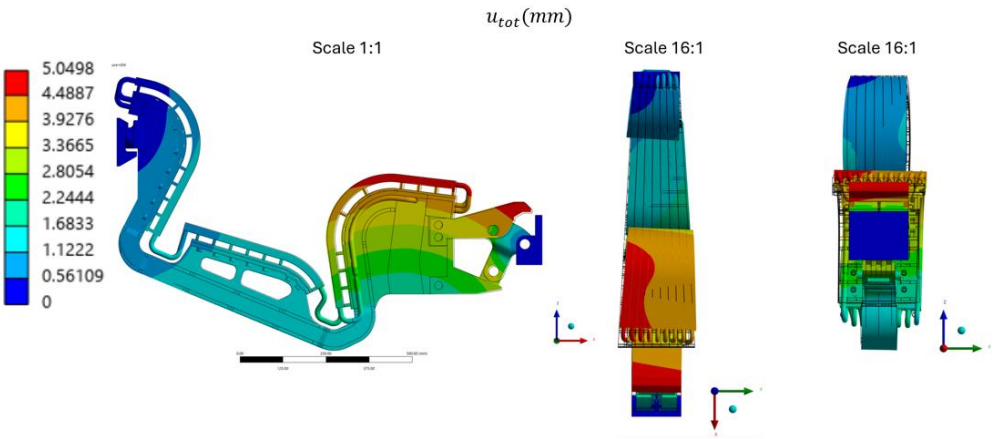

Figure 181 Total displacement at step 7 (Preload + Pin contacts activation + Dead Weight + Pressure + EM loads)

The introduction of the thermal map doesn’t lead to any significant displacement.

5.3.8 Stress results

This section presents the stress distribution at each analyzed time step . For each time step, a contour plot of the entire divertor system is provided. Additionally, depending on the specific case, a dedicated contour plot is included for the components of particular interest or those experiencing the highest stress. In all the plots the stress unit is MPa. Thanks to the quadratic element formulation and the fully connected mesh, the stress contours are smooth and continuous.

In the figures presented in this section, a 1:1 scale is assumed unless otherwise specified. The contour plots display an overlay of the deformed shape and the undeformed wireframe, generated using the embedded visualization tool in ANSYS Workbench. The stress contour are plotted using default Ansys Workbench averaging method. Moreover, even without averaging, since the element used for the mesh have quadratic formulation, there isn’t a huge stress gap between elements.

As shown in the Figure 182, most of the stress and strain after the application of the preload is concentrated in the elbows of the structure. This observation is consistent with previous studies and aligns with the expected results.

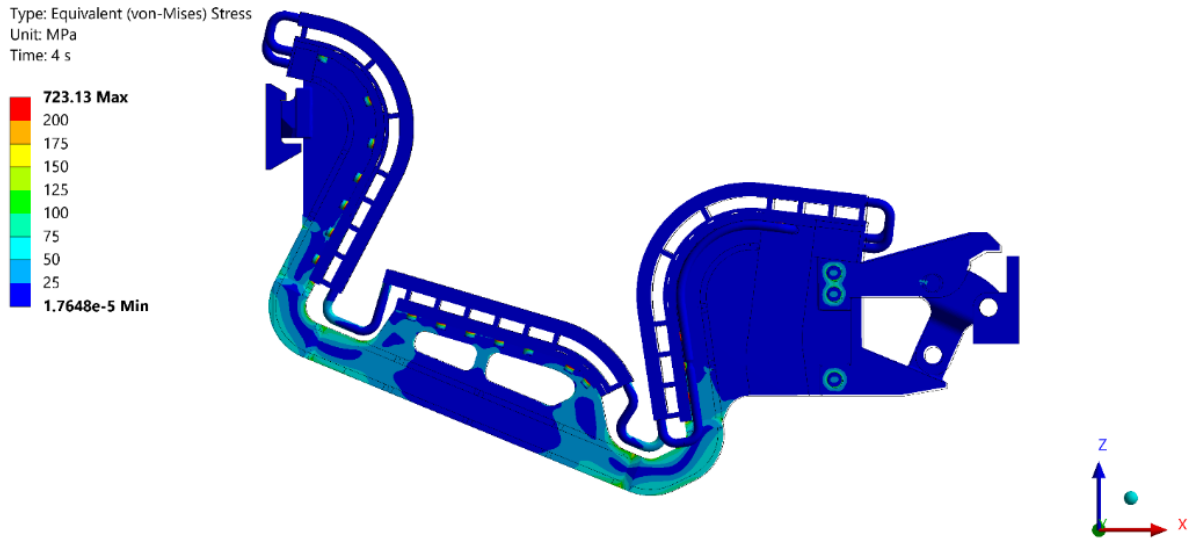

Figure 182 Equivalent von Mises stress contour on Divertor (Preload)

The elbows are the most highly stressed regions following the preload. This is one of the main reasons for selecting XM-19 as the material for the central body of the cassettes, as the elbows are already subjected to significant stress under operating loads.

Figure 183 shows a section of the Cassette Body, highlighting the stress state in its inner region. The stress distribution is approximately symmetric with respect to the XZ plane, as the preload is applied within this plane. Minor asymmetries may arise from slight deviations in the geometric symmetry of the model

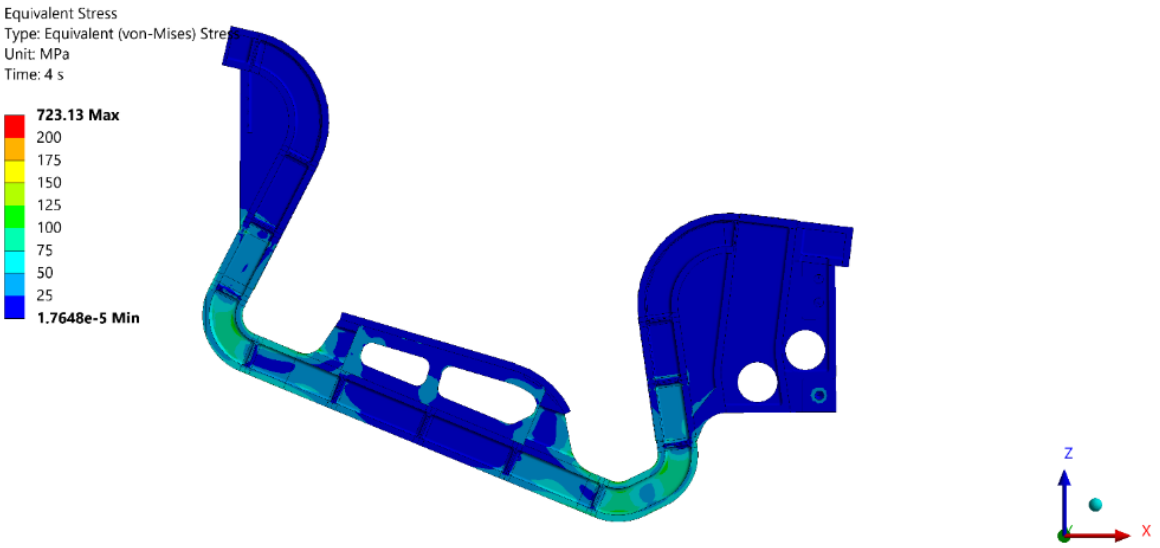

Figure 183 Equivalent von Mises stress contour on cassette body section (Preload)

Figure 184 shows the contact status, equivalent von Mises stress, and contact pressure on the nose. As anticipated, during the preload phase, the upper part of the hemispherical interface of the nose is the primary load-bearing region. This is confirmed by both the distribution of contact pressure and the contact status, which indicate that the upper area is either sliding or sticking. As expected, the inclined surface of the nose plays a lesser role compared to the hemispherical interface. This behavior is due to the preload action: as previously mentioned, the knuckle exerts an upward force. This rigid body motion has a dual effect—it pushes and compresses the outer branch of the cassette, while simultaneously forcing the entire cassette upward. As a result, the upper region of the hemispherical interface becomes the main contact area during this phase.

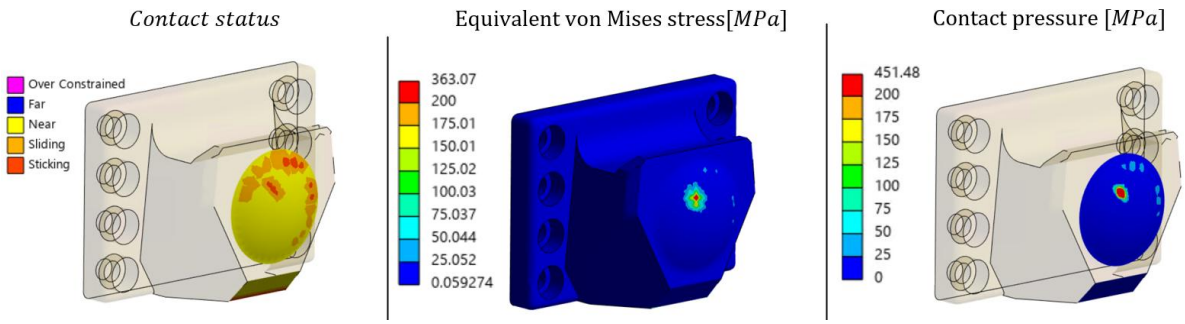

Figure 184 Contact status - Equivalent von Mises stress -Contact pressure on nose (Preload)

Figure 185 presents the contact status, equivalent von Mises stress, and contact pressure at the knuckle. By examining the contact interactions between the knuckle and the knuckle case, it is evident that the pin contact is properly activated and functioning as intended. As expected, the front part of the pin experiences the highest contact pressure. This behavior is consistent with the preload mechanism: after the preload is applied, the cassette tends to decompress, but this movement is effectively restrained by the pins, which remain locked into the knuckle case. As a result, the pins ensure the preload configuration is maintained

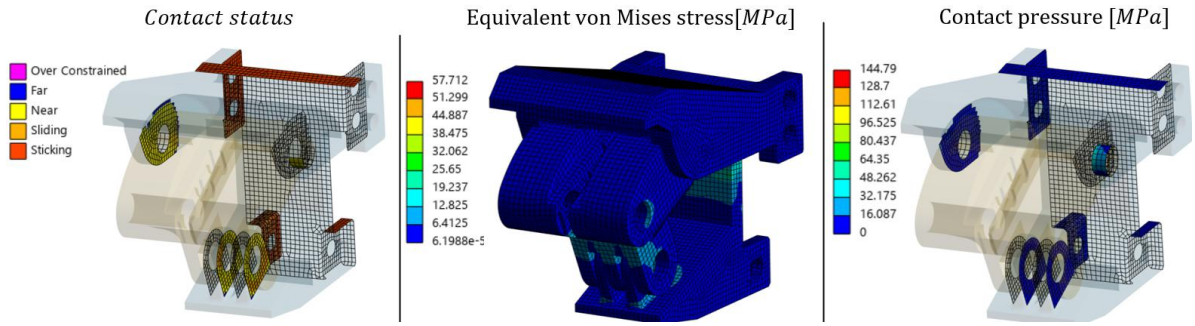

Figure 185 Contact status - Equivalent von Mises stress -Contact pressure on knuckle – knuckle case (Preload)

STEP 6 Preload + Dead Weight + Pressure

The dead weight has a minor influence on the overall behavior of the divertor and does not lead to any significant increase in stress. In contrast, although not critical, the applied pressure induces stress primarily in the larger regions where it is applied, namely, the inlet and outlet manifolds connected to the feeding pipes.

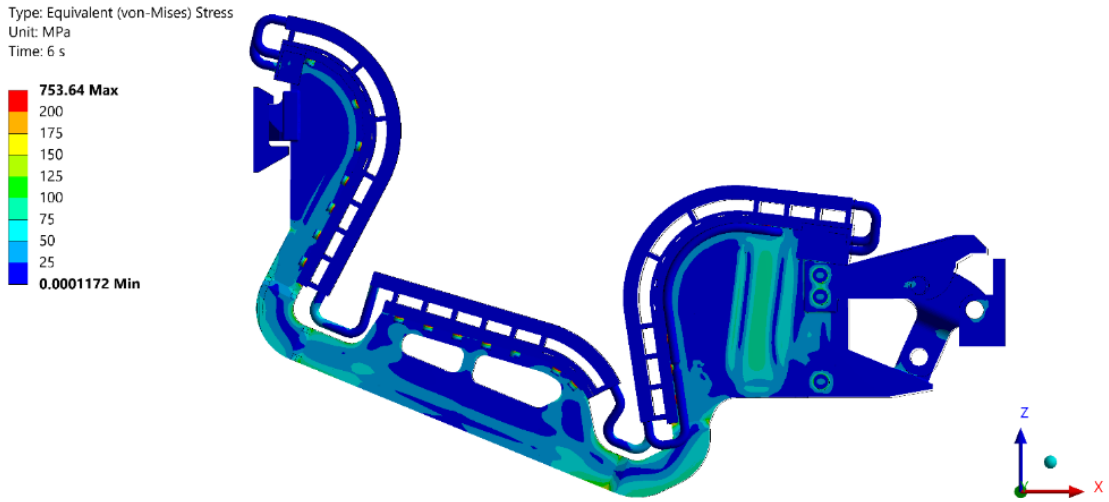

Figure 186 Equivalent von Mises stress contour on Divertor (Preload + Dead Weight + Pressure)

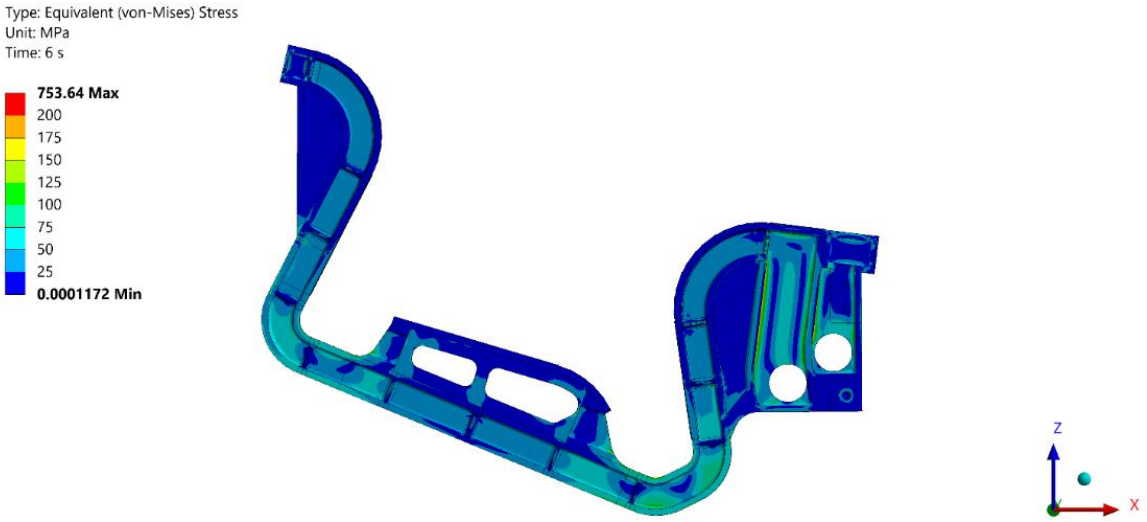

Figure 187 Equivalent von Mises stress contour on cassette body section (Preload + Dead Weight + Pressure)

For this reason, the manifolds stress state has been highlighted (see Figure 188), as it is one of the components most affected by the pressure load. However, as mentioned earlier, no significant concerns have been identified regarding the stress state in this region (Figure 189).

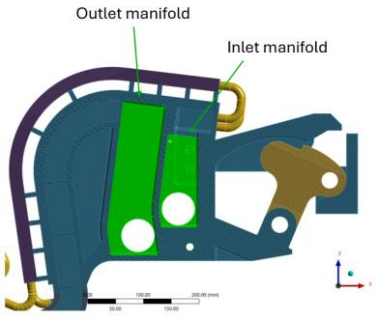

Figure 188 Outlet and inlet manifold

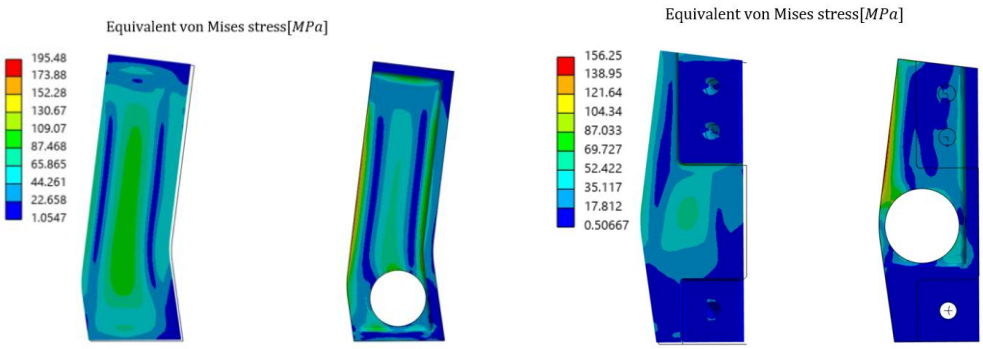

Figure 189 Outlet manifold Equivalent von Mises stress- Inlet manifold Equivalent von Mises stress

STEP 7 Preload + Dead Weight + Pressure + EM loads

As expected, the EM loads are the most sever for the structure. High stress occurrs close to the junction between the IVT back plate flanges and the cassette body, as well as in the region where the nose reinforcing ribs meet the cassette body main shell. Same thing can be observed at the outboard branch of the divertor.

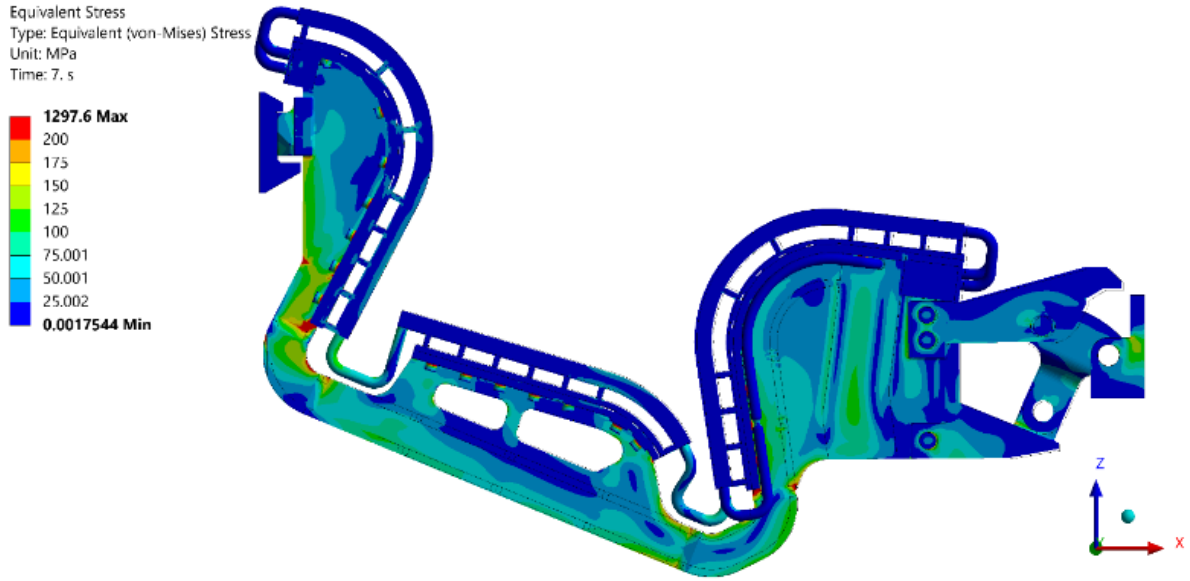

Figure 190 Equivalent von Mises stress contour on Divertor (Preload + Dead Weight + Pressure + EM loads)

Due to the high component of net vertical force, the nose is strongly pushed against the inclined sloped surface of the inboard rail. Moreover, the lorentz forces are such that the emispherical interface of the nose is pulled away from it's socket. The nose-rail interaction results in a steep stress gradient close to one of the vertex of the nose (Figure 191), thus implying highly localized contact pressure.

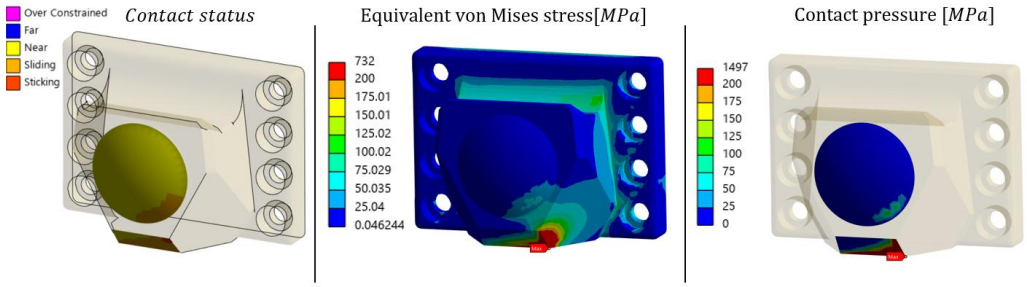

Figure 191 Contact status - Equivalent von Mises stress -Contact pressure on knuckle – knuckle case (Preload + Dead weight + Pressure + EM loads)

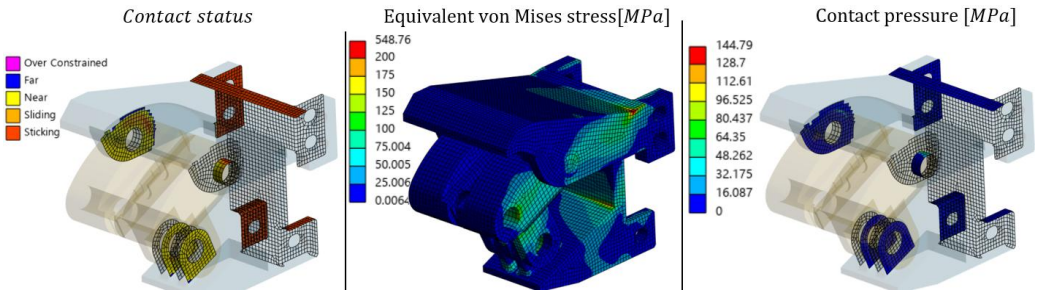

Figure 192 Contact status - Equivalent von Mises stress -Contact pressure on knuckle – knuckle case (Preload + Dead Weight + Pressure + EM loads)

STEP 8 Preload + Dead Weight + Pressure + EM loads + Thermal

To the heat flux coming from the radiating plasma on the divertor elbows , follow very high stresses on the radiated surfaces, but the stresses don't penetrate the skin of the divertor, affecting only a layer of few mm, withouth propagating into the thickness of the shell. To be further debait that the thermal loads have been assumed as secondary loads for the structural assessment

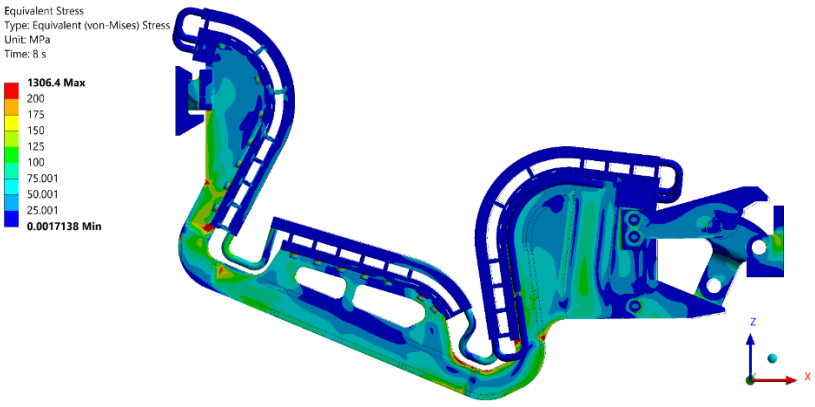

Figure 193 Equivalent von Mises stress contour on Divertor (Preload + Dead Weight + Pressure + EM loads + Thermal)

5.4 Stress classification lines (SCL) linearized stress assessment

For conservatism, all loads included in the simulation have been classified as Category A and thus treated as operational. However, it should be noted that the electromagnetic (EM) loads, being the most demanding for the verification, should also be assessed based on their likelihood. As such, it is likely that these loads would more appropriately fall under Category D. All the information included below are extracted from [93].

Loading Category	Category Conditions (Damage Limits)	SDC-IC Criteria Level
I Operational Loading	Normal	A
II Likely Loading	Upset	A
III Unlikely Loading	Emergency	C
IV Extremely Unlikely Loading	Faulted	D
Testing Loading	Testing	Test

Figure 194 SDC/IC criterial levels vs loading categories and damage limits

The criteria levels used to evaluate the above loadings are described in IC 2300. The philosophy of the SDC-IC is more conservative than is required for safety alone. The SDC-IC requires that a loading of a given category (I and II = normal or upset condition, III = emergency condition, IV = faulted condition) must be evaluated according to criteria limit of that category or better. That is, a Category III loading must be evaluated with Level C or A criteria. Service conditions cover those normal operating conditions, anticipated transients, and postulated accident conditions expected or postulated to occur during operation as defined below.

IC 2221 Normal and upset category conditions

Normal category conditions include start-up, hot standby, operation with plasma-on and plasma-off cycles, system shutdown, and any other loading which the component may be subjected in the performance of its specified service function. Upset category conditions include incidents of moderate frequency such as plasma disruptions, operator error, control malfunctions, loss of power, and any other loading which the component must withstand without damage requiring repair. The level A criteria shall be met for the normal and upset

category conditions.The verification will follow the first point of level A rules for protection against M-type damage

IC 3121 Level A criteria

At level A, the following rules for protection against M-type damage are applicable:

- immediate plastic collapse and plastic instability (IC 3121.1)
- immediate plastic flow localization (IC 3121.2)
- local fracture due to exhaustion of ductility (IC 3121.3)
- fast fracture (IC 3121.4)

IC 3121.1 Immediate plastic collapse and plastic instability

To prevent global fracture due to immediate plastic collapse and plastic instability, the following limits have to be satisfied at all times during the life of the component subjected to all loadings for which criteria level A is specified.

$$Membrane\ stress: P_m \leq S_m(T_m, \phi_{tm})$$

$$Membrane\ plus\ bending\ stress: P_m + P_b \leq K_{eff} S_m(T_m, \phi_{tm})$$

Where K_{eff} is an effective bending shape factor, which accounts for the increased maximum bending moment carrying capability of an elasto-plastic material with limited ductility as compared to that of an elastic-brittle material.

$$K_{eff} = 1 + 2\ (K - 1)(K_{eff,rect} - 1)$$

For unirradiated materials with unlimited ductility, Keff = K where K is the usual bending shape factor used in the RCC-MR and the ASME Code.

T_m and ϕ_{tm} are respectively the thickness average temperature and the thickness average neutron fluency (to be noted that this last one is negligible due to the low neutrons released in DTT). To evaluate K_{eff}, the value of K will be assumed the same of a rectangular cross section.

Table 36 reports $\boldsymbol{K_{eff,rect}}$ ***AISI 316 LN versus dpa dose.***

Table 36 AISI 316 LN variation of $K_{eff,rect}$ with irradiation displacement dose at 20-350 °C

T_{irr}, °C / Dose, dpa	20	50	100	150	200	250	300	350
0	1.50	1.50	1.50	1.50	1.50	1.50	1.50	1.50
0.5	1.50	1.50	1.50	1.50	1.50	1.50	1.50	1.50
1	1.50	1.50	1.50	1.50	1.50	1.50	1.50	1.50
1.5	1.50	1.50	1.50	1.50	1.50	1.50	1.50	1.50
2	1.50	1.50	1.50	1.50	1.50	1.49	1.49	1.49
2.5	1.50	1.50	1.50	1.50	1.50	1.49	1.48	1.48
3	1.50	1.50	1.50	1.50	1.49	1.47	1.21	1.20

Therefore, considering AISI 316 LN unirradiated (DTT won't suffer significant neutronic level/damage) and assuming a K for rectangular cross sections, the value of $K_{eff,rect}$ will be:

$$K_{eff\ AISI\ 316\ LN} = 1 + 2 * (1.5 - 1) * (1.5 - 1) = 1.5$$

Differently the $K_{eff,rect}$ for XM-19 shall be estimated using the general definition:

$$K_{eff,rect} = K_{rect}\left[\frac{3 - \gamma^2 + (\beta - 1)(1 - \gamma)(2 + \gamma)}{1 + 2\beta}\right]$$

Where:

$$\gamma = \gamma(T, \phi_t) = \frac{S_y(T, \phi_t)}{S_u(T, \phi_t) + E(T, \phi_t)\epsilon_u(T, \phi_t)}$$

$$\beta = \beta(T, \phi_t) = \frac{S_u(T, \phi_t)}{S_y(T, \phi_t)} = 1.5$$

The definition of these parameters are expanded in [93]. Therefore, for XM-19, after evaluating:

$$\beta_{XM-19} = 0.34,\ \gamma_{XM-19} = 1.82 \quad \Rightarrow \quad K_{eff_{rect}XM-19} = 1.53$$

therefore $K_{eff_{XM-19}} \cong 1.52$.

Therefore, summarizing, respectively for AISI 316 LN and XM-19 components, the rules for verification will be: For AISI 316 LN:

$$P_m \leq S_m(T_m, 0)$$

$$P_m + P_b \leq 1.5\ S_m(T_m, 0)$$

For XM-19:

$$P_m \leq S_m(T_m, 0)$$

$$P_m + P_b \leq 1.52\ S_m(T_m, 0)$$

Table 37 and Table 38 report the Sm values for AISI 316 LN and XM-19 steel.

Table 37 AISI 316 LN Sm values for unirradiated conditions

T, °C	20	50	75	100	125	150	175	200	225	250	275	300	325	350
S_m, MPa	147	147	147	147	147	141	135	130	125	121	118	115	112	109

T, °C	375	400	425	450	475	500	525	550	575	600	625	650	675
S_m, MPa	107	105	103	101	99	97	97	96	96	95	94	94	93

Table 38 XM-19 Sm values for unirradiated conditions

T, °C	20	100	150	200	250	300	350	400	450	500
S_m, MPa	230	207	197	191	187	184	182	179	175	171

For both materials, as reference temperature, the worst case has been selected (150°C) even though most of the bodies don't reach a temperature above 60 °C. This choice has been made to to keep the verification procedure more conservative. Since the rules for verifying immediate plastic collapse under Level A criteria refer to primary membrane and membrane-plus-bending stresses, the assessment was performed considering the stress results from Preload, Dead Weight, Pressure, and Electromagnetic (EM) loads. All these loads were treated as primary, even though Preload is typically considered a secondary load. However, from the standpoint of plastic collapse safety, this assumption is conservative.

5.4.1 XM-19 components

The regions where SCLs have been defined are reported in Figure 195, Figure 196, Figure 197.

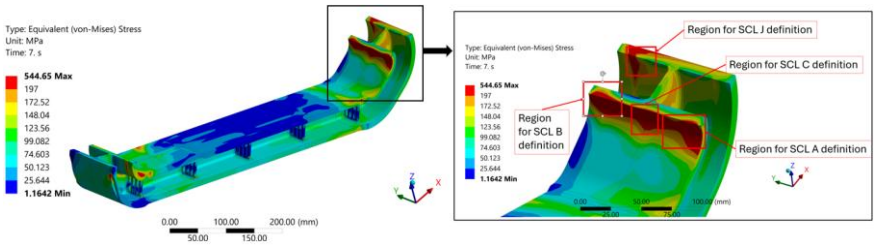

Figure 195 Outboard elbow region for SCL A, SCL B, SCL C, SCL J definition

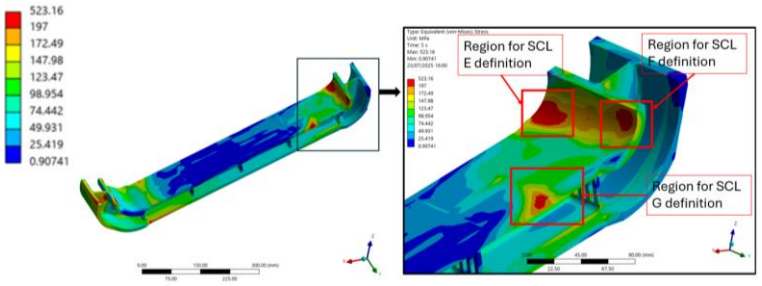

Figure 196 Inboard elbow region for SCL E, SCL F, SCL G definition

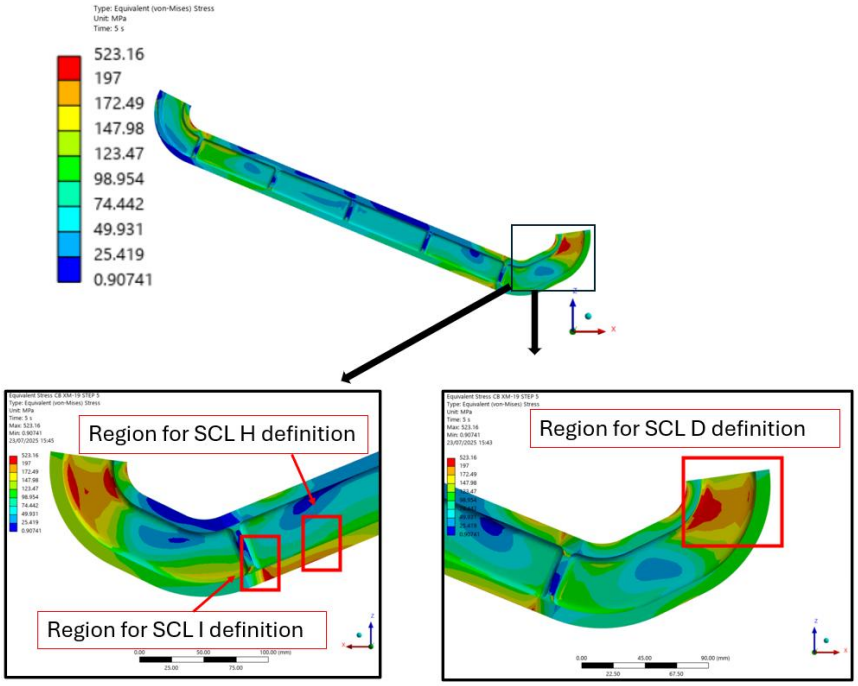

Figure 197 Outboard elbow region for SCL D, SCL H, SCL I definition

Table 39 reports the verification results.

Table 39 XM-19 components verification results

Component	SCL	Loc.	Material	Ref. T	SCL Results			
					Entities		Allowable Stress	Safety Factor
Outboard elbow	A	1	XM-19	150 °C	Pm	131.6 MPa	197 MPa	1.5
					Pm+Pb	228.7 MPa	300 MPa	1.3
Outboard elbow	B	1	XM-19	150 °C	Pm	167.9 MPa	197 MPa	1.2
					Pm+Pb	271.5 MPa	300 MPa	1.1
Outboard elbow	C	1	XM19	150 °C	Pm	137.2 MPa	197 MPa	1.4
					Pm+Pb	235.38 MPa	300 MPa	1.3

Ourboard elbow	D	1	XM19	150 °C	Pm	225.14 MPa	197 MPa	0.9
					Pm+Pb	241.7 MPa	300 MPa	1.2
Central body	E	1	XM-19	150 °C	Pm	132.1 MPa	197 MPa	1.5
					Pm+Pb	212.0 MPa	300 MPa	1.4
Inboard elbow	F	1	XM19	150 °C	Pm	130.8 MPa	197 MPa	1.5
					Pm+Pb	204.2 MPa	300 MPa	1.5
Central body	G	1	XM19	150 °C	Pm	173.2 MPa	197 MPa	1.1
					Pm+Pb	218.2 MPa	300 MPa	1.4
Outboard elbow	H	1	XM-19	150 °C	Pm	163.8 MPa	197 MPa	1.2
					Pm+Pb	204.4 MPa	300 MPa	1.5
Central body	I	1	XM19	150 °C	Pm	161.23 MPa	197 MPa	1.2
					Pm+Pb	219.4 MPa	300 MPa	1.4
Outboard elbow	J	1	XM19	150 °C	Pm	206.78 MPa	197 MPa	0.9
					Pm+Pb	241.25 MPa	300 MPa	1.2

5.4.2 AISI 316 LN components

Figure 198, Figure 199, Figure 200 highlight the regions where the path for stress classification have been located

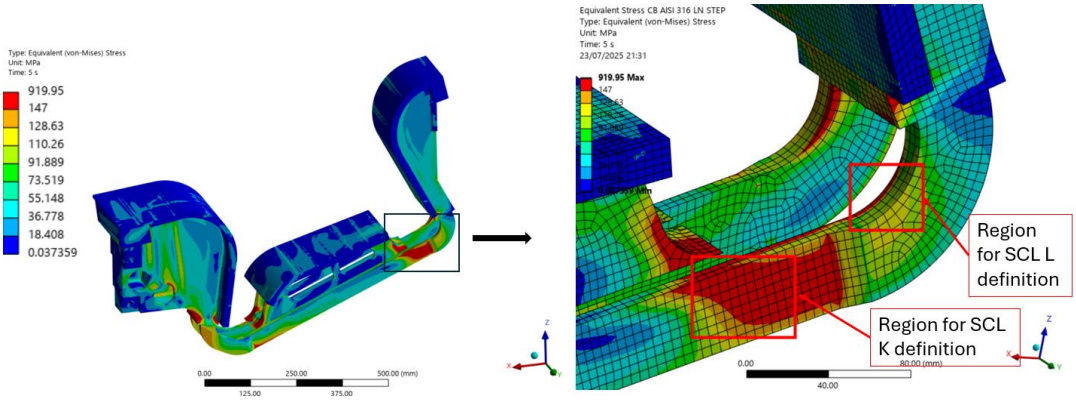

Figure 198 Region for SCL K, SCL L definition

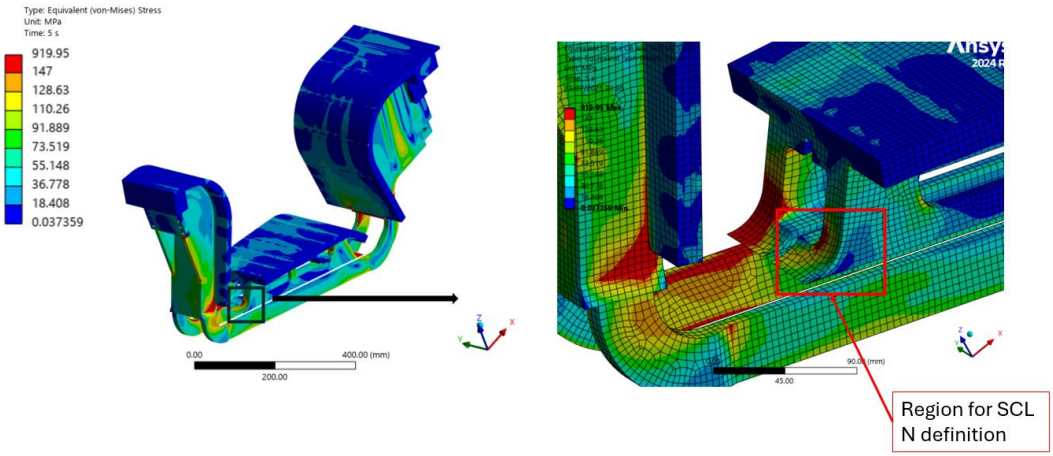

Figure 199 Region for SCL N definition

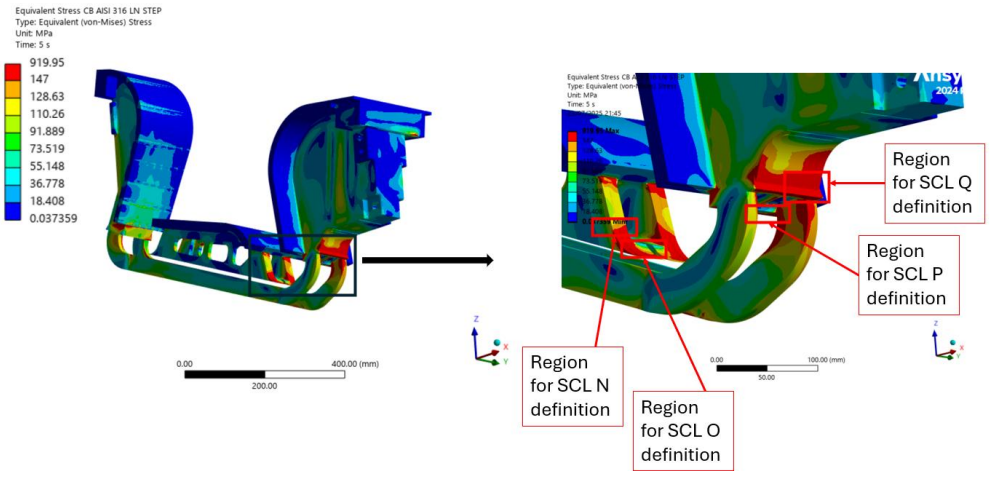

Figure 200 Region for SCL N, SCL O, SCL P, SCL Q definition

Table 40 AISI 316 LN verification results

Component	SCL	Loc.	Material	Ref. T	SCL Results			
					Entities		Allowable Stress	Safety Factor
Outboard lateral cover plate	K	1	AISI 316 LN	150 °C	Pm	150.1 MPa	147 MPa	1.0
					Pm+Pb	192 MPa	221 MPa	1.2
Outboard lateral cover plate	L	1	AISI 316 LN	150 °C	Pm	147.4 MPa	147 MPa	1.0
					Pm+Pb	169.3 MPa	221 MPa	1.3
DOME ribs	M	1	AISI 316 LN	150 °C	Pm	77.6 MPa	147 MPa	1.9
					Pm+Pb	147.8 MPa	221 MPa	1.5
DOME ribs	N	1	AISI 316 LN	150 °C	Pm	176.2 MPa	147 MPa	0.8
					Pm+Pb	197.1 MPa	221 MPa	1.1
DOME ribs	OE	1	AISI 316 LN	150 °C	Pm	128.2 MPa	147 MPa	1.1
					Pm+Pb	181.5 MPa	221 MPa	1.2
Outboard cassette body branch	P	1	AISI 316 LN	150 °C	Pm	135.9 MPa	147 MPa	1.1
					Pm+Pb	240 MPa	221 MPa	0.9
Outboard cassette body branch	Q	1	AISI 316 LN	150 °C	Pm	187.9 MPa	147 MPa	0.8
					Pm+Pb	247.1 MPa	221 MPa	0.9

In SCL N, SCL P, SCL Q the criteria were not met. This zones are very close to the XM-19 central body, therefore the issue could be tackled by extending the XM-19 material where this hotspot occur. This is something already foreseen and discussed and this strategy will surely be implemented into the next future. SCL D and SCL J were also characterized by stress above the allowable but this represent an easy fix since with minor modification on the design such as local increased thickness, the stress will surely mitigated and pushd down the allowable.

5.5 Bolted connections assessment

This section oultines the assessment carried out on the bolted connections included into the cassette body assembly. The assessment of the bolted connections was performed at two different time instances of the reference Unmitigated DVDE: the end of the current quench, corresponding to a simulation time of 10.203 s, and the thermal quench, corresponding to a simulation time of 10.1850 s. This choice is primarily motivated by the way currents circulate during a disruption event. The plasma displacement and the resulting perturbation of the magnetic field generate, locally—in this case on the PFU—forces of different nature: compressive on PFU 8 and PFU 2 at the end of the current quench, and tensile during the thermal quench. Therefore, although the highest global resultants occur at the end of the current quench, the most conservative time for assessing the bolted connections between the target backplates and their respective flanges is the thermal quench, which induces strong tensile forces on the PFU supports and, consequently, on the backplates. To support this, plots of the forces acting on the PFU fingers during both the thermal quench and the current quench are presented below. The shared force distributions refer to the centerline of each PFU finger, as explicitly requested by the DTT Divertor team, to better understand the local PFU conditions. It should be noted that this description serves only to justify why two instances were considered for the backplate-flange bolted connection assessment. These centerline force distributions are not the direct loads used in the engineering model discussed previously. The distributions shown here are line forces, discretized at keypoints selected by the EM analyst, whereas the forces integrated into the structural assessment are fully 3D. The plots that will be shown refer to local coordinate systems placed in each keypoints (where the localize force is evaluated) and with the Z axis normal to the segment connecting two consecutive kp. Therefore, positive forces acting along Z will be seen as traction on the PFU, compression instead.

Figure 201 PFC center lines keypoints on linear abscissa

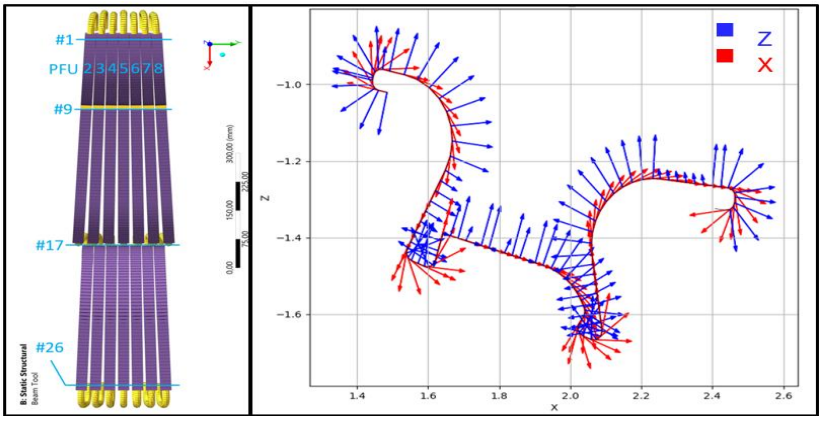

Figure 202 PFC center lines keypoints on linear abscissa and Local CSs on PFU support

5.5.1 Thermal quench PFU center lines force distribution (10.1850 s EM simulation time)

From Figure 203 to Figure 206 are reported the forces acting on PFU2 to PFU8 linear abscissa, defined as -0.2 m at the end of the IVT curved pipe branch and 2.2 m at the end of the OVT curved pipe branch, at the thermal quench of the reference unmitigated DVDE.

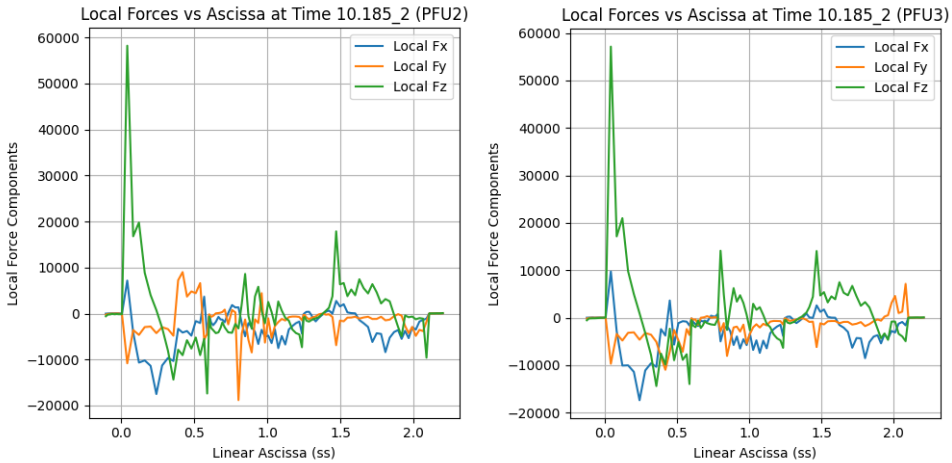

Figure 203 Local forces on linear abscissa-PFU 2 center line at thermal quench (10.1850 s)- Local forces on linear abscissa-PFU 3 center line at thermal quench (10.1850 s)

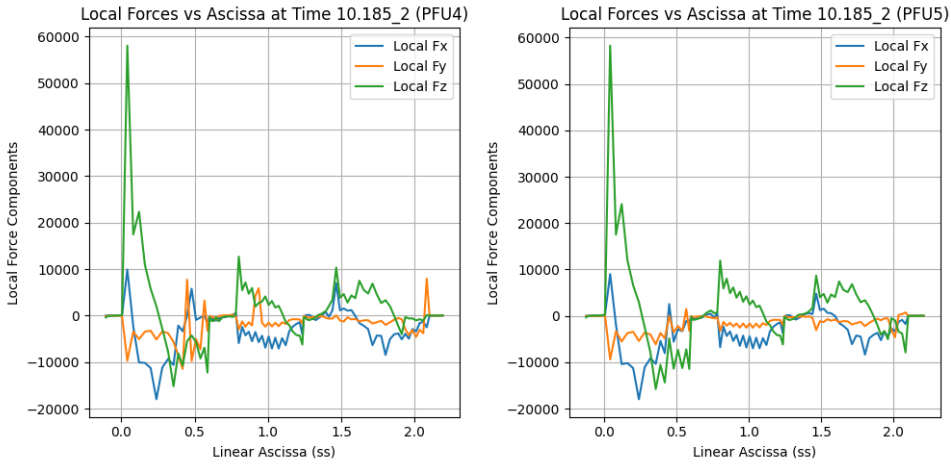

Figure 204 Local forces on linear abscissa-PFU 4 center line at thermal quench (10.1850 s) - Local forces on linear abscissa-PFU 5 center line at thermal quench (10.1850 s)

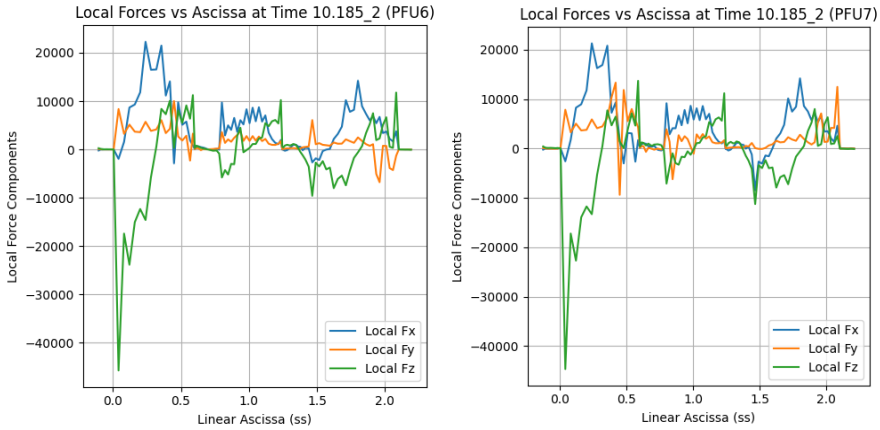

Figure 205 Local forces on linear abscissa-PFU 6 center line at thermal quench (10.1850 s) - Local forces on linear abscissa-PFU 7 center line at thermal quench (10.1850 s)

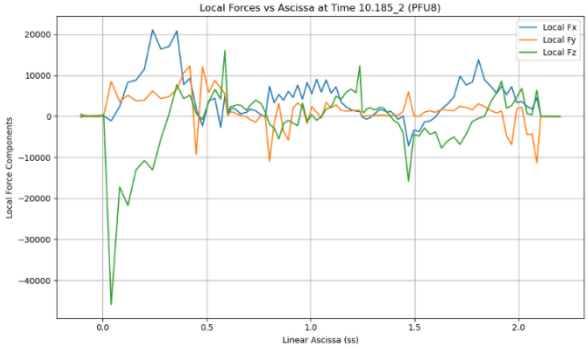

Figure 206 Local forces on linear abscissa-PFU 8 center line at thermal quench (10.1850 s)

5.5.2 End of current quench PFU center lines force distribution (10.203 s simulation time)

From Figure 207 to Figure 210 are reported the forces at the end of the current quench.

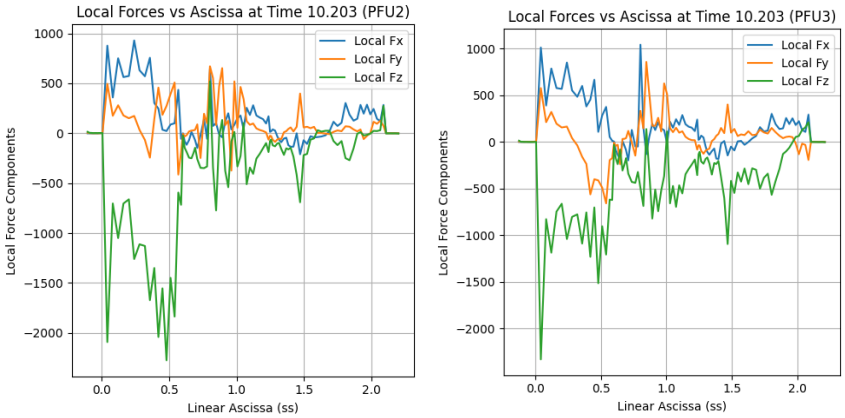

Figure 207 Local forces on linear abscissa-PFU 2 center line at the end of the current quench (10.203 s) - Local forces on linear abscissa-PFU 3 center line at the end of the current quench (10.203 s)

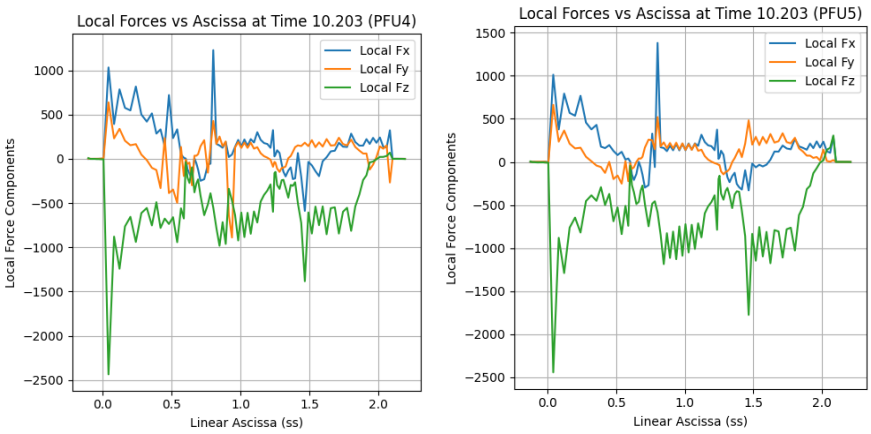

Figure 208 Local forces on linear abscissa-PFU 4 center line at the end of the current quench (10.203 s) - Local forces on linear abscissa-PFU 5 center line at the end of the current quench (10.203 s)

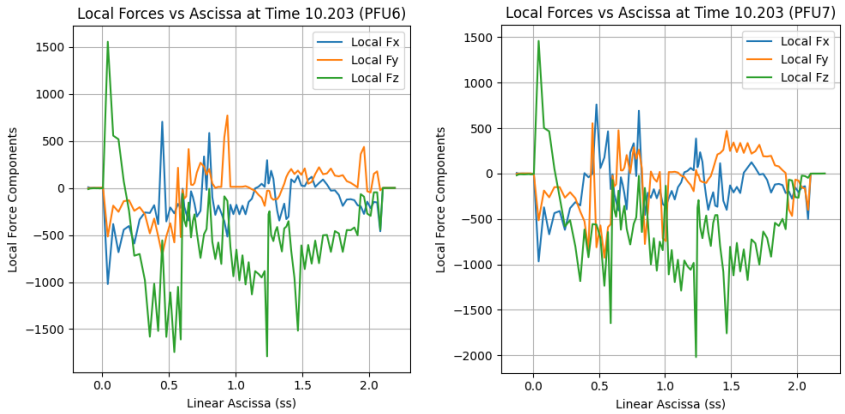

Figure 209 Local forces on linear abscissa-PFU 6 center line at the end of the current quench (10.203 s) - Local forces on linear abscissa-PFU 7 center line at the end of the current quench (10.203 s)

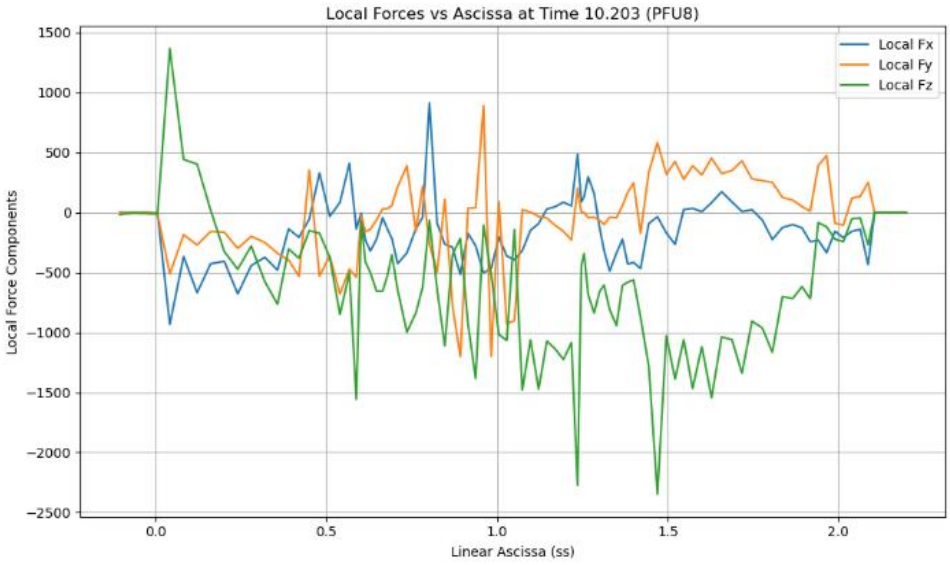

Figure 210 Local forces on linear abscissa-PFU 8 center line at the end of the current quench (10.203 s)

As can be seen, during the thermal quench, the peak forces localized on the IVT are opposite to those at the end of the current quench and are tensile in nature, as previously mentioned. Therefore, the 3D EM force distribution at both the thermal quench and at the end of the current quench has been used to assess the bolted connections. The results indicate that the thermal quench represents the most demanding condition for the bolted connections. Nevertheless, the EM loads computed during the thermal quench raise significant concerns. The thermal quench, modeled during the disruption simulation whose results were used as input for the EM calculations, may have been represented too coarsely, and this approximation could have introduced inaccuracies in the EM load calculations at that particular time.

5.5.3 Thermal quench assessment

In Figure 211 the connections between target back plates and respective flange are shown , with the associate ID (1 to 14 for used for each screw set). Moreover, Figure 212 shows the local coordinate systems defined to evaluate the solicitations acting on each screw, extracted as force reactions sum of the nodal forces on the contact surface of the seating below the head of the screw.

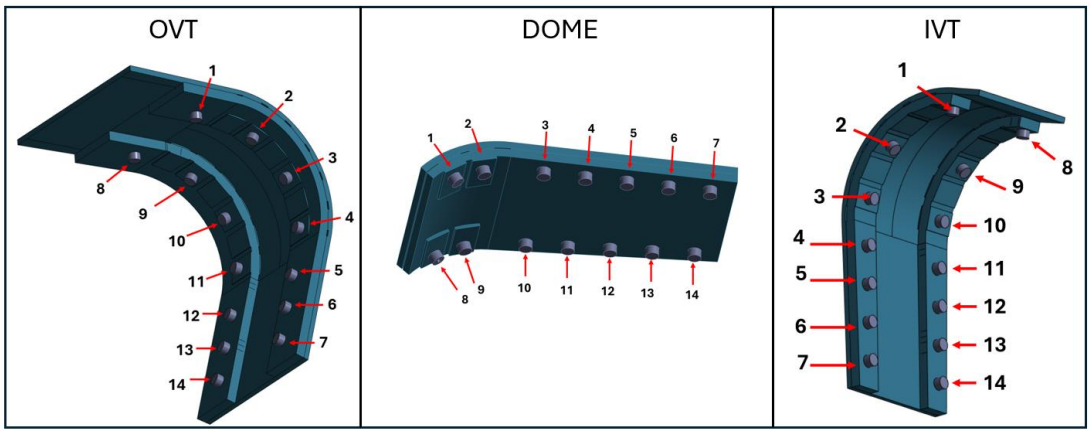

Figure 211 Back plates targets-flange bolted connections IDs

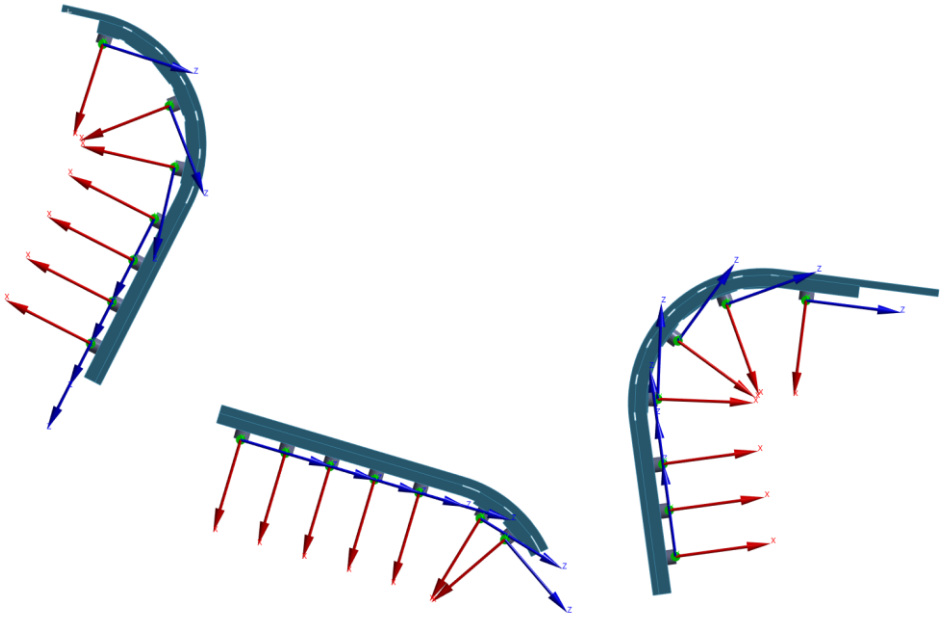

s

Figure 212 Local coordinate systems defined to evaluate the solicitations on the screws

The axial force (including the pretension contribution along X axis of each local coordinate system), the axial force (net of pretension along X axis of each local coordinate system) and the shear (in the plane YZ of each local coordinate system) acting on the screws are shown in

Table 41, Table 42, Table 43.

Table 41 OVT connections screws solicitations at the thermal quench

OVT connections screws solicitations			
Connection ID	**Axial force [N]**	**Axial force (net of pretension) [N]**	**Shear [N]**
1	21395	95	1875
2	21525	225	1049
3	21460	160	617
4	21452	152	260
5	21574	274	590
6	21745	445	1434
7	21804	504	2212
8	21173	-127	371
9	21303	3	510
10	21325	25	544
11	21397	97	368
12	21366	66	603
13	21429	129	1090
14	21538	21538	1498

Table 42 IVT connections screws solicitations at the thermal quench

IVT connections screws solicitations			
Connection ID	**Axial force [N]**	**Axial force (net of pretension) [N]**	**Shear [N]**
1	21171	-129	482
2	21375	75	653
3	21458	158	508
4	21475	175	483
5	21457	157	495
6	21453	153	998
7	21417	117	1532
8	18251	-37	1663
9	21432	132	1124
10	21470	170	619
11	21508	208	118
12	21484	184	628
13	21461	161	1453
14	21467	167	1820

Table 43 Dome connections screws solicitations at the thermal quench

Dome connections screws solicitations			
Connection ID	**Axial force [N]**	**Axial force (net of pretension) [N]**	**Shear [N]**
1	21683	383	364
2	21531	231	1195
3	21442	142	509
4	21476	176	314
5	21523	223	202
6	21528	228	446
7	21433	133	340
8	21469	169	73
9	21439	139	588
10	19417	417	2134
11	21489	189	359
12	21502	202	500
13	21511	211	780
14	21460	160	1047

Table 44, Table 45, Table 46 includes the main stress components computed using the solicitations in

Table 41, Table 42, Table 43 according to B 3812.2.6.1 and B3812.2.6.4 of [93].The last columns report the safety factors on the mean stress in the thread root section and on the threads according to IC 6121.1.3.1 and IC 6121.1.3.3 of [93].

Table 44 OVT bolted connections assessment results at the thermal quench

OVT	σ_N on thread root section [MPa]	σ_N on smooth shank section [MPa]	τ_{th_N} in the threads [MPa]	τ_{th_N} in the head [MPa]	τ_{th_T} on thread root section [MPa]	τ_{th_T} on the smooth shank section [MPa]	S_m $[MPa]$	S_f on σm (on the thread root section)	S_f on τ(thN due to normal load)
1	-6.62	-4.41	-1.44	-0.73	37.79	25.17	425.00	>>1	>>1
2	-2.33	-1.55	-0.51	-0.26	127.79	85.09	425.00	>>1	>>1
3	31.59	21.03	6.85	3.51	152.65	101.64	425.00	>>1	>>1
4	100.06	66.63	21.71	11.10	45.39	30.22	425.00	4.25	>>1
5	166.42	110.81	36.11	18.47	91.94	61.22	425.00	2.55	7.06
6	183.57	122.23	39.83	20.37	106.59	70.97	425.00	2.32	6.40
7	330.88	220.32	71.79	36.72	97.08	64.64	425.00	1.28	3.55
8	283.40	188.71	61.49	31.45	87.24	58.09	425.00	1.50	4.15
9	8.13	5.41	1.76	0.90	56.39	37.55	425.00	>>1	>>1
10	2.98	1.99	0.65	0.33	41.30	27.50	425.00	>>1	>>1
11	-6.54	-4.35	-1.42	-0.73	11.54	7.69	425.00	>>1	>>1
12	4.38	2.92	0.95	0.49	19.02	12.67	425.00	>>1	>>1
13	10.10	6.72	2.19	1.12	417.39		425.00	>>1	>>1
14	9.71	6.47	2.11	1.08	417.01	29.45	425.00	>>1	>>1

Table 45 IVT bolted connections assessment results at the thermal quench

IVT	σ_N on thread root section [MPa]	σ_N on smooth shank section [MPa]	τ_{th_N} in the threads [MPa]	τ_{th_N} in the head [MPa]	τ_{th_T} on thread root section [MPa]	τ_{th_T} on the smooth shank section [MPa]	S_m $[MPa]$	S_f on σm (on the thread root section)	S_f on τ(thN due to normal load)
1	221.78	147.67	48.12	24.61	136.49	69.81	425.00	1.92	5.30
2	-0.40	-0.27	-0.09	-0.04	88.29	45.16	425.00	>>1	>>1
3	0.19	0.13	0.04	0.02	88.41	45.22	425.00	>>1	>>1
4	-5.62	-3.74	-1.22	-0.62	87.15	44.58	425.00	>>1	>>1
5	-16.85	-11.22	-3.66	-1.87	84.72	43.33	425.00	>>1	>>1
6	-18.55	-12.35	-4.02	-2.06	84.35	43.14	425.00	>>1	>>1
7	-9.73	-6.48	-2.11	-1.08	86.26	44.12	425.00	>>1	>>1
8	-10.54	-7.02	-2.29	-1.17	73.59	37.64	425.00	>>1	>>1
9	3.35	2.23	0.73	0.37	89.10	45.57	425.00	>>1	>>1
10	25.70	17.11	5.58	2.85	93.95	48.05	425.00	>>1	>>1
11	122.02	81.25	26.47	13.54	114.85	58.74	425.00	3.48	9.63
12	92.49	61.59	20.07	10.26	108.44	55.46	425.00	4.59	>>1
13	50.48	33.61	10.95	5.60	99.33	50.80	425.00	8.42	>>1
14	12.60	8.39	2.73	1.40	91.11	46.60	425.00	>>1	>>1

Table 46 Dome bolted connections assessment results at the thermal quench

Dome	σ_N on thread root section [MPa]	σ_N on smooth shank section [MPa]	τ_{th_N} in the threads [MPa]	τ_{th_N} in the head [MPa]	τ_{th_T} on thread root section [MPa]	τ_{th_T} on the smooth shank section [MPa]	S_m [MPa	S_f on σm (on the thread root section)	S_f on τ(thN due to normal load)
1	-3.14	-2.09	-0.68	-0.35	24.41	16.25	425.00	>>1	>>1
2	-3.88	-2.58	-0.84	-0.43	61.99	41.28	425.00	>>1	>>1
3	2.39	1.59	0.52	0.27	43.14	28.72	425.00	>>1	>>1
4	20.98	13.97	4.55	2.33	46.59	31.02	425.00	>>1	>>1
5	35.74	23.80	7.75	3.97	58.95	39.25	425.00	>>1	>>1
6	37.17	24.75	8.07	4.13	59.62	39.70	425.00	>>1	>>1
7	516.08	343.63	111.98	57.27	131.23	87.38	425.00	0.82	2.28
8	10.61	7.07	2.30	1.18	15.07	10.04	425.00	>>1	>>1
9	9.35	6.23	2.03	1.04	57.31	38.16	425.00	>>1	>>1
10	-0.84	-0.56	-0.18	-0.09	35.95	23.94	425.00	>>1	>>1
11	-6.39	-4.25	-1.39	-0.71	25.25	16.81	425.00	>>1	>>1
12	-4.32	-2.88	-0.94	-0.48	13.58	9.04	425.00	>>1	>>1
13	-4.11	-2.74	-0.89	-0.46	1.72	1.15	425.00	>>1	>>1
14	-2.33	-1.55	-0.51	-0.26	12.59	8.38	425.00	>>1	>>1

On most of the screws the stress is far below the allowable value, moreover in accordance with the previsions the most loaded connection are the ones between IVT backplates and flanges, even though the criteria are always met.

The only connection that doesn't meet the criteria relates to the dome, with a value of 516 MPa of the mean stress on thread root section exceeding the allowable range.

Is here stated again that the loads related to the thermal quench raise major concerns and therefore this verification should be carefully reviewed as well as the input loads used for the assessment.

5.5.4 End of current quench assessment

The axial force (including the pretension contribution along X axis of each local coordinate system), the axial force (net of pretension along X axis of each local coordinate system) and the shear (in the plane YZ of each local coordinate system) acting on the screws are shown in Table 47, Table 48, Table 49.

Table 47 OVT connections screws solicitations at the end of current quench

OVT connections screws solicitations			
Connection ID	**Axial force [N]**	**Axial force (net of pretension) [N]**	**Shear [N]**
1	21395	95	1875
2	21525	225	1049
3	21460	160	617
4	21452	152	260
5	21574	274	590
6	21745	445	1434
7	21804	504	2212
8	21173	-127	371
9	21303	3	510
10	21325	25	544
11	21397	97	368
12	21366	66	603
13	21429	129	1090
14	21538	21538	1498

Table 48 IVT connections screws solicitations at the end of current quench

IVT connections screws solicitations			
Connection ID	**Axial force [N]**	**Axial force (net of pretension) [N]**	**Shear [N]**
1	21171	-129	482
2	21375	75	653
3	21458	158	508
4	21475	175	483
5	21457	157	495
6	21453	153	998
7	21417	117	1532
8	18251	-37	1663
9	21432	132	1124
10	21470	170	619
11	21508	208	118
12	21484	184	628
13	21461	161	1453
14	21467	167	1820

Table 49 Dome connections screws solicitations at the end of current quench

Dome connections screws solicitations			
Connection ID	**Axial force [N]**	**Axial force (net of pretension) [N]**	**Shear [N]**
1	21683	383	364
2	21531	231	1195
3	21442	142	509
4	21476	176	314
5	21523	223	202
6	21528	228	446
7	21433	133	340
8	21469	169	73
9	21439	139	588
10	19417	417	2134
11	21489	189	359
12	21502	202	500
13	21511	211	780
14	21460	160	1047

Table 50, Table 51, Table 52 includes the main stress components computed using the solicitations in Table 47, Table 48, Table 49 according to B 3812.2.6.1 and B3812.2.6.4 of REFERENCE SDCIC APPENDIX B GUIDELINES FOR ANALYSIS.The last columns of reports the safety factors on the mean stress in the thread root section and on the threads according to IC 6121.1.3.1 and IC 6121.1.3.3 of SDCIC MAIN BODY.

Table 50 OVT bolted connections assessment results at the end of current quench

OVT	σ_N on thread root section [MPa]	σ_N on smooth shank section [MPa]	τ_{th_N} in the threads [MPa]	τ_{th_N} in the head [MPa]	τ_{th_T} on thread root section [MPa]	τ_{th_T} on the smooth shank section [MPa]	S_m [MPa]	S_f on σm (on the thread root section)	S_f on τ(thN due to normal load)
1	1.82	1.21	0.39	0.20	35.86	23.88	425.00	>>1	>>1
2	4.30	2.86	0.93	0.48	20.07	13.36	425.00	>>1	>>1
3	3.06	2.04	0.66	0.34	11.81	7.86	425.00	>>1	>>1
4	2.91	1.94	0.63	0.32	4.97	3.31	425.00	>>1	>>1
5	5.24	3.49	1.14	0.58	11.28	7.51	425.00	>>1	>>1
6	8.51	5.67	1.85	0.94	27.42	18.26	425.00	>>1	>>1
7	9.64	6.42	2.09	1.07	42.29	28.16	425.00	>>1	>>1
8	-2.43	-1.62	-0.53	-0.27	7.10	4.73	425.00	>>1	>>1
9	0.06	0.04	0.01	0.01	9.74	6.49	425.00	>>1	>>1
10	0.48	0.32	0.10	0.05	10.40	6.92	425.00	>>1	>>1
11	1.85	1.24	0.40	0.21	7.04	4.69	425.00	>>1	>>1
12	1.26	0.84	0.27	0.14	11.54	7.68	425.00	>>1	>>1
13	2.47	1.64	0.54	0.27	20.85	13.88	425.00	>>1	>>1
14	4.55	3.03	0.99	0.51	28.64	19.07	425.00	>>1	>>1

Table 51 IVT bolted connections assessment results at the end of current quench

IVT	σ_N on thread root section [MPa]	σ_N on smooth shank section [MPa]	τ_{th_N} in the threads [MPa]	τ_{th_N} in the head [MPa]	τ_{th_T} on thread root section [MPa]	τ_{th_T} on the smooth shank section [MPa]	S_m [MPa	S_f on σm (on the thread root section)	S_f on τ(thN due to normal load)
1	-2.47	-1.64	-0.54	-0.27	9.22	6.14	425.00	>>1	>>1
2	1.43	0.95	0.31	0.16	12.49	8.32	425.00	>>1	>>1
3	3.02	2.01	0.66	0.34	9.72	6.47	425.00	>>1	>>1
4	3.35	2.23	0.73	0.37	9.24	6.15	425.00	>>1	>>1
5	3.00	2.00	0.65	0.33	9.46	6.30	425.00	>>1	>>1
6	2.93	1.95	0.63	0.32	19.08	12.70	425.00	>>1	>>1
7	2.24	1.49	0.49	0.25	29.29	19.50	425.00	>>1	>>1
8	-0.71	-0.47	-0.15	-0.08	31.79	21.17	425.00	>>1	>>1
9	2.52	1.68	0.55	0.28	21.50	14.31	425.00	>>1	>>1
10	3.25	2.16	0.71	0.36	11.83	7.88	425.00	>>1	>>1
11	3.98	2.65	0.86	0.44	2.26	1.50	425.00	>>1	>>1
12	3.52	2.34	0.76	0.39	12.01	7.99	425.00	>>1	>>1
13	3.08	2.05	0.67	0.34	27.79	18.50	425.00	>>1	>>1
14	3.19	2.13	0.69	0.35	34.80	23.17	425.00	>>1	>>1

Table 52 Dome bolted connections assessment results at the end of current quench

DOME	σ_N on thread root section [MPa]	σ_N on smooth shank section [MPa]	τ_{th_N} in the threads [MPa]	τ_{th_N} in the head [MPa]	τ_{th_T} on thread root section [MPa]	τ_{th_T} on the smooth shank section [MPa]	S_m [MPa	S_f on σm (on the thread root section)	S_f on τ(thN due to normal load)
1	7.32	4.88	1.59	0.81	6.96	4.63	425.00	>>1	>>1
2	4.42	2.94	0.96	0.49	22.85	15.21	425.00	>>1	>>1
3	2.72	1.81	0.59	0.30	9.74	6.48	425.00	>>1	>>1
4	3.37	2.24	0.73	0.37	6.00	4.00	425.00	>>1	>>1
5	4.26	2.84	0.93	0.47	3.87	2.58	425.00	>>1	>>1
6	4.36	2.90	0.95	0.48	8.54	5.68	425.00	>>1	>>1
7	2.54	1.69	0.55	0.28	6.50	4.33	425.00	>>1	>>1
8	3.23	2.15	0.70	0.36	1.39	0.93	425.00	>>1	>>1
9	2.66	1.77	0.58	0.29	11.24	7.49	425.00	>>1	>>1
10	7.97	5.31	1.73	0.88	40.80	27.17	425.00	>>1	>>1
11	3.61	2.41	0.78	0.40	6.87	4.58	425.00	>>1	>>1
12	3.86	2.57	0.84	0.43	9.56	6.36	425.00	>>1	>>1
13	4.03	2.69	0.88	0.45	14.92	9.94	425.00	>>1	>>1
14	3.06	2.04	0.66	0.34	20.02	13.33	425.00	>>1	>>1

As already expected, since the forces induced at the end of the current quench on the PFU and their respective supports are compressive, the frictional contacts between the faceted surfaces of the back plates and the flanges absorb most of the load. Consequently, in this case, the screws are subjected to significantly lower stress, and the verification on each of them is largely satisfied.

Conclusion and future work

This PhD thesis addressed the development and validation of an integrated design and verification workflow for the DTT divertor, with the aim of tackling the main engineering challenges associated with the design of complex in-vessel components for fusion devices. The work systematically combined parametric geometry definition, multiphysics analyses, and structural verification within a unified and iterative framework, with particular emphasis on interfaces, constraints, load paths, and assembly-related effects governing the mechanical behavior of the divertor system.

A major outcome of this work is the definition and application of a structured design framework that enables consistent integration of CAD modeling, thermal, electromagnetic, and structural analyses. Starting from a parametric geometric description, the workflow proved effective in managing the strong coupling between geometric constraints, cooling system requirements, remote handling interfaces, and structural integrity criteria. This approach allowed design iterations to be carried out in a controlled and traceable manner, ensuring coherence between evolving design solutions and the associated multiphysics load scenarios.

A significant contribution of the thesis lies in the methodology adopted for the assessment of electromagnetic loads induced by plasma disruptions. A wide set of disruption scenarios, previously analyzed using dedicated MHD tools, was critically reviewed and compared with specific reference to their impact on the divertor structure. Among these, the slow downward disruption characterized by a current quench duration of 40 ms was identified as the most critical case for the divertor cassette. The reliability of the electromagnetic load predictions was further strengthened through benchmarking against JOREK simulations, providing confidence in their suitability as input for structural verification activities.

The structural assessment of the divertor cassette body was performed using advanced finite element models featuring a detailed representation of contact interactions, preload application procedures, and load sequencing. Within this framework, two alternative outboard fixation concepts—the knuckle fixation system and the wedges fixation system—were developed and comparatively assessed. The knuckle system demonstrated a robust and well-defined preload mechanism, offering high kinematic determinacy, while the wedges system introduced some flexibility margin in preload regulation, with potential benefits in accommodating manufacturing tolerances and assembly misalignments.

In parallel with the numerical activities, a dedicated experimental campaign was carried out to investigate the mechanical behavior of the fixation systems. A representative test rig, designed to reproduce the stiffness characteristics of the real divertor structure, was developed and manufactured.

Beyond the specific application to the DTT divertor, one of the main outcomes of this thesis is the definition of a design workflow that can be regarded as a shared and transferable methodology for systems operating in environments characterized by similar constraints. In particular, the proposed framework is directly applicable to a wide range of in-vessel components of tokamak reactors, which are typically subject—although to different extents—

to comparable thermal loads, electromagnetic forces, geometric constraints, and remote handling requirements.

More generally, the workflow can be extended to engineering systems operating in environments affected by time-varying electromagnetic fields, even outside the tokamak context, whenever a strong coupling between geometry, multiphysics phenomena, and structural response must be addressed. Looking forward, a natural evolution of the present framework is the development of a comprehensive master model, acting as a centralized and authoritative representation of the system throughout the design process.

Such a model would enable significant reductions in design time by supporting predictive design strategies. In this perspective, the integration of surrogate models and response surface methodologies—trained in batch mode on pre-existing simulation datasets—would allow rapid prediction of system responses without the need to explicitly run full numerical analyses at each iteration. This approach would be particularly beneficial during early design phases, trade-off studies, and sensitivity analyses.

Further improvements may be achieved through increased automation and enhanced interoperability between the different software tools and numerical codes involved in the workflow. By enabling seamless and standardized data exchange—where outputs from one analysis stage automatically become inputs for subsequent stages—the inherently iterative nature of the design process can be preserved while being more efficiently controlled.

Within this context, the integration of automated verification tools, such as routines for the automatic generation of stress classification lines in the most critical regions of the structure, would further strengthen the robustness, repeatability, and objectivity of structural assessments. Such automation would also reduce the risk of information loss, inconsistencies, and operator-dependent errors that may arise in complex, manually managed workflows.

By minimizing human intervention in data transfer and post-processing tasks, the framework promotes a more reliable, traceable, and standardized design process.

Annex A – DTT Divertor System Requirements

System Requirements [Divertor]							
HEL	**Requirement**	**Object Type**	**Requirement Type**	**Requirement Comments**	**Status**	**Compliance Status**	**Verification Status**
	DESIGN REQUIREMENTS						
	GENERAL REQUIREMENTS						
RQT_DIV_#01	The divertor shall exhaust the major part of the plasma ions thermal power in a region far from plasma core.	Requirement	Functional	Thus, the main high-level requirements to be considered in the design of DTT divertor shall be related to the power exhaust and vacuum pumping needs.	Proposed		Neutronic analysis
RQT_DIV_#02	The divertor shall be compatible with plasma operation.	Requirement	Functional	The Divertor will restrict the backflow of neutrals to the main plasma, so as to be compatible with plasma operation.	Proposed		Neutronic analysis
RQT_DIV_#03	The divertor shall be made of 54 toroidal sectors or cassette assemblies that are installed through four RH ports and remotely replaceable in the shortest possible time.	Requirement	Interface	The DTT divertor must be segmented into modules (3 divertor modules per door; almost symmetrical with respect to the equatorial plane in the upper part for the DN configuration). Each divertor box must comprise a cassette body, which supports the plasma	Proposed	Yes[16]	Compliance with geometrical features

				coating (PFC) components, one internal (IVT) and one external vertical target (OVT) and a dome.			
RQT_DIV_#04	The cassette body shall support a variety of plasma-facing components and diagnostics, routing the water coolant into the PFCs and providing neutron shielding.	Requirement	Operational	Each divertor cassette comprises a cassette body, which supports the plasma facing components (PFCs), an inner (IVT) and outer vertical target (OVT) and a dome.	Proposed		Neutronic analysis Fluid dynamics analysis

RQT_DIV_#05	The first divertor shall have tungsten for all its plasma-facing surfaces.	Requirement	Operational	The baseline DTT design refers to an actively cooled conventional tungsten divertor, compatible with both SN and SF or XD configurations, segmented in 54 toroidal sectors or cassettes with inner and outer vertical target and a dome.	Proposed		Electromagnetic analysis
RQT_DIV_#06	The shape of the dome, together with the VTs, shall form a Vshaped channel route.	Requirement	Functional		Proposed	Yes	Compliance with geometrical features
RQT_DIV_#07	The term “Divertor Toroidal Rails” shall refer to the following parts: a. The "hard cover plates" of the divertor inner and outer toroidal rail b. The CCORs in front of each of the lower ports c. The divertor support pads of the CCORs.	Requirement	Functional		Proposed	Yes	Compliance with geometrical features

RQT_DIV_#08	The locking system shall be designed to carry the maximum halo and eddy currents in the event of VDEs.	Requirement	Functional		Proposed		Electromagnetic analysis
RQT_DIV_#09	The lower part of the inner and outer VTs should intercept the magnetic field lines.	Requirement	Functional		Proposed		Electromagnetic analysis Neutronic analysis
RQT_DIV_#10	The divertor toroidal rails and the support of the divertor cassette body shall ensure alignment and attachment of the cassette body to the VV during operation.	Requirement	Operational	During cassette body handling, the toroidal rails ensure the guiding and supporting of the cassette toroidal mover inside the vessel.	Proposed	Yes	Compliance with geometrical features
RQT_DIV_#11	The divertor rails shall be designed for the DTT lifetime.	Requirement	Functional		Proposed		Maintainability analysis
RQT_DIV_#12	The divertor shall receive coolant water via pipes router radially through the top section of the ports.	Requirement	Functional		Proposed	Yes	Compliance with geometrical features
RQT_DIV_#13	Cassette bodies will need to be devoted to various diagnostics.	Information	Interface		Proposed		Maintainability analysis
RQT_DIV_#14	The divertor shall support the DTT operational lifetime.	Requirement	Operational		Proposed		Maintainability analysis

RQT_DIV_#15	The divertor cassettes without any instrumentation or modifications shall refer to *Standard Cassette.*	Requirement	Non-Functional System		Proposed		Structural assessment Interface analysis
RQT_DIV_#16	The divertor design shall comply with the basic conditions and events specified [TBD] in the *Load Specification.*	Requirement	Functional	This includes the optimization of the required number of handling activities, the transfer trajectory and lifting height as well as protection measures to be put in place in the event of the failure (direct or indirect) of the handling system or an operation error.	Proposed		Structural assessment
RQT_DIV_#17	The divertor design shall be verified by analysis or qualification tests under the specified loads in the design review.	Requirement	Functional		proposed		Structural assessment
RQT_DIV_#18	The divertor shall receive cooling water with the appropriate water chemistry to prevent corrosion damage of materials in cooling circuits. The water chemistry shall be controlled with the established methods within specified limits for all modes of operation including commissioning, plasma operation, baking, and hot and cold standby states.	Requirement	Functional		Proposed		Material analysis
RQT_DIV_#19	The materials of inlet and outlet divertor cooling seamless pipes shall be stainless steel.	Requirement	Functional		Proposed		Material analysis

RQT_DIV_#20	The divertor shall be replaced frequently ([TBD] times during the nominal DTT operational life).	Requirement	Operational	Since the machine main purpose is to be a facility dedicated to test different divertor, the possibility to “easily” replace a divertor, with a new one completely different, must be taken in account from the very beginning of the full machine design (ports, coils, VV, support forces,…).	Proposed		Maintainability analysis
RQT_DIV_#21	The divertor project shall comply with the Structural Design Criteria.	Requirement	Non-Functional Implementation Requirements		Proposed		Structural assessment

RQT_DIV_#22	The divertor shall provide a means for rapid replacement and refurbishment.	Requirement	Functional	The divertor design shall provide an engineering solution that is compatible with today's plasma physics expectations; but, given the uncertainties in extrapolating the future progress in plasma physics, and thus in component durability, the design shall also provide a means for rapid replacement and refurbishment.	Proposed		Maintainability analysis
RQT_DIV_#23	The divertor design should be compatible, as much as possible, with quite different topologies of power load.	Requirement	Non-Functional System		Proposed		Structural assessment Neutronic analysis
RQT_DIV_#24	The divertor shall be capable of draining and drying for leak detection and before removal from the VV.	Requirement	Operational		Proposed		Maintainability analysis
RQT_DIV_#25	The divertor shall conform to the space envelope constraints and interface characteristics specified in the CAD assemblies, parts, and drawings in the Configuration Management Model.	Requirement	Interface		Proposed		Geometrical analysis Interface testing
RQT_DIV_#26	The divertor shall tolerate high heat loads while at the same time providing neutron shielding for the VV and magnet coils, in the vicinity of the divertor.	Requirement	Functional		Proposed		Neutronic analysis Thermomechanical analysis
RQT_DIV_#27	The design of the lower parts of the VTs shall allow for a surface heat flux up to 10 MW / m2 (time average on the strike point region) and the upper part of the VT (baffle region)	Requirement	Functional		Proposed		Thermomechanical analysis

	for a heat flux up to 5 MW / m2.						
RQT_DIV_#28	The lower parts of VTs shall be capable of receiving a surface heat flux of up to 20 MW/m2 up to 10 s, under slow transient thermal loading conditions.	Requirement	Functional		Proposed		Thermomechanical analysis
RQT_DIV_#29	The divertor cassette body and PFCs shall be capable of withstanding the radiation loads through gaps.	Requirement	Functional		Proposed		Structural assessment
RQT_DIV_#30	The divertor design must be built to accommodate 300 baking cycles by hot water from the commissioning phase to the end of the DTT life cycle.	Requirement	Functional		Proposed		Structural assessment

RQT_DIV_#31	The path for gas conductance from the divertor sub-volume to the main chamber shall be minimised by maintaining close proximity of the divertor cassette to the vacuum vessel, and by a proper design of the cassette locking system.	Requirement	Functional		Proposed		Geometrical analysis Vacuum analysis
	STRUCTURAL REQUIREMENTS						
RQT_DIV_#19-1	The support system of the divertor cassette to the inner and outer toroidal rails shall be designed to accommodate distortions of the rail and cassette.	Requirement	Functional	The distortions are due to thermal expansion which must be 4 mm in the radial direction.	Proposed	Yes	Mechanical analysis Compliance with geometrical features
RQT_DIV_#19-2	The support system of the divertor cassette to the inner and outer toroidal rails shall withstand the electromagnetic loads that are specified in the *Load Specifications.*	Requirement	Non-Functional System		Proposed		Electromagnetic loads analysis
RQT_DIV_#19-3	All components that are installed as part of the divertor (including diagnostics) shall be able to withstand nuclear heating and nuclear afterheat.	Requirement	Functional	Nuclear heating occurs during operation while reheating occurs during maintenance and downtime.	Proposed		Thermomechanical analysis Neutronic analysis
	MECHANICAL REQUIREMENTS (including load conditions)						

RQT_DIV_#14-1	The divertor shall withstand external forces caused by relative movement of the vessel and other in-vessel components within allowable stress and deflection allowable.	Requirement	Functional	Design analyses of the VV body is carried out in accordance with the criteria defined in ASME.	Proposed		Structural assessment
RQT_DIV_#14-2	The divertor cassette body shall withstand the various normal and off-normal combinations of loads.	Requirement	Functional		Proposed		Structural assessment
RQT_DIV_#32	The divertor design must be developed so as not to damage other components of the PIC due to the overall deformation of the cassettes even after any loads event, although the loss of integrity of the same the pressure limit of the cooling system is acceptable.	Requirement	Functional		Proposed		Structural assessment Regulatory verification

	SEISMIC REQUIREMENTS						
RQT_DIV_#33	The divertor shall be comply with anti-seimistic Italian standards.	Requirement	Non-Functional System		Proposed		Seismic analysis
	FIRE PROTECTION REQUIREMENTS						
RQT_DIV_#34	The management of the divertor shall take place in the area where the "defense in depth" fire protection program is established.	Requirement	Operational		Proposed		Thermal analysis
RQT_DIV_#35	The management of the divertor shall take place in the area where the quantity of combustible materials and loads in each room or area is limited to the minimum process requirements, with appropriate control and monitoring measures.	Requirement	Operational		Proposed		Thermal analysis Structural assessment
	ELECTRICAL REQUIREMENTS						
RQT_DIV_#36	The power shall be supplied in accordance with the DTT Electrical Design.	Requirement	Functional		Proposed		Electrical analysis
	GROUNDING AND INSULATION REQUIREMENTS						

RQT_DIV_#37	The divertor cassette shall be electrically connected to the VV via the inner and outer locking system.	Requirement	Operational		Proposed	Yes	Electrical analysis Compliance with geometrical features
RQT_DIV_#38	For Divertor cassettes with diagnostics and instrumentation, the required electrical connector should withstand the fraction of halo and eddy currents that may flow through them.	Requirement	Functional		Proposed		Electrical analysis

	INSTRUMENTATION AND CONTROL REQUIREMENTS						
RQT_DIV_#39	RM systems shall guarantee feedback to RM operators.	Requirement	Interface	Force/torque sensors as well as cameras are needed to get sensory information. Virtual reality and physics-based simulators are needed.	Proposed		Maintainability analysis
RQT_DIV_#40	The divertor shall have operational instrumentation that is aimed at measuring the thermo-mechanical response under operation (such as thermocouples, strain gauges, displacement sensors and Rogowski coils).	Requirement	Functional		Proposed		Thermomechanical analysis Maintainability analysis
RQT_DIV_#41	The operational instrumentation shall use electric cables and other materials which do not contribute to the spread of fire (C1 cables, or cables that are protected by a flame retardant material for a radiologically-controlled building) through a fire sector.	Requirement	Functional		Proposed		Electrical analysis
	VACUUM REQUIREMENTS AND VACUUM CLASSIFICATIONS						
RQT_DIV_#42	The divertor will be exposed to the primary vacuum under normal and off-normal conditions.	Information	Functional		Proposed		Vacuum analysis

RQT_DIV_#43	The design of divertor shall be such as to facilitate leak testing of individual welds during installation, and subsequent operations, as far as practical.	Requirement	Functional		Proposed		Geometrical analysis Magnetoscopic analysis Analysis with penetrating liquids Vacuum analysis
RQT_DIV_#44	The divertor design shall facilitate the detection and isolation of vacuum leaks.	Requirement	Functional		Proposed		Vacuum analysis
	THERMAL MANAGEMENT REQUIREMENTS						

RQT_DIV_#10-1	The divertor cooling channels shall be designed for a temperature of 240 ° C and a pressure of 5.5 MPa.	Requirement	Functional		Proposed		Thermal analysis
RQT_DIV_#46	The support system design of the divertor cassette to the internal and external toroidal rails shall accommodate the distortions of the rail and cassette caused by thermal bowing, neutron-induced swelling and vacuum application.	Requirement	Functional		Proposed		Geometrical analysis Structural assessment
RQT_DIV_#47	The margin on critical heat flux (CHF) on the Divertor under any circumstances shall be greater than 1.4.	Requirement	Functional		Proposed		Fluid-thermodynamic analysis
	NUCLEAR SHIELDING REQUIREMENTS						
RQT_DIV_#48	The divertor, together with the VV and the other in- and ex-vessel components, shall limit the peak nuclear heating in the in superconducting coil conductor to less than 1 mW/cm3.	Requirement	Functional	The maximum acceptable heat load is 1 mW/cm3 in order to meet the requirement of 1.5 K temperature margin.	Proposed		Neutronic analysis
RQT_DIV_#49	The divertor, together with the VV and the other in- and ex-vessel components, shall limit the insulator dose in the coils that are outside the VV to less than 10^7 Grays.	Requirement	Functional	The maximum absorbed dose in the IVC and TF coil insulator at the end of life are ~1.2 MGy and ~90 kGy (without safety factor), respectively. Assuming a design limit of 10 MGy on epoxy resin, the maximum dose in the insulator at the end of operations is expected to be well below the limit recommended for the replacement.	Proposed		Insulation test

RQT_DIV_#50	The divertor, together with the VV and the other in- and ex-vessel components, shall limit the peak nuclear heating in the superconducting coil steel case and structures to less than 2 kW/m3.	Requirement	Functional		Proposed		Neutronic analysis Thermal analysis
RQT_DIV_#51	The divertor, together with the VV and the other in- and ex-vessel components, shall limit the integrated nuclear heating in the TF coils to a value that is as low as reasonably achievable.	Requirement	Functional		Proposed		Nuclear analysis Thermal analysis

RQT_DIV_#52	The divertor, together with the VV and port mounted equipment, shall limit the dose rate in accessible areas of the cryostat to a level that would allow hands-on maintenance. The dose rate shall be as low as reasonably achievable.	Requirement	Functional		Proposed		Maintainability analysis
RQT_DIV_#24-1	The divertor design shall comply with the *Heat and Nuclear Load Specifications*.	Requirement	Non-Functional System		Proposed		Nuclear analysis Structural assessment
	MATERIAL REQUIREMENTS						
RQT_DIV_#17-1	Materials and environment chemistry should not cause local corrosion damage (such as pitting, stress corrosion cracking, or significant galvanic corrosion).	Requirement	Operational		Proposed		Corrosion test
RQT_DIV_#53	Materials composition shall provide ALARA requirements on radioactivity protection.	Requirement	Non-Functional System	So as to achieve the minimization of radioactive waste generation of corrosion products of activation and contact dose (as a limit on Co impurities).	Proposed		Radioactivity analysis
RQT_DIV_#54	The divertor shall use materials so that the hydrogen production is minimized and explosive mixtures of hydrogen with air/oxygen are avoided.	Requirement	Functional		Proposed		Thermal analysis Nuclear analysis

RQT_DIV_#55	The divertor shall use materials with no magnetic behaviour.	Requirement	Functional		Proposed		Material analysis
	MANUFACTURING REQUIREMENTS						
RQT_DIV_#56	The divertor shall be fabricated by processes considering the minimization of the error fields, whenever possible.	Requirement	Operational		Proposed		Maintainability analysis
	COSTRUCTION REQUIREMENTS						

RQT_DIV_#57	The divertor shall be packed and transported to the DTT site taking into account the meteorological conditions, the risks of abnormal conditions, and some Cadarache specific criteria that are imposed by Italy and European norms.	Requirement	Operational		Proposed		Maintainability analysis
	ASSEMBLY REQUIREMENTS						
RQT_DIV_#02-1	The divertor shall have PFCs design to avoid exposing the leading edges of the armour to the SOL.	Requirement	Functional		Proposed		Assembly analysis
RQT_DIV_#58	The reference directionality of the toroidal current and field shall be taken into account when determining the orientation of the tilting.	Requirement	Functional		Proposed		Magnetic analysis Geometrical analysis
RQT_DIV_#59	Each hard cover plate and divertor cassette shall have a unique identifier.	Requirement	Operational		Proposed		Maintainability analysis
RQT_DIV_#03-1	An inner and outer locking system shall be integrated into the cassette body to allow it to be locked and aligned in the VV.	Requirement	Functional		Proposed		Geometrical analysis
RQT_DIV_#60	Bolts used in divertor assemblies and rails shall be secured.	Requirement	Functional		Proposed		Fastening test
RQT_DIV_#61	The divertor shall be verified in the integrated commissioning including a mechanical verification of position, loads, stresses, strains, vibrations and temperatures under operational conditions.	Requirement	Non-Functional System		Proposed		Mechanical analysis Structural assessment Maintainability analysis
RQT_DIV_#08-1	The design of the divertor cassette to VV locking system shall minimise any dynamic	Requirement	Functional		Proposed		Geometrical analysis

	effect during off-normal events.						
RQT_DIV_#23-1	The Divertor design shall be based on a nominal step between PFCs on adjacent cassettes of approximately 5 mm.	Requirement	Functional		Proposed		Structural assessment

RQT_DIV_#62	The reference directionality of the current and the toroidal field shall be: plasma current in the negative direction (clockwise looking from above) with negative toroidal field (clockwise direction), giving a downward (towards the divertor X-point) ion grad-B drift direction (as shown in the following figure). The direction of the toroidal field and plasma current is reversible, in such a way the field line maintains the same pitch angle (that is, the directions of the toroidal field and the plasma current can only be changed together).	Requirement	Functional		Proposed		Neutronic analysis
	INSTALLATION REQUIREMENTS						
RQT_DIV_#63	The installation of the divertor shall respect the defined assembly tolerances.	Requirement	Operational		Proposed		Tolerance test
RQT_DIV_#09-1	The inner and outer divertor toroidal rails shall be procured with an extra thickness at the interface with the stainless steel rail body in such a way that final custom machining of these hard cover plates is possible after performing an accurate survey of the stainless-steel rail bodies that are welded to the vacuum vessel.	Requirement	Interface		Proposed		Manufacturing analysis

	DECOMMISSIONING REQUIREMENTS						
RQT_DIV_#20-1	The divertor shall be dismantled and disposed by the Host Member following deactivation of the facility.	Requirement	Operational		Proposed		Dismantling test
RQT_DIV_#64	The decommissioning phase will be described in a specific plan including the decontamination and/or the removal of structures, systems and components, and the management of the residual radiation waste.	Requirement	Functional		Proposed		Maintainability analysis

RQT_DIV_#65	Safety functions will need to be developed following strict standards that imply use of specialised hardware and software together with thorough documentation.	Requirement	Functional	The decommissioning process will be resumed in the technical documents attached to the license application.	Proposed		Maintainability analysis
	OTHER SERVICE						
RQT_DIV_#66	The divertor shall be handled by staff who are suitably trained and qualified to undertake DTT operations (including maintenance activities).	Requirement	Operational	Decommissioning typically includes dismantling of the facility (or part thereof) to reduce the associated radiation risks, but a facility could be decommissioned without dismantling and the existing structures subsequently put to another use (after decontamination).	Proposed		Maintainability analysis
	SAFETY DESIGN REQUIREMENTS						
	SAFETY RELATED OPERATIONS AND PROCEDURES						
RQT_DIV_#67	The divertor shall be handled in accordance with authorized procedure in ALARA principle and to ensure that worker exposures to radiological and other hazards are ALARA and in all cases within the General Safety Objectives and the guidelines for exposure to such hazards. The hazards shall be communicated to the workers prior to the entry. The workers' habitable space shall provide safe ingress and egress paths.	Requirement	Operational		Proposed		Maintainability analysis

	OCCUPATIONAL SAFETY						

RQT_DIV_#68	Design and operation (decontamination, shielding, remote operations, and flask transfer) shall minimise the dose to personnel in the course of maintenance and decommissioning.	Requirement	Operational	Ionizing radiation can trigger both deterministic and stochastic health effects. The aim of radiation protection is to prevent reliably the deterministic effects of radiation and to reduce the risk of stochastic effects to a reasonably achievable level. The dose limit values are set so that deterministic effects are ruled out. In order to keep the risk of stochastic damage from ionizing radiation as low as possible, three general principles have been set out in radiation protection for dealing with ionizing radiation: justification, optimization (or ALARA, principle) and dose limitation.	Proposed		Maintainability analysis
RQT_DIV_#69	The divertor shall be maintenance by remote handling once the VV becomes activated.	Requirement	Interface		Proposed		Maintainability analysis
	ENVIRONMENTAL IMPACT REQUIREMENTS						
RQT_DIV_#70	Amounts and radio toxicity of radioactive waste from operation and decommissioning of the divertor, shall be minimised within the limits that are set by the applicable materials.	Requirement	Functional		Proposed		Radioactivity analysis
	OTHER REQUIRMENTS						
RQT_DIV_#20-2	The divertor design should facilitate repair and decommissioning (including tritium	Requirement	Functional		Proposed		Radioactivity analysis

	reclamation) and should reduce occupational exposures.						
RQT_DIV_#71	The divertor shall be handled with equipment designed and operated so to prevent any injury to the personnel and any damage to the handled equipment or surrounding components.	Requirement	Operational		Proposed		Personnel safety testing Maintainability analysis
	OPERATION AND MAINTANACE						

	OPERATION						
RQT_DIV_#72	The divertor operational instrumentation shall provide the data to be displayed in the main control room.	Requirement	Interface		Proposed		Maintainability analysis
	MAINTENANCE						
RQT_DIV_#73	The divertor design shall guarantee remote leak tests after maintenance activities.	Requirement	Operational		Proposed		Maintainability analysis
RQT_DIV_#74	The divertor shall be maintained in accordance with the maintenance classification in order to manage the DTT maintenance planning.	Requirement	Operational		Proposed		Maintainability analysis
RQT_DIV_#75	The maintenance requirements of the divertor shall conform to the maintenance periods that are defined for DTT.	Requirement	Operational		Proposed		Maintainability analysis
RQT_DIV_#76	The divertor shall be supported and allowed for remote handling operation.	Requirement	Operational		Proposed		Maintainability analysis
RQT_DIV_#20-3	The divertor shall be designed to reduce the time to repair.	Requirement	Operational		Proposed		Maintainability analysis
RQT_DIV_#77	The divertor shall be maintenanced remotely once the vacuum vessel becomes activated.	Requirement	Operational		Proposed		Maintainability analysis
	QUALITY REQUIREMENTS						

RQT_DIV_#78	The divertor shall be designed, manufactured, tested, commissioned, operated, maintained and decommissioned in compliance with the DTT Quality Assurance Program.	Requirement	Operational		Proposed		Quality analysis

Annex B - DTT required data and IDS for JOREK initialization

Table 53 pf_active ids required data for disruption simulation

Path	Type	Units	Description
pf_active.coil[:].element (alpha)	STRUCT_ARRAY		Each PF coil is comprised of a number of cross-section elements described individually
pf_active.coil[:].element[:].area (alpha)	FLT_0D (uncertain)	m^2	Cross-sectional areas of the element
pf_active.coil[:].element[:].geometry (alpha)	STRUCTURE		Cross-sectional shape of the element
pf_active.coil[:].element[:].geometry.rectangle (alpha)	STRUCTURE		Rectangular description of the element
pf_active.coil[:].element[:].geometry.rectangle.height (alpha)	FLT_0D (uncertain)	m	Vertical full height
pf_active.coil[:].element[:].geometry.rectangle.r (alpha)	FLT_0D (uncertain)	m	Geometric centre R
pf_active.coil[:].element[:].geometry.rectangle.width	FLT_0D (uncertain)	m	Horizontal full width

(alpha)			
pf_active.coil[:].element[:].geometry.rectangle.z (alpha)	FLT_0D (uncertain)	m	Geometric centre Z
pf_active.coil[:].name (alpha)	STR_0D		Name of the coil
pf_active.coil[:].resistance (alpha)	FLT_0D (uncertain)	Ohm	Coil resistance
pf_active.ids_properties (alpha)	STRUCTURE		Interface Data Structure properties. This element identifies the node above as an IDS
pf_active.ids_properties.comment (alpha)	STR_0D		Any comment describing the content of this IDS
pf_active.ids_properties.creation_date (alpha)	STR_0D		Date at which this data has been produced
pf_active.ids_properties.homogeneous_time (alpha)	INT_0D		This node must be filled (with 0, 1, or 2) for the IDS to be valid. If 1, the time of this IDS is homogeneous, i.e. the time values for

			this IDS are stored in the time node just below the root of this IDS. If 0, the time values are stored in the various time fields at lower levels in the tree. In the case only constant or static nodes are filled within the IDS, homogeneous_time must be set to 2
pf_active.ids_properties.name (alpha)	STR_0D		User-defined name for this IDS occurrence
pf_active.ids_properties.occurrence	INT_0D		
pf_active.ids_properties.occurrence_type (alpha)	STRUCTURE		Type of data contained in this occurrence 1) reconstruction : Equilibrium reconstruction 2) prediction_fixed : Equilibrium prediction, fixed boundary

			3) prediction_free : Equilibrium prediction, free boundary 4) mapping : Used for mapping equilibrium results from one grid type / resolution to another, or for including variables not present in the first set such as the calculation of magnetic field of other derived parameters
pf_active.ids_properties.occurrence_type.description (alpha)	STR_0D		Verbose description
pf_active.ids_properties.occurrence_type.index (alpha)	INT_0D		Integer identifier (enumeration index within a list). Private identifier values must be indicated by a negative index.

pf_active.ids_properties.occurrence_type.name (alpha)	STR_0D		Short string identifier
pf_active.time (alpha)	FLT_1D_TYPE	s	Generic time

Table 54 equilibrium ids required data for disruption simulation

equilibrium ids	
equilibrium.ids_properties	equilibrium.ids_properties.homogeneous_time
	equilibrium.ids_properties.version_put.data_dictionary
	equilibrium.ids_properties.version_put.access_layer
	equilibrium.ids_properties.version_put.access_layer_language
equilibrium.vacuum_toroidal_field	equilibrium.vacuum_toroidal_field.r0
	equilibrium.vacuum_toroidal_field.b0
equilibrium.time_slice[].global_quantities	equilibrium.time_slice[].global_quantities.ip
	equilibrium.time_slice[].global_quantities.psi_axis
	equilibrium.time_slice[].global_quantities.psi_boundary
	equilibrium.time_slice[].global_quantities.magnetic_axis.r
	equilibrium.time_slice[].global_quantities.magnetic_axis.z
equilibrium.time_slice[].profiles_1d	equilibrium.time_slice[].profiles_1d.psi
	equilibrium.time_slice[].profiles_1d.pressure
	equilibrium.time_slice[].profiles_1d.f
	equilibrium.time_slice[].profiles_1d.dpressure_dpsi

	equilibrium.time_slice[].profiles_1d.f_df_dpsi
	equilibrium.time_slice[].profiles_1d.q
	equilibrium.time_slice[].profiles_1d.rho_tor_norm
equilibrium.time_slice[].profiles_2d	equilibrium.time_slice[].profiles_2d[].grid_type.index
	equilibrium.time_slice[].profiles_2d[].grid.dim1
	equilibrium.time_slice[].profiles_2d[].grid.dim2
	equilibrium.time_slice[].profiles_2d[].r
	equilibrium.time_slice[].profiles_2d[].z
	equilibrium.time_slice[].profiles_2d[].psi
	equilibrium.time_slice[].time
	equilibrium.time

Table 55 core_profiles ids required data for disruption simulation

Core profiles ids	
core_profiles.ids_properties	core_profiles.ids_properties.homogeneous_time
	core_profiles.ids_properties.version_put.data_dictionary
	core_profiles.ids_properties.version_put.access_layer
	core_profiles.ids_properties.version_put.access_layer_language
core_profiles.vacuum_toroidal_field	core_profiles.vacuum_toroidal_field.r0
	core_profiles.vacuum_toroidal_field.b0
core_profiles.profiles_1d[]	Grid • core_profiles.profiles_1d[].grid.rho_tor_norm • core_profiles.profiles_1d[].grid.psi • core_profiles.profiles_1d[].grid.psi_magnetic_axis core_profiles.profiles_1d[].grid.psi_boundary
	Electrons • core_profiles.profiles_1d[].electrons.temperature core_profiles.profiles_1d[].electrons.density

	Array of ion • ion[] o Array of element ▪ element[] • core_profiles.profiles_1d[].ion[].element[].a • core_profiles.profiles_1d[].ion[].element[].z_n • core_profiles.profiles_1d[].ion[].element[].atoms_n o core_profiles.profiles_1d[].ion[].z_ion o core_profiles.profiles_1d[].ion[].z_ion_1d o core_profiles.profiles_1d[].ion[].z_ion_square_1d core_profiles.profiles_1d[].ion[].density
	core_profiles.profiles_1d[].t_i_average
	core_profiles.profiles_1d[].zeff
	core_profiles.profiles_1d[].pressure_thermal
	core_profiles.profiles_1d[].j_tor
	core_profiles.profiles_1d[].j_non_inductive
	core_profiles.profiles_1d[].j_bootstrap
	core_profiles.profiles_1d[].conductivity_parallel
	core_profiles.profiles_1d[].q
	core_profiles.profiles_1d[].time

Table 56 pf_passive required data for disruption simulation

pf_passive
pf_passive.ids_properties.homogeneous_time
pf_passive.ids_properties.version_put.data_dictionary

pf_passive.ids_properties.version_put.access_layer
pf_passive.ids_properties.version_put.access_layer_language
pf_passive.loop[].name
pf_passive.loop[].identifier
pf_passive.loop[].resistance
pf_passive.loop[].temperature
pf_passive.loop[].element[] • pf_passive.loop[].element[].turns_with_sign • pf_passive.loop[].element[].geometry.geometry_type • pf_passive.loop[].element[].geometry.oblique.r • pf_passive.loop[].element[].geometry.oblique.z • pf_passive.loop[].element[].geometry.oblique.lenght_alpha • pf_passive.loop[].element[].geometry.oblique.lenght_beta • pf_passive.loop[].element[].geometry.oblique.alpha • pf_passive.loop[].element[].geometry.oblique.beta

Table 57 wall required data for disruption simulation

wall
wall.ids_properties
wall.ids_properties.homogeneous_time
wall.ids_properties.version_put.data_dictionary
wall.ids_properties.version_put.access_layer
wall.ids_properties.version_put.access_layer_language
wall.[]
wall.description_2d[].limiter.type.name
wall.description_2d[].limiter.type.index
wall.description_2d[0].limiter.type.description
wall.description_2d[].limiter.unit[].

- wall.description_2d[].limiter.unit[].name
- wall.description_2d[].limiter.unit[].closed
- wall.description_2d[].limiter.unit[].outline.r
- wall.description_2d[].limiter.unit[].outline.z

Annex C - Python routines for DTT IMAS shot integration

Routine for vessel loop discretization

```
# Loop through points in sets of 3
    for i in range(0, len(points), 3):
        # Extract points A, B, C
        A = np.array(points[i])
        B = np.array(points[i + 1])
        C = np.array(points[i + 2])

        # Calculate vectors AB and BC
        vector_AB = B - A
        vector_BC = C - B

        # Calculate lengths of first and second edges
        length_AB = distance(A, B)  # Length of the first edge
        length_BC = distance(B, C)  # Length of the second edge

        # Append lengths to respective arrays
        first_edge_lengths.append(length_AB)
        second_edge_lengths.append(length_BC)

        # Calculate angles
        beta = np.arctan2(vector_AB[1], vector_AB[0]) - np.pi / 2  # Angle with respect to
vertical (beta)
```

```
        alpha = np.arctan2(vector_BC[1], vector_BC[0])  # Angle with respect to x-axis
(alpha)

       # Adjust alpha for indices 16 to 31 (inclusive) by adding 180 degrees
        if i // 3 >= 108 and i // 3 <= len(points):
            alpha = alpha + np.pi



        # Convert angles from radians to degrees and normalize to [0, 360)
        alpha_deg = np.degrees(alpha) % 360
        beta_deg = np.degrees(beta) % 360

        # Append angles to respective arrays
        alpha_angles.append(alpha_deg)
        beta_angles.append(beta_deg)

        # Append the starting point (A) to the starting_points array
        starting_points.append(A)
```

Full routine for DTT IMAS Machine Description integration

```
#The script populates the DTT_MD database.
# Import necessary libraries
import numpy as np
import matplotlib.pyplot as plt
import imas
from imas import imasdef

#pf_active
# Define shot number, run number, database name, and user
credentials
```

```
shot = 111002
run = 1
database = 'DTT_MD'
user = 'massann'

# Create a new IMAS database entry for the specified shot and
run
# This initializes a new entry in the IMAS database with the
provided parameters
imas_entry = imas.DBEntry(imasdef.MDSPLUS_BACKEND, database,
shot, run, user, data_version='3')
imas_entry.create(mode=imasdef.CREATE_PULSE)  # Create a new
pulse entry

# Initialize the IDS
# Set the coil array size to 17, which includes Central
Solenoids (CS), Poloidal Field Coils (PF), and In-Vessel
Coils (IVC)
ids = imas.pf_active()
ids.coil.resize(17)  # Resize the coil array to hold 17 coils

#Specify number of elements for each type of coil
ne_cs = 2
ne_pf_ivc =1

# Resize and configure the coil elements based on their type
for i in range(6):
    ids.coil[i].element.resize(ne_cs)  #CS coils will have
two elements each
    for j in range(ne_cs):
        ids.coil[i].element[j].geometry.geometry_type = 2  #
Set geometry type for each coil element to "rectangle"
```

```
for i in range(6, len(ids.coil)):
    ids.coil[i].element.resize(ne_pf_ivc) #PF and IV coils
will have 1 element each
    ids.coil[i].element[0].geometry.geometry_type = 2 #Set
geometry type for each coil element to "rectangle"

# Set metadata and properties for the IDS entry
ids.ids_properties.homogeneous_time = 2  # Set the time mode
to homogeneous
ids.ids_properties.creation_date = "18/09/2024"  # Set the
creation date
ids.ids_properties.comment = "DTT Machine Description for
PF/CS Coil System"  # Add a general comment
ids.ids_properties.provider = "Nicola Massanova (University
of Trieste, CREATE Consortium), E-
mail:nicola.massanova@iter.org"  # Provide data provider
information
ids.ids_properties.source =
"DTT2024_06730,DTT2024_06731,DTT2020_02293"

# Assign names, identifiers, and geometric properties to
Central Solenoids
for i in range(6):
    ids.coil[i].name = central_solenoid_names[i]  # Assign
name
    ids.coil[i].identifier = central_solenoid_ids[i]  #
Assign identifier
    # Set geometry properties
    ids.coil[i].element[0].geometry.rectangle.r =
float(cs_r_hf[i])
```

```
    ids.coil[i].element[0].geometry.rectangle.z =
float(cs_z[i])
    ids.coil[i].element[0].geometry.rectangle.height =
float(cs_h[i])
    ids.coil[i].element[0].geometry.rectangle.width =
float(cs_w_hf[i])
    ids.coil[i].element[0].turns_with_sign =
float(cs_turn_hf[i])
    ids.coil[i].element[1].geometry.rectangle.r =
float(cs_r_lf[i])
    ids.coil[i].element[1].geometry.rectangle.z =
float(cs_z[i])
    ids.coil[i].element[1].geometry.rectangle.height =
float(cs_h[i])
    ids.coil[i].element[1].geometry.rectangle.width =
float(cs_w_lf[i])
    ids.coil[i].element[1].turns_with_sign =
float(cs_turn_lf[i])
    ids.coil[i].resistance = float(cs_resistance[i])
    # ids.coil[i].current.data = np.array(cs_currents[i])
    # ids.coil[i].current.time = np.array([16])
# Assign names, identifiers, and geometric properties to
Poloidal Field Coils
for i in range(6):
    ids.coil[i + 6].name = poloidal_field_base_name.format(i
+ 1, i + 1)  # Assign name
    ids.coil[i + 6].identifier = poloidal_field_ids[i]  #
Assign identifier
    # Set geometry properties
    ids.coil[i + 6].element[0].geometry.rectangle.r =
float(pf_r[i])
```

```
    ids.coil[i + 6].element[0].geometry.rectangle.z =
float(pf_z[i])
    ids.coil[i + 6].element[0].geometry.rectangle.height =
float(pf_h[i])
    ids.coil[i + 6].element[0].geometry.rectangle.width =
float(pf_w[i])
    ids.coil[i + 6].element[0].turns_with_sign =
float(pf_turn[i])
    ids.coil[i + 6].resistance = float(pf_resistance[i])
    # ids.coil[i+6].current.data = np.array(pf_currents[i])
    # ids.coil[i+6].current.time = np.array([16])
# Assign names, identifiers, and geometric properties to In-
Vessel Coils
for i in range(5):
    ids.coil[i + 12].name = ivc_base_name.format(i + 1, i +
1)  # Assign name
    ids.coil[i + 12].identifier = ivc_ids[i]  # Assign
identifier
    # Set geometry properties
    ids.coil[i + 12].element[0].geometry.rectangle.r =
float(ivc_r[i])
    ids.coil[i + 12].element[0].geometry.rectangle.z =
float(ivc_z[i])
    ids.coil[i + 12].element[0].geometry.rectangle.height =
float(ivc_h[i])
    ids.coil[i + 12].element[0].geometry.rectangle.width =
float(ivc_w[i])
    ids.coil[i + 12].element[0].turns_with_sign =
float(ivc_turn[i])
    ids.coil[i + 12].resistance = float(ivc_resistance[i])

# Save the updated IDS entry to the IMAS database
```

```
imas_entry.put(ids)  # Save the IDS entry to the database
%%%%%%%%%%%%%%%%%%%%%%%%%%%%%%%%%%%%%%%%%%%%%%%%%%%%%%%%%%%%%




#pf_passive
# Define shot number, run number, database name, and user credentials
shot = 115006
run = 1
database = 'DTT_MD'
user = 'massann'

# Create a new IMAS database entry for the specified shot and run
# This initializes a new entry in the IMAS database with the provided parameters
imas_entry = imas.DBEntry(imasdef.MDSPLUS_BACKEND, database, shot, run, user, data_version='3')
imas_entry.create(mode=imasdef.CREATE_PULSE)  # Create a new pulse entry

# Initialize the IDS
# Set the size of the loop to the number of loops included for the pf_passive
ids = imas.pf_passive()
ids.loop.resize(212)  # Resize

#Define the number of elements of which each loop will be composed
ne_vv = 1
ne_sp = 3
```

```
# Resize and configure the pf_passive elements based on their
type
#Vessel oblique loops
for i in range(155):
    ids.loop[i].element.resize(ne_vv)  # Each vv loop has one
element
    ids.loop[i].element[0].geometry.geometry_type = 3  # Set
geometry type for each coil element to "oblique"
#Vessel  rectangular loops
for i in range(155,211):
    ids.loop[i].element.resize(ne_vv)
    ids.loop[i].element[0].geometry.geometry_type = 2
#Stabilizing plates
for i in range(211,212):
    ids.loop[i].element.resize(ne_sp)
    for j in range (3):
        ids.loop[i].element[j].geometry.geometry_type = 3


# Set metadata and properties for the IDS entry
ids.ids_properties.homogeneous_time = 2 # Set the time mode
to homogeneous
ids.ids_properties.creation_date = "02/10/2024"  # Set the
creation date
ids.ids_properties.comment = "Vacuum Vessel and Stabilizing
Plates" #Add a general comment
ids.ids_properties.provider = "Nicola Massanova (University
of Trieste, CREATE Consortium), E-
mail:nicola.massanova@iter.org"  # Provide data provider
information
ids.ids_properties.source = "DTT2021_05599,DTT2021_04594"
```

```
#Compute area, length and resistance of each loop
for i in range (155):
    area = float(l_a[i])*float(l_b[i])
    resistance = 2*np.pi*float(r[0])*rho_SS316/area
    ids.loop[i].resistance = resistance

for i in range (155,211):
    area = float(vv_w[i-155])*float(vv_h[i-155])
    resistance = 2*np.pi*float(vv_r[i-155])*rho_SS316/area
    ids.loop[i].resistance = resistance

for i in range (211,212):
    area = [(sp_la[0])*float(sp_lb[0]),
float(sp_la[1])*float(sp_lb[1]),float(sp_la[2])*float(sp_lb[2
])]
    resistance =
(2*np.pi*sp_r[0]*rho_SS316/area[0])+(2*np.pi*sp_r[1]*rho_SS31
6/area[1])+(2*np.pi*sp_r[2]*rho_SS316/area[2])
    ids.loop[i].resistance = resistance

# Assign names, identifiers, and geometric properties to
pf_passive components
for i in range(212):
    if i != 211 :
        ids.loop[i].name = ves_names[i]
    else:
        ids.loop[i].name = sp_name

for i in range(155):
    # Set geometry properties
    ids.loop[i].element[0].geometry.oblique.r = float(r[i])
```

```
    ids.loop[i].element[0].geometry.oblique.z = float(z[i])
    ids.loop[i].element[0].geometry.oblique.length_alpha =
float(l_a[i])
    ids.loop[i].element[0].geometry.oblique.length_beta=
float(l_b[i])
    ids.loop[i].element[0].geometry.oblique.alpha =
float(alpha[i])
    ids.loop[i].element[0].geometry.oblique.beta =
float(beta[i])
    ids.loop[i].element[0].turns_with_sign = float(1)

for i in range(155, 211):
    # Set geometry properties
    ids.loop[i].element[0].geometry.rectangle.r =
float(vv_r[i-155])
    ids.loop[i].element[0].geometry.rectangle.z =
float(vv_z[i-155])
    ids.loop[i].element[0].geometry.rectangle.height =
float(vv_h[i-155])
    ids.loop[i].element[0].geometry.rectangle.width =
float(vv_w[i-155])
    ids.loop[i].element[0].turns_with_sign = float(1)

for i in range (211,212):
    for j in range(3):
        ids.loop[i].element[j].geometry.oblique.r =
float(sp_r[j])
        ids.loop[i].element[j].geometry.oblique.z =
float(sp_z[j])
        ids.loop[i].element[j].geometry.oblique.length_alpha
= float(sp_la[j])
```

```
        ids.loop[i].element[j].geometry.oblique.length_beta =
float(sp_lb[j])
        ids.loop[i].element[j].geometry.oblique.alpha =
float(sp_alpha[j])
        ids.loop[i].element[j].geometry.oblique.beta =
float(sp_beta[j])
        if j!=2:
            ids.loop[i].element[j].turns_with_sign = float(1)
        else:
            ids.loop[i].element[j].turns_with_sign = float(-
1)

# Save the pf_passive configuration into the IMAS database
imas_entry.put(ids)



#wall
#FW and Divertor
shot = 116001
run = 1
database = 'DTT_MD'
user ='massann'

imas_entry = imas.DBEntry(imasdef.MDSPLUS_BACKEND, database,
shot, run, user, data_version='3')
imas_entry.create(mode=imasdef.CREATE_PULSE)  # Create a new
pulse entry

ids = imas.wall()
ids.description_2d.resize(1)
ids.description_2d[0].limiter.unit.resize(2)
```

```
ids.ids_properties.homogeneous_time =
imasdef.IDS_TIME_MODE_HOMOGENEOUS
ids.ids_properties.source = "DTT2024_07505,DTT2023_06427"
ids.ids_properties.creation_date = "02/10/2024"  # Set the
creation date
ids.ids_properties.comment = "First Wall and Divertor
outline"  # Add a general comment
ids.ids_properties.provider = "Nicola Massanova (University
of Trieste, CREATE Consortium), E-
mail:nicola.massanova@iter.org"  # Provide data provider
information

ids.description_2d[0].type.index = 1
ids.description_2d[0].limiter.type.name= "Divertor and FW"
ids.description_2d[0].limiter.type.index = 1

#First Wall IDS Specification
ids.description_2d[0].limiter.unit[0].name = "First Wall"
ids.description_2d[0].limiter.unit[0].closed = 0
ids.description_2d[0].limiter.unit[0].outline.r =
np.array(r_wall)
ids.description_2d[0].limiter.unit[0].outline.z =
np.array(z_wall)

#Divertor IDS Specification
ids.description_2d[0].limiter.unit[1].name = "Divertor"
ids.description_2d[0].limiter.unit[1].closed = 0
ids.description_2d[0].limiter.unit[1].outline.r =
np.array(r_div)
ids.description_2d[0].limiter.unit[1].outline.z =
np.array(z_div)
```

```
# Save the wall configuration into the IMAS database
imas_entry.put(ids)
```

Full routine for DTT IMAS integrated equilibrium scenario integration

```
import pandas as pd
from read_eqdsk import read_eqdsk
import numpy as np
import matplotlib.pyplot as plt
from scipy.interpolate import interp1d
import csv
import imas
from imas import imasdef
from read_JINTRAC_DATA import process_core_profiles
from scipy.interpolate import interp1d
import numpy as np
# Read the EQDSK file and extract the data
eqdsk_file =
'Equil_DTT_v16_Ipl_5d5MA_betap_0d65_li_0d8_t_at_43s_COCOS11.e
qdsk'
data = read_eqdsk(eqdsk_file)


# Read Jintrac file and load the core profile data
filename = 'E1(3347)_averaging3345_DTT2023_04519.txt'
output_filename = 'output_data_core.csv'
core_data_dict, data_core_array =
process_core_profiles(filename, output_filename)
rho_tor_norm_JINTRAC = data_core_array[:, 0]
psi_norm_JINTRAC = data_core_array[:, 2]
```

```
f_rho_tor_norm = interp1d(psi_norm_JINTRAC,
rho_tor_norm_JINTRAC, kind='linear',fill_value =
'extrapolate')



# IMAS database setup
shot = 100008
run = 1
database = 'DTT'
user = 'massann'

# Create a new entry in the IMAS database for the specified
shot, run, and user
imas_entry = imas.DBEntry(imasdef.MDSPLUS_BACKEND, database,
shot, run, user, data_version='3')
imas_entry.create(mode=imasdef.CREATE_PULSE)  # Create a new
pulse entry

# Initialize the equilibrium IDS object for writing equilibrium data
eq = imas.equilibrium()
eq.ids_properties.homogeneous_time = 1  # Set time mode to
homogeneous (single time slice)
eq.ids_properties.source = "DTT2024_01493"
eq.ids_properties.provider = "Nicola Massanova (University of
Trieste, CREATE Consortium), E-
mail:nicola.massanova@iter.org"  # Provide data provider
information
```

```
# Resize and set the time slice
eq.time.resize(1)  # Only one time slice
eq.time[0] = 43
eq.time_slice.resize(1)
eq.time_slice[0].time = float(43)  # Set time for the slice

# Set vacuum toroidal field values
eq.vacuum_toroidal_field.r0 = float(data['rcentr'])  # Major radius of the vacuum toroidal field
eq.vacuum_toroidal_field.b0 = np.array([data['bcentr']])  # Toroidal magnetic field at R0

# Plasma boundary (LCFS) settings: r, z, psi values
eq.time_slice[0].boundary.type = 1  # Type of plasma boundary (0 = diverted, 1 = limiter, clarify this)
eq.time_slice[0].boundary.outline.r = np.array(data['rbdry'])
# r-coordinates of plasma boundary
eq.time_slice[0].boundary.outline.z = np.array(data['zbdry'])
# z-coordinates of plasma boundary
eq.time_slice[0].boundary.psi = float(data['sibdry'])  # Poloidal magnetic flux at plasma boundary in Weber

# Global quantities for the time slice
eq.time_slice[0].global_quantities.ip = float(data['cpasma'])
# Plasma current
eq.time_slice[0].global_quantities.magnetic_axis.r = float(data['rmagx'])
# Radial position of the magnetic axis
```

```
eq.time_slice[0].global_quantities.magnetic_axis.z = float(data['zmagx'])
# Vertical position of the magnetic axis

eq.time_slice[0].global_quantities.psi_axis = float(data['simagx'] )   #
Poloidal flux at the magnetic axis in Weber

eq.time_slice[0].global_quantities.psi_boundary = float(data['sibdry'])  #
Poloidal flux at the magnetic axis in Weber


# Initialize 1D array for normalized psi

psi_1d = np.zeros(data['nx'])
psi1d_norm = np.zeros(data['nx'])


# Obtain the necessary quantities from the equilibrium data

psi_axis = eq.time_slice[0].global_quantities.psi_axis
psi_boundary =
eq.time_slice[0].global_quantities.psi_boundary

# Calculate psi_1d and normalize

for i in range(data['nx']):
    # Calculate the non-normalized poloidal flux (psi)

    psi_1d[i] = psi_axis + (psi_boundary - psi_axis) * (i) /
(data['nx'] - 1)


    # Normalize the poloidal flux

    psi1d_norm[i] = (psi_1d[i] - psi_axis) / (psi_boundary -
psi_axis)


# Assign profiles_1d: psi, pressure, and q values

eq.time_slice[0].profiles_1d.psi = psi_1d
```

```
rho_tor_norm_eq_new = f_rho_tor_norm(psi_1d)
eq.time_slice[0].profiles_1d.rho_tor_norm = rho_tor_norm_eq_new

eq.time_slice[0].profiles_1d.psi_norm = psi1d_norm
eq.time_slice[0].profiles_1d.f = np.array(data['fpol'])
eq.time_slice[0].profiles_1d.pressure = np.array(data['pressure'])

eq.time_slice[0].profiles_1d.f_df_dpsi = np.array(data['ffprim']) #FF'

eq.time_slice[0].profiles_1d.dpressure_dpsi   =   np.array(data['pprime'])
#PP'

eq.time_slice[0].profiles_1d.q = np.array(data['qpsi'])


eq.time_slice[0].profiles_1d.rho_tor_norm =
rho_tor_norm_eq_new


# Resize profiles_2d and specify the grid type

eq.time_slice[0].profiles_2d.resize(1)

eq.time_slice[0].profiles_2d[0].grid_type.name = "RZ rectangular"

eq.time_slice[0].profiles_2d[0].grid_type.index = 1

eq.time_slice[0].profiles_2d[0].grid_type.description = "RZ
rectangular free-boundary"


# Extract the r and z grid coordinates from the data

r_values = data.get('r')

z_values = data.get('z')
```

```
# Check and process r and z values
if isinstance(r_values, (np.ndarray, list)) and isinstance(z_values, (np.ndarray, list)):
    r_values = np.array(r_values)  # Convert to numpy arrays if they are lists
    z_values = np.array(z_values)

    # Extract the first column of r and the first row of z for 2D grid
    r_first_column = r_values[:, 0]  # First column of radial grid
    z_first_row = z_values[0, :]     # First row of vertical grid

# Set the grid dimensions and values in profiles_2d
eq.time_slice[0].profiles_2d[0].grid.dim1 = r_first_column  # Set r grid (dim1)
eq.time_slice[0].profiles_2d[0].grid.dim2 = z_first_row     # Set z grid (dim2)
eq.time_slice[0].profiles_2d[0].r = np.array(data['r'])     # Radial grid data
eq.time_slice[0].profiles_2d[0].z = np.array(data['z'])    # Vertical grid data
eq.time_slice[0].profiles_2d[0].psi = np.array(data['psi']) # Poloidal flux values

# Store the equilibrium data in the IMAS database
imas_entry.put(eq)
```

```
# ########################################################################

# ################core_profiles
```

```
# Extract the necessary variables from the core data

rho_tor_norm = data_core_array[:, 0]

rho_pol_norm = data_core_array[:,1]

psi = data_core_array[:, 3] * 2 * np.pi  # psi, scaled by 2*pi

psi_norm = data_core_array[:, 2]

Ti = data_core_array[:,14] * 1e3  # ion temperature in eV

ne = data_core_array[:, 15]  # Electron density

pressure = eq.time_slice[0].profiles_1d.pressure

j_tor = data_core_array [:, 44] #toroidal total current

j_bootstrap = data_core_array[:,46]

j_non_inductive = data_core_array[:,45]



# Create the interpolation functions with extrapolation

f_1 = interp1d(psi_norm, ne, kind='linear',fill_value = 'extrapolate')  #
Interpolating ne as a function of psi

f_2  =  interp1d(psi_norm,  rho_tor_norm,  kind='linear',fill_value  =
'extrapolate')  # Interpolating rho_tor_norm as a function of psi

f_3  =  interp1d(psi_norm,  rho_pol_norm,  kind  =  'linear',  fill_value  =
'extrapolate')

f4 = interp1d(psi_norm, j_tor, kind = 'linear', fill_value = 'extrapolate')

f5=  interp1d(psi_norm,  j_bootstrap,  kind  =  'linear',  fill_value  =
'extrapolate')

f6=  interp1d(psi_norm,  j_non_inductive,  kind  =  'linear',  fill_value  =
'extrapolate')



psi_eq = eq.time_slice[0].profiles_1d.psi
```

```
psi_eq_norm = eq.time_slice[0].profiles_1d.psi_norm


# Perform the interpolation with extrapolation
ne_new = f_1(psi_eq_norm)  # Interpolated ne values
rho_tor_norm_new = f_2(psi_eq_norm)  # Interpolated rho_tor_norm values
rho_pol_norm_new = f_3(psi_eq_norm)
j_tor_new = f4(psi_eq_norm)
j_bootstrap_new = f5(psi_eq_norm)
j_non_inductive_new = f6(psi_eq_norm)


# Interpolate the pressure to the psi_eq grid with extrapolation
# Now, compute Te_new using the formula: Te_new[i] = (pressure_new[i] / ne_new[i]) - Ti_new[i]
Te_new = (pressure / (2*ne_new * 1.6e-19))
Zeff=np.ones(len(Te_new))


# --- Routine to calculate Coulmb's log ei
def coulomb_log(Te, ne):  # Te in eV, ne in SI
    if np.ndim(Te)>0:
        mask1 = Te < 10
        mask2 = Te > 10
        Coulomb_Log = np.copy(Te)
        Coulomb_Log[mask1] = 23.0000 - np.log((ne[mask1]*1e-6)**0.5*Te[mask1]**(-1.5))
```

```
        Coulomb_Log[mask2]     =     24.1513     -     np.log((ne[mask2]*1e-
6)**0.5*Te[mask2]**(-1.0))

    else:

        if (Te<10):

            Coulomb_Log = 23.0000 - np.log((ne*1e-6)**0.5*Te**(-1.5))

        else:

            Coulomb_Log = 24.1513 - np.log((ne*1e-6)**0.5*Te**(-1.0))

    return Coulomb_Log



#Routine to calculate etc_spitzer

def eta_spitzer(Te, ne, Zeff):  # Te in eV, ne in SI, eta in SI

    coef_Zeff                                                                =
Zeff*(1.+1.198*Zeff+0.222*Zeff**2)/(1.+2.966*Zeff+0.753*Zeff**2)        /
((1.+1.198+0.222)/(1.+2.966+0.753))

    eta = 1.65e-9 * coulomb_log(Te, ne) * (Te*0.001)**(-1.5) * coef_Zeff #
From Wesson

    return eta


#Calculating conductivity parallel which is the inverse of  eta_spitzer

conductivity_parallel = 1/(eta_spitzer(Te_new,ne_new,Zeff))


# Initialize the equilibrium IDS object for writing equilibrium data

cp = imas.core_profiles()

cp.ids_properties.homogeneous_time = 1   # Set time mode to homogeneous
(single time slice)
```

```
cp.ids_properties.source = "JINTRAC DATA related to: https://git.frascati.enea.it/theory/falcon/-/blob/master/examples/dtt_full_power_1184/EQDSK_COCOS_02_POS.OUT_jetto_eqdsk_finale_1184.eqdsk?ref_type=heads"

cp.ids_properties.provider = "Nicola Massanova (University of Trieste, CREATE Consortium), E-mail:nicola.massanova@iter.org"   # Provide data provider information


n_time_slice = 1

n_ion = 2


# Resize and set the time slice

cp.time.resize(n_time_slice)

cp.time[0] = 43


cp.profiles_1d.resize(1)

cp.profiles_1d[0].time = float(43)


#Resizing ion and elements

cp.profiles_1d[0].ion.resize(n_ion)

cp.profiles_1d[0].ion[0].element.resize(1)

cp.profiles_1d[0].ion[1].element.resize(1)


#Moving with the other profiles

cp.profiles_1d[0].grid.rho_tor_norm = rho_tor_norm_new

cp.profiles_1d[0].grid.psi = psi_eq
```

```
cp.profiles_1d[0].grid.rho_pol_norm = rho_pol_norm_new

cp.profiles_1d[0].pressure_thermal = pressure

cp.profiles_1d[0].electrons.temperature = Te_new

cp.profiles_1d[0].t_i_average = Te_new

cp.profiles_1d[0].electrons.density = ne_new

cp.profiles_1d[0].zeff= Zeff

cp.profiles_1d[0].conductivity_parallel= conductivity_parallel

cp.profiles_1d[0].grid.psi_magnetic_axis                                    =
eq.time_slice[0].global_quantities.psi_axis

cp.profiles_1d[0].grid.psi_boundary                                         =
eq.time_slice[0].global_quantities.psi_boundary

cp.profiles_1d[0].j_tor = j_tor_new

cp.profiles_1d[0].j_non_inductive = j_non_inductive_new

cp.profiles_1d[0].j_bootstrap = j_bootstrap_new

cp.profiles_1d[0].q = eq.time_slice[0].profiles_1d.q



cp.profiles_1d[0].ion[0].density = ne_new

cp.profiles_1d[0].ion[0].z_ion_1d= np.ones(len(psi_1d))

cp.profiles_1d[0].ion[0].z_ion=float(1)

cp.profiles_1d[0].ion[0].z_ion_square_1d = np.ones(len(psi_1d))

cp.profiles_1d[0].ion[0].element[0].a = float(1)

cp.profiles_1d[0].ion[0].element[0].z_n = float(1)

cp.profiles_1d[0].ion[0].element[0].atoms_n = 1



cp.profiles_1d[0].ion[1].density = ne_new
```

```
cp.profiles_1d[0].ion[1].z_ion_1d= np.ones(len(psi_1d))

cp.profiles_1d[0].ion[1].z_ion=float(1)

cp.profiles_1d[0].ion[1].z_ion_square_1d = np.ones(len(psi_1d))

cp.profiles_1d[0].ion[1].element[0].a = float(1)

cp.profiles_1d[0].ion[1].element[0].z_n = float(1)

cp.profiles_1d[0].ion[1].element[0].atoms_n = 1



cp.vacuum_toroidal_field.r0 = eq.vacuum_toroidal_field.r0

cp.vacuum_toroidal_field.b0 = eq.vacuum_toroidal_field.b0

imas_entry.put(cp)









################################################################################
########## pf_active

# Initialize the IDS

# Set the coil array size to 17, which includes Central Solenoids (CS),
Poloidal Field Coils (PF), and In-Vessel Coils (IVC)

ids = imas.pf_active()

ids.coil.resize(12)  # Resize the coil array to hold 17 coils



#Specify number of elements for each type of coil

ne_cs = 2

ne_pf_ivc =1
```

```
# Resize and configure the coil elements based on their type

for i in range(6):

    ids.coil[i].element.resize(ne_cs)   #CS coils will have two elements each

    for j in range(ne_cs):

        ids.coil[i].element[j].geometry.geometry_type = 2  # Set geometry type for each coil element to "rectangle"



for i in range(6, len(ids.coil)):

    ids.coil[i].element.resize(ne_pf_ivc) #PF and IV coils will have 1 element each

    ids.coil[i].element[0].geometry.geometry_type = 2 #Set geometry type for each coil element to "rectangle"



# Set metadata and properties for the IDS entry

ids.ids_properties.homogeneous_time = 1  # Set the time mode to homogeneous

ids.ids_properties.creation_date = "18/09/2024"  # Set the creation date

ids.ids_properties.comment = "DTT Machine Description for PF/CS Coil System"  # Add a general comment

ids.ids_properties.provider = "Nicola Massanova (University of Trieste, CREATE Consortium), E-mail:nicola.massanova@iter.org"   # Provide data provider information

ids.ids_properties.source = "DTT2024_06730,DTT2024_06731,DTT2020_02293"

ids.time.resize(1)

ids.time[0] = 43

# Define names and identifiers for Central Solenoids and Poloidal Field Coils
```

```
# Central Solenoids: Define names and identifiers

……

# Poloidal Field Coils: Define base names and generate identifiers

……

# In-Vessel Coils (IVC): Define base names and generate identifiers

……

# Define geometric properties and currents for Central Solenoids

……

# Define geometric properties and currents for Poloidal Field Coils

……

# Define geometric properties (no currents set) for In-Vessel Coils (IVC)

……

# Assign names, identifiers, and geometric properties to Central Solenoids

for i in range(6):

……

    ids.coil[i].current.data = np.array(cs_currents[i])


# Assign names, identifiers, and geometric properties to Poloidal Field
Coils

for i in range(6):

……

    ids.coil[i+6].current.data = np.array(pf_currents[i])
```

```
# Save the updated IDS entry to the IMAS database

imas_entry.put(ids)  # Save the IDS entry to the database
```

Annex D – Set of contacts for structural assessment

Frictional contacts

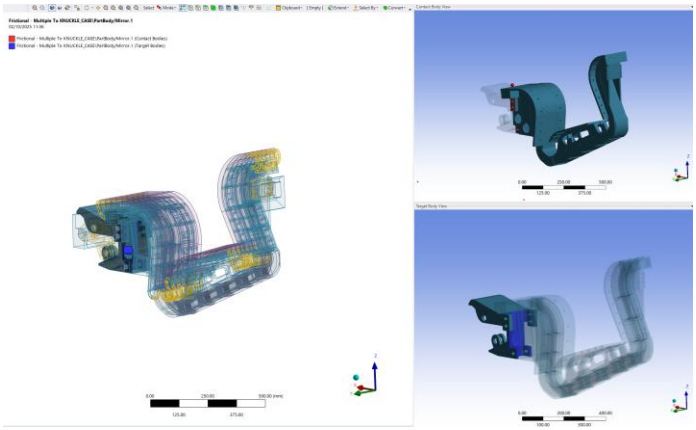

Figure 213 Frictional contacts between knuckle case surfaces and cassette body interface

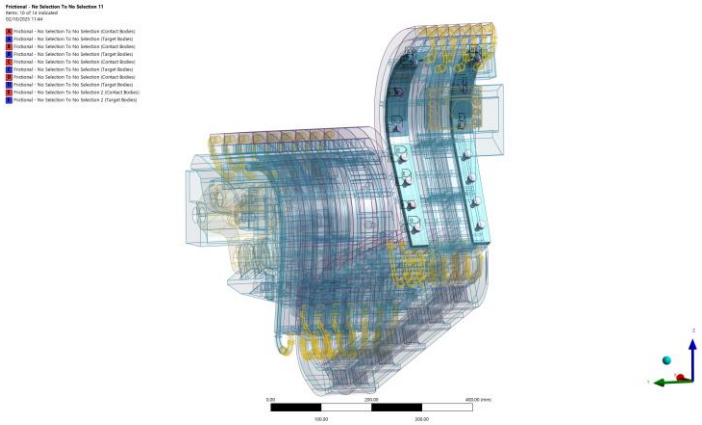

Figure 214 Frictional contacts between IVT connection screws heads and IVT back plate flanges

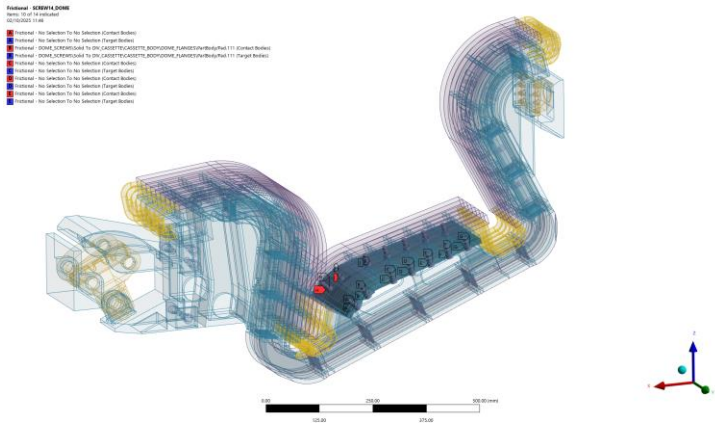

Figure 215 Frictional contacts between Dome connection screws heads and Dome flanges

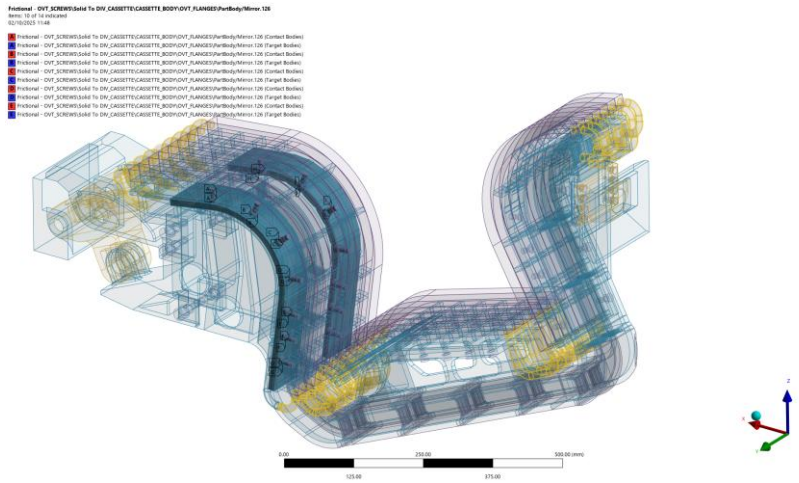

Figure 216 Frictional contacts between OVT connection screws heads and OVT flanges

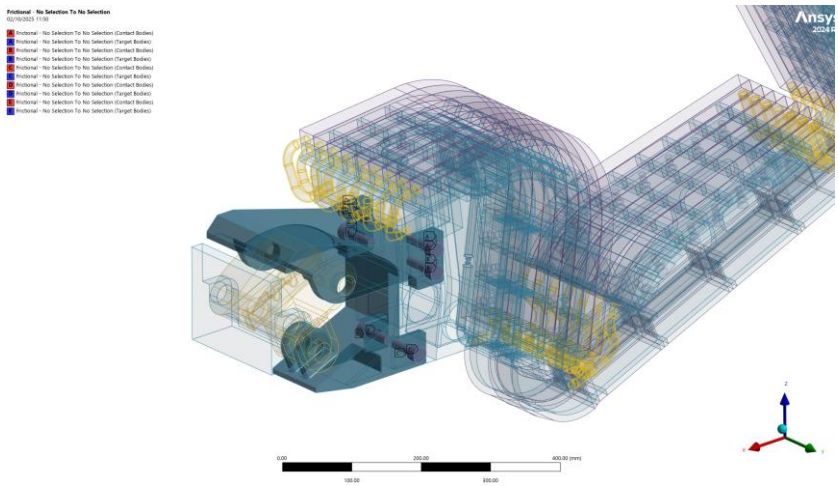

Figure 217 Frictional contacts between knuckle case connection screw heads and knuckle case

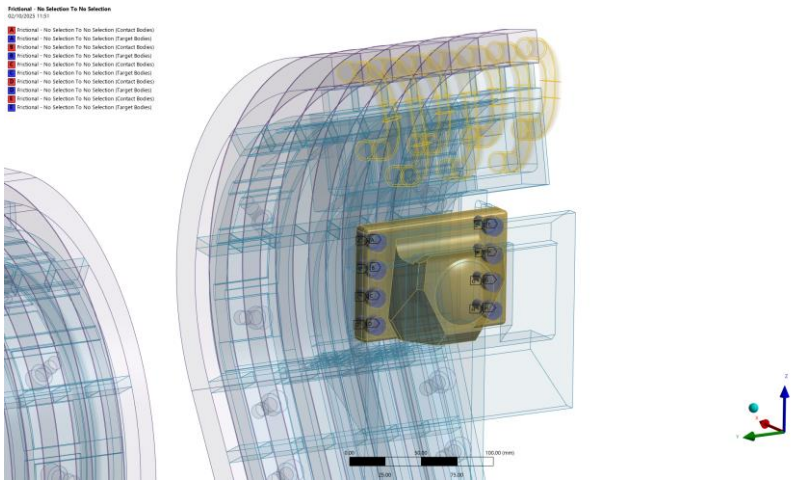

Figure 218 Frictional contacts between nose connection screws heads and nose

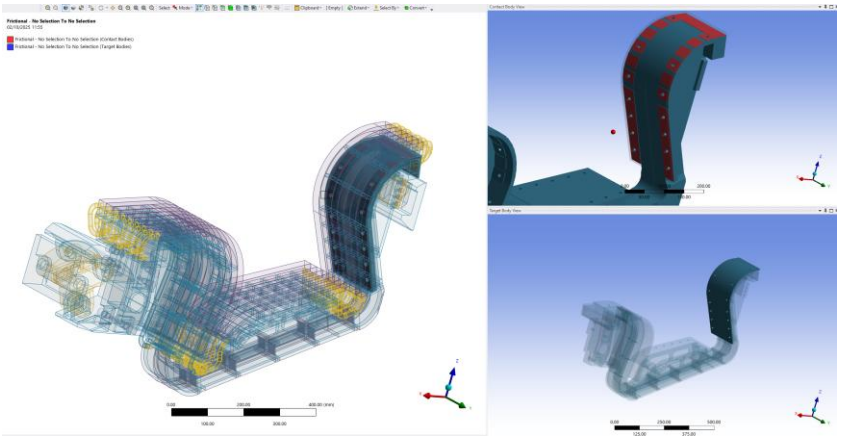

Figure 219 Frictional contacts between IVT back plate and IVT flanges (as shown in figure the connection is faceted type)

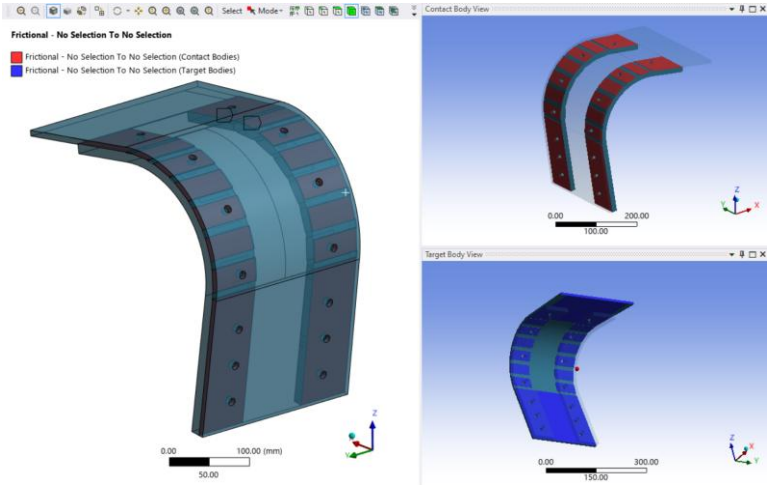

Figure 220 Frictional contacts between OVT back plate and OVT flanges (as shown in figure the connection is faceted type)

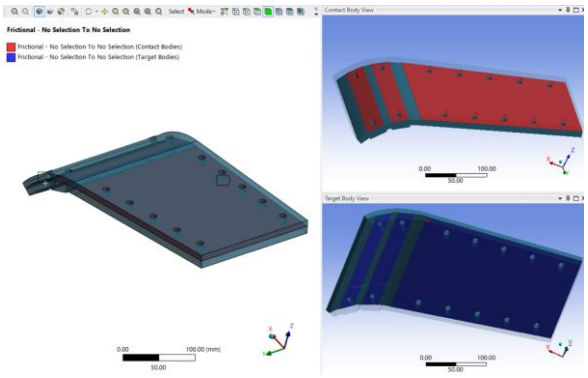

Figure 221 Frictional contacts between Dome back plate and Dome flange (as shown in figure the connection is faceted type)

Bonded contacts

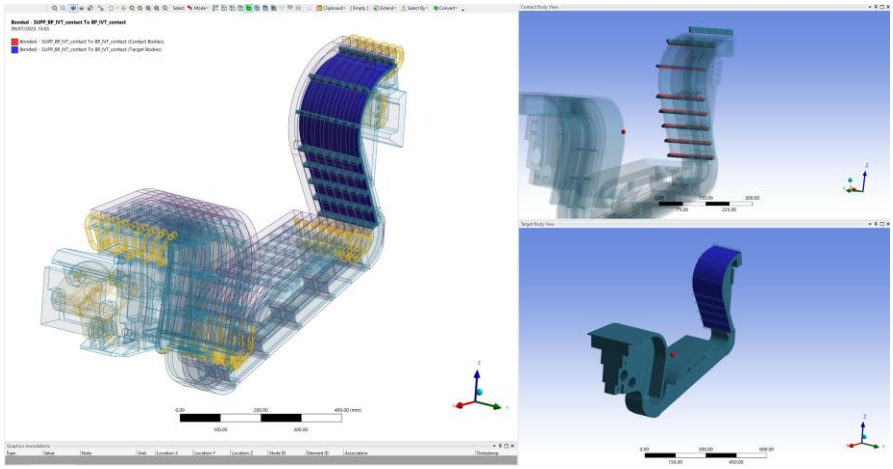

Figure 222 Bonded contacts between IVT back plate and PFU

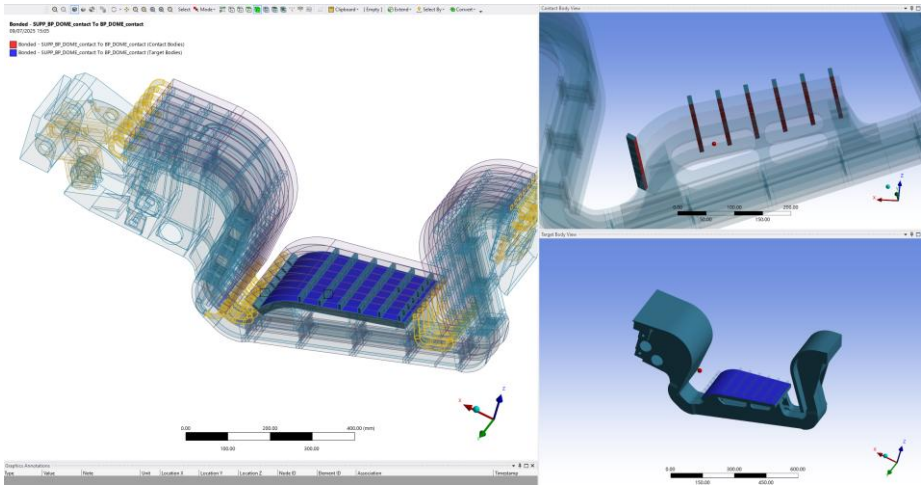

Figure 223 Bonded contacts between DOME back plate and PFU

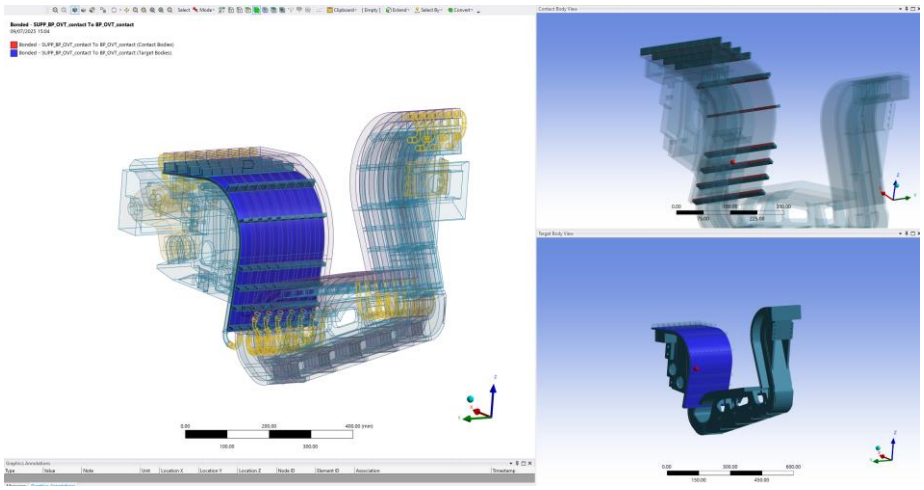

Figure 224 Bonded contacts between OVT back plate and PFU

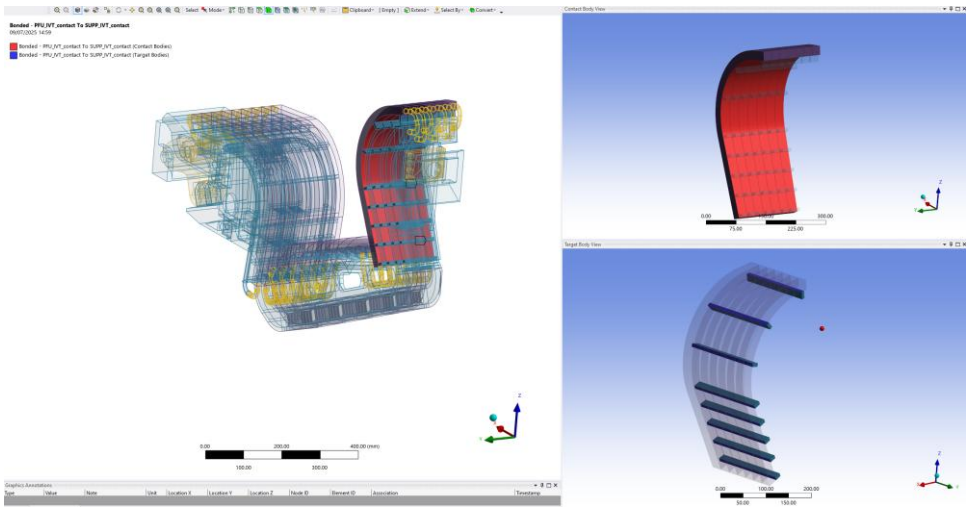

Figure 225 Bonded contacts between IVT PFU and PFU supports

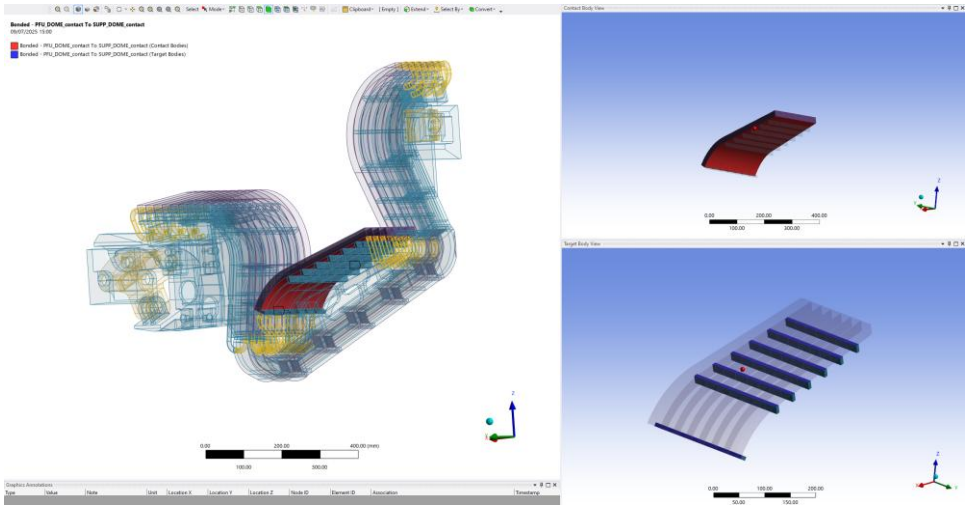

Figure 226 Bonded contacts between DOME PFU and PFU supports

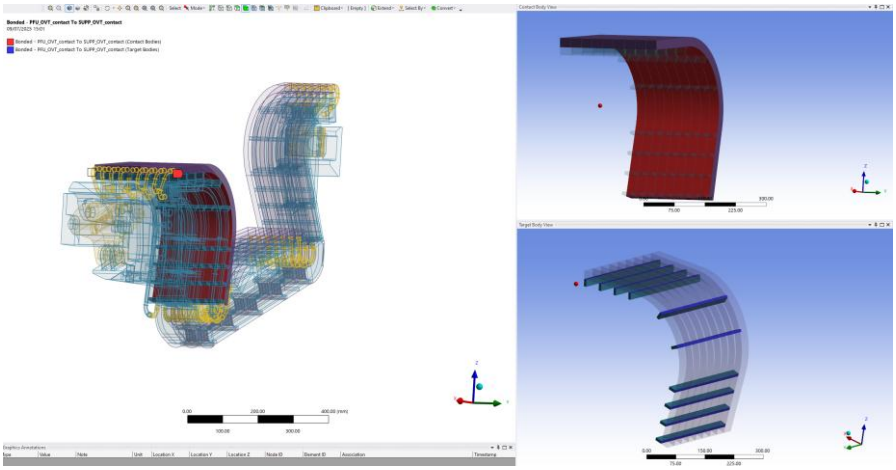

Figure 227 Bonded contacts between OVT PFU and PFU supports

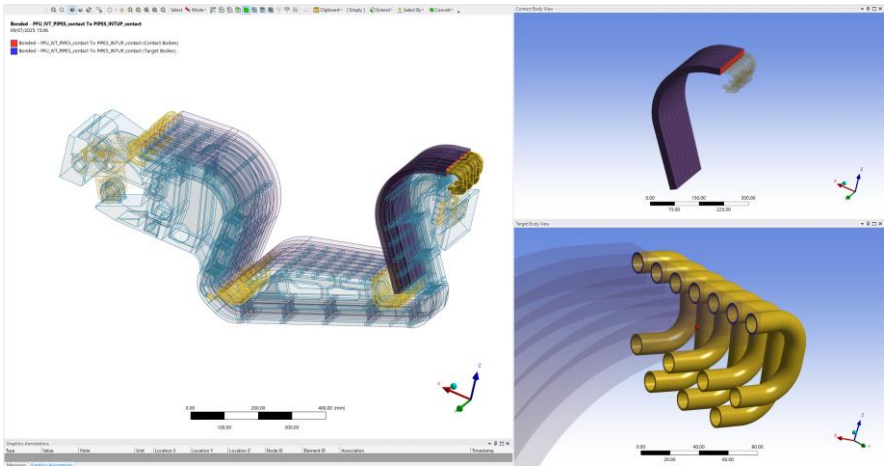

Figure 228 Bonded contacts between upper IVT pipes and PFU

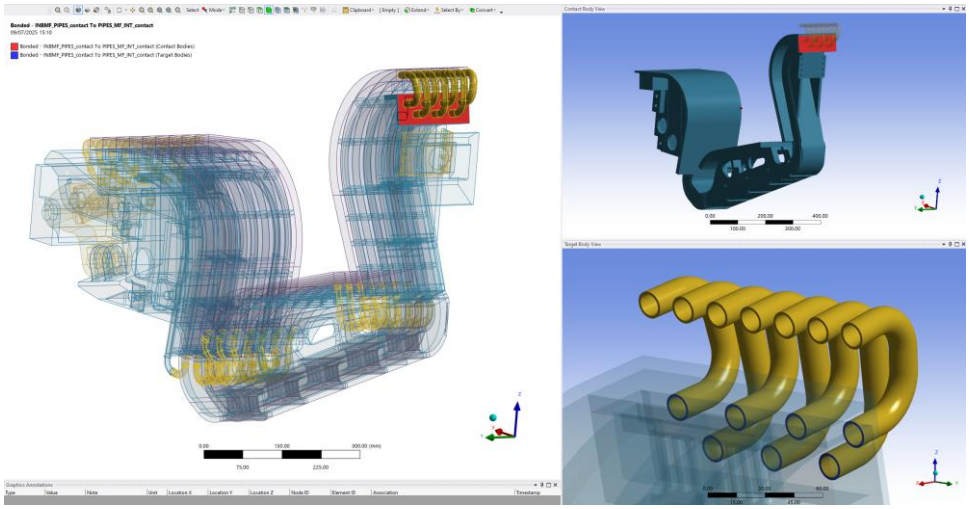

Figure 229 Bonded contacts between inner manifold and IVT upper pipes

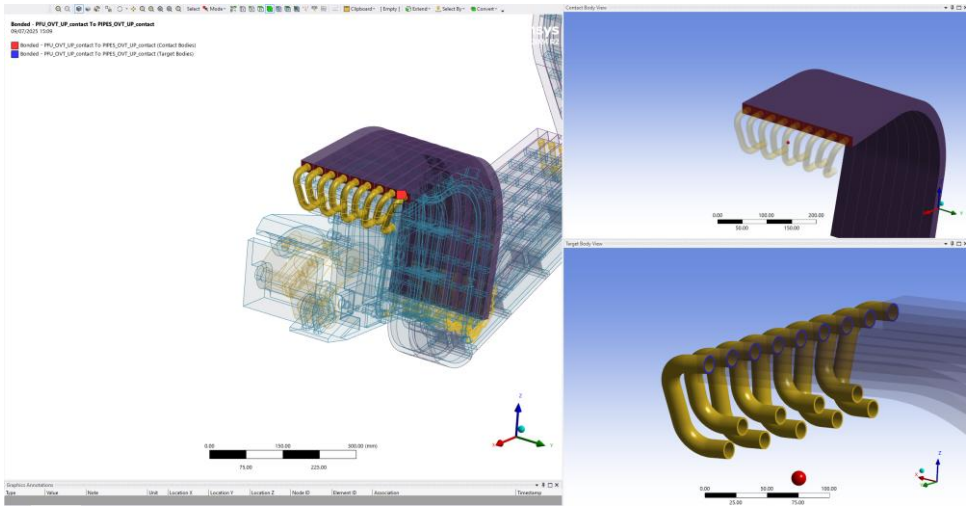

Figure 230 Bonded contacts between OVT upper pipes and PFU

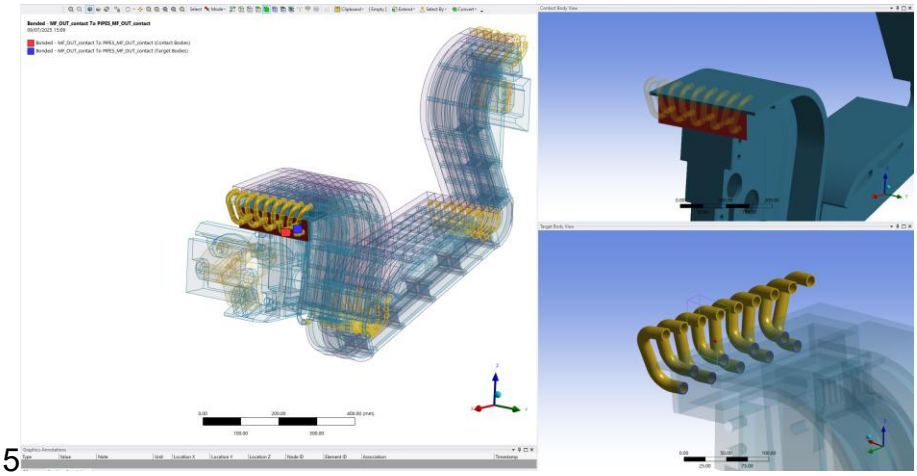

Figure 231 Bonded contacts between outer manifold and OVT upper pipes

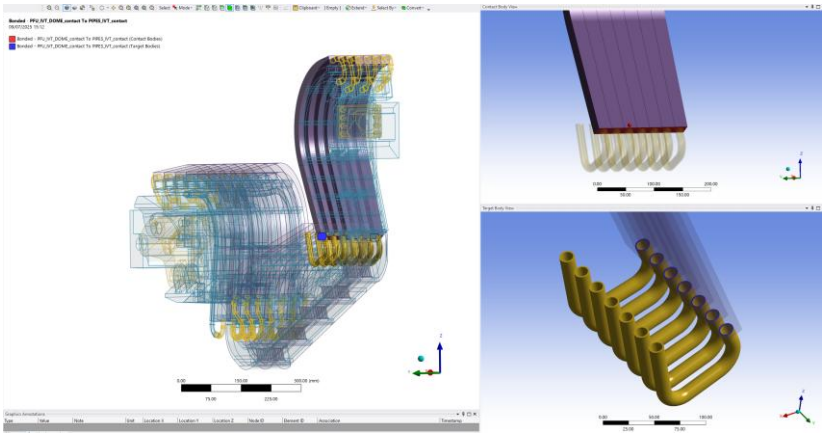

Figure 232 Bonded contacts between DOME-IVT pipes and IVT PFU

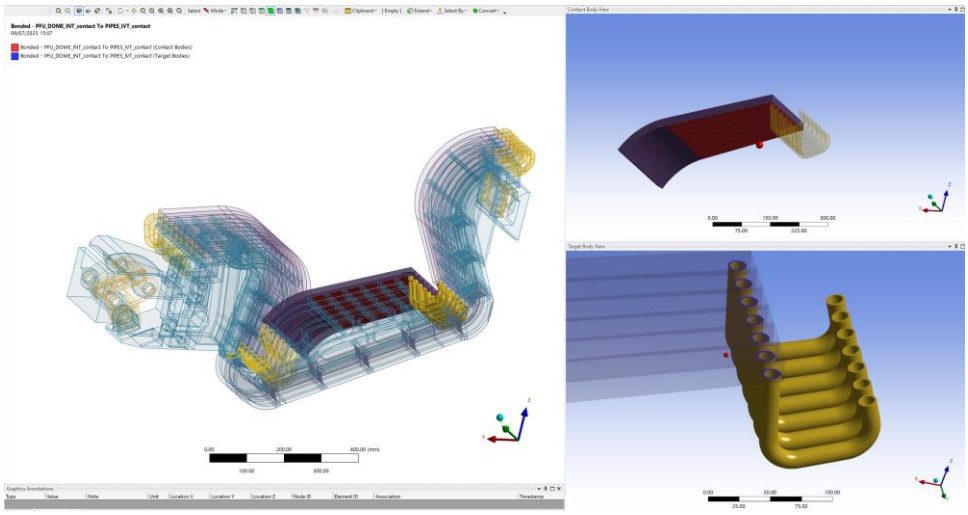

Figure 233 Bonded contacts between DOME-IVT pipes and DOME PFU

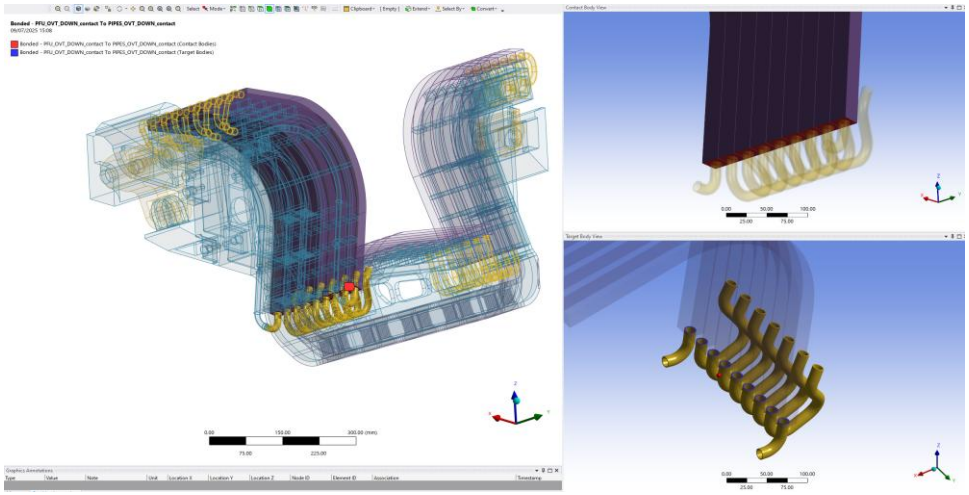

Figure 234 Bonded contacts between DOME-OVT pipes and OVT PFU

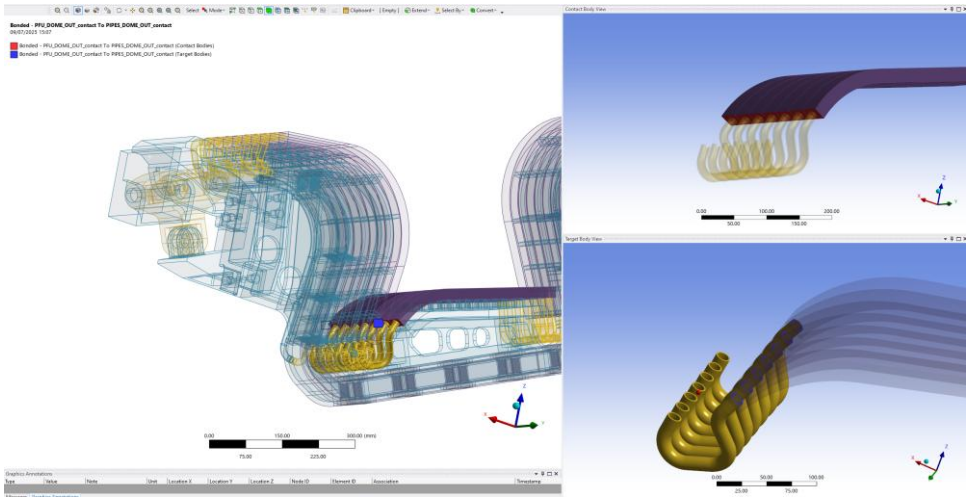

Figure 235 Bonded contacts between DOME-OVT pipes and DOME PFU

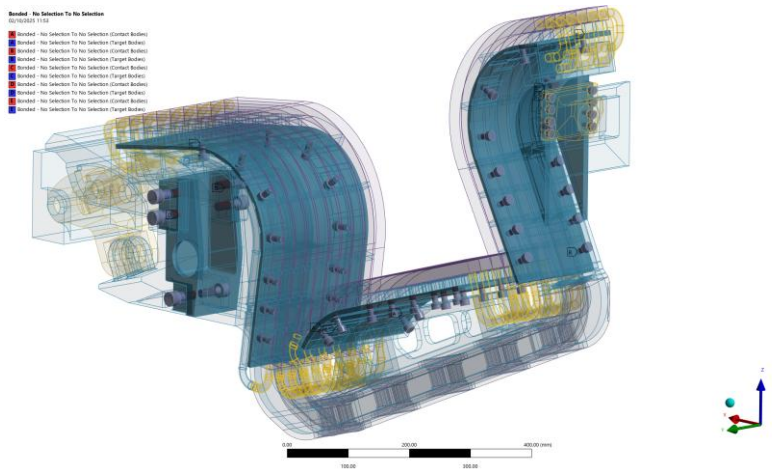

Figure 236 Bonded connections between bolts thread and back plates threaded holes

Annex E – DTT Divertor Fixation System Test Rig Technical Drawings

Knuckle test rig

DTT_DIVERTOR_KNUCKLE_TEST_RIG_DWGs

Wedges fixation system

DTT_DIVERTOR_WEDGE_TEST_RIG_DWGs.p

Geared Knuckle

GEARED_FIXATION_SYSTEM_20250721.pdf

References

[1] PITTS, Richard; BUTTERY, Richard; PINCHES, Simon. Fusion: the way ahead. *Physics World*, 2006, 19.3: 20.

[2] KEILHACKER, M., et al. The scientific success of JET. *Nuclear fusion*, 2001, 41.12: 1925.

[3] ZOHM, H., et al. On the physics guidelines for a tokamak DEMO. *Nuclear Fusion*, 2013, 53.7: 073019.

[4] BOOZER, Allen H. Stellarators as a fast path to fusion. *Nuclear Fusion*, 2021, 61.9: 096024.

[5] AYMAR, R.; BARABASCHI, P.; SHIMOMURA, Y. The ITER design. *Plasma physics and controlled fusion*, 2002, 44.5: 519.

[6] IOKI, Kimihiro, et al. Design improvements and R&D achievements for vacuum vessel and in-vessel components towards ITER construction. *Nuclear fusion*, 2003, 43.4: 268.

[7] WANG, X., et al. Design of ITER vacuum vessel in-wall shielding. *Fusion Engineering and Design*, 2014, 89.7-8: 1814-1819.

[8] ARIOLA, Marco; PIRONTI, Alfredo. *Magnetic control of tokamak plasmas*. London: Springer London, 2008.

[9] SAVARY, F., et al. The toroidal field coils for the ITER project. *IEEE transactions on applied superconductivity*, 2011, 22.3: 4200904-4200904.

[10] GRANUCCI, Gustavo, et al. The heating & current drive system of divertor tokamak test (DTT). In: *2020 IEEE 20th Mediterranean Electrotechnical Conference (MELECON)*. IEEE, 2020. p. 629-633.

[11] YOU, J. H., et al. European DEMO divertor target: Operational requirements and material-design interface. Nuclear materials and Energy, 2016, 9: 171-176.

[12] https://www.energyencyclopedia.com/en/free-downloads/images/tokamak-schematic-diagram-159

[13] TAO, J., et al. ITER coil power supply and distribution system. In: *2011 IEEE/NPSS 24th Symposium on Fusion Engineering*. IEEE, 2011. p. 1-8.

[14] NORDLUND, Kai Henrik, et al. European research roadmap to the realisation of fusion energy. 2018.

[15] Turnyanskiy, M., Neu, R., Albanese, R., Ambrosino, R., Bachmann, C., Brezinsek, S., ... & You, J. H. (2015). European roadmap to the realization of fusion energy: Mission for solution on heat-exhaust systems. *Fusion Engineering and Design*, *96*, 361-364.

[16] ITERRAFFRAY, A. R., et al. High heat flux components—Readiness to proceed from near term fusion systems to power plants. *Fusion Engineering and Design*, 2010, 85.1: 93-108.

[17] ROMANELLI, Francesco, et al. Divertor Tokamak Test facility project: status of design and implementation. *Nuclear Fusion*, 2024, 64.11: 112015.

[18] LABOMBARD, B., et al. ADX: a high field, high power density, advanced divertor and RF tokamak. *Nuclear Fusion*, 2015, 55.5: 053020.

[19] China's superconducting EAST tokamak has been upgraded to test alternative divertor magnetic configurations, though its plasma conditions are still far from reactor-relevant levelsWU, Songtao, et al. An overview of the EAST project. *Fusion Engineering and Design*, 2007, 82.5-14: 463-471.

[20] FEDERICI, G., et al. European DEMO design strategy and consequences for materials. *Nuclear Fusion*, 2017, 57.9: 092002.

[21] LOARTE, Alberto, et al. Plasma detachment in JET Mark I divertor experiments. *Nuclear Fusion*, 1998, 38.3: 331.

[22] ISOBE, Yugo, et al. Characterization of Transition to Detachment of Magnetic Confinement Plasmas via Data Driven Approach in LHD. *Plasma and Fusion Research*, 2025, 20: 1402024.

[23] POLLI, Gian Mario, et al. DTT's role, characteristics & design status. In: *2020 IEEE 20th Mediterranean Electrotechnical Conference (MELECON)*. IEEE, 2020. p. 640-645.

[24] ALBANESE, R., et al. Design review for the Italian divertor tokamak test facility. *Fusion Engineering and Design*, 2019, 146: 194-197.

[25] ZITO, Pietro, et al. Conceptual design and modeling of the toroidal field coils circuit of DTT. In: *2020 IEEE 20th Mediterranean Electrotechnical Conference (MELECON)*. IEEE, 2020. p. 617-622.

[26] GIANNINI, Lorenzo, et al. Magnetostructural calculations and design study of the DTT central solenoid. *IEEE Transactions on Applied Superconductivity*, 2019, 30.4: 1-5.

[27] AMBROSINO, R., et al. The DTT device: Poloidal field coil assessment for alternative plasma configurations. *Fusion Engineering and Design*, 2017, 122: 322-332.

[28] GIANNINI, L., et al. Conceptual design studies of an HTS insert for the DTT central solenoid. *IEEE Transactions on Applied Superconductivity*, 2022, 32.4: 1-5.

[29] DALLA PALMA, M., et al. DTT vacuum vessel, in-vessel coils, and out vessel systems: overview of design and procurement. *Book of Abstracts SOFE 2023*, 2023.

[30] AMBROSINO, Roberto, et al. Magnetic configurations and electromagnetic analysis of the Italian DTT device. *Fusion Engineering and Design*, 2019, 146: 1246-1253.

[31] ITER PITTS, R. A., et al. Status and physics basis of the ITER divertor. *Physica scripta*, 2009, 2009.T138: 014001.

[32] YOU, J. H., et al. Conceptual design studies for the European DEMO divertor: Rationale and first results. *Fusion Engineering and Design*, 2016, 109: 1598-1603.

[33] ITER PITTS, Richard A., et al. A full tungsten divertor for ITER: Physics issues and design status. *Journal of Nuclear Materials*, 2013, 438: S48-S56.

[34] ROCCELLA, Selanna, et al. Armor thickness assessment for the Divertor Tokamak Test facility (DTT) Divertor targets. *IEEE Transactions on Plasma Science*, 2024, 52.9: 4167-4173.

[35] CRISANTI, F., et al. The DTT device: rationale for the choice of the parameters. *Fusion Engineering and Design*, 2017, 122: 288-298.

[36] CAPRINI, Davide, et al. Hydraulic analysis of the DTT divertor module. *Fusion Engineering and Design*, 2025, 219: 115234.

[37] MARZULLO, Domenico, et al. Requirements engineering in complex systems design. In: *International Conference on Design, Simulation, Manufacturing: The Innovation Exchange*. Cham: Springer International Publishing, 2021. p. 658-667.

[38] MARZULLO, Domenico, et al. Iterative and participative axiomatic design process to improve conceptual design of large-scale engineering systems. In: *International Conference of the Italian Association of Design Methods and Tools for Industrial Engineering*. Cham: Springer International Publishing, 2019. p. 492-505.

[39] MARZULLO, Domenico, et al. Mechanical design of ITER radial neutron camera Ex-Port system. *Fusion Engineering and Design*, 2024, 203: 114477.

[40] OSBORNE, Leon F., et al. *Clarus: Concept of operations*. United States. Federal Highway Administration, 2005.

[41] MARZULLO, Domenico, et al. Systems engineering approach for pre-conceptual design of DEMO divertor cassette. *Fusion Engineering and Design*, 2017, 124: 649-654.

[42] INNOCENTE, P., et al. Design of a multi-configurations divertor for the DTT facility. Nuclear Materials and Energy, 2022, 33: 101276.

[43] ROCCELLA, S., et al. Design of the First Divertor in the DTT Facility. In: *32nd Symposium on Fusion Technology (SOFT 2022)*. 2022.

[44] MASSANOVA, N., et al. Parametric design optimization of DTT divertor cassette using a tool for Simulation Process and Data Management. *Fusion Engineering and Design*, 2025, 217: 115117.

[45] YOU, J. H., et al. Conceptual design studies for the European DEMO divertor: Rationale and first results. *Fusion Engineering and Design*, 2016, 109: 1598-1603.

[46] MARZULLO, D., et al. Design progress of DTT divertor fixation system. *Fusion Engineering and Design*, 2024, 203: 114429.

[47] DI GIRONIMO, Giuseppe, et al. Preliminary architecture of the DTT remote handling test and training facility. *Fusion Engineering and Design*, 2023, 195: 113978.

[48] ZOPPOLI, A.; BUONOCORE, S.; DI GIRONIMO, G. Kinematic Simulation of Divertor Remote Handling Equipment for DTT. *IEEE Transactions on Plasma Science*, 2024, 52.9: 4082-4089.

[49] BOSCARY, J., et al. Divertor conceptual design of the European Volumetric Neutron Source. *Fusion Engineering and Design*, 2025, 212: 114861.

[50] MASSANOVA, Nicola, et al. Systems Engineering and Multi-criteria Decision Making Technique for Concept Design of DTT Divertor Fixation System. In: *International Conference of the Italian Association of Design Methods and Tools for Industrial Engineering*. Cham: Springer Nature Switzerland, 2023. p. 225-234.

[51] MARZULLO, Domenico, et al. Experiences of Additive Manufacturing for nuclear fusion applications: the case of the wishbone of the divertor of DEMO project. In: International Joint Conference on Mechanics, Design Engineering & Advanced Manufacturing. Cham: Springer International Publishing, 2022. p. 1030-1041.

[52] MARZULLO, Domenico, et al. Progress in the pre-conceptual CAD engineering of European DEMO divertor cassette. *Fusion Engineering and Design*, 2019, 146: 942-945.

[53] KOMAROV, V., et al. Design progress of the ITER divertor cassette-to-vacuum vessel locking system. *Fusion engineering and design*, 2007, 82.15-24: 1866-1870.

[54] GUERRINI, Laurent, et al. Fabrication of ITER divertor Cassette body prototypes. *Fusion Engineering and Design*, 2021, 162: 112054.

[55] IS-006B Second Cassette rev. 1.1 _DTT2025_04324.

[56] IS-006A Central Cassette_DTT2025_04322.

[57] RHS-2024-RHS-RWP-01_DTT2025_01747.

[58] DIV-IDTT.P.1-T025-D002_2023 Progress on integration, interface issues and critical path analysis_ENEA_DTT2024_01314.

[59] RICCARDO, V., et al. Disruptions and disruption mitigation. *Plasma physics and controlled fusion*, 2003, 45.12A: A269.

[60] ARTOLA, F. J., et al. Modelling of vertical displacement events in tokamaks: status and challenges ahead. *Plasma Physics and Controlled Fusion*, 2024, 66.5: 055015.

[61] WANG, C., et al. The effect of vertical displacements on the runaway electron avalanche in ITER mitigated disruptions. *Nuclear Fusion*, 2024, 65.1: 016012.

[62] IMBEAUX, Frédéric, et al. Design and first applications of the ITER integrated modelling & analysis suite. *Nuclear Fusion*, 2015, 55.12: 123006.

[63] ROMANELLI, M., et al. Code integration, data verification, and models validation using the ITER integrated modeling and analysis system (IMAS) in EUROfusion. *Fusion Science and Technology*, 2020, 76.8: 894-900.

[64] Introduction to the Integrated Modelling & Analysis Suite (IMAS).

[65] IMAS Data Dictionary- pf_active ids.

[66] AMBROSINO, R., et al. The DTT device: Poloidal field coil assessment for alternative plasma configurations. *Fusion Engineering and Design*, 2017, 122: 322-332.

[67] GIANNINI, Lorenzo, et al. Design studies, magnetic calculations and structural assessment for the DTT central solenoid. *IEEE Transactions on Applied Superconductivity*, 2021, 31.5: 1-5.

[68] IMAS Data Dictionary- pf_passive ids.

[69] IMAS Data Dictionary – wall ids.

[70] IMAS Data Dictionary – equilibrium ids.

[71] MUKHOVATOV, V. S.; SHAFRANOV, V. D. Plasma equilibrium in a tokamak. *Nuclear Fusion*, 1971, 11.6: 605.

[72] ROMANELLI, Michele, et al. JINTRAC: a system of codes for integrated simulation of tokamak scenarios. *Plasma and Fusion research*, 2014, 9: 3403023-3403023.

[73] KHAYRUTDINOV, R. R., et al. Comparing DINA code simulations with TCV experimental plasma equilibriumresponses. *Plasma Physics and Controlled Fusion*, 2001, 43.3: 321.

[74] SAUTER, O.; MEDVEDEV, S. Yu. Tokamak coordinate conventions: COCOS. *Computer Physics Communications*, 2013, 184.2: 293-302.

[75] INNOCENTE, P., et al. Design of a multi-configurations divertor for the DTT facility. *Nuclear Materials and Energy*, 2022, 33: 101276.

[76] HOELZL, Matthias, et al. The JOREK non-linear extended MHD code and applications to large-scale instabilities and their control in magnetically confined fusion plasmas. *Nuclear Fusion*, 2021, 61.6: 065001.

[77] SPARAGO, Raffaele; ARTOLA, Francisco Javier; HOELZL, Matthias. Self-consistent full MHD coupling of JOREK and STARWALL for advanced plasma free boundary simulation. *Plasma Physics and Controlled Fusion*, 2025, 67.4: 045021.

[78] HOELZL, M., et al. Coupling JOREK and STARWALL codes for non-linear resistive-wall simulations. In: *Journal of Physics: Conference Series*. IOP Publishing, 2012. p. 012010.

[79] ARTOLA, F. J., et al. Understanding the reduction of the edge safety factor during hot VDEs and fast edge cooling events. *Physics of Plasmas*, 2020, 27.3.

[80] WESLEY, J. C., et al. Disruption characterization and database activities for ITER. In: *Proc. 21st IAEA Fusion Energy Conf., Chengdu, China*. 2006.

[81] ARTOLA, F. J., et al. 3D MHD simulations of unmitigated Vertical Displacements Events in ITER. In: *48th EPS Conference on Plasma Physics*. European Physical Society, 2022.

[82]) BAYLOR, Larry R., et al. Disruption mitigation system developments and design for ITER. *Fusion Science and Technology*, 2015, 68.2: 211-215.

[83] MELARAGNI, Letizia, et al. Preliminary Modeling of Disruption Plasma Scenario in View of a Shattered Pellet Injection in DTT Machine. *Fusion Science and Technology*, 2025, 1-15.

[84] ARTOLA, F. J., et al. Modelling of vertical displacement events in tokamaks: status and challenges ahead. *Plasma Physics and Controlled Fusion*, 2024, 66.5: 055015.

[85] ARTOLA, F. J., et al. Non-axisymmetric MHD simulations of the current quench phase of ITER mitigated disruptions. *Nuclear Fusion*, 2022, 62.5: 056023.

[86] PITTS, R. A., et al. Plasma-wall interaction impact of the ITER re-baseline. *Nuclear Materials and Energy*, 2025, 42: 101854.

[87] PUTVINSKI, S., et al. Halo current, runaway electrons and disruption mitigation in ITER. *Plasma Physics and Controlled Fusion*, 1997, 39.12B: B157.

[88] maxfeahandbook

[89] LOARTE, Alberto. Effects of divertor geometry on tokamak plasmas. *Plasma Physics and Controlled Fusion*, 2001, 43.6: R183.

[90] Appendix_A,_Materials_Design_Limit_Data_222RLN

[91] Memo_on_static_co-efficient_of_friction__VLFDKB

[92] DTT Divertor Description Document

[93] SDC-IC_-_Main_Body_24BE3L

UNIVERSITÀ
DEGLI STUDI
DI TRIESTE

La borsa di dottorato è cofinanziata con risorse dell'Unione europea, NextGeneration EU - Piano Nazionale di Ripresa e Resilienza, Missione 4 – Componente 2 – Investimento 3.3 CUP J92B22000980007